UNIVERSITY OF OXFORD

Electronic Structure of Low-Valent Transition Metal Oxide Phases

Dihao Zeng

New College

supervised by

Prof. John McGrady



A thesis submitted in fulfilment of the requirements for the degree of

Doctor of Philosophy in Inorganic Chemistry

July 2018

"So we beat on, boat against the current, borne back ceaselessly into the past."

F. Scott Fitzgerald

Declaration of Authorship

I, Dihao Zeng, declare that this thesis, titled "Electronic Structure of Low-Valent Transition Metal Oxide Phases", and the work presented in it are my own. I confirm that:

- This work was done wholly while in candidature for the Doctor of Philosophy in Inorganic Chemistry at University of Oxford.
- Where I have consulted the published work of others, this is always clearly attributed.
- Where I have quoted from the work of others, the source is always given. With the exception of such quotations, this thesis is entirely my own work.
- Where the thesis is based on work done by myself jointly with others, I have made clear exactly what was done by others and what I have contributed myself.
- I have acknowledged all main sources of help.

Signed:

_____

Date:

_____

Abstract

UNIVERSITY OF OXFORD

Department of Chemistry

Doctor of Philosophy in Inorganic Chemistry

Electronic Structure of Low-Valent Transition Metal Oxide Phases

Dihao Zeng

Transition metal oxide phases have been studied intensively in recent years due to their flexible chemistry that may potentially lead to novel physical and chemical properties. Low-temperature synthetic strategies allow for the reduction of traditional high-valent transition metal oxides into low-valent ones, where the metal-oxide frameworks have lower dimensions and the central metal cations have lower coordination numbers. In particular, for the perovskite family, the reduced phases consist of two-dimensional layers with the metals located in square-planar coordination environments. The structural stability of these apparently two-dimensional systems comes from the strong intrinsic electronic interactions. In this thesis, the electronic structure of layered oxides containing the low-valent metal cations V^{3+}, Ti^{3+}, Ni^{+} and Ru^{2+} is discussed in detail.

Acknowledgements

Sincerest gratitude to my supervisor, Professor John McGrady, who has always been there for me: whenever I make a progress, he is there, encouraging and inspiring; whenever I make a mistake, he is there, tolerant and considerate.

Deepest love to my parents, without whom my life, let alone this thesis, would not be possible.

Special thanks to my dearest friends, who have made my time in Oxford, and everywhere else, pleasant and unforgettable.

Special thanks to Professor Michael Hayward and Professor Hiroshi Kageyama, who have kindly shared their wisdom during our time of collaboration.

Special thanks to members of the McGrady group and the Paton group in the years from 2013 to 2018, who have always been helpful and awesome to work with.

Contents

Declaration of Authorship i

Abstract ii

Acknowledgements iii

Overview 1

1 Theory: From Molecular to Solid-state Systems 2

1.1 Introduction to Quantum Chemistry 2

1.1.1 The Schrödinger Equation 2

1.1.2 The Born-Oppenheimer Approximation 3

1.1.3 The Variational Theorem 4

1.1.4 Basis Sets for Molecular Systems 5

1.1.5 Molecular Orbitals and Hartree Product 8

1.2 The Hartree-Fock Theory 9

1.2.1 Slater Determinant 9

1.2.2 The Hartree-Fock Energy 10

1.2.3 The Hartree-Fock Equations 11

1.2.4 The Roothaan Equations 12

1.2.5 The Self-consistent-field Method 15

1.2.6 Electron Correlation 17

1.3 Density Functional Theory 17

1.3.1 The Hohenberg-Kohn Theorems . . . 18
1.3.2 The Kohn-Sham Approach . . . 19
1.3.3 Exchange-Correlation Functional . . . 21
1.3.4 The Self-interaction Problem . . . 23
1.4 Extensions to Solid-state Systems . . . 24
1.4.1 Plane Wave and Bloch's Theorem . . . 24
1.4.2 Reciprocal Lattice and First Brillouin Zone . . . 25
1.4.3 The Born-von Karman Boundary Condition . . . 27
1.4.4 k-point Sampling and Energy Cut-off . . . 28
1.4.5 The Hubbard U Approach . . . 29
1.4.6 Representations of the Wavefunction . . . 32
1.4.7 The Projector-augmented-wave Method . . . 36

2 General Introduction: The Family of Perovskite Oxides 38
2.1 Traditional Perovskite Oxides . . . 38
2.2 Layered Perovskite Oxides . . . 41
2.3 The Reduction of Perovskite Oxides . . . 43
2.4 Perovskite Oxyhydrides . . . 45
2.5 The Electronic Structure of $SrFeO_2$ . . . 46

3 $SrVO_2H$: Pressure Dependence and π-blocking Hydrides 51
3.1 Introduction . . . 51
3.2 Summary of Experimental Data . . . 53
3.2.1 Pressure Dependence of the Structure . . . 53
3.2.2 Pressure-induced Insulator-to-Metal Transition . . . 55
3.3 Methodology . . . 57
3.3.1 Expansion of the Primitive Unit Cell . . . 57
3.3.2 Convergence Tests . . . 60
3.3.3 Validation of U_{eff} . . . 61

3.4 Computational Results . . . 62
3.4.1 Electronic Structure at Ambient Pressure . . . 62
3.4.2 Electronic Structure at Elevated Pressure . . . 63
3.4.3 Transmission Analysis . . . 67
3.4.4 Exchange Coupling Pathways . . . 69
3.4.5 Effects of U_{eff} . . . 72
3.5 Discussion . . . 75

4 $SrV_{0.95}Ti_{0.05}O_{1.5}H_{1.5}$: Effects of Titanium-doping **78**
4.1 Introduction . . . 78
4.2 Summary of Experimental Data . . . 80
4.2.1 Reaction Process . . . 80
4.2.2 Structure Comparison . . . 81
4.3 Methodology . . . 82
4.3.1 Construction of the Unit Cells . . . 82
4.4 Computational Results . . . 84
4.4.1 $SrVO_2H$, $SrTiO_2H$ and $SrV_{0.75}Ti_{0.25}O_2H$ . . . 84
4.4.2 $SrCrO_2H$ . . . 85
4.5 Discussion . . . 89

5 $LaSrNiRuO_4$ and $LaSr_3NiRuO_4H_4$: Reduced Perovskite Oxide and Oxyhydride Containing Ru^{2+} **91**
5.1 Introduction . . . 91
5.2 $LaSrNiRuO_4$ . . . 93
5.2.1 Summary of Experimental Data . . . 93
5.2.2 Methodology . . . 95
5.2.3 Computational Results . . . 98
5.2.4 Discussion . . . 100
5.3 $LaSr_3NiRuO_4H_4$ . . . 103

5.3.1 Summary of Experimental Data 103
5.3.2 Methodology 105
5.3.3 Computational Results 106
5.3.4 Discussion 110
5.4 Generalisation 111

Concluding Remarks **112**

References **113**

List of Publications **120**

List of Figures

1.1 A comparison of simplified STO (e^{-r}) and GTO (e^{-r^2}) 7
1.2 The self-consistent-field method 16
1.3 The first Brillouin zone for the face-centred cubic lattice 26
1.4 A qualitative illustration of the solid-state wavefunction 33

2.1 Crystal structure of a cubic ABX_3 phase (A: light green; B: grey; X: red) 38
2.2 Crystal structure of $BiNiO_3$ (Bi: pink; Ni: dark green; O: red) 39
2.3 Crystal structure of $CH_3NH_3PbI_3$ (C: grey; H: yellow; N: blue; Pb: black; I: purple) 40
2.4 Crystal structure of Sr_2FeMoO_6 (Sr: light green; Fe: bronze; Mo: cyan; O: red) 41
2.5 Crystal structures of Sr_2RuO_4, $Sr_3Ru_2O_7$ and $Sr_4Ru_3O_{10}$ (Sr: light green; Ru: purple; O: red) 42
2.6 Crystal structure of $SrFeO_2$ (Sr: light green; Fe: bronze; O: red) 43
2.7 Crystal structure of $Sr_3Fe_2O_5$ (Sr: light green; Fe: bronze; O: red) 44
2.8 Crystal structure of $LaSrCoO_3H_{0.7}$ (La: pink; Sr: light green; Co: brown; O: red; H: yellow) 46
2.9 Electronic configurations of Fe^{2+} in $SrFeO_2$ 47
2.10 PDOS of $SrFeO_2$ 48
2.11 The G-type antiferromagnetic structure of $SrFeO_2$ (only the Fe atoms are shown) 49

3.1 Crystal structure of $SrVO_2H$ (Sr: light green; V: blue; O: red; H: yellow) 52

3.2 Side-view of the crystal structure of $SrVO_2H$ . . . 52
3.3 Pressure dependence of lattice parameters for the experimental (red) and the DFT-computed (blue) values of $SrVO_2H$ (solid lines represent linearised Birch-Murnaghan fits to the data) . . . 53
3.4 Relative lattice parameters, a/a_0 and c/c_0, of $SrVO_2H$ (red), $SrFeO_2$ (green) and $SrVO_3$ (blue) as functions of pressure (Solid lines represent linearised Birch-Murnaghan fits to the data) . . . 54
3.5 Electrical resistance of $SrVO_2H$ under external pressure . . . 56
3.6 Temperature dependence of the resistance of $SrVO_2H$ at various pressures . . . 56
3.7 Primitive unit cell of $SrVO_2H$ . . . 58
3.8 $\sqrt{2} \times \sqrt{2} \times 2$ expansion of the primitive unit cell of $SrVO_2H$, for the exploration of magnetic properties . . . 58
3.9 Four distinct magnetic configurations of $SrVO_2H$ (Only the V^{3+} cations are shown) . . . 59
3.10 PDOS plots and band structures of $SrVO_2H$ at three distinct levels of pressure . . . 64
3.11 The first Brillouin zone of a tetragonal unit cell . . . 65
3.12 Variation of band structures of $SrVO_2H$ as a function of lattice parameters a and c (units in Å) . . . 66
3.13 Total DOS plots of $SrVO_2H$ obtained from VASP and ATK . . . 68
3.14 Transmission spectrum of $SrVO_2H$ . . . 68
3.15 $\sqrt{2} \times 2\sqrt{2} \times 2$ expanded cells of $SrVO_2H$ in five magnetic configurations 70
3.16 Schematic picture of exchange coupling pathways of $SrVO_2H$ for the intra- and inter-plane antiferromagnetism . . . 73
3.17 Pressure-dependent PDOS of $SrVO_2H$ computed using different computational protocols . . . 74

4.1 Crystal structure of $SrV_{0.95}Ti_{0.05}O_{1.5}H_{1.5}$ (Sr: light green; V: blue; Ti: grey; O: red; H: yellow) . . . 79
4.2 Schematic diagram qualitatively showing the difference in activation energy for the reduction of $SrVO_3$ and $SrV_{0.95}Ti_{0.05}O_3$ . . . 80
4.3 *trans*-$SrVO_2H$ and five hypothetical structures . . . 83
4.4 Orbital illustrations and PDOS of *trans*-$SrVO_2H$ and *cis*-$SrTiO_2H$ . . . 86
4.5 Structures and PDOS of *trans*- and *cis*-$SrCrO_2H$ . . . 88

5.1 Crystal structures of $LaSrNiRuO_4$ and $LaSr_3NiRuO_4H_4$ (La: pink; Sr: light green; Ni: dark green; Ru: purple; O: red; H: yellow) . . . 92
5.2 Magnetic moments (black arrows) and bond lengths (units in Å) of $LaSrNiRuO_4$ at 300 K and 5 K (La^{3+}/Sr^{2+} cations are omitted and O^{2-} anions are shown as displacement ellipsoids) . . . 94
5.3 F, C and A magnetic configurations of $LaSrNiRuO_4$ . . . 98
5.4 Computed spin density (in brackets) and bond lengths for the F configuration of $LaSrNiRuO_4$ . . . 100
5.5 PDOS and electronic configurations for $LaSrNiRuO_4$ . . . 101
5.6 Crystal structures of $LaSrNiRuO_6$ and $LaSr_3NiRuO_8$ . . . 104
5.7 $2\sqrt{2} \times 2\sqrt{2} \times 1$ expansion of the primitive unit cell of $LaSr_3NiRuO_4H_4$ in "checkerboard" configuration (La^{3+} and Sr^{2+} cations are omitted) . . . 105
5.8 F, AF0, AF1 and AF2 configurations of $LaSr_3NiRuO_4H_4$ . . . 107
5.9 PDOS and electronic configurations for $LaSr_3NiRuO_4H_4$ . . . 108
5.10 Structures and PDOS for the "checkerboard", "striped" and "double-striped" configurations of $LaSr_3NiRuO_4H_4$ (the labels of orbitals are omitted) . . . 109

List of Tables

2.1 Computed J_1 and J_2 values of $SrFeO_2$ 49

3.1 Linear compressibilities of $SrVO_2H$, $SrFeO_2$ and $SrVO_3$ at ambient pressure 55
3.2 Convergence test for $SrVO_2H$: energy cut-off 60
3.3 Convergence test for $SrVO_2H$: **k**-point sampling 61
3.4 Effect of U_{eff} on the lattice parameters of $SrVO_2H$ 62
3.5 Energy of the G, C, A, X and F configurations 72

4.1 Experimental lattice parameters 82
4.2 Computed energy and lattice parameters of the six structures 84
4.3 Computed energy and lattice parameters of the *trans*- and *cis*-$SrCrO_2H$ 87

5.1 Test of U_{eff} on Ni and Ru based on the F configuration 96
5.2 Computed energy of the F, C and A configurations 99
5.3 Computed energy of the F, AF0, AF1 and AF2 configurations 106
5.4 Computed energy and lattice parameters of the "checkerboard", "striped" and "double-striped" configurations of $LaSr_3NiRuO_4H_4$ 110

Abbreviations

AO	Atomic orbital
MO	Molecular orbital
STO	Slater-type orbital
GTO	Gaussian-type orbital
SCF	Self-consistent-field
HF	Hartree-Fock
DFT	Density functional theory
KS	Kohn-Sham
LDA	Local density approximation
LSDA	Local spin-density approximation
BZ	Brillouin zone
APW	Augmented plane-wave
LAPW	Linearised augmented plane-wave
OPW	Orthogonalised plane-wave
AE	All-electron
PS	Pseudo
PAW	Projector-augmented-wave
DOS	Density of states
PDOS	Projected density of states

For my parents

Overview

This thesis discusses in detail the projects that I worked on during my D.Phil study at University of Oxford, under the supervision of Professor John McGrady. By performing first principle calculations on representative examples of low-valent transition metal oxide phases, namely $SrVO_2H$, the Ti-doped analogues of $SrVO_2H$, the two Ru^{2+}-containing phases $LaSrNiRuO_4$ and $LaSr_3NiRuO_4H_4$, we hope to obtain non-superficial understandings about these systems and discover general trends on their electronic structure. The thesis has been structured as follows:

Chapter 1 gives a brief introduction to the methodology that we employed in our calculations, with focuses on the Hartree-Fock method, the Density Functional Theory, and the applications of them on solid state systems.

Chapter 2 introduces the traditional perovskite oxide systems, the Ruddlesden-Popper phases, reduced oxides and oxyhydrides, followed by an emphasis on the electronic structure of the well-known $SrFeO_2$ system.

Chapter 3 analyses the electronic structure of the $SrVO_2H$ system at both ambient and elevated pressure, focusing on investigating the pressure-induced metal-insulator transition and establishes the theory of π-blocking hydrides.

Chapter 4 discusses doping Ti^{3+} ions into the $SrVO_2H$ phases, analysing the correlation of the *d*-electron count and the crystal structure.

Chapter 5 compares the structures and electronic properties of $LaSrNiRuO_4$ and $LaSr_3NiRuO_4H_4$ systems, providing a general observation on the relationship of the *d*-electron count and the occupancy of d_{z^2} orbital.

Chapter 1

Theory: From Molecular to Solid-state Systems

1.1 Introduction to Quantum Chemistry

The systems of interest in this thesis are transition metal oxides and their derivatives in solid-state phases. To understand the properties of these systems, the details of their components, namely nuclei and electrons, must be studied. For this purpose, quantum chemistry, the chemical application of quantum mechanics, needs to be employed. Before going into the solid-state applications of quantum chemistry, we have to, inevitably, make a detour to first look at molecular systems, because most of the development of quantum chemistry mainly focuses on such systems[1]. The techniques required to deal with solid-state systems will be covered later in this chapter.

1.1.1 The Schrödinger Equation

Our systems of interest can be studied by solving the well-known time-independent Schrödinger equation[2]:

$$\mathcal{H}\Psi = E\Psi \tag{1.1}$$

where the wavefunction Ψ contains all information of the system. The Hamiltonian is the sum of the kinetic energy operator $\mathcal{T}$ and the potential energy operator $\mathcal{V}$:

$$\mathcal{H} = \mathcal{T} + \mathcal{V} \tag{1.2}$$

These systems normally contain more than one nucleus and electron. For many-body systems, the Schrödinger equation can be written as:

$$\mathcal{H}\Psi(\mathbf{x}_1, \mathbf{x}_2, \ldots, \mathbf{x}_N, \mathbf{R}_1, \mathbf{R}_2, \ldots, \mathbf{R}_M) = E\Psi(\mathbf{x}_1, \mathbf{x}_2, \ldots, \mathbf{x}_N, \mathbf{R}_1, \mathbf{R}_2, \ldots, \mathbf{R}_M) \tag{1.3}$$

where the vectors $\mathbf{x}_1, \mathbf{x}_2, \ldots, \mathbf{x}_N$ and $\mathbf{R}_1, \mathbf{R}_2, \ldots, \mathbf{R}_M$ denote the coordinates of the N electrons (both spatial and spin) and the M nuclei (spatial only), respectively. In atomic units and without relativistic corrections, the total Hamiltonian for a system consisting of nuclei and electrons can be explicitly written as:

$$\mathcal{H} = -\frac{1}{2}\sum_{i=1}^{N}\nabla_i^2 - \frac{1}{2}\sum_{A=1}^{M}\frac{1}{M_A}\nabla_A^2 - \sum_{i=1}^{N}\sum_{A=1}^{M}\frac{Z_A}{r_{iA}} + \sum_{i=1}^{N}\sum_{j>i}^{N}\frac{1}{r_{ij}} + \sum_{A=1}^{M}\sum_{B>A}^{M}\frac{Z_A Z_B}{R_{AB}} \tag{1.4}$$

where i and j denote the N electrons, A and B run over the M nuclei in the system. The first two terms describe the kinetic energy of the electrons and nuclei, respectively, where M_A is the mass of the nucleus A. The remaining three terms are the potential energy operators that represent electron-nucleus attraction, electron-electron repulsion and nucleus-nucleus repulsion, respectively.

1.1.2 The Born-Oppenheimer Approximation

The Hamiltonian can be simplified if we consider the fact that the nuclei are much heavier than the electrons – the mass of the lightest nucleus possible, a proton, is $\sim$1800 times larger than that of an electron[3]. Due to their significantly greater mass,

the velocities of the nuclei are substantially smaller than those of the electrons. Therefore, as a reasonably good approximation, we can treat the system as if the electrons are moving in the field of fixed nuclei, resulting in a zero kinetic energy of the nuclei and a constant nucleus-nucleus repulsion. This is the famous Born-Oppenheimer approximation[4], which eliminates the second and the final terms of the total Hamiltonian, leading to its reduction to the electronic Hamiltonian:

$$\mathcal{H}_{\text{elec}} = -\frac{1}{2}\sum_{i=1}^{N}\nabla_i^2 - \sum_{i=1}^{N}\sum_{A=1}^{M}\frac{Z_A}{r_{iA}} + \sum_{i=1}^{N}\sum_{j>i}^{N}\frac{1}{r_{ij}} = \mathcal{T} + \mathcal{V}_{\text{Ne}} + \mathcal{V}_{\text{ee}} \tag{1.5}$$

The Schrödinger equation then becomes:

$$\mathcal{H}_{\text{elec}}\Psi_{\text{elec}}(\mathbf{x}_1, \mathbf{x}_2, \ldots, \mathbf{x}_N) = E_{\text{elec}}\Psi_{\text{elec}}(\mathbf{x}_1, \mathbf{x}_2, \ldots, \mathbf{x}_N) \tag{1.6}$$

where Ψ_{elec} is the electronic wavefunction. The total energy is then the sum of the electronic energy and the constant nucleus-nucleus repulsion:

$$E = E_{\text{elec}} + \sum_{A=1}^{M}\sum_{B>A}^{M}\frac{Z_A Z_B}{R_{AB}} \tag{1.7}$$

1.1.3 The Variational Theorem

Now that the form of the energy operator, the Hamiltonian, is clear, we can move on to look at the energy E in the Schrödinger equation, which is the expectation value of $\mathcal{H}$. This value is not the true energy of the system unless the wavefunction and the Hamiltonian are exact, which is normally not the case with the exceptions of one-electron systems such as H, He^+, Li^{2+}, *etc*. For many-electron systems where the Schrödinger equation can not be solved analytically, the application of the variational theorem[4] is crucial. The variational theorem states that the energy calculated from any trial wavefunction must be greater than or equal to the true ground-state energy

of the system:

$$E_{\text{trial}} = \frac{\int \cdots \int \Psi^*_{\text{trial}} \mathcal{H} \Psi_{\text{trial}} \mathrm{d}\mathbf{x}_1 \mathrm{d}\mathbf{x}_2 \cdots \mathrm{d}\mathbf{x}_N}{\int \cdots \int \Psi^*_{\text{trial}} \Psi_{\text{trial}} \mathrm{d}\mathbf{x}_1 \mathrm{d}\mathbf{x}_2 \cdots \mathrm{d}\mathbf{x}_N} = \frac{\langle \Psi_{\text{trial}} | \mathcal{H} | \Psi_{\text{trial}} \rangle}{\langle \Psi_{\text{trial}} | \Psi_{\text{trial}} \rangle} \geq E_0 \tag{1.8}$$

where $\mathcal{H}$ must be time-independent and Ψ_{trial} must be well-behaved (Ψ_{trial} must be finite and single-valued, both Ψ_{trial} and its first derivative must be continuous).

1.1.4 Basis Sets for Molecular Systems

The variational theorem provides a mathematical tool to approach the ground-state energy, for which the explicit forms of the trial wavefunctions are needed. For many-body molecular systems, the basic building blocks are atomic wavefunctions, or in a more chemical language, atomic orbitals (AOs), which in spherical coordinates take the form:

$$\phi_{nlm}(\mathbf{r}) \equiv \phi_{nlm}(r, \theta, \varphi) = R_n(r) Y_{lm}(\theta, \varphi) \tag{1.9}$$

where n is the principal quantum number, l is the angular-momentum quantum number and m is the magnetic quantum number of the individual atomic orbital. The radial part $R(r)$ controls the size while the angular part $Y(\theta, \varphi)$ determines the shape of the atomic orbital. For one-electron atoms, both of these two terms can be expressed analytically. For many-electron atoms, $Y(\theta, \varphi)$ stays unchanged while $R(r)$ has to take some approximated forms.

The exact forms of $R(r)$ for one-electron atomic orbitals generally have some e^{-r} dependence. For example, the analytic expression of the 2s orbital is written as[5]:

$$\phi_{2s}(r, \theta, \varphi) = R_2(r) Y_s(\theta, \varphi) = \frac{1}{4\sqrt{2\pi}} \left(\frac{Z}{a_0}\right)^{\frac{3}{2}} \left(2 - \frac{Zr}{a_0}\right) e^{-\frac{Zr}{2a_0}} \tag{1.10}$$

where a_0 is the Bohr radius ($\sim$0.53 Å) and Z is the nuclear charge. For s orbitals $Y(\theta, \varphi)$ is unity.

For many-electron atoms, the wavefunctions have to be approximated with sets of one-electron atomic wavefunctions, the so-called basis sets. The most frequently employed ones in molecular calculations are the Slater-type orbitals (STOs)[6] and the Gaussian-type orbitals (GTOs)[7]. An STO can be written as:

$$\phi_{nlm}(r,\theta,\varphi) \sim r^{n-1}e^{-\zeta r}Y_{lm}(\theta,\varphi) \tag{1.11}$$

where ζ is the orbital exponent and can be determined by, for example, applying the variational theorem to $\phi_{nlm}(r,\theta,\varphi)$. When higher accuracy is needed, two (or more) STOs can be combined to form a double-ζ expansion:

$$\phi_{nlm}(r,\theta,\varphi) \sim r^{n-1}(c_1e^{-\zeta_1 r} + c_2e^{-\zeta_2 r})Y_{lm}(\theta,\varphi) \tag{1.12}$$

where now the energy is minimised with respect to ζ_1 and ζ_2. Comparing Equation 1.10 and 1.11, it can be seen that an STO resembles the exact form of a one-electron atomic wavefunction in that the form of exponential is e^{-r}. This is the main advantage of using STOs to form basis sets – it is the most straightforward and natural way to do!

On the other hand, the general expression for a GTO is:

$$\phi_{nlm}(x,y,z) \sim x^i y^j z^k e^{-\zeta r^2} \tag{1.13}$$

which is typically expressed in Cartesian coordinates. Here i, j and k are non-zero integers describing the angular-momentum contribution, with $i+j+k = 0/1/2/3$ for $s/p/d/f$ orbitals, respectively. Comparing the shape of a simplified STO and a GTO (Figure 1.1), it is immediately seen that the latter deviates severely from the true atomic wavefunction (represented by the former), especially at the limits of large/small electron-nucleus distance, namely the "centres" and "tails" of the wavefunction. The great convenience of GTOs, however, lies in the significantly improved

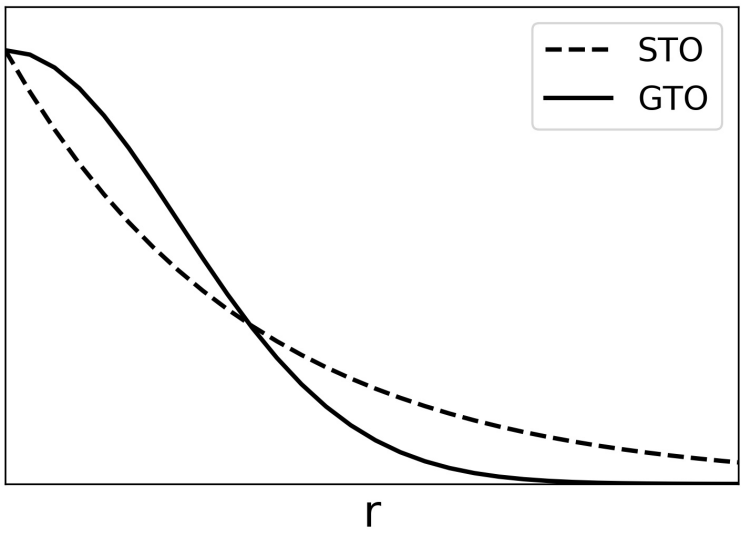


FIGURE 1.1: A comparison of simplified STO (e^{-r}) and GTO (e^{-r^2})

efficiency that they offer in the evaluation of integrals, simply because the product of two GTOs is just a single GTO on a different centre with a different orbital exponent. This is the greatest property of GTOs that the STOs do not share[8]. To take advantage of this convenience and to improve the quality of the basis sets, it has proved useful to form linear combinations of several GTOs, in order to mimic the shape of a single STO:

$$e^{-\zeta r} = c_1 e^{-\zeta_1 r^2} + c_2 e^{-\zeta_2 r^2} + c_3 e^{-\zeta_3 r^2} + \cdots \tag{1.14}$$

If n GTOs are used to fit one STO, the basis set is termed STO-nG, as in the famous STO-3G. A better basis set is designated as 3-21G, which means the core region is described by three primitive Gaussian functions, the valence region is constructed by two, with another more diffuse one added. Therefore, the 3-21G is of double-ζ quality, analogous to the similar construction for STOs (Equation 1.12). There is a large number of other more accurate basis sets available, and for any given problem, the choice of which ones to use relies heavily on previous experience[5, 9].

1.1.5 Molecular Orbitals and Hartree Product

Now that we have identified a correct form for the atomic orbitals, we are ready to generate the more advanced building blocks of the many-body wavefunctions, the molecular orbitals (MOs). In order to do this, the linear combination of atomic orbitals (LCAO) approximation[10, 11] is normally employed:

$$\psi_i(\mathbf{r}) = \sum_\mu C_{\mu i}\phi_\mu(\mathbf{r}) \tag{1.15}$$

where the atomic orbital $\phi_\mu(\mathbf{r})$ is the μ-th component of the i-th molecular orbital $\psi_i(\mathbf{r})$.

We know from the Pauli exclusion principle that a one-electron wavefunction is uniquely identified by four quantum numbers: the n, l, m alluded to above, and the spin quantum number, m_s. However, the atomic orbitals (Equation 1.9) that constitute the molecular orbitals are only dependent on the first three, with the dependence on m_s missing. Therefore, to completely describe one-electron wavefunctions, the spin-dependence needs to be absorbed and thus the definition of the spin orbital:

$$\chi_i(\mathbf{x}) = \psi_i^\sigma(\mathbf{r})\sigma(s) \qquad \sigma = \alpha/\beta \tag{1.16}$$

where the orthonormal functions $\alpha(s)/\beta(s)$ describe the spin up ($\uparrow$)/spin down ($\downarrow$) character of electrons, respectively. A spin orbital is the product of a spatial (molecular) orbital and one of the two spin functions.

If we now consider the electrons to be independent, with the repulsion neglected, the total wavefunction Ψ can be expressed as a product of the one-electron spin orbitals:

$$\Psi(\mathbf{x}_1, \mathbf{x}_2, \ldots, \mathbf{x}_N) = \chi_1(\mathbf{x}_1)\chi_2(\mathbf{x}_2)\cdots\chi_N(\mathbf{x}_N) \tag{1.17}$$

This expression is called a Hartree product[4], a first (and over-simplified) approximation to the total many-body wavefunction Ψ.

1.2 The Hartree-Fock Theory

The Hartree-Fock theory[12, 13] is perhaps one of the most profound and influential theory in the realm of quantum chemistry. It is not only an important theory itself, but also a starting point for more accurate calculations. Now let us start from the beginning.

1.2.1 Slater Determinant

The Pauli exclusion principle states that upon exchange of two electrons, the wavefunction must change sign:

$$\Psi(\mathbf{x}_1, \ldots, \mathbf{x}_i, \mathbf{x}_j, \ldots, \mathbf{x}_N) = -\Psi(\mathbf{x}_1, \ldots, \mathbf{x}_j, \mathbf{x}_i, \ldots, \mathbf{x}_N) \tag{1.18}$$

Obviously the Hartree product (Equation 1.17) violates this rule, and is therefore not a satisfactory representation of the wavefunction. To describe the ground state of an N-electron system, an antisymmetric wavefunction can be formed by taking a linear combination of Hartree products, leading to a Slater determinant[14]:

$$\Psi_0 = \frac{1}{\sqrt{N!}} \begin{vmatrix} \chi_1(\mathbf{x}_1) & \chi_2(\mathbf{x}_1) & \cdots & \chi_N(\mathbf{x}_1) \\ \chi_1(\mathbf{x}_2) & \chi_2(\mathbf{x}_2) & \cdots & \chi_N(\mathbf{x}_2) \\ \vdots & \vdots & \ddots & \vdots \\ \chi_1(\mathbf{x}_N) & \chi_2(\mathbf{x}_N) & \cdots & \chi_N(\mathbf{x}_N) \end{vmatrix} \tag{1.19}$$

where $\frac{1}{\sqrt{N!}}$ is a normalisation factor and the spin orbitals are chosen to be orthonormal so that $\chi_i\chi_j = \delta_{ij}$. Within a Slater determinant, the rows are labelled by electrons and the columns are labelled by spin orbitals. Interchanging the rows means interchanging the coordinates of two electrons, which changes the sign of the determinant. Having two identical columns means having two electrons occupying the same spin orbital, which makes the determinant zero. Therefore, a Slater determinant satisfies the Pauli exclusion principle: the wavefunctions must be antisymmetric, meaning no more than one electron can occupy a single spin orbital. In a more convenient notation which absorbs the normalisation factor and shows only the diagonal elements, a Slater determinant can be written as:

$$\Psi_0 = |\chi_1\chi_2\cdots\chi_N\rangle \tag{1.20}$$

1.2.2 The Hartree-Fock Energy

Now that we have the proper form of the wavefunction, we can apply the electronic Hamiltonian (Equation 1.5) on the Slater determinant (Equation 1.19), in order to obtain the ground-state Hartree-Fock energy:

$$E^{\mathrm{HF}} = \langle\Psi_0|\mathcal{H}_{\mathrm{elec}}|\Psi_0\rangle = \sum_i^N \langle i|h_i(\mathbf{x}_1)|i\rangle + \frac{1}{2}\sum_i^N\sum_j^N [ii|jj] - [ij|ji] \tag{1.21}$$

where

$$\langle i|h_i(\mathbf{x}_1)|i\rangle = \int \chi_i^*(\mathbf{x}_1)\left(-\frac{1}{2}\nabla_i^2 - \sum_A^M \frac{Z_A}{r_{iA}}\right)\chi_i(\mathbf{x}_1)\mathrm{d}\mathbf{x}_1 \tag{1.22}$$

uses the Dirac bracket notation, describing the kinetic energy of the electrons and electron-nucleus attraction, while

$$[ii|jj] = \iint \chi_i^*(\mathbf{x}_1)\chi_i(\mathbf{x}_1)\frac{1}{r_{12}}\chi_j^*(\mathbf{x}_2)\chi_j(\mathbf{x}_2)\mathrm{d}\mathbf{x}_1\mathrm{d}\mathbf{x}_2 \tag{1.23}$$

$$[ij|ji] = \iint \chi_i^*(\mathbf{x}_1)\chi_j(\mathbf{x}_1)\frac{1}{r_{12}}\chi_j^*(\mathbf{x}_2)\chi_i(\mathbf{x}_2)\mathrm{d}\mathbf{x}_1\mathrm{d}\mathbf{x}_2 \tag{1.24}$$

are the Coulomb and exchange integrals, respectively, which represent the energy from two types of interactions between two electrons, as discussed in more details below.

1.2.3 The Hartree-Fock Equations

The ground-state Hartree-Fock energy is apparently a functional of the spin orbitals $\{\chi_i\}$, subject to the constraint that they form an orthonormal set. According to the variational theorem, the set of $\{\chi_i\}$ that minimises E^{HF} are the best spin orbitals, which can be determined through solving the Hartree-Fock equations:

$$\mathcal{F}_i(\mathbf{x}_1)\chi_i(\mathbf{x}_1) = \varepsilon_i\chi_i(\mathbf{x}_1) \tag{1.25}$$

where $\mathcal{F}_i(\mathbf{x}_1)$ is a one-electron operator defined as the Fock operator:

$$\mathcal{F}_i(\mathbf{x}_1) = -\frac{1}{2}\nabla_i^2 - \sum_A^M \frac{Z_A}{r_{iA}} + \mathcal{V}_i^{\mathrm{HF}}(\mathbf{x}_1) \tag{1.26}$$

where $\mathcal{V}_i^{\mathrm{HF}}(\mathbf{x}_1)$ is the Hartree-Fock potential. It is an average repulsive potential experienced by the i-th electron due to the presence of the other $(N-1)$ electrons. This ingenious idea proposed by Hartree[15, 16] transforms the complicated two-electron operator $\frac{1}{r_{ij}}$ in $\mathcal{H}_{\mathrm{elec}}$ into a much simpler one-electron operator $\mathcal{V}_i^{\mathrm{HF}}(\mathbf{x}_1)$, which has the explicit form:

$$\mathcal{V}_i^{\mathrm{HF}}(\mathbf{x}_1) = \sum_j^N \mathcal{J}_j(\mathbf{x}_1) - \mathcal{K}_j(\mathbf{x}_1) \tag{1.27}$$

The Coulomb operator $\mathcal{J}_j(\mathbf{x}_1)$ is defined as:

$$\mathcal{J}_j(\mathbf{x}_1) = \int |\chi_j(\mathbf{x}_2)|^2 \frac{1}{r_{12}}\mathrm{d}\mathbf{x}_2 \tag{1.28}$$

The exchange operator $\mathcal{K}_j(\mathbf{x}_1)$ is defined as:

$$\mathcal{K}_j(\mathbf{x}_1)\chi_i(\mathbf{x}_1) = \int \chi_j^*(\mathbf{x}_2)\frac{1}{r_{12}}\chi_i(\mathbf{x}_2)\mathrm{d}\mathbf{x}_2\chi_j(\mathbf{x}_1) \tag{1.29}$$

From the definitions above, it can be seen that $\mathcal{J}_j(\mathbf{x}_1)$ represents the classical Coulomb repulsion that one electron experiences due to the average charge distribution of another electron. This exists for all electrons, regardless of their spins. On the other hand, $\mathcal{K}_j(\mathbf{x}_1)$ leads to an exchange of the variables in the two spin orbitals, which has no classical equivalence and so is purely quantum-mechanical. Unlike the Coulomb interactions, these exchange contributions exist only for electrons with parallel spins, simply because of the orthonormality of the spin orbitals[3]. It is not difficult to see that the Coulomb and exchange integrals (Equations 1.23 and 1.24) are the expectation values of these two operators, respectively.

1.2.4 The Roothaan Equations

To illustrate how Hartree-Fock calculations are really performed, here we consider the classical restricted closed-shell scenario. By saying restricted we mean that within the definition of the spin orbitals (Equation 1.16), the spatial orbitals ψ_i^α and ψ_i^β are treated as the same for electrons with α/β spins. By saying closed-shell we mean that the system under study has even number of electrons which are all paired. Under these assumptions, the spin dependence can be dropped and the ground-state wavefunction is written as:

$$\Psi_0 = |\chi_1\chi_2\cdots\chi_N\rangle \equiv \left|\psi_1\psi_1\psi_2\psi_2\cdots\psi_{\frac{N}{2}}\psi_{\frac{N}{2}}\right\rangle \tag{1.30}$$

Now the Hartree-Fock equations (Equation 1.25) that are based on spin orbitals become:

$$\mathcal{F}_i(\mathbf{r}_1)\psi_i(\mathbf{r}_1) = \varepsilon_i\psi_i(\mathbf{r}_1) \tag{1.31}$$

where

$$\mathcal{F}_i(\mathbf{r}_1) = h_i(\mathbf{r}_1) + \sum_{j}^{\frac{N}{2}} 2\mathcal{J}_j(\mathbf{r}_1) - \mathcal{K}_j(\mathbf{r}_1) \tag{1.32}$$

with

$$\mathcal{J}_j(\mathbf{r}_1) = \int |\psi_j(\mathbf{r}_2)|^2 \frac{1}{r_{12}} \mathrm{d}\mathbf{r}_2 \tag{1.33}$$

$$\mathcal{K}_j(\mathbf{r}_1)\psi_i(\mathbf{r}_1) = \int \psi_j^*(\mathbf{r}_2) \frac{1}{r_{12}} \psi_i(\mathbf{r}_2) \mathrm{d}\mathbf{r}_2 \psi_j(\mathbf{r}_1) \tag{1.34}$$

As shown by Roothaan[17], the Hartree-Fock equations can be solved by expanding the spatial orbitals into a set of known functions (basis sets), employing the LCAO approximation (Equation 1.15):

$$\psi_i = \sum_{\mu=1}^{K} C_{\mu i}\phi_\mu \qquad i = 1, 2, \ldots, K \tag{1.35}$$

where a set of K basis functions $\{\phi_\mu | \mu = 1, 2, \ldots, K\}$ is introduced. Substituting Equation 1.35 into Equation 1.31 and using the index ν, multiplying by ϕ_u^* on the left and integrating both sides lead to:

$$\sum_{\nu=1}^{K} C_{\nu i} \underbrace{\int \phi_\mu^*(\mathbf{r}_1)\mathcal{F}_i(\mathbf{r}_1)\phi_\nu(\mathbf{r}_1)\mathrm{d}\mathbf{r}_1}_{F_{\mu\nu}=\langle\mu|\mathcal{F}_i(\mathbf{r}_1)|\nu\rangle} = \varepsilon_i \sum_{\nu=1}^{K} C_{\nu i} \underbrace{\int \phi_\mu^*(\mathbf{r}_1)\phi_\nu(\mathbf{r}_1)\mathrm{d}\mathbf{r}_1}_{S_{\mu\nu}=\langle\mu|\nu\rangle} \tag{1.36}$$

where $F_{\mu\nu}$ and $S_{\mu\nu}$ define the Fock matrix and the overlap matrix, respectively. These equations are called the Roothaan equations, which have the forms of secular equations and can be written compactly as:

$$\mathbf{FC} = \mathbf{SC}\boldsymbol{\varepsilon} \tag{1.37}$$

where

$$\mathbf{C} = \begin{pmatrix} C_{11} & C_{12} & \cdots & C_{1K} \\ C_{21} & C_{22} & \cdots & C_{2K} \\ \vdots & \vdots & \ddots & \vdots \\ C_{K1} & C_{K2} & \cdots & C_{KK} \end{pmatrix} \tag{1.38}$$

is the coefficient matrix, and

$$\boldsymbol{\varepsilon} = \begin{pmatrix} \varepsilon_1 & & & \\ & \varepsilon_2 & & \mathbf{0} \\ & & \ddots & \\ \mathbf{0} & & & \varepsilon_K \end{pmatrix} \tag{1.39}$$

is the energy eigenvalue matrix.

In the case where spin-polarisation is present, unrestricted Hartree-Fock calculations must be performed. This is generally the same as the restricted case, with the spatial orbitals ψ_i^α and ψ_i^β treated differently:

$$\psi_i^\alpha = \sum_{\mu=1}^{K} C_{\mu i}^\alpha \phi_\mu \qquad i = 1, 2, \ldots, K \tag{1.40}$$

$$\psi_i^\beta = \sum_{\mu=1}^{K} C_{\mu i}^\beta \phi_\mu \qquad i = 1, 2, \ldots, K \tag{1.41}$$

and now two sets of secular equations need to be solved:

$$\mathbf{F}^\alpha \mathbf{S}^\alpha = \mathbf{S}\mathbf{C}^\alpha \boldsymbol{\varepsilon}^\alpha \tag{1.42}$$

$$\mathbf{F}^\beta \mathbf{S}^\beta = \mathbf{S}\mathbf{C}^\beta \boldsymbol{\varepsilon}^\beta \tag{1.43}$$

1.2.5 The Self-consistent-field Method

From the discussion above we can see that the Hartree-Fock equations consist of Coulomb and the exchange operators which depend on the spin orbitals. These spin orbitals are themselves solutions to these equations (constructed from the coefficient matrix and basis set), therefore, the Hartree-Fock equations are not simple eigenvalue problems and must be solved iteratively. The technique used is called the self-consistent-field (SCF) method. Before going into details, we need to define one more term and obtain the explicit form of the Fock matrix. The electron density of a closed-shell system is defined as:

$$\rho(\mathbf{r}) = 2\sum_{i}^{\frac{N}{2}} |\psi_i(\mathbf{r})|^2 \tag{1.44}$$

Substituting Equation 1.35 into this gives:

$$\rho(\mathbf{r}) = \sum_{\mu\nu}^{K} \underbrace{2\sum_{i}^{\frac{N}{2}} C_{\mu i}^{*} C_{\nu i}}_{P_{\mu\nu}} \phi_{\mu}^{*}(\mathbf{r})\phi_{\nu}(\mathbf{r}) \tag{1.45}$$

where $P_{\mu\nu}$ defines the density matrix. In the basis of $\{\phi_\mu\}$, combining Equations 1.32 and 1.45 gives:

$$F_{\mu\nu} = \underbrace{\langle\mu|h_i(\mathbf{r}_1)|\nu\rangle}_{H_{\mu\nu}^{\text{core}}} + \underbrace{\sum_{\lambda\sigma}^{K} P_{\mu\nu}\{[\mu\nu|\sigma\lambda] - \frac{1}{2}[\mu\lambda|\sigma\nu]\}}_{G_{\mu\nu}} \tag{1.46}$$

where $H_{\mu\nu}^{\text{core}}$ defines the one-electron core-Hamiltonian matrix and $G_{\mu\nu}$ is the two-electron part of the Fock matrix, which depends on the element of density matrix $P_{\mu\nu}$. Evaluation of the two-electron integrals is the major bottleneck in Hartree-Fock calculations, simply because of the very large number of them.

With the definitions above, the SCF method can now be introduced (Figure 1.2).

For the initial guess at the density matrix **P**, the simplest possible way is to use a zero matrix, which is equivalent to neglecting all electron-electron interactions with the system. The iterations outlined do not always converge, simply because the Roothaan equations are nonlinear. The process can oscillate or diverge, sometimes due to a poor initial guess. A number of techniques have been developed to improve the convergence[4].

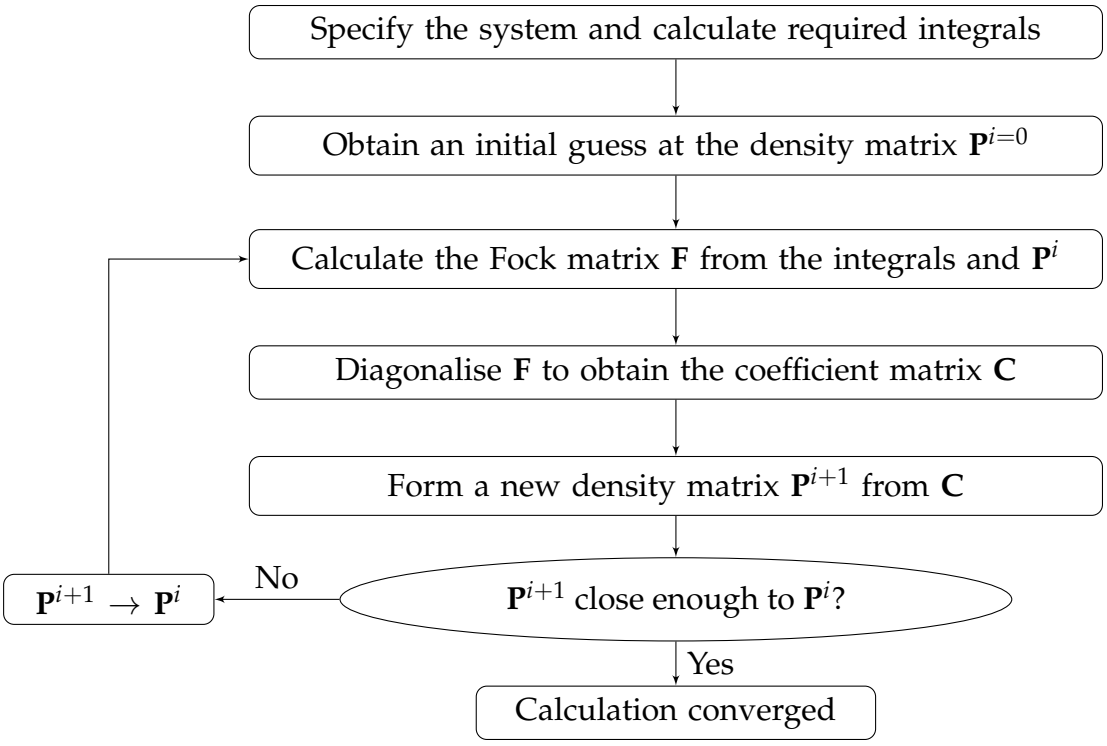


FIGURE 1.2: The self-consistent-field method

1.2.6 Electron Correlation

The major weakness of Hartree-Fock theory is that due to its mean-field nature which treats each electron in an average field formed by other electrons, it completely ignores an important contribution to the true ground-state energy, the so-called electron correlation energy E_C^{HF}[18]:

$$E_C^{HF} = E_0 - E^{HF} \tag{1.47}$$

According to the variational theorem, E^{HF} must be larger than E_0, thus E_C^{HF} is a negative quantity. Electron correlation is traditionally divided into two types, dynamical and non-dynamical. The former refers to the instantaneous electron-electron repulsion that is not covered by the average Hartree-Fock potential, while the latter refers to cases where a single Slater determinant of Hartree-Fock theory is not a good approximation to the true ground state, because there exist other Slater determinants with comparable energy[3]. Despite that, this electron correlation is generally smaller in magnitude than the electron exchange, which the Hartree-Fock calculations do include, and that is why these calculations give reasonably good results in most cases. However, for the sake of more accurate calculations, this wavefunction-related difficulty of incorporating electron correlation needs to be solved, or circumvented. This has been elegantly done by the theory introduced below, which, instead of resting on the N-electron wavefunction as in the Hartree-Fock theory, is based on the electron density.

1.3 Density Functional Theory

Attempts to approximate the Schrödinger equation with electron-density-based theories dated back to the pioneering work by L. H. Thomas[19] and E. Fermi[20–22], which provided a method of statistically describing the distribution of electrons in

an atom[1]. Slater[23] also tried to replace the exchange part of the Hartree-Fock potential with functions of the electron density. However, neither of these methods were systematic, nor exact, just like the Hartree-Fock theory. In contrast, the density functional theory (DFT) is in principle an exact theory, which includes both electron exchange and correlation. It was not until 1964, however, that the two Hohenberg-Kohn theorems[24] provided the physical justification for the validity of density functional theory.

1.3.1 The Hohenberg-Kohn Theorems

Before going into details of the theorems, first, the definition of electron density needs to be revisited. We can define the density as:

$$\rho(\mathbf{r}) = \sum_{i=1}^{N} f_i |\psi_i(\mathbf{r})|^2 \tag{1.48}$$

where f_i denotes the occupation number of the spatial orbital i. This is in fact nothing but a generalisation of Equation 1.44.

The first Hohenberg-Kohn theorem states that the external potential, and therefore the Hamiltonian, is a unique functional of the electron density. Therefore, the ground state wavefunction is uniquely determined by the electron density. Given the electron density of the system, the Schrödinger equation can be solved and all ground-state properties of interest can be obtained. In fact, the term "density functional" originates from the fact that the ground-state energy of the system is a function of the electron density, which is itself a function of the spatial coordinates of the electrons. With the form of the electronic Hamiltonian under the Born-Oppenheimer approximation (Equation 1.5), the ground-state energy can be written as:

$$E_0[\rho_0(\mathbf{r})] = \underbrace{T[\rho_0(\mathbf{r})] + E_{ee}[\rho_0(\mathbf{r})]}_{F[\rho_0(\mathbf{r})]} + \underbrace{E_{\mathrm{Ne}}[\rho_0(\mathbf{r})]}_{\int \rho_0(\mathbf{r}) \mathcal{V}_{\mathrm{Ne}} \mathrm{d}\mathbf{r}} \tag{1.49}$$

The last term depends on the actual system, while the first two terms summed as $F[\rho_0(\mathbf{r})]$ are universally valid and contain non-classical contributions due to electron exchange, correlation and self-interaction. Therefore, $F[\rho_0(\mathbf{r})]$ has to be approximated.

The second Hohenberg-Kohn theorem states that Equation 1.49 delivers the lowest energy if and only if the input electron density is the true ground-state density. This is actually the DFT version of the variational theorem (Equation 1.8):

$$E_0[\rho_{\text{trial}}(\mathbf{r})] \geq E_0 \tag{1.50}$$

These two theorems indeed provide the physical foundation of density functional theory, but they do not show at all how the functional ($F[\rho(\mathbf{r})]$ in particular) that delivers the ground-state energy should be constructed. This is where the famous Kohn-Sham approach comes into play.

1.3.2 The Kohn-Sham Approach

The universal functional in Equation 1.49 can be further split into three parts:

$$F[\rho(\mathbf{r})] = T[\rho(\mathbf{r})] + J[\rho(\mathbf{r})] + E_{\text{ncl}}[\rho(\mathbf{r})] \tag{1.51}$$

where the first term is the kinetic energy, the second term is the classical Coulomb interaction and the third term incorporates the non-classical contributions including exchange and correlation. Of these, only $J[\rho(\mathbf{r})]$ is explicitly known, while the other two terms remain mysteries. $T[\rho(\mathbf{r})]$ is especially difficult to find, because the relationship between the velocities of electrons and their spatial distributions as provided by the electron density, which are needed for the kinetic energy, is not that trivial[3]. Kohn and Sham[25] ingeniously solved this problem by introducing a reference system of non-interacting electrons which has the same density as the real

system. On top of this non-interacting system, extra potentials can be added to account for the differences from the real system. Then we have:

$$F[\rho(\mathbf{r})] = T_0[\rho(\mathbf{r})] + J[\rho(\mathbf{r})] + E_{\mathrm{XC}}[\rho(\mathbf{r})] \tag{1.52}$$

with

$$E_{\mathrm{XC}}[\rho(\mathbf{r})] = \{T[\rho(\mathbf{r})] - T_0[\rho(\mathbf{r})]\} + E_{\mathrm{ncl}}[\rho(\mathbf{r})] \tag{1.53}$$

where $T_0[\rho(\mathbf{r})]$ is the kinetic energy for the non-interacting system, and $E_{\mathrm{XC}}[\rho(\mathbf{r})]$ is the so-called exchange-correlation energy which absorbs the non-classical contributions and the residual part of the true kinetic energy.

Formally, the functional of the true total energy can be written as:

$$E[\rho(\mathbf{r})] = T_0[\rho(\mathbf{r})] + \frac{1}{2}\iint \frac{\rho(\mathbf{r}_1)\rho(\mathbf{r}_2)}{r_{12}}\mathrm{d}\mathbf{r}_1\mathrm{d}\mathbf{r}_2 + E_{\mathrm{XC}}[\rho(\mathbf{r})] + \int \rho(\mathbf{r})\mathcal{V}_{\mathrm{Ne}}\mathrm{d}\mathbf{r} \tag{1.54}$$

Similar to what we have seen in the Hartree-Fock theory (Equation 1.25), the problem now is minimising this energy with respect to a set of orbitals by solving the Kohn-Sham equations:

$$\mathcal{F}_i^{\mathrm{KS}}[\rho(\mathbf{r})]\varphi_i = \varepsilon_i\varphi_i \tag{1.55}$$

with the Kohn-Sham operator:

$$\mathcal{F}_i^{\mathrm{KS}}[\rho(\mathbf{r})] = -\frac{1}{2}\nabla^2 + \underbrace{\int \frac{\rho(\mathbf{r}_2)}{r_{12}}\mathrm{d}\mathbf{r}_2 + \mathcal{V}_{\mathrm{XC}}(\mathbf{r}) - \sum_{A=1}^{M}\frac{Z_A}{r_{1A}}}_{\mathcal{V}_{\mathrm{eff}}(\mathbf{r})} \tag{1.56}$$

$\{\varphi_i\}$ are the so-called Kohn-Sham orbitals and $\mathcal{V}_{\mathrm{eff}}(\mathbf{r})$ is the effective one-electron potential. The exchange-correlation potential is defined as:

$$\mathcal{V}_{\mathrm{XC}}(\mathbf{r}) = \frac{\partial E_{\mathrm{XC}}[\rho(\mathbf{r})]}{\partial\rho(\mathbf{r})} \tag{1.57}$$

The solution then follows a similar procedure used in the Hartree-Fock calculations (Equation 1.37), and the Kohn-Sham equations have the familiar secular structure:

$$\mathbf{F}^{\mathrm{KS}}\mathbf{C} = \mathbf{S}\mathbf{C}\boldsymbol{\varepsilon} \tag{1.58}$$

where the only major difference lies in the elements of the matrix $\mathbf{F}^{\mathrm{KS}}$:

$$F_{\mu\nu}^{\mathrm{KS}} = \langle\mu|h_i(\mathbf{r}_1)|\nu\rangle + \left\langle\mu\right| \int \frac{\rho(\mathbf{r}_2)}{r_{12}} \mathrm{d}\mathbf{r}_2 \left|\nu\right\rangle + \langle\mu|\mathcal{V}_{\mathrm{XC}}(\mathbf{r}_1)|\nu\rangle \tag{1.59}$$

In the case where spin-polarisation is present, the transformation from DFT to spin-DFT can be achieved by decomposing $\rho(\mathbf{r})$ into $\rho^{\alpha}(\mathbf{r})$ and $\rho^{\beta}(\mathbf{r})$, a similar approach as in the unrestricted Hartree-Fock method (Equations 1.40 and 1.41).

1.3.3 Exchange-Correlation Functional

The exchange-correlation functional $E_{\mathrm{XC}}[\rho(\mathbf{r})]$ contains all the unknown contributions to the total energy of the system under study. Therefore, in order to apply the Kohn-Sham approach to perform real calculations, the explicit form of the exchange-correlation functional needs to be known. In fact, the quality and accuracy of DFT calculations significantly depend on how $E_{\mathrm{XC}}[\rho(\mathbf{r})]$ is approximated[3].

Most approximations of the exchange-correlation functional are based on a hypothetical system, the so-called uniform electron gas, where all electrons move on a positive background charge distribution so that the whole system is neutral. The importance of the uniform electron gas lies in that it is the only system for which we know the form of $E_{\mathrm{XC}}[\rho(\mathbf{r})]$ exactly or at least to a very high accuracy[3]. One of the most influential and successful approximations based on this hypothetical system is the local density approximation (LDA), which is defined as:

$$E_{\mathrm{XC}}^{\mathrm{LDA}}[\rho(\mathbf{r})] = \int \rho(\mathbf{r})\varepsilon_{\mathrm{XC}}[\rho(\mathbf{r})]\mathrm{d}\mathbf{r} \tag{1.60}$$

where $\varepsilon_{XC}[\rho(\mathbf{r})]$ is the exchange-correlation energy per electron in the uniform electron gas with density $\rho(\mathbf{r})$. It can be further split into the exchange and correlation parts:

$$\varepsilon_{XC}[\rho(\mathbf{r})] = \varepsilon_X[\rho(\mathbf{r})] + \varepsilon_C[\rho(\mathbf{r})] \tag{1.61}$$

For unrestricted calculations, we have the spin-dependent version of LDA, the local spin-density approximation (LSDA):

$$E_{XC}^{LSDA}[\rho^\alpha(\mathbf{r}), \rho^\beta(\mathbf{r})] = \int \rho(\mathbf{r}) \varepsilon_{XC}[\rho^\alpha(\mathbf{r}), \rho^\beta(\mathbf{r})] d\mathbf{r} \tag{1.62}$$

LDA and LSDA can only yield results with moderate accuracy, which is most of the time not sufficient for modern computational chemistry. A more advanced method is the generalised gradient approximation (GGA), which includes terms that depend not only on the electron density but also its gradients:

$$E_{XC}^{GGA}[\rho^\alpha(\mathbf{r}), \rho^\beta(\mathbf{r})] = \int f[\rho^\alpha(\mathbf{r}), \rho^\beta(\mathbf{r}), \nabla\rho^\alpha(\mathbf{r}), \nabla\rho^\beta(\mathbf{r})] d\mathbf{r} \tag{1.63}$$

This can be again split into the exchange and correlation parts:

$$E_{XC}^{GGA} = E_X^{GGA} + E_C^{GGA} \tag{1.64}$$

which can be developed separately. In fact, most of the exchange-correlation functionals in use today fall in the GGA category. Historically, the realisation of E_X^{GGA} followed two distinct pathways. The first one is based on a GGA exchange functional developed by Becke in 1988[26] (abbreviated as B or B88), which contains an empirical parameter fitted to the known exchange energy of rare gas atoms. One of the most famous example related to this approach is the PW91 exchange functional[27, 28]. In contrast, the second pathway is free of (semi)empirical parameters, with the popular

(especially for solid-state calculations) PBE[29] functional one of the prominent representatives. For the correlation functionals, the most widely-used ones are P86[30, 31] and LYP[32]. It should be noted that the LYP correlation functional is not based on the model of uniform electron gas. In principle, any of the exchange and correlation functionals can be combined to form a valid E_{XC}^{GGA}, but the most popular ones are BP86 and BLYP.

To further improve the efficiency of DFT-based methods, the so-called hybrid functionals have been developed by mixing exchange and correlation from very different sources, which normally contain both DFT and Hartree-Fock components. One of the most successful hybrid functionals, B3LYP[33], has the form of:

$$E_{XC}^{B3LYP} = 0.8E_X^{LSDA} + 0.2E_X^{HF} + 0.72E_X^{B} + 0.19E_C^{LSDA} + 0.81E_C^{LYP} \tag{1.65}$$

Another widely-used hybrid functional, especially for solid-state calculations, is the HSE[34]. It is particularly useful for dealing with the issue of long-range Hartree-Fock exchange interaction and reducing the computational cost. The general form of HSE functional is:

$$E_{XC}^{HSE}(\omega) = aE_X^{HF,SR}(\omega) + (1-a)E_X^{PBE,SR}(\omega) + E_X^{PBE,LR}(\omega) + E_C^{PBE} \tag{1.66}$$

where SR and LR stand for short-range and long-range, respectively. a is the mixing parameter and ω controls the contribution of SR interactions. For the most updated version of HSE functional, the HSE06[35], $a = 0.5$ and $\omega = 0.2$.

1.3.4 The Self-interaction Problem

The most notable weakness of DFT lies in the self-interaction problem, which is an inevitable consequence of the approximation of exchange-correlation functionals. In Hartree-Fock theory, this problem is elegantly solved: for $i = j$ in the second term of

Equation 1.21, the Coulomb and exchange integrals exactly cancel each other, leaving only the kinetic energy and electron-nucleus attraction contributions for the one-electron case. However, in real-life DFT where the exchange-correlation functional is approximated, the Coulomb part does not exactly cancel the exchange-correlation energy (Equation 1.52). None of the functionals currently in use can completely escape from this self-interaction error.

1.4 Extensions to Solid-state Systems

The theories and methods mentioned above, historically developed for molecular systems, are applicable to solid-state systems as well. After all, these two types of systems all consist of electrons and therefore, looking for better approximations to solve the Schrödinger equation is always the key. However, solid-state systems normally contain considerably more electrons than molecules. Therefore, to incorporate the features of the former, within the Schrödinger equation, the exact form of the wavefunction needs to be adjusted, as we will see shortly.

1.4.1 Plane Wave and Bloch's Theorem

For solid-state systems, the structures are infinitely extended with translational symmetry so localised orbitals are less obviously appropriate as basis functions. Instead of using STOs or GTOs, it is therefore natural to employ the so-called plane waves, $e^{i\mathbf{kr}}$, as basis functions. Similar to STOs, the evaluation of the exchange integrals (Equation 1.24) is very slow for plane waves. As a result, for solid-state systems, DFT prevails and Hartree-Fock calculations are only performed if necessary (within hybrid functionals).

Now we have the proper form of the basis set, but the problem is still intractable, because introducing a more appropriate form of basis function has not reduced the

effectively infinite number of electrons that need to be dealt with. However, if we consider that in a perfect crystal the ions are arranged periodically with translational symmetry, then the electrons are positioned in a potential $\mathcal{V}^{\mathrm{L}}(\mathbf{r})$ with the periodicity of the crystal lattice, expressed by a lattice vector $\mathbf{R}$[36]:

$$\mathcal{V}^{\mathrm{L}}(\mathbf{r}+\mathbf{R}) = \mathcal{V}^{\mathrm{L}}(\mathbf{r}) \tag{1.67}$$

With this periodic potential, Bloch's theorem[37] states that a one-electron wavefunction can be chosen as the product of a plane wave and a function with the periodicity of the crystal lattice:

$$\psi_{n\mathbf{k}}(\mathbf{r}) = e^{i\mathbf{k}\mathbf{r}} u_{n\mathbf{k}}(\mathbf{r}) \tag{1.68}$$

with

$$u_{n\mathbf{k}}(\mathbf{r}+\mathbf{R}) = u_{n\mathbf{k}}(\mathbf{r}) \tag{1.69}$$

where $\mathbf{k}$ is the wave vector and n is the band index denoting the order of independent eigenstates for a given $\mathbf{k}$. Now the problem of analysing the infinitely extended crystal becomes one of solving the Schrödinger equation of the periodic wavefunction within the unit cell of the system.

1.4.2 Reciprocal Lattice and First Brillouin Zone

Normally a general plane wave, $e^{i\mathbf{k}\mathbf{r}}$, does not share the same periodicity $\mathbf{R}$ of the crystal lattice, but for certain choices of wave vector $\mathbf{k}$ it does. The set of all wave vectors that yield plane waves with the periodicity of a given crystal lattice is known as its reciprocal lattice[36], and the three-dimensional space that contains the reciprocal lattice is called the reciprocal space. The corresponding crystal lattice in real space is often referred to as the direct lattice. The reciprocal lattice can be constructed from

the primitive vectors of the direct lattice:

$$\begin{aligned}\mathbf{b}_1 &= 2\pi\frac{\mathbf{a}_2 \times \mathbf{a}_3}{\mathbf{a}_1 \cdot (\mathbf{a}_2 \times \mathbf{a}_3)} \\ \mathbf{b}_2 &= 2\pi\frac{\mathbf{a}_3 \times \mathbf{a}_1}{\mathbf{a}_1 \cdot (\mathbf{a}_2 \times \mathbf{a}_3)} \\ \mathbf{b}_3 &= 2\pi\frac{\mathbf{a}_1 \times \mathbf{a}_2}{\mathbf{a}_1 \cdot (\mathbf{a}_2 \times \mathbf{a}_3)}\end{aligned} \tag{1.70}$$

where $\mathbf{b}_1$, $\mathbf{b}_2$ and $\mathbf{b}_3$ are the reciprocal lattice vectors, while $\mathbf{a}_1$, $\mathbf{a}_2$ and $\mathbf{a}_3$ are the direct lattice vectors. It is easily appreciated that:

$$\mathbf{b}_i\mathbf{a}_j = 2\pi\delta_{ij} \tag{1.71}$$

Now in the reciprocal space, any vector $\mathbf{k}$ can be expressed as a linear combination of the reciprocal lattice vectors:

$$\mathbf{k} = k_1\mathbf{b}_1 + k_2\mathbf{b}_2 + k_3\mathbf{b}_3 \tag{1.72}$$

The direct and reciprocal lattice can be converted into each other through fast Fourier transforms, and plane waves allow highly efficient computations of these transforms.

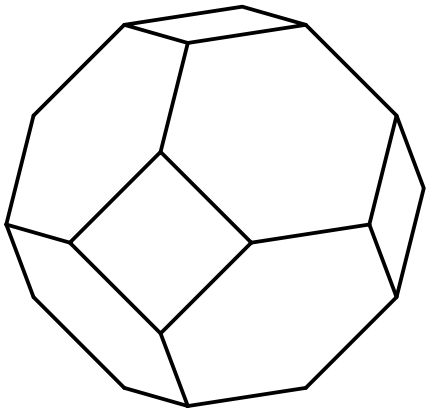


FIGURE 1.3: The first Brillouin zone for the face-centred cubic lattice

As there are primitive unit cells for the direct lattice, there exist a similar construction for the reciprocal space as well. This is known as the first Brillouin zone, which is simply the Wigner-Seitz primitive cell[38] for the reciprocal lattice. The first Brillouin zone for the face-centred cubic lattice is shown as an example (Figure 1.3).

1.4.3 The Born-von Karman Boundary Condition

We have mentioned that in the reciprocal lattice, the wave vector can only take certain values. In the direct lattice, an appropriate boundary condition can be applied on the wavefunction to impose further restrictions on $\mathbf{k}$:

$$\psi(\mathbf{r} + N_i\mathbf{a}_i) = \psi(\mathbf{r}) \qquad i = 1, 2, 3 \tag{1.73}$$

where N_i denotes integers of order $N^{\frac{1}{3}}$ with the total number of primitive cells $N = N_1N_2N_3$. This is the Born-von Karman boundary condition[36].

Applying Bloch's theorem to this boundary condition leads to:

$$\psi_{n\mathbf{k}}(\mathbf{r} + N_i\mathbf{a}_i) = e^{iN_i\mathbf{k}\mathbf{a}_i}\psi_{n\mathbf{k}}(\mathbf{r}) \qquad i = 1, 2, 3 \tag{1.74}$$

which means

$$e^{iN_i\mathbf{k}\mathbf{a}_i} = 1 \qquad i = 1, 2, 3 \tag{1.75}$$

With Equations 1.71 and 1.72, we have:

$$e^{2\pi iN_ik_i} = 1 \qquad i = 1, 2, 3 \tag{1.76}$$

thus

$$k_i = \frac{m_i}{N_i} \qquad m_i \in \{\text{integer}\} \tag{1.77}$$

Therefore, the allowed wave vectors $\mathbf{k}$ have the general form:

$$\mathbf{k} = \sum_{i=1}^{3} \frac{m_i}{N_i} \mathbf{b}_i \qquad m_i \in \{\text{integer}\} \tag{1.78}$$

which are called Bloch wave vectors.

From Equation 1.78 it can be seen that for each allowed $\mathbf{k}$, there is an associated volume $\Delta\mathbf{k}$ within the reciprocal space:

$$\Delta\mathbf{k} = \frac{1}{N} \mathbf{b}_1 \cdot (\mathbf{b}_2 \times \mathbf{b}_3) \tag{1.79}$$

As a result, it can be concluded that the number of allowed wave vectors $\mathbf{k}$ is finite for a given crystal lattice.

1.4.4 k-point Sampling and Energy Cut-off

DFT requires the electron density to be constructed as the input, which in the solid-state regime involves an integral over the first Brillouin zone:

$$\rho(\mathbf{r}) = \frac{1}{\Omega_{\text{BZ}}} \sum_n \int_{\text{BZ}} f_{n\mathbf{k}} |\psi_{n\mathbf{k}}(\mathbf{r})|^2 \mathrm{d}\mathbf{k} \tag{1.80}$$

where Ω_{BZ} is the volume of the first Brillouin zone and $f_{n\mathbf{k}}$ denotes the occupation number of the wavefunction. For the sake of computational efficiency, based on the symmetry of the first Brillouin zone, this integral can be simplified with a weighted sum over a discrete set of $\mathbf{k}$-points:

$$\rho(\mathbf{r}) = \sum_{n\mathbf{k}} \omega_{\mathbf{k}} f_{n\mathbf{k}} |\psi_{n\mathbf{k}}(\mathbf{r})|^2 \tag{1.81}$$

where $\omega_{\mathbf{k}}$ is the weight. This defines the $\mathbf{k}$-point sampling procedure of solid-state calculations. For a specific task of calculation, the number of $\mathbf{k}$-points can be explicitly specified, which determines how accurately the first Brillouin zone is sampled.

To construct the wavefunction with plane-wave basis sets, the periodic function $u_{n\mathbf{k}}(\mathbf{r})$ can be chosen as:

$$u_{n\mathbf{k}}(\mathbf{r}) = \frac{1}{\sqrt{\Omega_{\mathrm{BZ}}}} \sum_{\mathbf{G}} C_{\mathbf{G}n\mathbf{k}} e^{i\mathbf{G}\mathbf{r}} \tag{1.82}$$

thus

$$\psi_{n\mathbf{k}}(\mathbf{r}) = \frac{1}{\sqrt{\Omega_{\mathrm{BZ}}}} \sum_{\mathbf{G}} C_{\mathbf{G}n\mathbf{k}} e^{i(\mathbf{G}+\mathbf{k})\mathbf{r}} \tag{1.83}$$

where $\mathbf{G}$ is the reciprocal lattice vector. In practice, only a finite set of the plane waves are chosen, which satisfies:

$$\frac{1}{2}|\mathbf{G}+\mathbf{k}|^2 < E_{\mathrm{cut}} \tag{1.84}$$

This defines the energy cut-off of solid-state calculations.

1.4.5 The Hubbard *U* Approach

Now that we have covered the essential theories to perform solid-state calculations, we are almost ready to apply them on real-life systems. Before stepping into that, there is one modification to the DFT method to be introduced, the Hubbard U approach. The reason for this is that for transition-metal solid-state phases where the ions are close-packed and the electrons are strong-correlated, DFT fails to correctly describe the structural and electronic properties (the band gap, in particular) of the so-called Mott insulators, even in a qualitative sense[39]. Mott insulators are the class of materials that should be conducting according to traditional band theory, but experimentally turn out to be insulators due to unaccounted electron correlation[40]. Examples of well-known Mott insulators include the 3*d* transition-metal oxides MnO, FeO, CoO and NiO, *etc*. Due to the previously-mentioned self-interaction error, traditional DFT methods such as LDA over-delocalise the d or f electrons that should be highly localised, resulting in incorrect predictions of metallic CoO and FeO, and they also give band gaps in MnO and NiO that are too small

by almost an order of magnitude[41].

In order to solve this problem, or at least to improve the accuracy of DFT in describing strong-correlated systems, the Hubbard U model has been employed. The U parameter describes the Coulomb repulsion between electrons within the Hubbard model, and is defined as the energy required to remove an electron from one site and pair it with an electron on another site (in other words, the energy cost to place two electrons at the same site)[39, 41]:

$$U_{nl}^{M} = E(d^{n+1}) + E(d^{n-1}) - 2E(d^{n}) = \mathrm{IP}_{nl}^{M} - \mathrm{EA}_{nl}^{M} \tag{1.85}$$

where U is the difference between the ionisation potential (IP) and electron affinity (EA) for a particular metal centre (M) and subshell (nl) of electrons. We have specifically focused on d electrons here, but the reasoning for f electrons should follow the same logic.

The method that is commonly used to estimate the electron-electron interaction within the Hubbard model is based on Hartree-Fock (mean-field) theory, simply because it is free of self-interaction errors, as mentioned before. In the context of Hartree-Fock theory, the localised on-site Coulomb interactions between d electrons are described by the energy term:

$$E_{U}^{\mathrm{HF}} = \frac{U}{2} \sum_{i \neq j} n_i n_j \tag{1.86}$$

where n_i and n_j are the occupation numbers for d electrons on the sites i and j. In the scope of this description, DFT is structured as a weak-coupling theory, where the Coulomb interactions U are assumed to be small compared to the bandwidth W, although in Mott insulators this is obviously not the case[41]. However, it has been shown that this approximation can still be valid for systems with strong couplings, especially for half-filled orbitals[42, 43]. The weakness of this approach lies in that

Hartree-Fock theory does not include the screening effect of electrons. This results in overestimated U parameters ($\sim$15 – 20 eV), while screening in solid-state systems leads to much smaller values ($\sim$8 eV)[44]. The following discussions are all based on screening-corrected U parameters, unless otherwise stated.

In order to correct the DFT energy, the term that describes electron-electron interaction must be replaced by the Hartree-Fock one. To illustrate how this is done, let us consider a single metal centre with a total number of N fluctuating d electrons[45]. If we assume the Coulomb energy of d-d interactions is a function of $N = \sum n_i$, then we have the DFT electron-electron interaction (neglecting the exchange part for now):

$$E_U^{\mathrm{DFT}} = U\frac{N(N-1)}{2} \tag{1.87}$$

where U is the screened Coulomb parameter. Subtracting this term from the DFT total energy and adding the Hartree-Fock term (Equation 1.86) lead to the corrected energy[46]:

$$E^{\mathrm{corr}} = E^{\mathrm{DFT}} - U\frac{N(N-1)}{2} + \frac{U}{2}\sum_{i\neq j} n_i n_j \tag{1.88}$$

Then by taking partial derivative of this energy with respect to each orbital occupation we can obtain the orbital energy:

$$\varepsilon_i = \frac{\partial E}{\partial n_i} = \varepsilon^{\mathrm{DFT}} + U(\frac{1}{2} - n_i) \tag{1.89}$$

It can be seen that this equation shifts the DFT orbital energy by $+\frac{U}{2}$ for empty orbitals (n_i = 0) and by $-\frac{U}{2}$ for occupied orbitals (n_i = 1), hence these two types of orbitals are separated by the on-site interaction U[45].

The currently widely-used version of the Hubbard U approach (the so-called "effective" Hubbard U method) was developed by Duradev *et al.* in 1998. Taking the orbital degeneracy of the 3d shell into account, we have the energy functional in the

form of[39, 47]:

$$E^{\mathrm{DFT+}U} = E^{\mathrm{DFT}} + \frac{U_{\mathrm{eff}}}{2}\sum_{m,\sigma}(n_{m,\sigma} - n_{m,\sigma}^2) \tag{1.90}$$

where U_{eff} is the so-called "effective" Hubbard U parameter which absorbs both the screened Coulomb (U) and exchange (J) interactions. The summation runs over the spin of electrons ($\sigma = \alpha/\beta$) and m denotes the magnetic quantum number (m = -2, -1, 0, 1, 2 for d electrons). The terms in the bracket define the on-site occupation matrix. As can be seen from this equation, U_{eff} determines the magnitude of the energy penalty of putting two electrons with opposite spin at the same site. It should be noted that U_{eff} can be calculated[48], or more commonly, tuned[49] and is specific to each atom and subshell[39].

1.4.6 Representations of the Wavefunction

Performing real solid-state calculations requires specific representations of the wavefunction. We know that solid-state systems are composed of atoms, which means that there exist core regions where the wavefunction oscillates rapidly, and interstitial valence regions where the wavefunction oscillates relatively slowly (Figure 1.4). It has been shown that the wavefunction can be approximated by linear combinations of plane-wave basis functions. However, to mimic the alternating core/valence nature of the wavefunction, a large number of plane waves are required, and hence a huge amount of computational resources. Therefore, in order to improve the efficiency of calculations, further approximations to the wavefunction are needed.

The augmented plane-wave (APW) method[50] represents the valence region of the wavefunction with a finite number of plane waves, while forcing it to have a more rapid oscillatory atomic behaviour in the core region[36]. This construction is established in the so-called muffin-tin potential, where the core and valence regions are described by spherical and flat potentials, respectively. The wavefunction is expanded in a set of augmented plane waves, which take the form of atomic functions

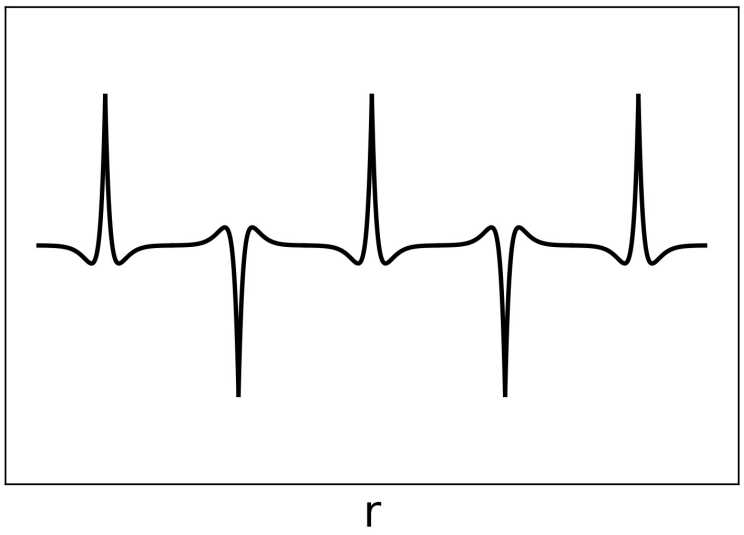


FIGURE 1.4: A qualitative illustration of the solid-state wavefunction

(also called partial waves) within the spherical muffin-tin potential radius r_{MT}:

$$\phi^{\mathrm{c}}_{\mathbf{k}}(\mathbf{r},\varepsilon) = \sum_{lm} C_{lm} R_l(r,\varepsilon) Y_{lm}(\theta,\varphi) \qquad r < r_{\mathrm{MT}} \tag{1.91}$$

while single plane waves are employed for describing the valence regions:

$$\phi^{\mathrm{v}}_{\mathbf{k}}(\mathbf{r},\varepsilon) = e^{i\mathbf{kr}} \qquad r \geq r_{\mathrm{MT}} \tag{1.92}$$

The band index n has been dropped for general arguments of the wavefunction, and the core/valence regions are denoted by the letter c/v. It should be noted that the term ε has no relation to $\mathbf{k}$ and is merely an extra variable added to control the energy of $\phi_{\mathbf{k}}(\mathbf{r},\varepsilon)$. These two parts are connected at the muffin-tin border r_{MT} through the so-called augmentation process, which is equivalent to finding the correct coefficient C_{lm} for different orbitals[1]. Finally, the augmented plane waves are summed up to

the reciprocal lattice vector **G** to form the wavefunction:

$$\psi_{\mathbf{k}}(\mathbf{r}) = \sum_{\mathbf{G}} C_{\mathbf{G}} \phi_{\mathbf{k}+\mathbf{G}}(\mathbf{r}, \varepsilon) \tag{1.93}$$

An extension of the APW approach is called the linearised augmented plane-wave (LAPW) method, which reduces the computational costs while retaining a reasonable accuracy by taking the Taylor expansion of the radial part of the core-region partial wave near a certain energy ε°:

$$R_l(r, \varepsilon) = R_l(r, \varepsilon^{\circ}) + \left.\frac{\partial R_l}{\partial \varepsilon}\right|_{\varepsilon^{\circ}} (\varepsilon - \varepsilon^{\circ}) + O(\varepsilon - \varepsilon^{\circ})^2 \tag{1.94}$$

The terms denoted by $O(\varepsilon - \varepsilon^{\circ})^2$ are truncated, so that the radial function becomes linear and energy-independent within the vicinity of the chosen energy ε°.

The orthogonalised plane-wave (OPW) method[51] forces valence-region plane waves to be orthogonal to the core-region plane waves:

$$\phi_{\mathbf{k}} = \sum_{\mathrm{c}} C^{\mathrm{c}}_{\mathbf{k}} \psi^{\mathrm{c}}_{\mathbf{k}}(\mathbf{r}) + e^{i\mathbf{kr}} \tag{1.95}$$

with

$$C^{\mathrm{c}}_{\mathbf{k}} = -\int \psi^{\mathrm{c}*}_{\mathbf{k}}(\mathbf{r}) e^{i\mathbf{kr}} \mathrm{d}\mathbf{r} \tag{1.96}$$

As in the APW method, the wavefunction can be written as:

$$\psi_{\mathbf{k}}(\mathbf{r}) = \sum_{\mathbf{G}} C_{\mathbf{G}} \phi_{\mathbf{k}+\mathbf{G}}(\mathbf{r}) \tag{1.97}$$

A more systematic way to describe the core region is given by the pseudopotential approach[52, 53], which is a development of the OPW method. Given Equation 1.95,

the valence part of the wavefunction can be written as:

$$\psi_{\mathbf{k}}^{\mathrm{v}}(\mathbf{r}) = -\sum_{\mathrm{c}} \left(\int \psi_{\mathbf{k}}^{\mathrm{c}*}(\mathbf{r}) \phi_{\mathbf{k}}^{\mathrm{v}}(\mathbf{r}) \mathrm{d}\mathbf{r} \right) \psi_{\mathbf{k}}^{\mathrm{c}}(\mathbf{r}) + \phi_{\mathbf{k}}^{\mathrm{v}}(\mathbf{r}) \tag{1.98}$$

Since both $\psi_{\mathbf{k}}^{\mathrm{c}}(\mathbf{r})$ and $\psi_{\mathbf{k}}^{\mathrm{v}}(\mathbf{r})$ are exact core/valence-region wavefunctions, they satisfy the Schrödinger equations:

$$\mathcal{H}\psi_{\mathbf{k}}^{\mathrm{c}}(\mathbf{r}) = \varepsilon_{\mathbf{k}}^{\mathrm{c}} \psi_{\mathbf{k}}^{\mathrm{c}}(\mathbf{r}) \tag{1.99}$$

$$\mathcal{H}\psi_{\mathbf{k}}^{\mathrm{v}}(\mathbf{r}) = \varepsilon_{\mathbf{k}}^{\mathrm{v}} \psi_{\mathbf{k}}^{\mathrm{v}}(\mathbf{r}) \tag{1.100}$$

Then it can be shown that:

$$(\mathcal{H} + \mathcal{V}^{\mathrm{R}})\psi_{\mathbf{k}}^{\mathrm{v}}(\mathbf{r}) = \varepsilon_{\mathbf{k}}^{\mathrm{v}} \psi_{\mathbf{k}}^{\mathrm{v}}(\mathbf{r}) \tag{1.101}$$

where $\mathcal{V}^{\mathrm{R}}$ is defined as:

$$\mathcal{V}^{\mathrm{R}}\psi = \sum_{\mathrm{c}} (\varepsilon_{\mathbf{k}}^{\mathrm{v}} - \varepsilon_{\mathbf{k}}^{\mathrm{c}}) \left(\int \psi_{\mathbf{k}}^{\mathrm{c}*}(\mathbf{r}) \psi \mathrm{d}\mathbf{r} \right) \psi_{\mathbf{k}}^{\mathrm{c}}(\mathbf{r}) \tag{1.102}$$

Then the pseudopotential $\mathcal{V}^{\mathrm{pseudo}}$ is defined to be the sum of $\mathcal{V}^{\mathrm{R}}$ and the lattice periodic potential $\mathcal{V}^{\mathrm{L}}$ (Equation 1.67)[36]:

$$\mathcal{V}^{\mathrm{pseudo}} = \mathcal{V}^{\mathrm{R}} + \mathcal{V}^{\mathrm{L}} \tag{1.103}$$

The significance of this approach lies in that $\mathcal{V}^{\mathrm{R}}$ is positive because $\varepsilon_{\mathbf{k}}^{\mathrm{v}} > \varepsilon_{\mathbf{k}}^{\mathrm{c}}$ always holds, thus the negative periodic potential is partially cancelled, resulting in a small $\mathcal{V}^{\mathrm{pseudo}}$. As a result, the pseudopotential can be treated as a weak perturbation. Within this scheme, the all-electron (AE) wavefunction for the core region is replaced by a nodeless pseudo (PS) wavefunction[54], which successfully circumvents the difficulties of approximating the rapidly-oscillating core-region wavefunction thus significantly improves the efficiency of solid-state calculations.

1.4.7 The Projector-augmented-wave Method

A new approach combining the essence of LAPW and pseudopotential methods emerged in 1990s, called projector-augmented-wave (PAW) method[55], which allows faster and more accurate calculations. Using the Dirac bracket notation, the AE wavefunction $|\psi_n\rangle$ is derived from the PS wavefunction $|\tilde{\psi}_i\rangle$ by a process called linear transformation[56]:

$$|\psi_n\rangle = |\tilde{\psi}_n\rangle + \sum_i (|\phi_i\rangle - |\tilde{\phi}_i\rangle) \langle \tilde{p}_i|\tilde{\psi}_n\rangle \tag{1.104}$$

with the projector function:

$$\langle \tilde{p}_i|\tilde{\phi}_j\rangle = \delta_{ij} \tag{1.105}$$

where $|\phi_i\rangle$ is the AE partial wave and $|\tilde{\phi}_i\rangle$ is the PS partial wave. In this representation the band index n re-enters while the wave vector $\mathbf{k}$ is dropped.

It can be shown that the AE density is given by:

$$\rho(\mathbf{r}) = \tilde{\rho}(\mathbf{r}) + \rho^1(\mathbf{r}) - \tilde{\rho}^1(\mathbf{r}) \tag{1.106}$$

where

$$\tilde{\rho}(\mathbf{r}) = \sum_n f_n \langle \tilde{\psi}_n|\mathbf{r}\rangle \langle \mathbf{r}|\tilde{\psi}_n\rangle \tag{1.107}$$

$$\rho^1(\mathbf{r}) = \sum_{ij} q_{ij} \langle \phi_i|\mathbf{r}\rangle \langle \mathbf{r}|\phi_j\rangle \tag{1.108}$$

$$\tilde{\rho}^1(\mathbf{r}) = \sum_{ij} q_{ij} \langle \tilde{\phi}_i|\mathbf{r}\rangle \langle \mathbf{r}|\tilde{\phi}_j\rangle \tag{1.109}$$

with

$$q_{ij} = \sum_n f_n \langle \tilde{\psi}_n|\tilde{p}_i\rangle \langle \tilde{p}_j|\tilde{\psi}_n\rangle \tag{1.110}$$

The PAW method is an exact AE method for a complete set of partial waves, therefore, it yields results as accurate as any other pseudopotential approach. In fact, the

pseudopotential for the PAW method, which appears as an auxiliary quantity, is generated on-the-fly and thus instantaneously adapts to the electronic environment[1]. This avoids the transferability problem of traditional pseudopotential approaches and is the major success of the PAW method.

Chapter 2

General Introduction: The Family of Perovskite Oxides

From this point, we are leaving the regime of theories of quantum chemistry and instead going to look at real-life problems. This chapter serves as a general introduction to the solid-state systems that we are interested in, perovskite oxides and their derivatives. Detailed introductions to specific systems discussed in later chapters are given at the beginning of them.

2.1 Traditional Perovskite Oxides

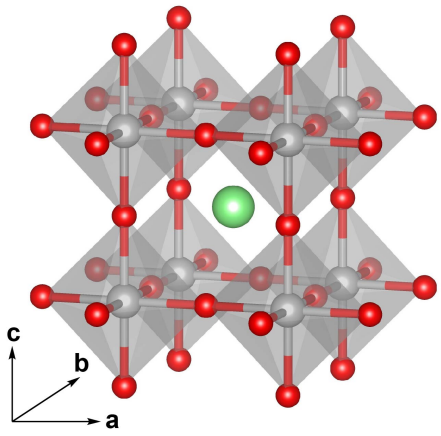


FIGURE 2.1: Crystal structure of a cubic ABX_3 phase
(A: light green; B: grey; X: red)

The name "perovskite" originates from the mineral calcium titanium oxide, which was first discovered in the Ural Mountains of Russia in 1839 and was named after the Russian mineralogist Lev Perovsky[57]. "Perovskite" defines a family of solid-state systems, which share a common type of crystal structure, ABX_3. The A-site cations are generally larger in size than the B-site ones, while the interesting properties of these systems mostly come from the latter, as we will see in the following chapters. The X^{2-} anions are positioned in between each pair of B-site cations, forming a local BX_6 octahedral coordination environment. The unit cell of perovskites can take various shapes (cubic, tetragonal, orthogonal, *etc.*), depending on both structural (*e.g.* the size of ions) and electronic factors (*e.g.* the presence of Jahn-Teller active metal centres). In a traditional illustration of the primitive unit cell, A is usually positioned at the body centre, with B at the corners and X along the edges (Figure 2.1). All the crystal structures plotted in later parts of this thesis follow the conventional Cartesian coordinate shown in Figure 2.1, unless otherwise stated.

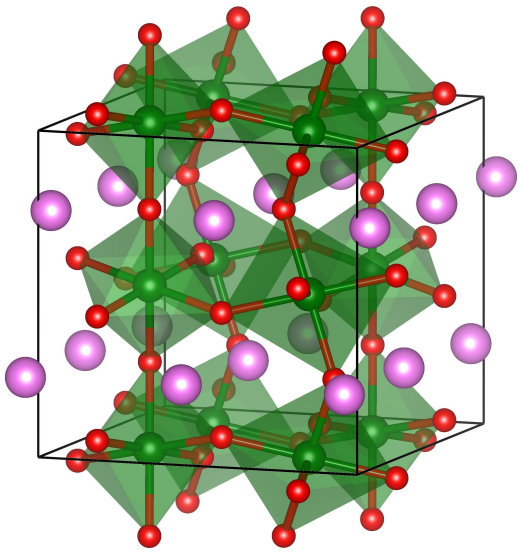


FIGURE 2.2: Crystal structure of $BiNiO_3$
(Bi: pink; Ni: dark green; O: red)

This thesis mainly focuses on transition-metal perovskite oxides (ABO_3) and their

derivatives, which have been studied intensively in recent decades due to their flexible chemistry, which is the origin of a large number of unusual chemical and physical properties. As the ABX_3 phases, perovskite oxides can be perfectly cubic, where all the ions stay in high-symmetry positions (as shown in Figure 2.1). A representative phase of this kind is $SrTiO_3$, which is itself a superconducting semiconductor[58]. On the other hand, instead of having all the ions "eclipsed" with respect to each other, the bond angles may change, resulting in tilted BO_6 octahedra within the structure. The $BiNiO_3$ system (Figure 2.2) falls in this category and exhibits colossal negative thermal expansion, which means the system undergoes a non-intuitive contraction upon heating[59]. The composition of the perovskite oxide phases can be readily altered through chemical substitution on the A- or/and B-sites of the ABO_3 framework, resulting in novel properties or even the formation of a completely new category of compounds. For example, the famous perovskite solar cell, $CH_3NH_3PbI_3$[60], an organic-inorganic hybrid phase of lead iodide, has the molecular cation $(CH_3NH_3)^+$ at the A-site, surrounded by the PbI_6 octahedra (Figure 2.3).

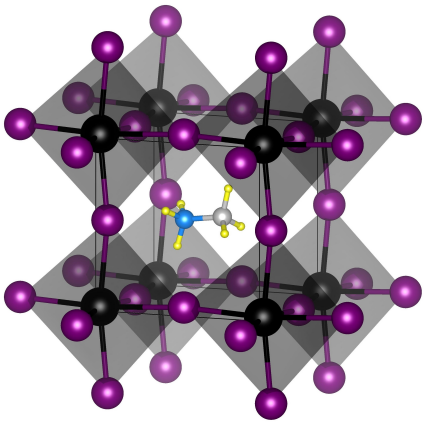


FIGURE 2.3: Crystal structure of $CH_3NH_3PbI_3$
(C: grey; H: yellow; N: blue; Pb: black; I: purple)

Following a similar chemical substitution route, a second type of ion can be added into the A- or/and B-sites, leading to the double perovskite oxides $A_2BB'O_6$, $AA'B_2O_6$

and $AA'BB'O_6$, with mixed cations. The A/A' and B/B' cation pairs can be either ordered or disordered, the degree of ordering being generally controlled by the size and charge differences between the cations: those with very different sizes and charges tend to avoid each other, leading to an ordered phase, while a disordered phase normally results from significant similarities in sizes or/and charges of the cation pairs. The strength of interactions along the B-O-B' (or B-O-B/B'-O-B' in a disordered phase) bonds also influences the preference of ordered/disordered structure. An example of the double perovskite phase exhibiting room-temperature colossal magnetoresistance is Sr_2FeMoO_6[61] (Figure 2.4), which consists of Fe^{3+}/Mo^{5+} cations and features a "checkerboard" ordered structure.

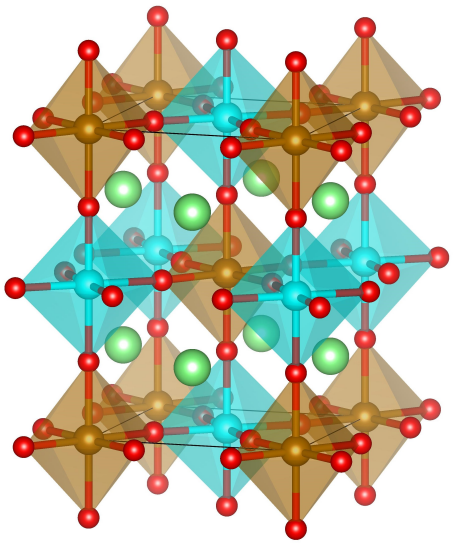


FIGURE 2.4: Crystal structure of Sr_2FeMoO_6
(Sr: light green; Fe: bronze; Mo: cyan; O: red)

2.2 Layered Perovskite Oxides

The perovskite oxide phases can be stacked together to form layered structures (intervening rock-salt layers), resulting in the so-called Ruddlesden-Popper phase represented by Sr_2TiO_4, and named after S. N. Ruddlesden and P. Popper, who described

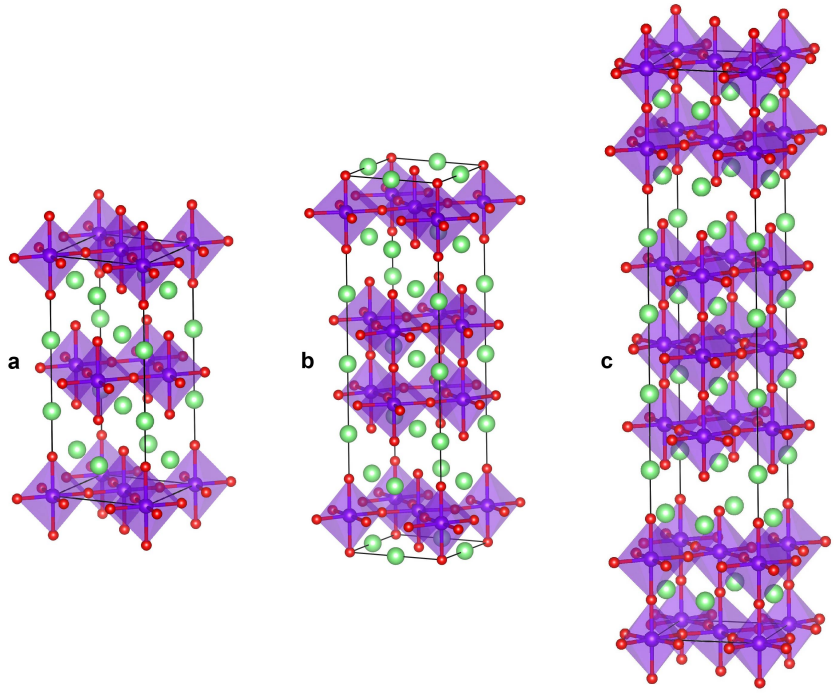


FIGURE 2.5: Crystal structures of Sr_2RuO_4, $Sr_3Ru_2O_7$ and $Sr_4Ru_3O_{10}$ (Sr: light green; Ru: purple; O: red)

the first synthesis in 1957[62]. In this type of structure, the adjacent layers of perovskite oxide units (separated by the A-site cations) are "staggered" with respect to each other, with the offset vector $(\frac{1}{2}a, 0, \frac{1}{2}c)$ (Figure 2.5a). The Ruddlesden-Popper phase has a general formula of $A_{n+1}B_nO_{3n+1}$, where n determines the size (or more accurately, "height", along the c-axis) of the two-dimensional layers. With $n = \infty$ the structure goes back to the aforementioned traditional perovskite oxide ABO_3[63], thus this expression is universal for these two types of phases. Typical examples showing the change in structure for step-wise increases in n from 1 to 3 are the Sr_2RuO_4, $Sr_3Ru_2O_7$ and $Sr_4Ru_3O_{10}$ systems (Figure 2.5a, b, c).

Just like their single-layered analogues, Ruddlesden-Popper phases show a large number of novel chemical and physical properties as well. For example, the Ru-containing systems mentioned above, Sr_2RuO_4, was found to be the first superconductor with no Cu in the lattice[64], while $Sr_3Ru_2O_7$ exhibits spin-density-wave magnetic order in external magnetic fields[65].

2.3 The Reduction of Perovskite Oxides

Most perovskite oxide phases can be synthesised through high-temperature (∼1500 K) routes, with the parent metal oxides as reactants. This always leads to thermodynamically stable products, and therefore has the disadvantage that the reactions can not be controlled to isolate meta-stable intermediates. Therefore, the products from such synthesis routes usually have predictable and traditional coordination environments, a typical example being the family of Fe-containing perovskite oxides, which, for most cases, have three-dimensional polyhedra such as octahedra or tetrahedra around the Fe centre. At the beginning of this century, hydrides of electropositive metals have been found to be ideal reducing agents for reduction of perovskite oxides at low temperature (< 800 K). For example, the employment of NaH reduces $LaSrCoO_4$ to $LaSrCoO_{3.8}$[66] and $YSr_2Mn_2O_7$ to $YSr_2Mn_2O_{5.5}$[67]. The greatest advantage of this method of reduction lies in the low-temperature reaction condition, which allows the product to preserve the overall framework of its parent perovskite structure.

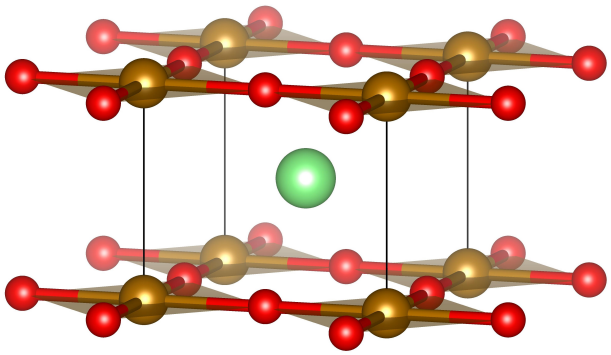


FIGURE 2.6: Crystal structure of $SrFeO_2$
(Sr: light green; Fe: bronze; O: red)

Following this low-temperature synthetic strategy, the famous $SrFeO_2$ system was successfully made in 2007 by Tsujimoto *et al.*[68], featuring a tetragonal unit

cell with a = 3.991 Å and c = 3.475 Å. It consists of infinitely-extended iron oxide layers with square-planar coordination, which is unprecedented and intriguing. The $SrFeO_2$ phase can be synthesised through the reaction of the perovskite oxide $SrFeO_3$ with CaH_2, which reduces the metal centre from d^4 Fe^{4+} to d^6 Fe^{2+}. In terms of the structure, all oxide anions within the Fe-O-Fe chains along the c-axis in $SrFeO_3$ are replaced with vacancies, leading to a phase with two-dimensional layers of corner-sharing $Fe^{2+}O_4$ square-planes separated by Sr^{2+} cations (Figure 2.6), which is isostructural to the well-known parent phases of Cu-containing superconductors $(Ca_{0.86}Sr_{0.14})CuO_2$[69], $(Sr_{1-x}Nd_x)CuO_2$[70] and $(Sr_{1-x}Ca_x)_{1-y}CuO_2$[71]. Despite the two-dimensional nature of the structure, $SrFeO_2$ is surprisingly stable and exhibits a strong G-type antiferromagnetic order with a Néel temperature T_N = 473 K[68].

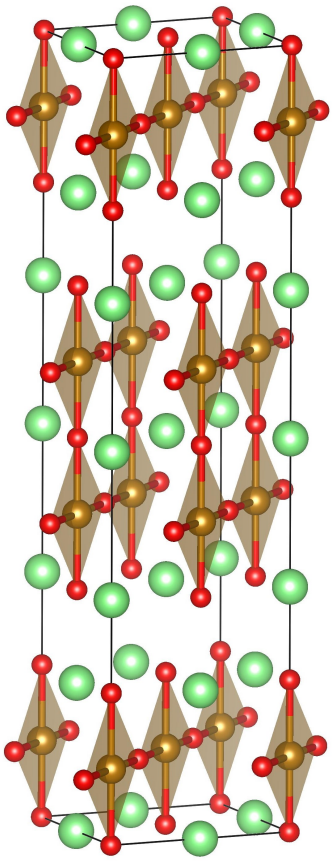


FIGURE 2.7: Crystal structure of $Sr_3Fe_2O_5$
(Sr: light green; Fe: bronze; O: red)

Other than the $SrFeO_2$ system, this recently-developed strategy of using metal hydrides to reduce perovskite oxides has led to a large number of structures containing square-planar metal centres. It can be applied to reduce the Ruddlesden-Popper phases as well. A typical example is the direct analogue of the $SrFeO_2$ phase within the $A_{n+1}B_nO_{3n+1}$ family, $Sr_3Fe_2O_5$[72] (Figure 2.7), where the layered two-dimensional structure is very similar to that in $SrFeO_2$, with the direction of layer extension along the *c*-axis, rather than in the *ab*-plane.

2.4 Perovskite Oxyhydrides

In some cases, the reduction of perovskite oxides with metal hydrides results in a hydride-for-oxide substitution, which introduces hydride anions into the lattice, leading to the so-called oxyhydride phases. The first example of perovskite oxyhydride, $LaSrCoO_3H_{0.7}$, was synthesised by Hayward *et al.* in 2002[73], where the two-dimensional cobalt oxide layers are bridged by H^- anions (Figure 2.8). The discovery of this oxyhydride phase is remarkable because oxide and hydride anions very rarely coexist in the same lattice (especially in such a stoichiometric perovskite structure), simply due to their different electronegativities, and the redox reaction leading to the formation of H_2O is generally favoured during the process of synthesis[73]. Interestingly, because of the presence of both O^{2-} and H^- anions, $LaSrCoO_3H_{0.7}$ possesses a strong magnetic order with T_N ~350 K.

Following this strategy of substituting O^{2-} and inserting H^- into the lattice, the family of perovskite oxyhydrides has been expanded, but the total number of such systems reported is still limited. Most of them exist in the form of traditional perovskites ($n = \infty$), with rare exceptions including $Sr_3Co_2O_{4.33}H_{0.84}$[74] in Ruddlesden-Popper phase. An example worth mentioning with $n = \infty$ is the disordered oxyhydride $BaTiO_{3-x}H_x$[75], featuring an observed hydride exchange with hydrogen gas at ~ 700 K. In fact, such non-stoichiometry is common among the reported oxyhydride

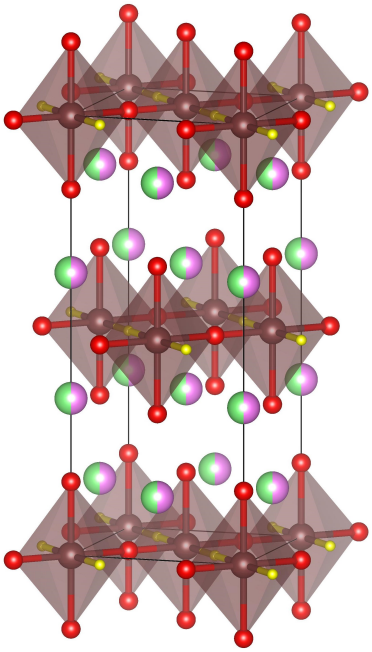


FIGURE 2.8: Crystal structure of $LaSrCoO_3H_{0.7}$
(La: pink; Sr: light green; Co: brown; O: red; H: yellow)

systems, with the notable exception of $SrCrO_2H$[76], where the O^{2-}/H^- anions are disordered, and $SrVO_2H$[77], where the H^- anions are *trans* with respect to each other as in $LaSrCoO_3H_{0.7}$. The electronic structure of $SrVO_2H$ is the subject of Chapter 3.

2.5 The Electronic Structure of $SrFeO_2$

The structure of $SrFeO_2$ is novel and, at the time of its synthesis, unprecedented, as its electronic structure. Much of this thesis is inspired by analogies to $SrFeO_2$, therefore its properties deserve an extensive introduction. At first sight, the square-planar environment of the d^6 Fe^{2+} centre is striking, as the commonly known coordination polyhedra for Fe^{2+} in perovskite oxide phases are octahedra and tetrahedra. Based on this traditional ligand-field view of coordination chemistry, the electronic configuration of Fe^{2+} in $SrFeO_2$ was first proposed to be $(d_{xz/yz})^3(d_{xy})^1(d_{z^2})^1(d_{x^2-y^2})^1$ (Figure 2.9a) based on the results of ^{57}Fe Mössbauer spectroscopy[68]. If this is true, the system should undergo a Jahn-Teller distortion that lifts the degeneracy of the

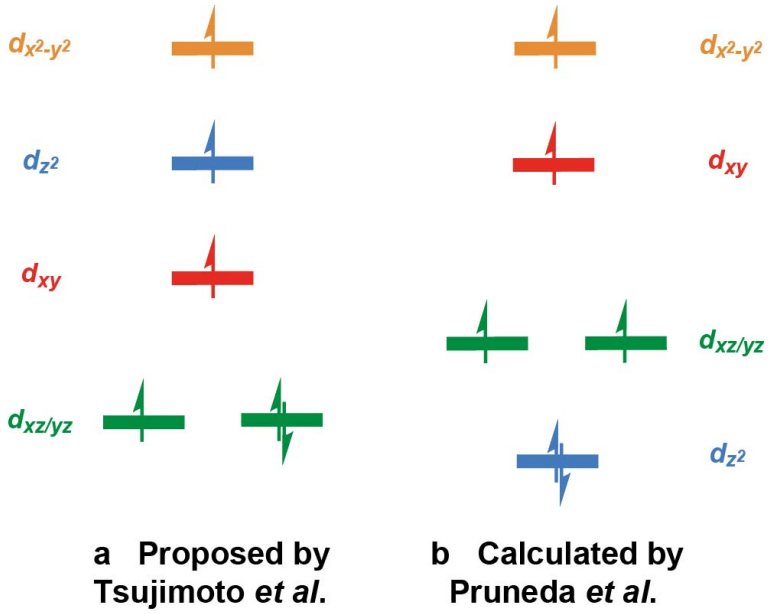


FIGURE 2.9: Electronic configurations of Fe^{2+} in $SrFeO_2$

$d_{xz/yz}$ orbitals, leading to structural instability. However, experiments showed that the framework of $SrFeO_2$ is robustly tetragonal, such that it maintained the space group $P4/mmm$ even at a temperature as low as 4.2 K[68].

The puzzle was resolved by DFT calculations by Pruneda *et al.* and Xiang *et al.*[78, 79] Their PDOS plot is reproduced in Figure 2.10 with PBE+U (U_{eff} = 4.0 eV for Fe, with an energy cut-off of 600 eV and a **k**-point sampling of $4 \times 4 \times 4$), indicating the electronic configuration of Fe^{2+} centres to be $(d_{z^2})^2(d_{xz/yz})^2(d_{xy})^1(d_{x^2-y^2})^1$ (Figure 2.9b), where the extra β-spin electron occupies the d_{z^2} orbital, not $d_{xz/yz}$ as Tsujimoto *et al.* previously proposed. This immediately explains the absence of Jahn-Teller instability, but at first glance, it may seem to be counter-intuitive from the view of traditional coordination chemistry, where the t_{2g} orbitals are normally expected to be of lower energy than the e_g sets, as in the proposed electronic configuration (Figure 2.9a). However, a closer look at the PDOS plot can provide an explanation: the low-energy nature of the d_{z^2} orbital of Fe^{2+} in $SrFeO_2$ can be traced back to the mixing of 3*d* and 4*s* bands, illustrated by the extensive overlap of the blue (d_{z^2}) and black (*s*) lines in Figure 2.10. This mixing is more significant for the d_{z^2} α band than the

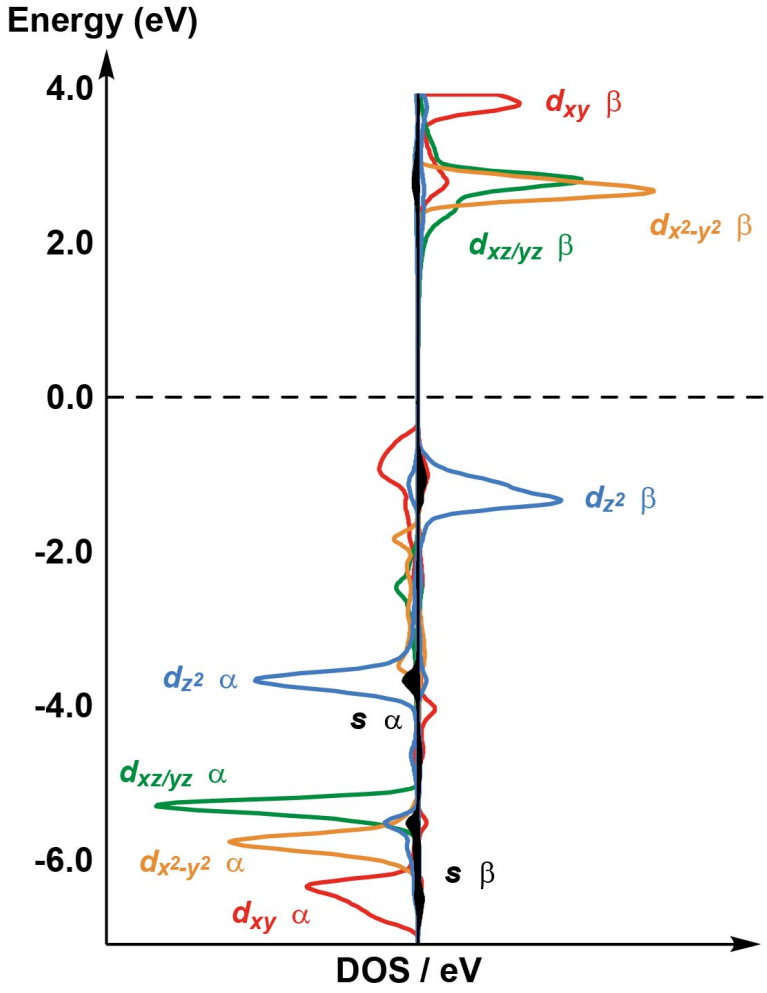


FIGURE 2.10: PDOS of $SrFeO_2$

d_{z^2} β band, which can be seen from the larger width for the former (roughly triple-peaked, ranging from ∼-6.5 eV to -0.5 eV) than the much more localised band for the latter (obviously single-peaked, ranging from ∼-2.0 eV to -0.5 eV). This observation, first made by Pruneda *et al.*[78], reveals the mechanism by which the energy of this system is minimised: the repulsion between the two electrons in the d_{z^2} orbital is reduced by having a different extent of mixing with the 4*s* orbital for the spin-α and spin-β components.

The magnetic properties of $SrFeO_2$ are also worth mentioning. Experiments have shown that the system is G-type antiferromagnetic, with the magnetic order lying

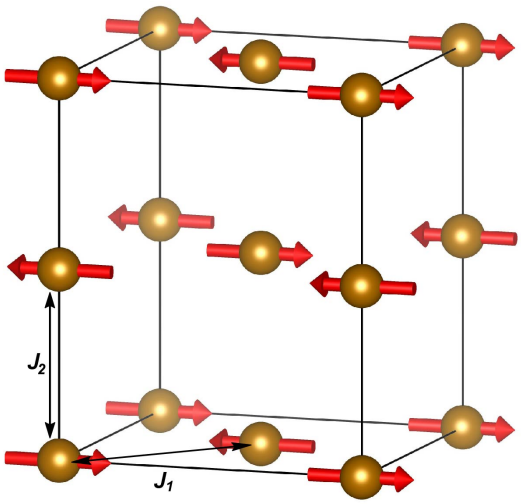


FIGURE 2.11: The G-type antiferromagnetic structure of $SrFeO_2$ (only the Fe atoms are shown)

parallel to the *ab*-plane (Figure 2.11), but the Néel temperature (T_N = 473 K) is extremely high for a seemingly two-dimensional system. In order to search for the origin of this unusual magnetism, two independent sets of calculations on the magnetic coupling parameters were performed by Xiang *et al*. and Pruneda *et al*, respectively (Table 2.1). The two sets of data match with each other at the same magnitude, with J_1 substantially larger than J_2, where the former indicates strong intra-plane super-exchange within the Fe-O-Fe chain, suggested by the Goodenough-Kanamori rule[80]. Interestingly, the inter-plane coupling parameter J_2 is smaller than J_1 only by a factor of $\sim$3, which implies significant interactions along *c*-axis as well. All in all, these calculated magnetic coupling parameters explain the unusually strong magnetic order within the $SrFeO_2$ system, which then leads to a surprisingly high Néel temperature, and indicates that this system is in fact magnetically three-dimensional.

TABLE 2.1: Computed J_1 and J_2 values of $SrFeO_2$

Source of data	J_1 (meV)	J_2 (meV)
Xiang *et al*.	7.9	2.3
Pruneda *et al*.	6.6	1.8

This behaviour, structurally 2D while magnetically 3D, is rare but not unique to $SrFeO_2$, as we shall see in the following chapters on $SrVO_2H$. On the other hand, the unusual double occupation of d_{z^2} orbital, as in Fe^{2+}, strongly correlates to a square-plannar coordination environment, which will be elucidated with the examples of $LaSrNiRuO_4$ and $LaSr_3NiRuO_4H_4$.

Chapter 3

$SrVO_2H$: Pressure Dependence and π-blocking Hydrides

3.1 Introduction

$SrVO_2H$ (Figure 3.1), a tetragonal oxyhydride phase with an anion-ordered and layered structure consisting of planes of vertex-linked $V^{3+}O_4$ units separated by ordered SrH layers, can be synthesised through the reaction of cubic $SrVO_3$ with CaH_2 as a reducing agent[77]. This hydride-for-oxide anion exchange converts the apex-linked $V^{4+}O_6$ units in $SrVO_3$ into *trans*-$V^{3+}O_4H_2$ centres in $SrVO_2H$, lifting the degeneracy of the $3d$ t_{2g} orbitals of V^{3+} cations[77]. On-site electron–electron repulsion further splits the half-filled $3d_{xz/yz}$ orbitals, leading to an insulating ground state that has been observed on thin film samples using photoemission and X-ray absorption spectroscopy[81]. The neutron diffraction measurements on $SrVO_2H$ reveal G-type antiferromagnetic order at relatively high Néel temperature ($T_N > 300$ K), indicating the presence of significant antiferromagnetic interactions. The strong super-exchange intra-plane coupling via the oxide anions (J_1) is unremarkable (Figure 3.2), and has been confirmed by recent computational studies from Wei *et al.* and Liu *et al.* (J_1 = 42.7 meV and 23.5 meV, respectively)[82, 83]. In the absence of π-symmetry orbitals on the bridging hydride anions, inter-layer coupling (J_2) might be expected

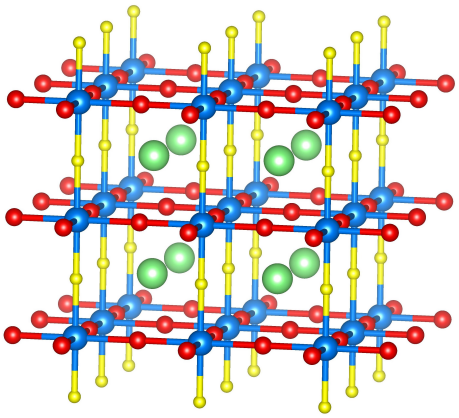


FIGURE 3.1: Crystal structure of $SrVO_2H$
(Sr: light green; V: blue; O: red; H: yellow)

to be very small. Indeed, it has been shown that this inter-layer coupling is substantially weaker than its intra-layer counterpart, although it is not negligible (J_1 = 5.7 meV and 1.9 meV, respectively)[82, 83]. $SrVO_2H$ can therefore be viewed as a strongly correlated quasi-two-dimensional Mott-insulator.

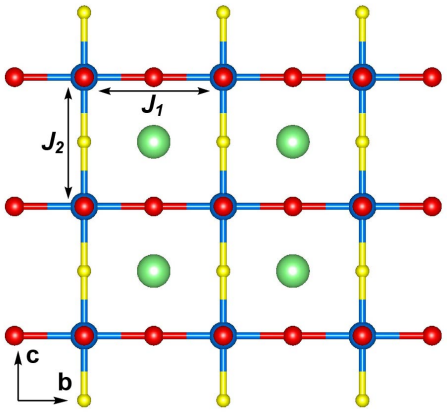


FIGURE 3.2: Side-view of the crystal structure of $SrVO_2H$

The structurally related phase, $SrFeO_2$, is also an antiferromagnetically ordered Mott-insulator at ambient pressure[68], as noted in Chapter 2. With the application of external pressure, the interactions between the $Fe^{2+}O_2$ layers are enhanced, leading to a spin-state transition accompanied by insulator-to-metal transitions[84]. Given

this phenomenon, it would be interesting to see how pressure can be used as a probe to investigate the structural and electronic properties of $SrVO_2H$. The only significant difference between these two systems is the absence/presence of hydride anions between metal centres along the *c*-axis, thus the motivation here is to understand how these spherical anions influence the structural and electronic properties of the perovskite lattice under external pressure.

The results of this project have been published in *Nat. Commun.*, 2017, **8**, 1217.

3.2 Summary of Experimental Data

The relevant experiments were conducted by Yamamoto *et al.* from Kyoto University, Japan and Amano Patino *et al.* from University of Oxford, UK[85].

3.2.1 Pressure Dependence of the Structure

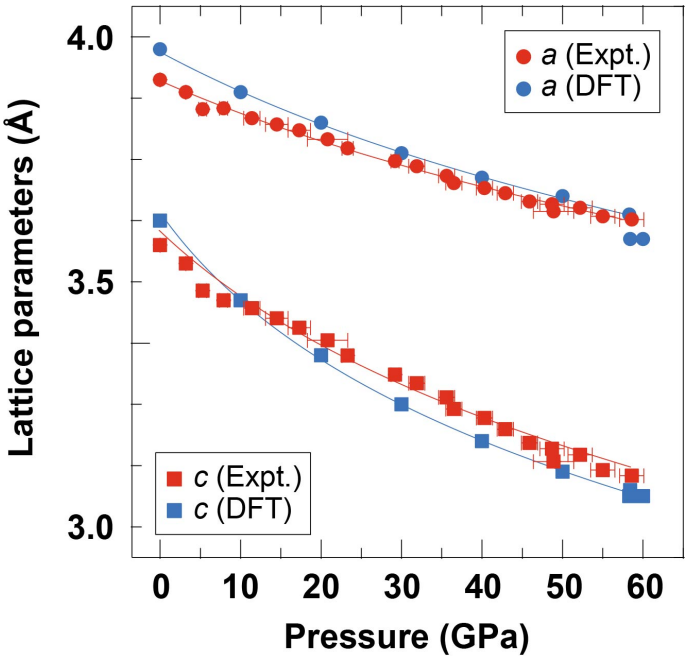


FIGURE 3.3: Pressure dependence of lattice parameters for the experimental (red) and the DFT-computed (blue) values of $SrVO_2H$ (solid lines represent linearised Birch-Murnaghan fits to the data)

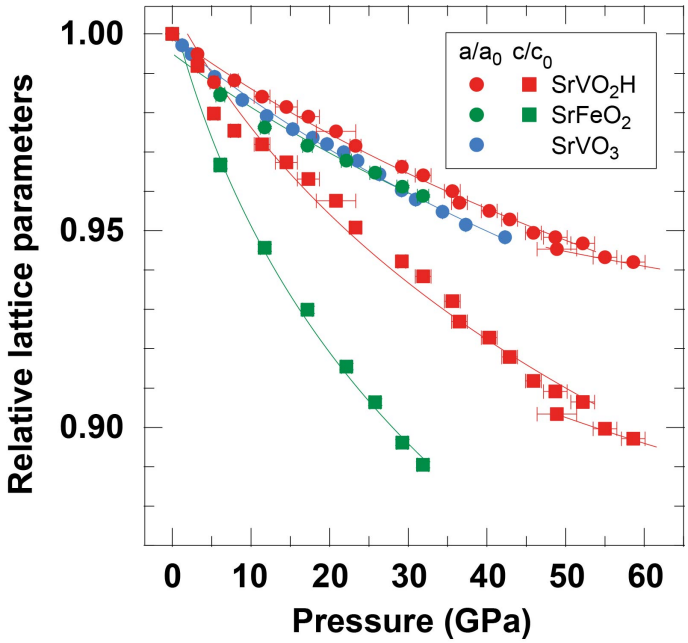


FIGURE 3.4: Relative lattice parameters, a/a_0 and c/c_0, of $SrVO_2H$ (red), $SrFeO_2$ (green) and $SrVO_3$ (blue) as functions of pressure (Solid lines represent linearised Birch-Murnaghan fits to the data)

The pressure dependence of $SrVO_2H$ is shown in Figure 3.3 along with the analogous data of $SrFeO_2$[84] and $SrVO_3$ (Figure 3.4) systems for comparison. As pressure increases, the volume of the system decreases, which leads to a more compact structure as normally expected. Linearised Birch-Murnaghnan fits[86] to these data allow the zero-pressure linear compressibility β_l of the lattice parameters (a and c) to be estimated:

$$P = \frac{3}{2}K_{l_0}\left[\left(\frac{l_0}{l}\right)^7 - \left(\frac{l_0}{l}\right)^5\right]\left\{1 + \frac{3}{4}\left(K'_{l_0} - 4\right)\left[\left(\frac{l_0}{l}\right)^2 - 1\right]\right\} \tag{3.1}$$

where P is the pressure, l is the length of the lattice parameters (a and c) while l_0 is their reference length, K_{l_0} is the axial modulus and K'_{l_0} is its derivative with respect to pressure. For all the fittings shown in Figure 3.3 and 3.4, K'_{l_0} is fixed at 4. Then the

zero-pressure linear compressibility β_l is given by:

$$\beta_l = -\frac{1}{l_0}\left(\frac{\partial l}{\partial P}\right)_T = \frac{1}{3K_{l_0}} \tag{3.2}$$

The calculated β_l values are collected in Table 3.1. β_a quantifies the compression along the a-axis, which corresponds to the contraction of in-plane M–O bonds. Across the three distinct structures, $SrVO_2H$, $SrFeO_2$ and $SrVO_3$, the β_a values are relatively similar (within ~18%). For the cubic $SrVO_3$, the compression is isotropic, so $\beta_a = \beta_c$. This similarity in compression indicates that in all three phases, the stiffness of the M–O bonds is similar. In contrast, the β_c values are very different. The substantially lower β_c of $SrVO_2H$, compared to that of $SrFeO_2$, where no ligand is present along the Fe–Fe vector, suggests that the presence of hydride anions significantly reduces the compressibility. On the other hand, the fact that β_c of $SrVO_2H$ is much larger than that of $SrVO_3$ indicates that the V–H bonds are almost twice as compressible as the V–O bonds.

TABLE 3.1: Linear compressibilities of $SrVO_2H$, $SrFeO_2$ and $SrVO_3$ at ambient pressure

System	β_a (GPa^{-1})	β_c (GPa^{-1})
$SrVO_2H$	1.47×10^{-3}	3.72×10^{-3}
$SrFeO_2$	1.51×10^{-3}	5.02×10^{-3}
$SrVO_3$	1.72×10^{-3}	-

3.2.2 Pressure-induced Insulator-to-Metal Transition

The measured resistance, ~300 Ω, of $SrVO_2H$ at ambient pressure and 300 K is typical of a semiconductor and consistent with the Mott-insulating picture proposed in the literature[77] (Figure 3.5). Application of up to 50 GPa pressure leads to a drop

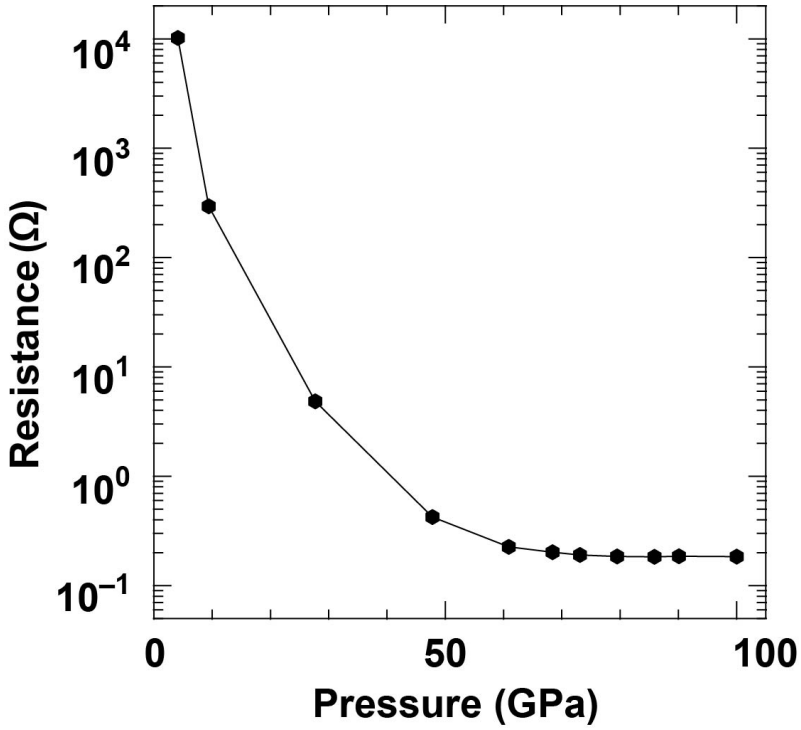


FIGURE 3.5: Electrical resistance of $SrVO_2H$ under external pressure

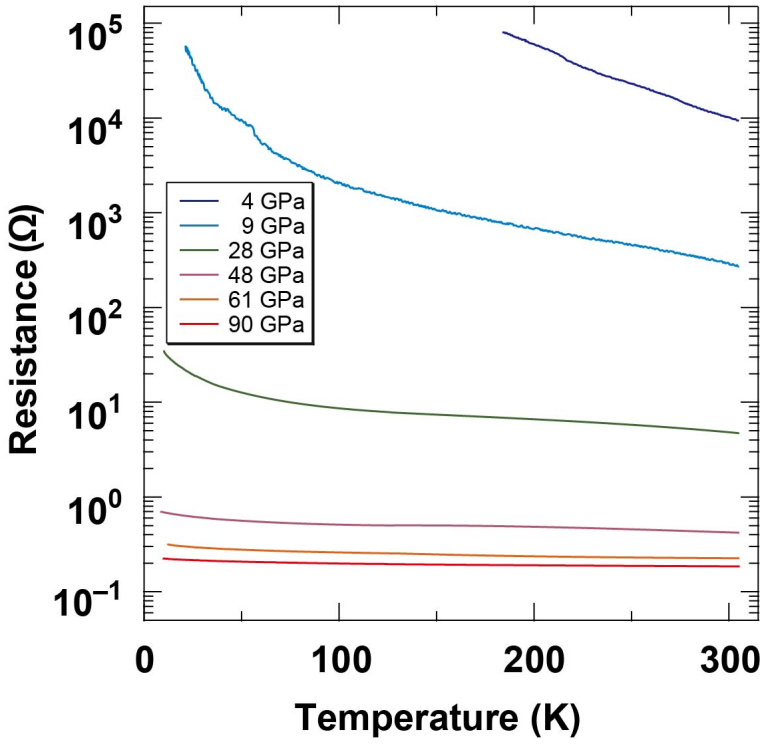


FIGURE 3.6: Temperature dependence of the resistance of $SrVO_2H$ at various pressures

of four orders of magnitude in the resistance and a change in the temperature dependence, $\Delta R/\Delta T$ (Figure 3.6). At this pressure, the resistance becomes essentially independent of the temperature, indicating an insulator-to-metal transition.

3.3 Methodology

All calculations were performed at the PBE+U level using the plane-wave basis code Vienna Ab initio Simulation Package (VASP 5.3.2)[87], based on a $\sqrt{2} \times \sqrt{2} \times 2$ expansion of the primitive unit cell. Convergence tests were done to finalise the plane-wave energy cut-off of 600 eV and the Γ-centred **k**-point sampling of $8 \times 8 \times 7$. The optimisations were done with all the geometrical constraints released, so the ions were allowed to move freely. For DOS calculations, a $24 \times 23 \times 22$ **k**-point sampling was used to improve the quality of the plots. The U_{eff} value was fixed at 2.0 eV for all V^{3+} centres. The hybrid functional HSE06[88], with 25% Hartree-Fock exchange and a range constant $\omega = 0.2$ was also considered, as a comparison to the PBE+U scheme. Transport analysis was performed using the Atomistix ToolKit (ATK 2016.4)[89, 90] with the same PBE density functional and $U_{\text{eff}} = 2.0$ eV used in the VASP calculations. A localised double-ζ basis set, extended with single polarisation function DZP, was used to describe all atoms. The Brillouin zone was sampled on a $21 \times 21 \times 21$ Monkhorst-Pack **k**-point grid.

3.3.1 Expansion of the Primitive Unit Cell

The primitive unit cell of $SrVO_2H$ features a perovskite structure, containing one Sr^{2+}, one V^{3+}, two O^{2-} and one H^- ions (Figure 3.7). By definition, this single formula unit imposes the restriction that all the V^{3+} cations must be identical. This prevents us from exploring the potentially interesting properties of the system that originate from the complex interactions between adjacent metal centres. Therefore,

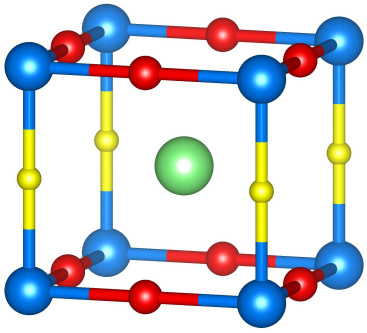


FIGURE 3.7: Primitive unit cell of $SrVO_2H$

it is necessary to transform the primitive cell into a $\sqrt{2} \times \sqrt{2} \times 2$ expanded cell by performing a matrix operation on the coordinate system of the lattice parameters:

$$\begin{bmatrix} 1 & -1 & 0 \\ 1 & 1 & 0 \\ 0 & 0 & 2 \end{bmatrix} \begin{bmatrix} a \\ b \\ c \end{bmatrix} = \begin{bmatrix} a-b \\ a+b \\ 2c \end{bmatrix} \tag{3.3}$$

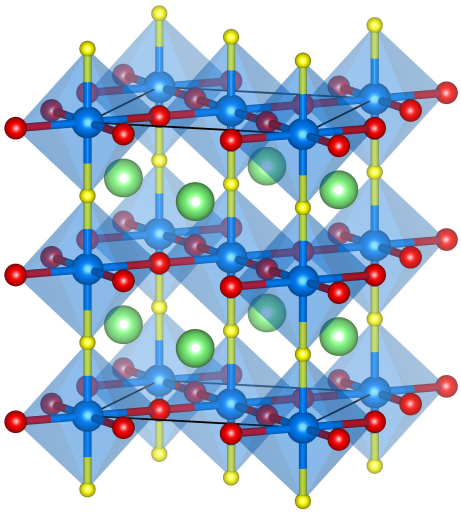


FIGURE 3.8: $\sqrt{2} \times \sqrt{2} \times 2$ expansion of the primitive unit cell of $SrVO_2H$, for the exploration of magnetic properties

The expanded cell (Figure 3.8) now contains four formula units with four Sr^{2+}, four V^{3+}, eight O^{2-} and four H^- ions. The four V^{3+} centres can now be independently

labelled and identified, allowing us to configure the interactions between them. As mentioned above, $SrVO_2H$ is experimentally identified as a G-type antiferromagnetic system. In order to confirm this G-type energy ground state, we have constructed four distinct magnetic configurations, namely G, C, A (antiferromagnetic) and F (ferromagnetic) types (Figure 3.9).

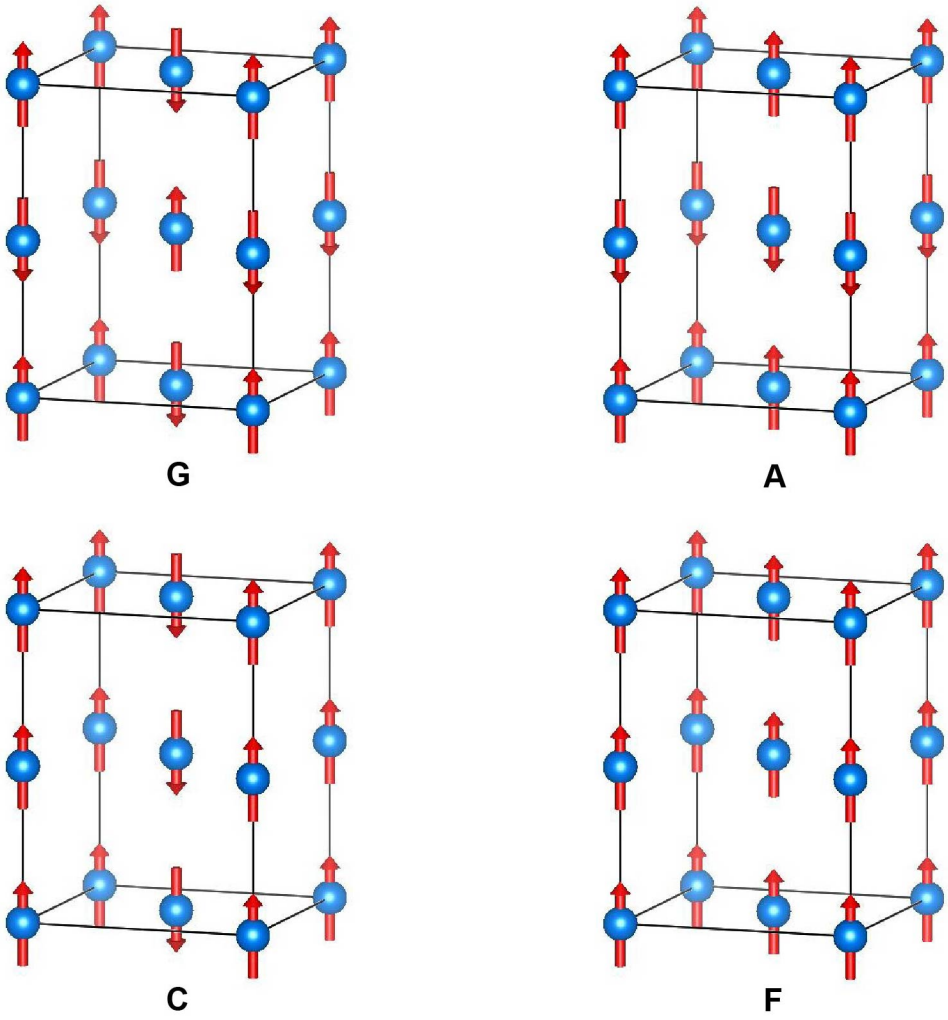


FIGURE 3.9: Four distinct magnetic configurations of $SrVO_2H$ (Only the V^{3+} cations are shown)

3.3.2 Convergence Tests

The validity of computational results relies on the appropriateness and consistency of the methodology. For solid state calculations, two of the most important methodological parameters are the plane-wave energy cut-off and the **k**-point sampling. Therefore, before doing more complex calculations, it is essential to perform convergence tests to select proper settings for these two parameters. For our $SrVO_2H$ system, the energy cut-off was tested before the **k**-point sampling. The tests were done on the four magnetic configurations by performing sequential single-point calculations with increased value of the two parameters (Table 3.2). At 600 eV, the energy difference between adjacent test calculations, ΔE, is smaller than 0.02 eV ($\sim$0.15%) for all four cases. This marks the point of convergence and there is no need to go for a higher value of energy cut-off. The **k**-point sampling was tested by following the same procedure at an elevated cut-off (750 eV). At $8 \times 8 \times 7$ the energy is converged within a 0.0002 eV tolerance (Table 3.3). As a result, the setting of a plane-wave energy cut-off of 600 eV and a **k**-point sampling of $8 \times 8 \times 7$ has been used for all calculations discussed later in this chapter, unless otherwise stated.

TABLE 3.2: Convergence test for $SrVO_2H$: energy cut-off

Cut-off (eV)	**k**-point	G (eV)	C (eV)	A (eV)	F (eV)
200	$4 \times 4 \times 4$	-125.82877	-126.02919	-125.59783	-125.55663
250	$4 \times 4 \times 4$	-128.02833	-127.91873	-127.48622	-127.45666
300	$4 \times 4 \times 4$	-126.48075	-126.44021	-126.01169	-125.98010
350	$4 \times 4 \times 4$	-125.66269	-125.67121	-125.24054	-125.21036
400	$4 \times 4 \times 4$	-125.41839	-125.41608	-124.98555	-124.95520
450	$4 \times 4 \times 4$	-125.30748	-125.30452	-124.87334	-124.84298
500	$4 \times 4 \times 4$	-125.29646	-125.29197	-124.86139	-124.83108
550	$4 \times 4 \times 4$	-125.29809	-125.29540	-124.86468	-124.83434
600	$4 \times 4 \times 4$	-125.31563	-125.31277	-124.88241	-124.85187
650	$4 \times 4 \times 4$	-125.33224	-125.32911	-124.89886	-124.86827
700	$4 \times 4 \times 4$	-125.34192	-125.33859	-124.90845	-124.87767
750	$4 \times 4 \times 4$	-125.35212	-125.34713	-124.91642	-124.88573
800	$4 \times 4 \times 4$	-125.35433	-125.35045	-124.91993	-124.88897
850	$4 \times 4 \times 4$	-125.35499	-125.35098	-124.92039	-124.88958

TABLE 3.3: Convergence test for $SrVO_2H$: **k**-point sampling

Cut-off (eV)	**k**-points	G (eV)	C (eV)	A (eV)	F (eV)
750	$2 \times 2 \times 2$	-125.19113	-125.19284	-124.76131	-124.72394
750	$3 \times 3 \times 3$	-125.34277	-125.33831	-124.90726	-124.87579
750	$4 \times 4 \times 4$	-125.35216	-125.34713	-124.91641	-124.88573
750	$5 \times 5 \times 4$	-125.35276	-125.34779	-124.91715	-124.88641
750	$5 \times 5 \times 5$	-125.35306	-125.34810	-124.91747	-124.88688
750	$6 \times 6 \times 4$	-125.35282	-125.34774	-124.91715	-124.88642
750	$6 \times 6 \times 5$	-125.35320	-125.34812	-124.91751	-124.88691
750	$6 \times 6 \times 6$	-125.35326	-125.34822	-124.91758	-124.88701
750	$7 \times 7 \times 5$	-125.35318	-125.34816	-124.91755	-124.88697
750	$7 \times 7 \times 6$	-125.35320	-125.34824	-124.91762	-124.88708
750	$7 \times 7 \times 7$	-125.35324	-125.34823	-124.91757	-124.88703
750	$8 \times 8 \times 6$	-125.35328	-125.34820	-124.91756	-124.88706
750	$8 \times 8 \times 7$	-125.35325	-125.34818	-124.91755	-124.88701
750	$8 \times 8 \times 8$	-125.35322	-125.34821	-124.91757	-124.88704
750	$9 \times 9 \times 6$	-125.35321	-125.34822	-124.91760	-124.88706
750	$9 \times 9 \times 7$	-125.35329	-125.34825	-124.91761	-124.88708
750	$9 \times 9 \times 8$	-125.35320	-125.34825	-124.91760	-124.88704
750	$9 \times 9 \times 9$	-125.35325	-125.34822	-124.91759	-124.88707

3.3.3 Validation of U_{eff}

For a strongly correlated system as $SrVO_2H$, the setting of U_{eff} is no less important than the plane-wave energy cut-off and the **k**-point sampling. To locate an appropriate U_{eff}, it is essential to perform a series of test calculations and compare the results with experimental data. First, it is the lattice parameters that should be compared (Table 3.4). As U_{eff} goes up from 0.0 to 5.0 eV, a' and c' both increase, and deviate from the experimental lattice parameters. Therefore, from this perspective, the lower U_{eff} provides closer agreement to the experiments. On the other hand, as U_{eff} decreases, the band gap of the system shrinks, and in the limit of very low U_{eff}, the band gap vanishes and the system becomes a metal at U_{eff} = 0.0 eV and a pressure of 0 GPa (Figure 3.17). This prediction is not consistent with the fact that $SrVO_2H$ is experimentally a Mott-insulator at ambient pressure: the first data point of Figure 3.5 shows an electrical resistance of 10^4 Ω at 0 GPa, clearly indicating a non-zero band gap. In summary, a finite value of $U_{\text{eff}} > 0$ is needed such that the computational

lattice parameters are as close to the experimental ones as possible, while the system remains an insulator at ambient pressure. For this purpose, we have selected U_{eff} = 2.0 eV, which is typical of similar calculations in the literature[49, 91, 92]. At this value of U_{eff}, the spin density on the V^{3+} centres confirm strong localisation of the valence electrons, with ρ(V) = $\pm$1.73 being typical of a formally d^2 ion in an oxide lattice.

TABLE 3.4: Effect of U_{eff} on the lattice parameters of $SrVO_2H$

U_{eff} (eV)	a' (Å)	c' (Å)	Spin density
0.0	5.562	7.381	$\pm$1.39
0.5	5.588	7.392	$\pm$1.56
1.0	5.603	7.381	$\pm$1.64
2.0	5.631	7.389	$\pm$1.73
3.0	5.658	7.397	$\pm$1.80
4.0	5.680	7.409	$\pm$1.84
5.0	5.696	7.445	$\pm$1.88
Exp.	5.562	7.334	-

3.4 Computational Results

From the results of the convergence tests, at an energy cut-off of 600 eV and a **k**-point sampling of 8 $\times$ 8 $\times$ 7, the energy of the test calculations converge and the G-type antiferromagnetic configuration is the most stable among the four, consistent with the experimental data. Therefore, for all the following discussions, we focus on the configuration with G-type antiferromagnetism, unless otherwise stated.

3.4.1 Electronic Structure at Ambient Pressure

The DOS at ambient pressure with its projection onto selected valence orbitals is shown in Figure 3.10a. The high spin moment on each metal centre means that each of the metal 3*d* bands in the PDOS is split into majority- and minority-spin components. For the V-based 3*d* manifold, only the majority-spin $3d_{xz/yz}$ orbitals lie below E_f, with their minority-spin counterparts being located $\sim$3 eV above it. The strong

splitting of the octahedral t_{2g} manifold arises because whilst the $3d_{xz}$ and $3d_{yz}$ orbitals are destabilised by only two in-plane V–O π^* interactions, $3d_{xy}$ is destabilised by four. Therefore this anisotropy, combined with the finite U_{eff}, leads to the emergence of a band gap and hence to the semiconducting properties of $SrVO_2H$ at ambient pressure. The band structure plot (Figure 3.10a) highlights one further point that becomes significant in the context of the pressure-dependent properties, which are elaborated in later sections: the dispersion of the bands just above E_f and below the $3d_{xy}$ band is more prominent in the *ab*-plane (Γ→X→M, Z→R→A) than along the *c*-axis (M→A, X→R, Γ→Z) (the first Brillouin zone is shown in Figure 3.11). In direct contrast, the $3d_{z^2}$ band is more strongly dispersed along the *c*-axis due to σ-type interaction via hydride anions, but the bottom of this band lies ∼1.6 eV above E_f.

3.4.2 Electronic Structure at Elevated Pressure

The variation of optimised lattice parameters as a function of applied external pressure is displayed alongside the experimental data (Figure 3.3). Whilst the computed lattice parameters are marginally more sensitive to pressure than those measured experimentally, the agreement between theory and experiment is striking, both in terms of the absolute values and in the differentiation between *a* and *c*, where the compressibility along the latter is approximately double that along the former (Table 3.1). The corresponding PDOS plots and band structure diagrams at 30 GPa (Figure 3.10b) and 60 GPa (Figure 3.10c) are shown as well. As the pressure increases to 30 GPa, the most conspicuous change in the DOS is that the vacant majority-spin $3d_{xy}$ band broadens substantially (the dashed red lines in Figure 3.10 mark the upper and lower limits of it), and the corresponding band structure confirms that this arises primarily from increased dispersion in the *ab*-plane (Γ→X→M, Z→R→A). The occupied $3d_{xz/yz}$ band also broadens, albeit to a lesser extent, which can again be traced to greater dispersion in the *ab*-plane rather than along the *c*-axis (compare changes

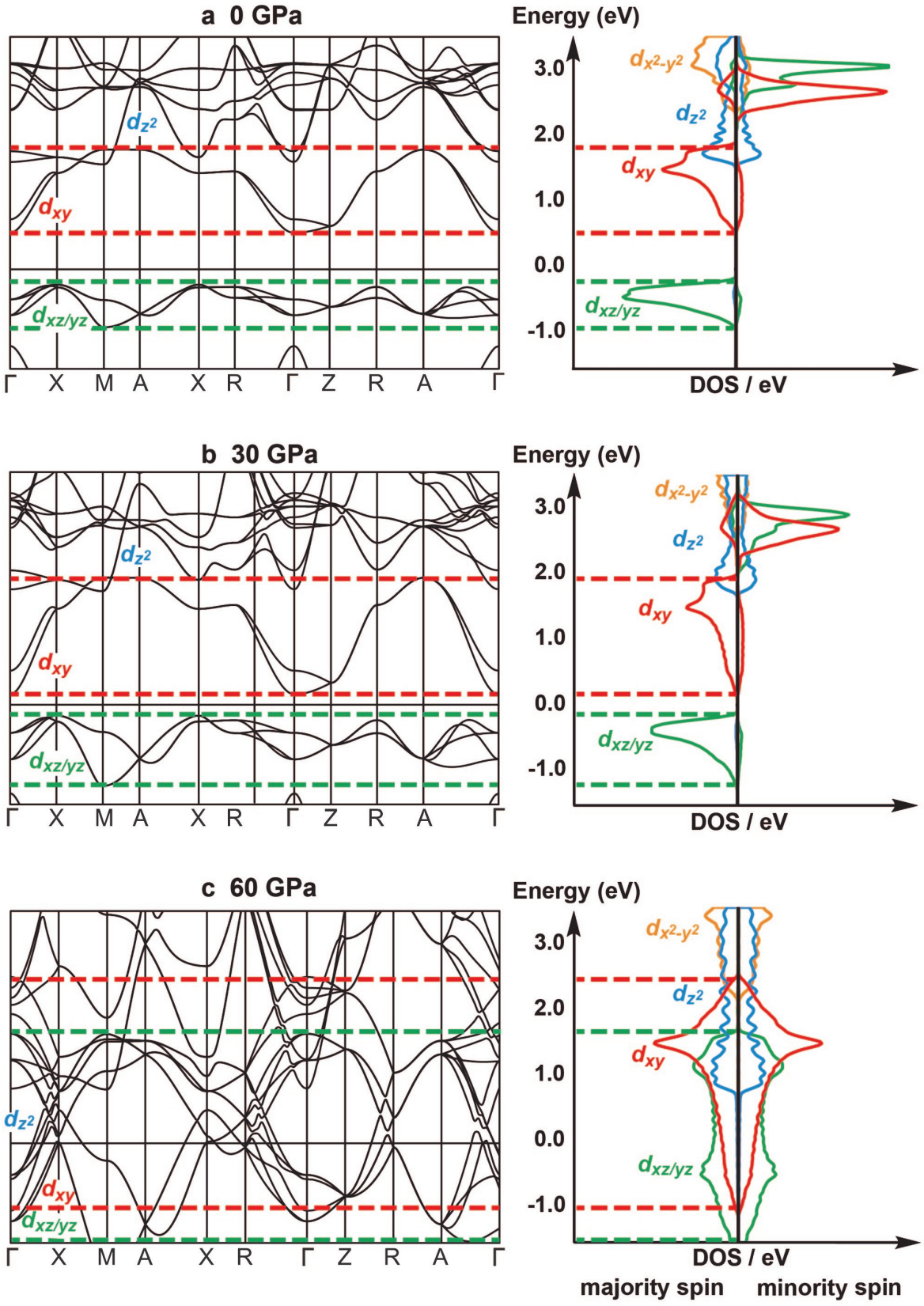


FIGURE 3.10: PDOS plots and band structures of $SrVO_2H$ at three distinct levels of pressure

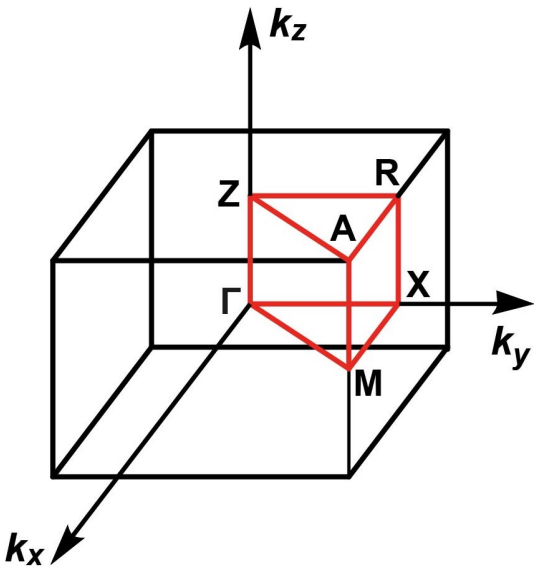


FIGURE 3.11: The first Brillouin zone of a tetragonal unit cell

in dispersion along X→M *vs.* Γ→Z). At 60 GPa, the broadening is sufficient to induce overlap between the occupied $3d_{xz/yz}$ and unoccupied $3d_{xy}$ bands, resulting in the complete loss of spin density and the emergence of a metallic state with an associated discontinuity in the optimised lattice parameters. This is consistent with the features observed in the experimental resistance data around 50 GPa (Figure 3.5). Even at 60 GPa, it is clear that it is the dispersion in the *ab*-plane, and not along the *c*-axis, that is the driving force for the insulator-to-metal transition: a clear band gap is maintained along Γ→Z and M→A.

To reinforce this point, we have tried to computationally mimic the effects of an anisotropic pressure source by varying either *a* or *c* while keeping the other constant (Figure 3.12). If we maintain *a* at its ambient-pressure value of 3.93 Å but reduce *c* to its 60 GPa optimised value of 3.25 Å, we note that the dispersion of the $3d_{xz/yz}$ band increases, but critically not to the extent that the band gap closes: the system remains an insulator. Conversely if we maintain *c* at its ambient-pressure value of 3.69 Å but contract *a* to its 60 GPa value of 3.67 Å, the band gap closes and a metallic state

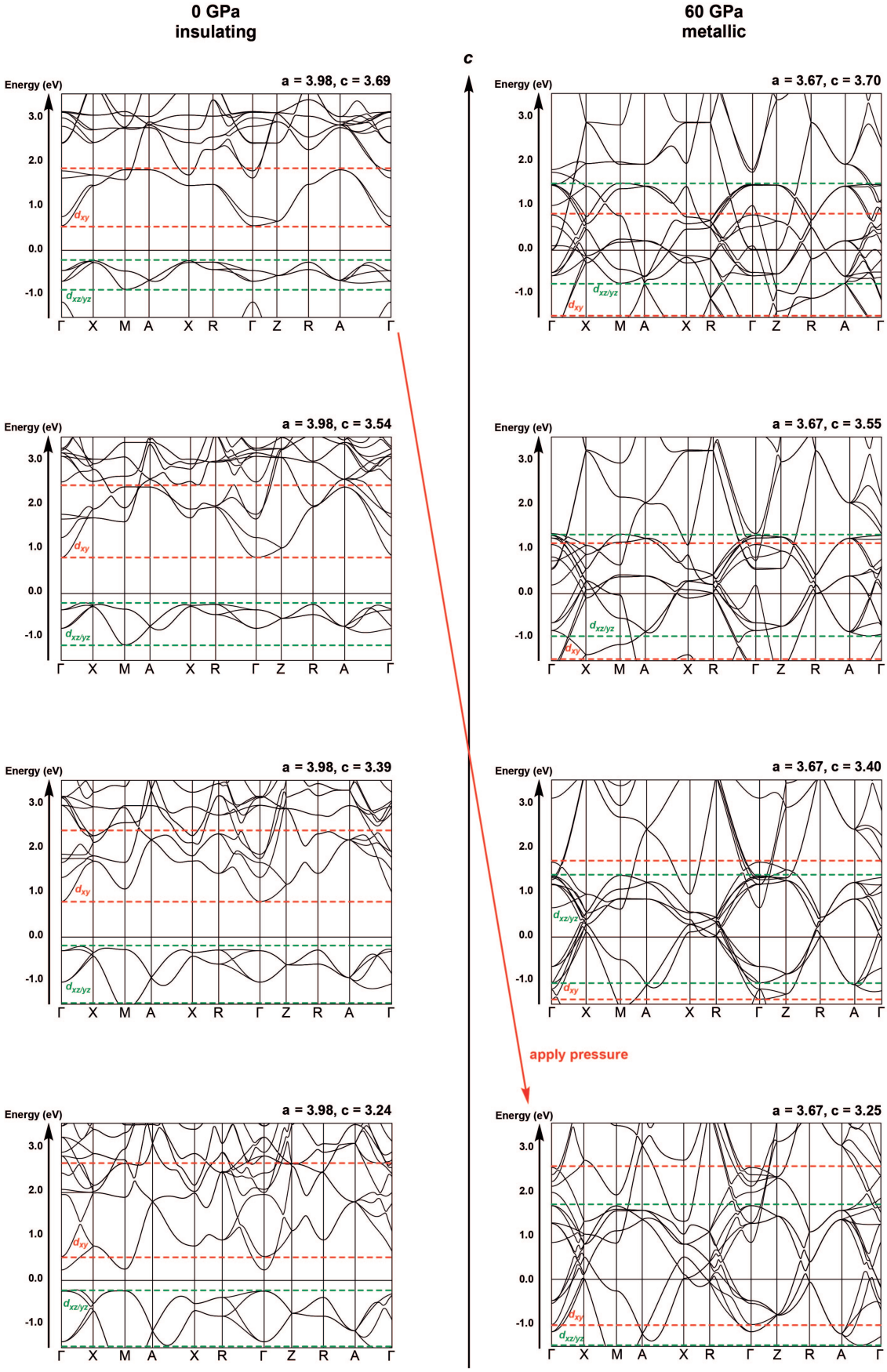


FIGURE 3.12: Variation of band structures of $SrVO_2H$ as a function of lattice parameters a and c (units in Å)

emerges. From the analysis above, we conclude that it is the contraction in the *ab*-plane and not along the *c*-axis that drives the formation of the metallic state, despite the fact that the magnitude of the contraction in the latter is larger in absolute terms.

3.4.3 Transmission Analysis

In order to further illustrate the contrast in the directions of conduction, a transmission analysis was done, which necessitated a change in methodology, from a plane-wave basis as used in VASP to a localised basis set in ATK. Therefore, we need to establish first that the two codes are giving qualitatively similar descriptions of the electronic structure. In fact, the total DOS for the system computed with VASP and ATK (for the 60GPa structure optimised with the former) are almost identical (Figure 3.13). We are therefore confident that the transmission spectrum from ATK can be mapped onto the PDOS computed using VASP. With this in mind, we then have explicitly computed the energy-dependent transmission spectrum for current flow both in the *ab*-plane and along the *c*-axis for the 60 GPa structure (Figure 3.14). The major peak in T_{ab} is coincident with the broad $3d_{xy}$ band that spans E_f. In comparison, transmission along *c* (T_c) becomes significant only above $\sim$0.8 eV, coincident with the bottom of the $3d_{z^2}$ band (Figure 3.10c). As a result, transmission at E_f is approximately five times stronger in the *ab*-plane than along the *c*-axis, indicating the metallic behaviour is strongly two-dimensional.

From this we have further proved that the emergence of metallic behaviour is not connected directly to the very substantial compression along the *c*-axis, which simply reflects the intrinsically higher compressibility of hydride *vs.* oxide anions. Instead, the high-pressure metallic state should be considered as a quasi-two-dimensional metal with a conduction band made up mainly of the overlapping $3d_{xz/yz}$ and $3d_{xy}$ bands, with substantial dispersion only in the *ab*-plane.

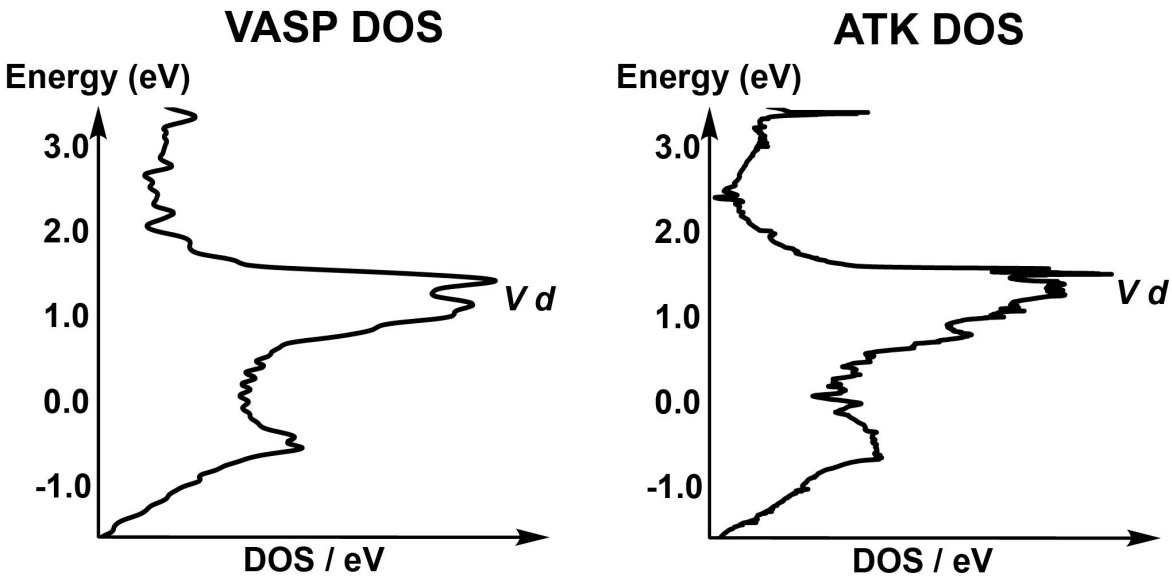


FIGURE 3.13: Total DOS plots of $SrVO_2H$ obtained from VASP and ATK

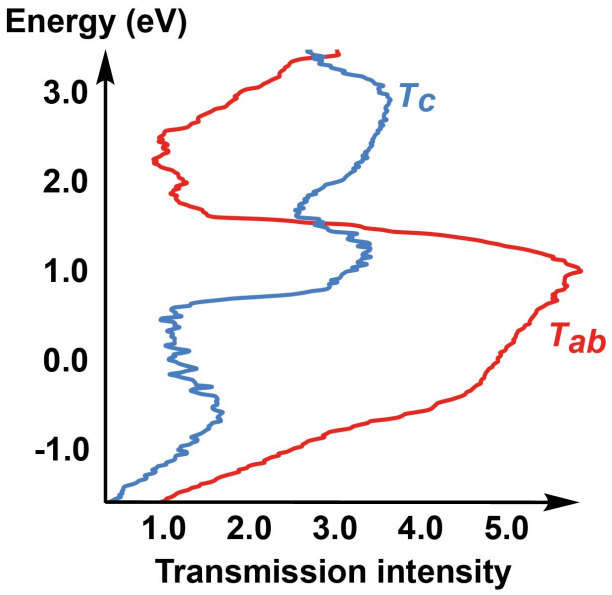


FIGURE 3.14: Transmission spectrum of $SrVO_2H$

3.4.4 Exchange Coupling Pathways

The observed G-type antiferromagnetism of $SrVO_2H$ indicates the presence of strong intra-layer coupling (J_1) via the bridging oxide anions, which results from efficient super-exchange between the singly occupied $3d_{xz}$ and $3d_{yz}$ orbitals, mediated by the O^{2-} $2p$ orbitals. The origin of the strong inter-layer exchange (J_2) is less obvious, as both $3d_{z^2}$ orbitals are formally vacant. In order to evaluate the strength of these exchange interactions within $SrVO_2H$, it has proved necessary to expand the unit cells again and add one more magnetic configuration, X (Figure 3.15). We then have mapped the DFT-computed energy of the G, C, A, X and F configurations onto the diagonal elements of the Heisenberg Spin Hamiltonian computed in the basis of $3d_{z^2}$ uncoupled states:

$$\mathcal{H}_{\text{Heisenberg}} = 2J_{ij}\sum_{j>i}\widehat{S}_i \cdot \widehat{S}_j \tag{3.4}$$

where J_{ij} is the effective exchange coupling constant between sites i and j with $S_i = S_j = 1$ for d^2 V^{3+} centres. In the $\sqrt{2} \times 2\sqrt{2} \times 2$ expanded cell defined in Figure 3.15 we can identify four symmetry-distinct exchange coupling pathways, J_{1-4}: J_1 corresponds to the nearest neighbour intra-plane V-O-V coupling while J_2, in contrast, is the nearest neighbour inter-plane V-H-V coupling. A Sr^{2+} cation lies directly along the line of the J_3 pathway while there is no bridging ion directly along the J_4 pathway. Explicitly expressing the Heisenberg Spin Hamiltonian in the form of $\mathbf{A}x = \mathbf{b}$ and substituting $2\sum_{j>i} S_i \cdot S_j$ into matrix $\mathbf{A}$ lead to:

$$\begin{bmatrix} 32 & 16 & 32 & -64 \\ 32 & -16 & -32 & 64 \\ -32 & 16 & 32 & 64 \\ 0 & 16 & 0 & 0 \\ -32 & -16 & -32 & -64 \end{bmatrix} \begin{bmatrix} J_1 \\ J_2 \\ J_3 \\ J_4 \end{bmatrix} = \begin{bmatrix} E_G + \Delta \\ E_C + \Delta \\ E_A + \Delta \\ E_X + \Delta \\ E_F + \Delta \end{bmatrix} \tag{3.5}$$

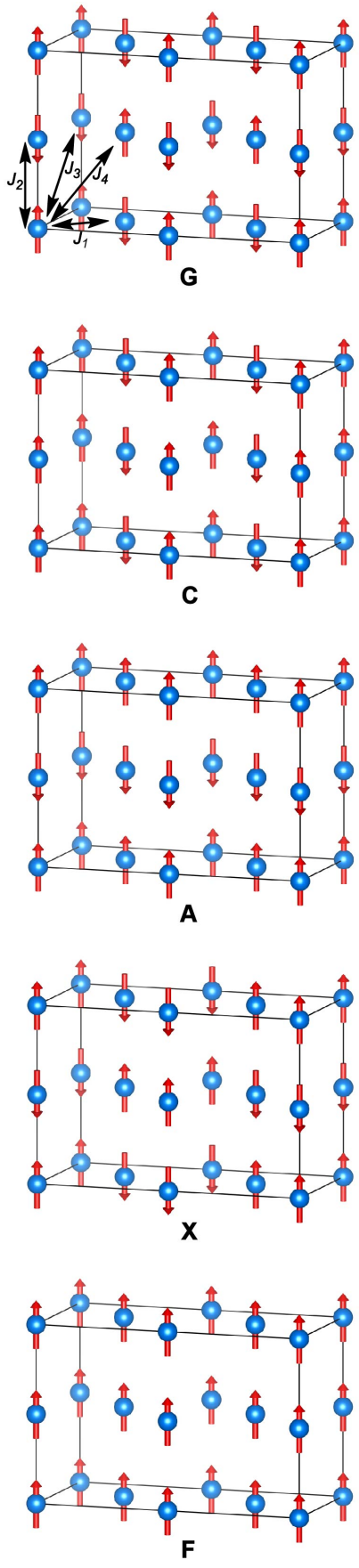


FIGURE 3.15: $\sqrt{2} \times 2\sqrt{2} \times 2$ expanded cells of $SrVO_2H$ in five magnetic configurations

where Δ denotes the extra term of the Heisenberg Spin Hamiltonian, which is considered to be the same across the five configurations as an approximation. Taking the differences between each pair of the five linear equations and substituting the energy differences obtained from Table 3.5 into **b** lead to:

$$\begin{bmatrix} 0 & 32 & 64 & -128 \\ 64 & 0 & 0 & -128 \\ 64 & 32 & 64 & 0 \\ 32 & 0 & 32 & -64 \\ 64 & -32 & -64 & 0 \\ 64 & 0 & 0 & 128 \\ 32 & -32 & -64 & 64 \\ 0 & 32 & 64 & 128 \\ -32 & 0 & 32 & 64 \\ -32 & -32 & -32 & -64 \end{bmatrix} \begin{bmatrix} J_1 \\ J_2 \\ J_3 \\ J_4 \end{bmatrix} = \begin{bmatrix} -0.11526 \\ -1.31228 \\ -1.36572 \\ -0.62684 \\ -1.19702 \\ -1.25046 \\ -0.51158 \\ -0.05344 \\ 0.68544 \\ 0.73888 \end{bmatrix} \tag{3.6}$$

Solving this system of linear equations by least-square method leads to: J_1 = 20.0 meV, J_2 = 4.5 meV, J_3 = 0.9 meV and J_4 = 0.2 meV. The two last small values indicate that the interactions J_3 and J_4 are small and can safely be neglected in this analysis. Like Wei *et al.* and Liu *et al.*, we conclude that the experimentally observed G-type antiferromagnet is the most stable configuration, with stronger coupling in the *ab*-plane (V–O–V, J_1 = 20.0 meV) than along the *c*-axis (V–H–V, J_2 = 4.5 meV). The significant antiferromagnetic J_1 is reasonable and is to be anticipated based on the Goodenough-Kanamori rules[80]. The rather large value for J_2, the inter-planar exchange coupling, is in contrast somewhat unexpected given that the V-H-V coupling pathway via the metal orbitals corresponds to a formally "empty-empty" interaction, which usually leads to only weak coupling. Nevertheless, our value of J_2 is

TABLE 3.5: Energy of the G, C, A, X and F configurations

Configuration	Energy (eV)
G	-259.87007
C	-259.75481
A	-258.55779
X	-259.24323
F	-258.50435

consistent with those reported previously. Wei *et al*. have argued for direct through-space interactions between the two V^{3+} centres along the *c*-axis, although the V–V separation here is greater than the bonding distance in, for example, VO_2, suggesting that such overlap should be rather small. An alternative explanation comes from the significant covalent character of the V–H bonds. The Goodenough-Kanamori rules predict an antiferromagnetic contribution to the coupling in this case because charge transfer from H^- 1*s* to the vacant V^{3+} $3d_{z^2}$ orbitals is most efficient when the two electrons in the H^- 1*s* orbital are transferred to different metal centres. In a ferromagnetic arrangement, in contrast, only one of the H^- 1*s* electrons can undergo a virtual transfer to the metal $3d_{z^2}$ orbitals (Figure 3.16). Similar factors lead to the high ordering temperature in $LaSrCoO_3H_{0.7}$[93].

3.4.5 Effects of U_{eff}

The DOS plots as a function of pressure for U_{eff} = 0.0, 2.0 and 4.0 eV show that increasing U_{eff} increases the band gap at ambient pressure, and therefore pushes the insulator-to-metal transition to higher levels of pressure. Thus even at 60 GPa, the U_{eff} = 4.0 eV calculations predict an insulating state with a finite band gap (Figure 3.17). An alternative strategy that does not require a parameter choice is to use a hybrid functional such as HSE06, which in principle alleviates some of the self-interaction error that compromises the accuracy of the band gap in GGA functionals such as PBE. The DOS plots computed in this way are rather similar to those obtained

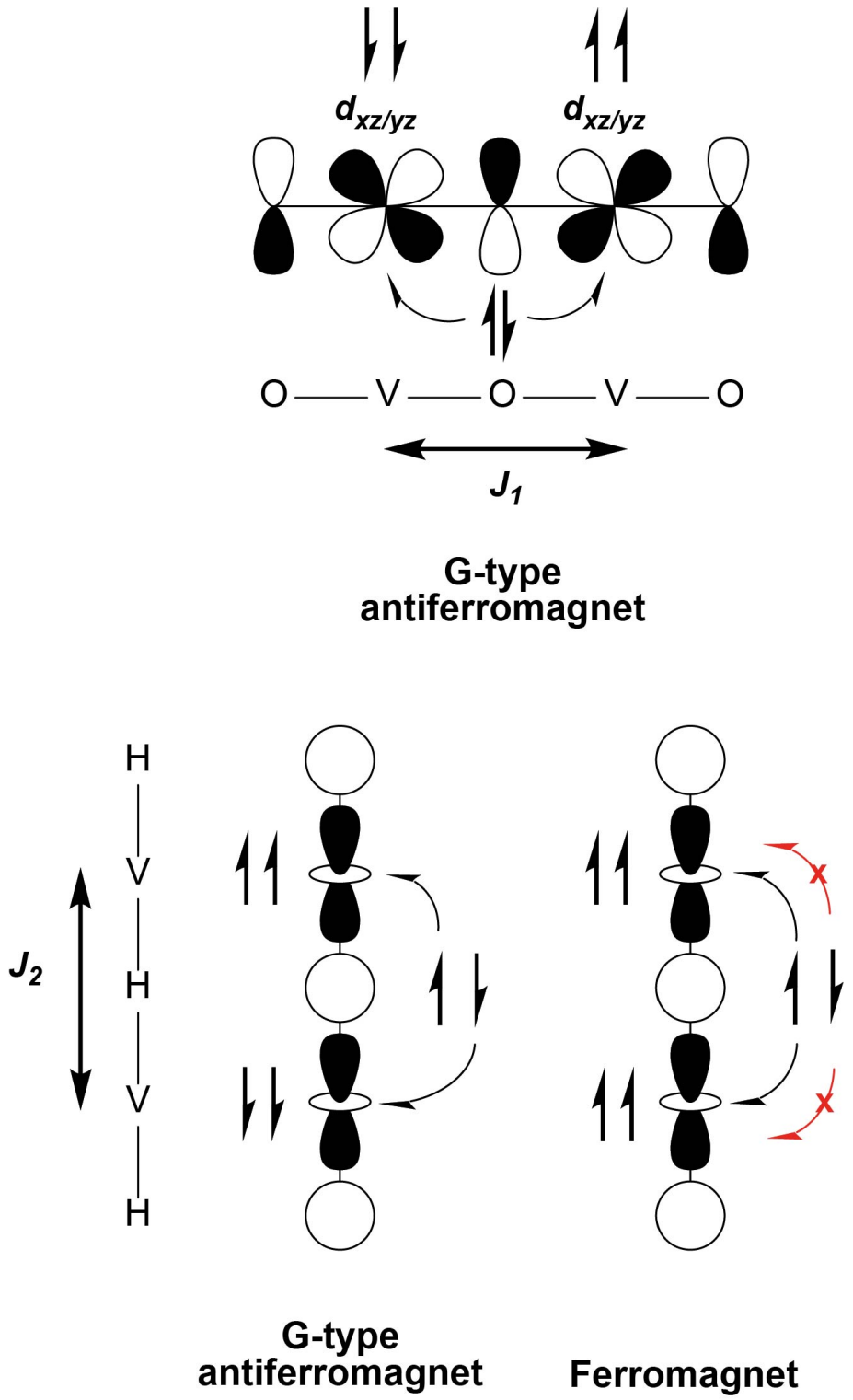


FIGURE 3.16: Schematic picture of exchange coupling pathways of $SrVO_2H$ for the intra- and inter-plane antiferromagnetism

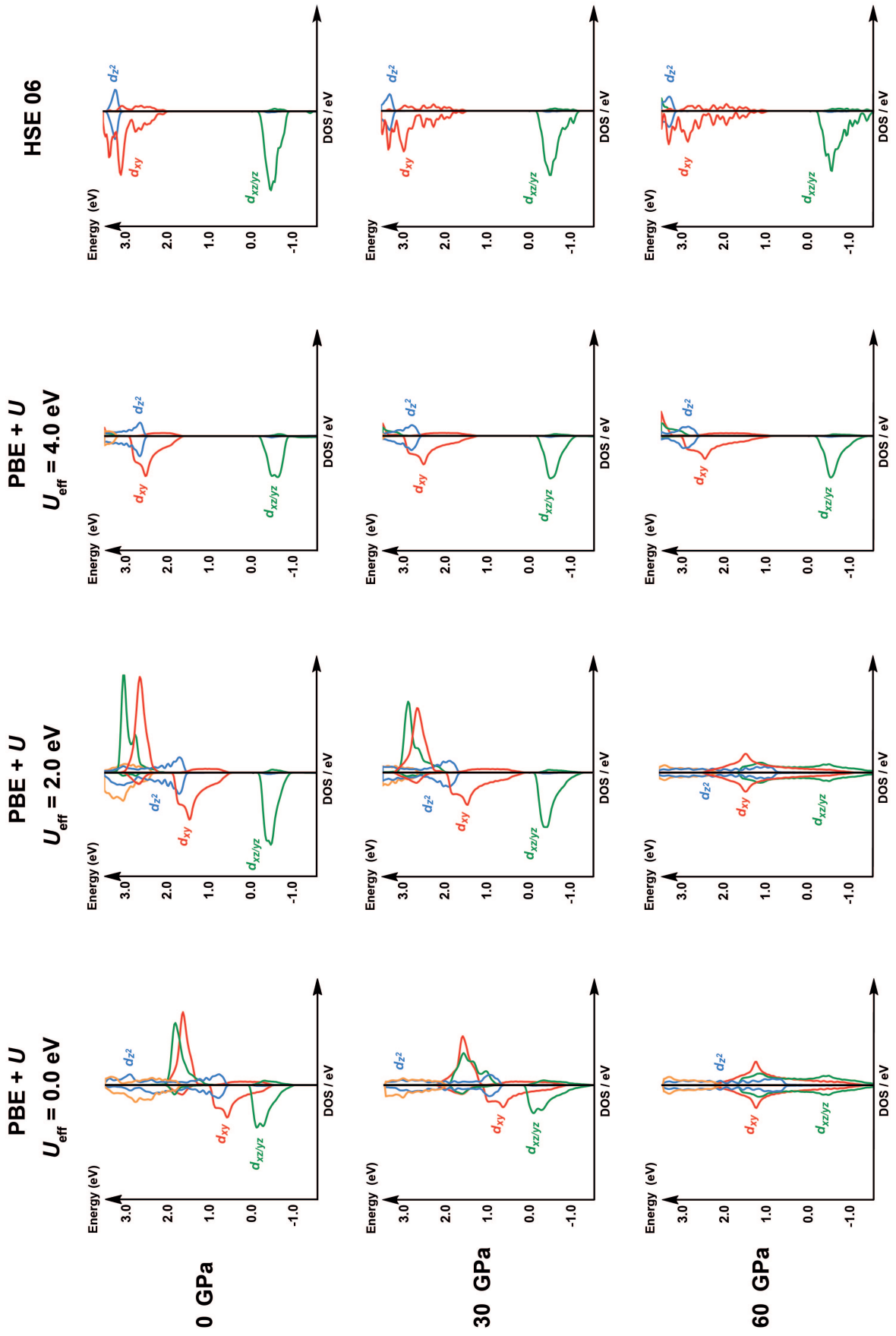


FIGURE 3.17: Pressure-dependent PDOS of $SrVO_2H$ computed using different computational protocols

with U_{eff} = 4.0 eV across the entire pressure range, and indeed the system remains insulating even at 60 GPa (Figure 3.17). Despite the absolute differences in these plots, it is clear that the effects of pressure are qualitatively the same in all cases: the dominant feature is the greater dispersion in the $3d_{xy}$ conduction band. Thus while the exact value of the critical pressure is strongly dependent on methodology, our conclusions regarding the underlying mechanism are not. We do not, therefore, claim to be able to pinpoint the critical pressure exactly, but rather note that the pressure-induced dispersion of the $3d_{xy}$ band is the driving force in all cases.

3.5 Discussion

At first sight the pressure-induced insulator-to-metal transition in $SrVO_2H$ appears remarkably similar to that in $SrFeO_2$[84] – both phases are antiferromagnetic insulators at ambient pressure, both undergo strongly anisotropic lattice contractions on the application of pressure (Table 3.1) and both eventually become metallic (at 34 GPa and 50 GPa, respectively). A closer inspection however reveals profound differences between the two systems. In the case of $SrFeO_2$, the transition from insulating to metallic behaviour is intimately connected to a change in spin state from S = 2 at ambient pressure to S = 1 above the critical pressure P_c. The ambient-pressure electronic structure has been discussed at some length[78, 79], and it is the $3d_{z^2}$ orbitals of Fe^{2+} centres that are doubly-occupied: $(d_{z^2})^2(d_{xz/yz})^2(d_{xy})^1(d_{x^2-y^2})^1$. The band gap is primarily a consequence of the large spin polarisation that splits the majority- and minority-spin manifolds. Above P_c (34 GPa), however, the relative destabilisation of the Fe–O σ^* orbital as the Fe–O bond lengths are compressed leads to a local $(d_{z^2})^2(d_{xz/yz})^3(d_{xy})^1(d_{x^2-y^2})^0$ electronic configuration (S = 1)[94]. At even higher pressures, the compression along the c-axis leads to repulsion between the $3d_{z^2}$ orbitals in adjacent layers, causing a partial transfer of electron density out of the $3d_{z^2}$ band into $3d_{xy}$, and thus a substantial increase in the DOS at E_f. The result is a metallic state

where the electron density distribution is approximately isotropic[84]. In contrast, our calculations on the $SrVO_2H$ system suggest that the greater compressibility along the *c*-axis is not directly related to the emergence of the metallic behaviour: even at the high-pressure limit the inter-layer V–V separation (3.25 Å at 60 GPa) is too large to afford significant direct V_{3d_π}–V_{3d_π} overlap. The significant difference in behaviours of $SrFeO_2$ and $SrVO_2H$ arises simply because the electronic configurations are very different (d^6 *vs.* d^2) and as mentioned earlier, the band gap in the latter is determined by the different number of V_{3d_π}–O_{2p_π}–V_{3d_π} interactions experienced by the $3d_{xy}$ and $3d_{xz/yz}$ orbitals (four and two, respectively). The hydride anions in $SrVO_2H$ can therefore be viewed as π-orbital blockers in the sense that they have no π-symmetry valence orbitals to interact with the V^{3+} π-symmetry $3d_{xz/yz}$ orbitals. The metallic behaviour then emerges because the compression in the *ab*-plane, although smaller in magnitude than that along the *c*-axis, increases the V_{3d_π}–O_{2p_π}–V_{3d_π} interactions, hence the dispersion of the $3d_{xz/yz}$ and the $3d_{xy}$ bands, to the extent that they overlap and form a single continuous band. In a word, when $SrVO_3$ is converted to $SrVO_2H$, the three-dimensional V_{3d_π}–O_{2p_π}–V_{3d_π} network is reduced to a two-dimensional one as a result of the π-blocking SrH layer, with dramatic consequences for the physical properties simply because the band gap falls in the middle of the V_{3d_π} band.

Insulator-to-metal transitions in strongly correlated systems have been a central subject in condensed matter physics for many decades, and the transitions of a large number of metal oxide systems with different *d*-electron counts have been studied in some detail[40]. The physics of low *d*-electron count systems (d^1 or d^2 systems such as VO_2, V_2O_3, Ti_2O_3, and $REVO_3$ where RE = rare earth, for example) is, however, complicated because the splitting of the M_{d_π} manifold is very sensitive to the subtle details of the distortions and tilting of the MO_6 octahedra. In contrast, the highly anisotropic coordination environment of V^{3+} centres in $SrVO_2H$ simplifies the problem by causing a substantial zeroth-order splitting of this manifold, and the

unusual pressure-dependent electronic properties of $SrVO_2H$ highlight the importance of the π-blocking nature of hydrides. We note that the use of π-blockers differs markedly from conventional strategies for reducing dimensionality, where bulky blocking layers are typically used to separate (super)conducting layers. These observations provide a strong motivation for the synthesis of new transition metal oxyhydride phases with novel and elaborate anion-ordering schemes. Wider studies of the oxyhydride family will undoubtedly increase our ability to control the connectivity of π-symmetry orbitals, in phases with reduced dimensions and hence engineer materials with novel properties.

Chapter 4

$SrV_{0.95}Ti_{0.05}O_{1.5}H_{1.5}$: Effects of Titanium-doping

4.1 Introduction

As we have seen in chapter 3, low-temperature structure-conserving reactions can be used to manipulate the anion lattices of transition metal oxides, offering routes to highly metastable phases that can not be readily prepared via conventional high-temperature synthesis. This type of reaction has been used to generate extended solids containing arrays of transition metal cations in unusual oxidation state and co-ordination geometry combinations[95, 96]. Apart from this, hydride-for-oxide anion-exchange reactions can also occur, leading to the formation of oxyhydride phases such as $LaSrCoO_3H_{0.7}$ and $Sr_3Co_2O_{4.33}H_{0.84}$, mentioned in chapter 2. The very unusual electronic structure of these metastable solid-state compounds means that they are of intrinsic chemical interest, but their electronic and magnetic properties, which arise from the cooperative interactions between the paramagnetic metal centres, also offer the potential for novel materials properties. However, just like the $SrVO_2H$ system discussed previously, most transition metal oxyhydride phases are antiferromagnetic insulators, simply because the large on-site electron-electron repulsion tends to localise the unpaired *d* electrons on discrete cation sites. Valence-electron

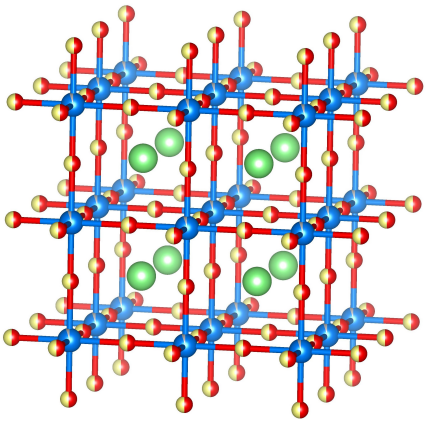


FIGURE 4.1: Crystal structure of $SrV_{0.95}Ti_{0.05}O_{1.5}H_{1.5}$
(Sr: light green; V: blue; Ti: grey; O: red; H: yellow)

localisation of this type is frequently observed and is particularly common in oxide phases containing 3*d* transition metal centres with integer oxidation states[97]. Itinerant electrons can, however, be generated via chemical doping, which drives the transition metal cations into non-integer or mixed-valent states, resulting in potential novel chemical and physical properties. A famous example is the Cu^{2+} phase La_2CuO_4, which is a simple antiferromagnetic insulator in its pure form. However, doping the system via Ba^{2+}-for-La^{3+} substitution leads to a mixed-valent Cu^{2+}/Cu^{3+} state, which exhibits both metallic conductivity and superconductivity[98]. Likewise, the Mn^{3+} and Mn^{4+} phases, $LaMnO_3$ and $CaMnO_3$, are both antiferromagnetic insulators[99, 100], but the mixed-valent $La_{1-x}Ca_xMnO_3$ solid solution exhibit metal-insulator-transition and large magnetoresistive ratios[101]. These remarkable properties originate from doping the parent phases, and provide strong motivation to explore the effects of doping on stoichiometric oxide systems and their derivatives. In this project, the oxyhydride phase $SrVO_2H$ was doped with Ti^{3+}, resulting in the system with mixed cations, $SrV_{0.95}Ti_{0.05}O_{1.5}H_{1.5}$, where the V^{3+}/Ti^{3+} and O^{2-}/H^- pairs are disordered, respectively (Figure 4.1).

The results of this project have been published in *Inorg. Chem.*, 2018, **57**, 2890.

4.2 Summary of Experimental Data

The relevant experiments were conducted by Amano Patino *et al.* from University of Oxford, UK[102].

4.2.1 Reaction Process

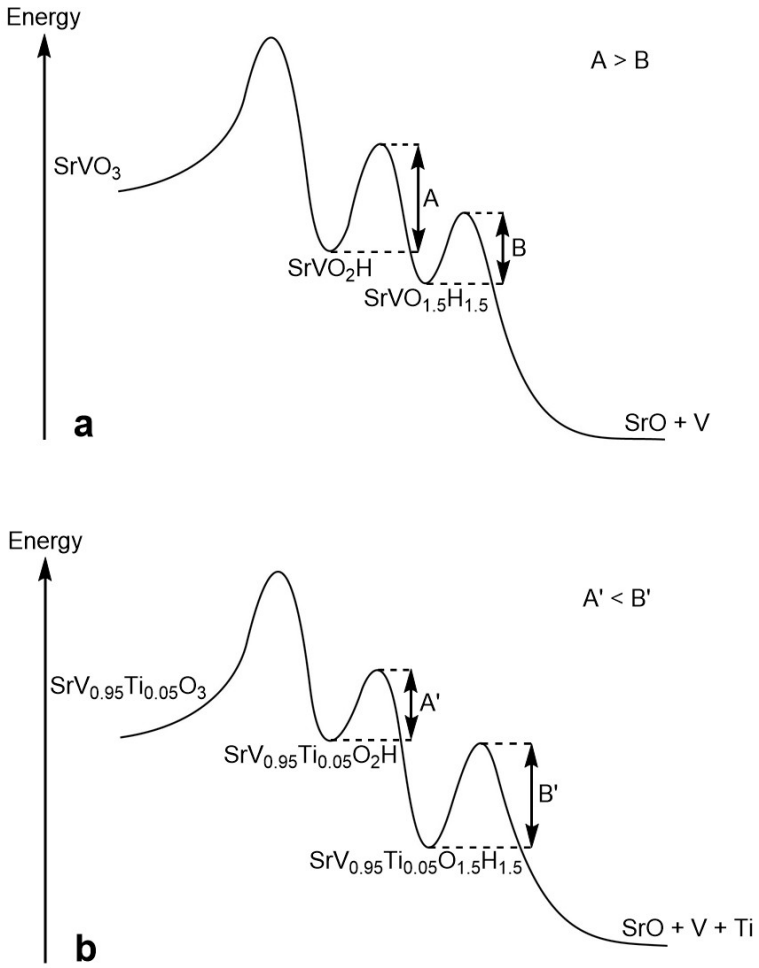


FIGURE 4.2: Schematic diagram qualitatively showing the difference in activation energy for the reduction of $SrVO_3$ and $SrV_{0.95}Ti_{0.05}O_3$

$SrVO_2H$ was doped with Ti^{3+} following an indirect route. The parent phase $SrV_{0.95}Ti_{0.05}O_3$ was first synthesised then reduced by CaH_2, as in the topochemical reduction of $SrVO_3$ to yield $SrVO_2H$[77]. The difference in reactivity between these two

reduction processes with similar reducing agents but very distinct products is striking, and a schematic potential energy surface is plotted in Figure 4.2. Unsubstituted $SrVO_3$ reacts readily with CaH_2 to yield $SrVO_2H$, but attempts to advance this reaction further by raising the reaction temperature lead to non-topochemical reactions and, ultimately, to the formation of SrO and metallic V. The activation energies related to these two reaction intermediates are denoted as A and B, respectively (Figure 4.2a). Since in the reduction of $SrVO_3$, $SrVO_2H$ stays as the product experimentally while $SrVO_{1.5}H_{1.5}$ is not observed, A is expected to be larger than B, which traps the kinetically more stable $SrVO_2H$. In contrast, the reduction of $SrV_{0.95}Ti_{0.05}O_3$ proceeds all the way to cubic $SrV_{0.95}Ti_{0.05}O_{1.5}H_{1.5}$, with the direct analogue of $SrVO_2H$, tetragonal $SrV_{0.95}Ti_{0.05}O_2H$, appearing only transiently as an intermediate phase. Here the activation energies are denoted as A′ and B′ (Figure 4.2b), and in this case the former is expected to be smaller than the latter, leading to the kinetically and thermodynamically more stable $SrV_{0.95}Ti_{0.05}O_{1.5}H_{1.5}$. These very different reaction outcomes suggest that the presence of even small amounts of Ti^{3+} cations destabilises $SrV_{0.95}Ti_{0.05}O_2H$ in some way, forcing it to react further to form $SrV_{0.95}Ti_{0.05}O_{1.5}H_{1.5}$.

4.2.2 Structure Comparison

The lattice parameters of the $SrV_{0.95}Ti_{0.05}O_2H$ intermediate phase can offer some clues to the origin of its relative instability (Table 4.1). It can be seen that while *a* is marginally shorter than that in the unsubstituted $SrVO_2H$ (3.929 Å *vs.* 3.933 Å), *c* is significantly elongated (3.738 Å *vs.* 3.667 Å). These differences are consistent with a degree of anion-disorder in the Ti-containing phase, with small concentrations of O^{2-} along *c*-axis and H^- in the *ab*-plane causing elongation and contraction, respectively. It is interesting to note that $SrCrO_2H$[76], the Cr-analogue of $SrVO_2H$, adopts a cubic and anion-disordered structure which is quite different from that of $SrVO_2H$, suggesting the anion-ordered tetragonal phase is uniquely stable for a d^2

electronic configuration of the transition-metal centre. The deviations to either lower ($SrV_{0.95}Ti_{0.05}O_2H$, $d^{1.95}$) or higher ($SrCrO_2H$, d^3) electron counts appear to drive the system into alternative anion-disordered phases. The partial disordering of the anion lattice adds a large degree of strain to the framework because V-O-V connections are inserted into a lattice optimised for V-H-V links and vice versa, which significantly destabilises $SrV_{0.95}Ti_{0.05}O_2H$ with respect to the anion-ordered $SrVO_2H$.

TABLE 4.1: Experimental lattice parameters

System	a (Å)	c (Å)
$SrV_{0.95}Ti_{0.05}O_{1.5}H_{1.5}$	3.888	3.888
$SrV_{0.95}Ti_{0.05}O_2H$	3.929	3.738
$SrVO_2H$	3.933	3.667

4.3 Methodology

All calculations were performed at the PBE+U level using the plane-wave basis code Vienna Ab initio Simulation Package (VASP 5.3.2)[87], based on a $\sqrt{2} \times \sqrt{2} \times 2$ expansion of the primitive unit cell. As in the $SrVO_2H$ case, a plane-wave energy cut-off of 600 eV was imposed and the Γ-centred **k**-point grid of $8 \times 8 \times 7$ was used to sample the first Brillouin zone. The optimisations were done with all the geometrical constraints released, so the ions were allowed to move freely. For DOS calculations, a $24 \times 23 \times 22$ **k**-point sampling was used to improve the quality of the plots. The U_{eff} value was fixed at 2.0 eV for all V^{3+}, Ti^{3+} and Cr^{3+} centres.

4.3.1 Construction of the Unit Cells

To see how Ti-doping affects the stability and electronic structure of the anion-ordered and disordered tetragonal phases, on top of the existing *trans*-$SrVO_2H$, we have constructed five hypothetical structures for comparison and analysis purposes, where the *trans* and *cis* labels are used to indicate the positions of H^- anions. In the *trans*

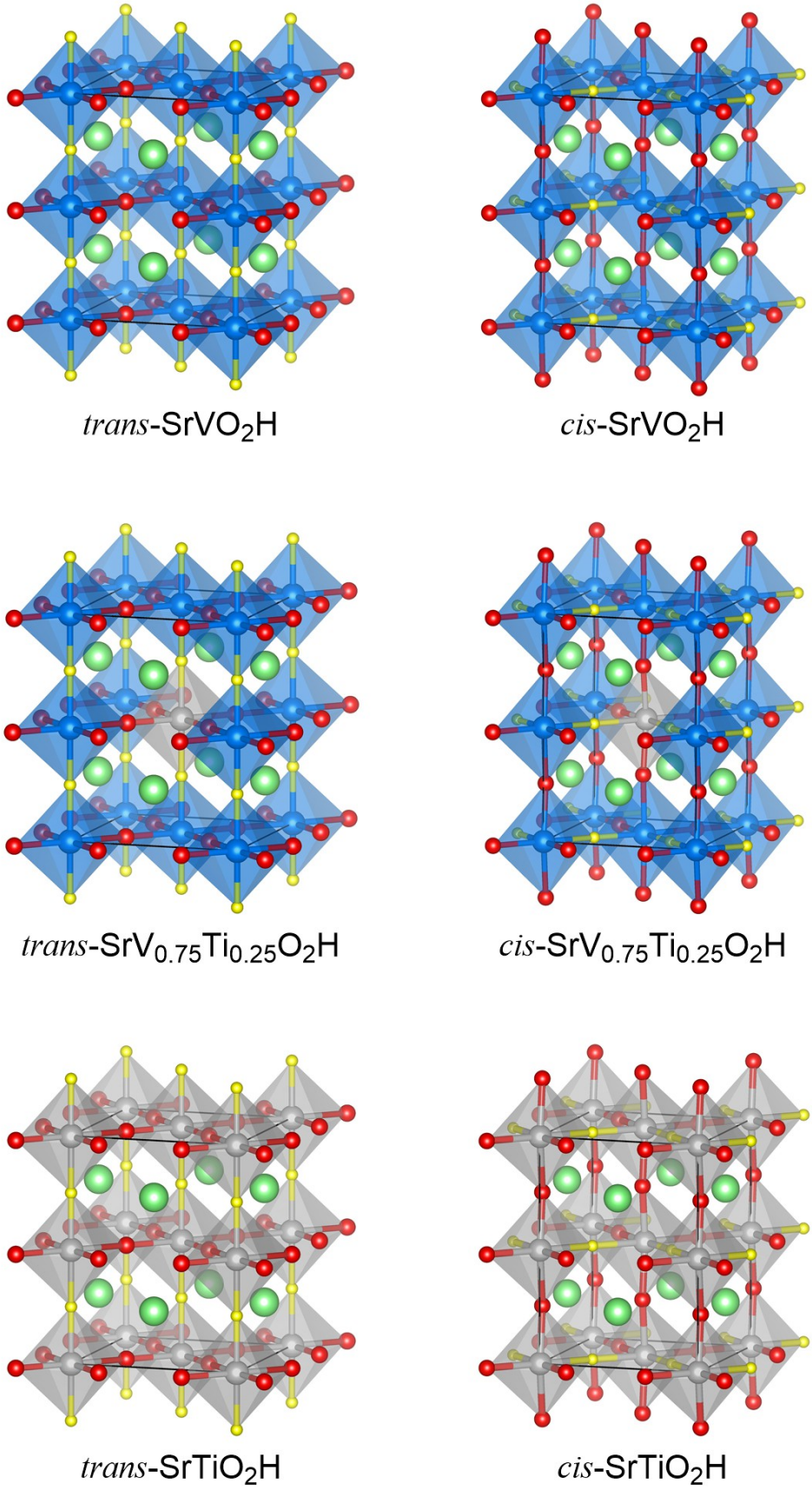


FIGURE 4.3: *trans*-$SrVO_2H$ and five hypothetical structures

structures, the anions are arranged in the same ordered array as that in the existed *trans*-$SrVO_2H$, with the two H^- ligands aligned mutually *trans* along the *c*-axis. In the *cis* isomers, the H^- anions are shifted into the *ab*-plane, where they are eclipsed in successive *ab*-planes (Figure 4.3). The alternative configurations where the H^- anions are staggered in successive planes were computed to be higher in energy in all cases and thus not considered further here.

The $\sqrt{2} \times \sqrt{2} \times 2$ expanded cells contain four formula units, which means the lowest level of Ti-doping allowed is 25% ($SrV_{0.75}Ti_{0.25}O_2H$). Although this is substantially higher than the actual Ti-doping level of 5% as in $SrV_{0.95}Ti_{0.05}O_2H$, the computational results of the former should still provide a qualitative understanding of the effects of Ti-doping.

4.4 Computational Results

As mentioned in Chapter 3, for *trans*-$SrVO_2H$, the G-type antiferromagnetic configuration has proved the ground state. Therefore, for the purposes of direct comparison and limiting the number of variables, all the five hypothetical structures were modelled as G-type antiferromagnets, unless otherwise stated.

4.4.1 $SrVO_2H$, $SrTiO_2H$ and $SrV_{0.75}Ti_{0.25}O_2H$

TABLE 4.2: Computed energy and lattice parameters of the six structures

System	Energy (eV)	a' (Å)	b' (Å)	c' (Å)
trans-$SrVO_2H$	-129.923	5.634	5.634	7.385
cis-$SrVO_2H$	-128.865	5.448	5.608	7.864
trans-$SrV_{0.75}Ti_{0.25}O_2H$	-129.924	5.672	5.672	7.412
cis-$SrV_{0.75}Ti_{0.25}O_2H$	-129.560	5.540	5.527	7.914
trans-$SrTiO_2H$	-129.166	5.694	5.694	7.517
cis-$SrTiO_2H$	-130.022	5.679	5.683	7.819

The ground state energy and lattice parameters of $SrVO_2H$ and $SrTiO_2H$ systems were calculated, with the results collected in Table 4.2, where $a'/b'/c'$ denote calculated lattice parameters in the $\sqrt{2} \times \sqrt{2} \times 2$ expanded cell. We acknowledge that the *cis*-arrangement represents only one possible arrangement among the many that could contribute to the anion-disordered cubic phase, but nevertheless a comparison of the two types of structures allows us to assess the energetic cost of moving the H^- anions around the lattice. For the case of $SrVO_2H$, the *trans* arrangement of H^- proves to be substantially more stable than the *cis* alternative (ΔE = +0.265 eV per formula unit), consistent with its established preference for the tetragonal phase. In $SrTiO_2H$, in contrast, the order is reversed, with a strong preference for the *cis* arrangement over *trans* (ΔE = -0.214 eV). The system with mixed cations, $SrV_{0.75}Ti_{0.25}O_2H$, is intermediate between the limits of $SrVO_2H$ and $SrTiO_2H$, where the *trans* structure is favoured but to a much lesser degree (ΔE = +0.091 eV) than in $SrVO_2H$. These calculations therefore indicate that the *trans* arrangement is optimal for the d^2 configuration of V^{3+} and is progressively destabilised relative to its *cis* analogue as the concentration of Ti^{3+} is increased, meaning as well that the total *d*-electron count of the whole system is decreased.

The computed DOS and orbital illustrations of $SrTiO_2H$ are shown in Figure 4.4, with those of $SrVO_2H$ side-by-side as comparison; the latter has been discussed in-depth in Chapter 3. For Ti^{3+} in *cis*-$SrTiO_2H$, unlike V^{3+} in *trans*-$SrVO_2H$, where the two *d* electrons occupy the $d_{xz/yz}$ orbitals, the single *d* electron of Ti^{3+} fills half of the d_{xy} band.

4.4.2 $SrCrO_2H$

To further explore the relationship between *d*-electron count and structural disorder of the square-planar oxyhydride phases, calculations on the $SrCrO_2H$ system with d^3 Cr^{3+} centres have been performed. As in the previous $SrVO_2H$, $SrTiO_2H$

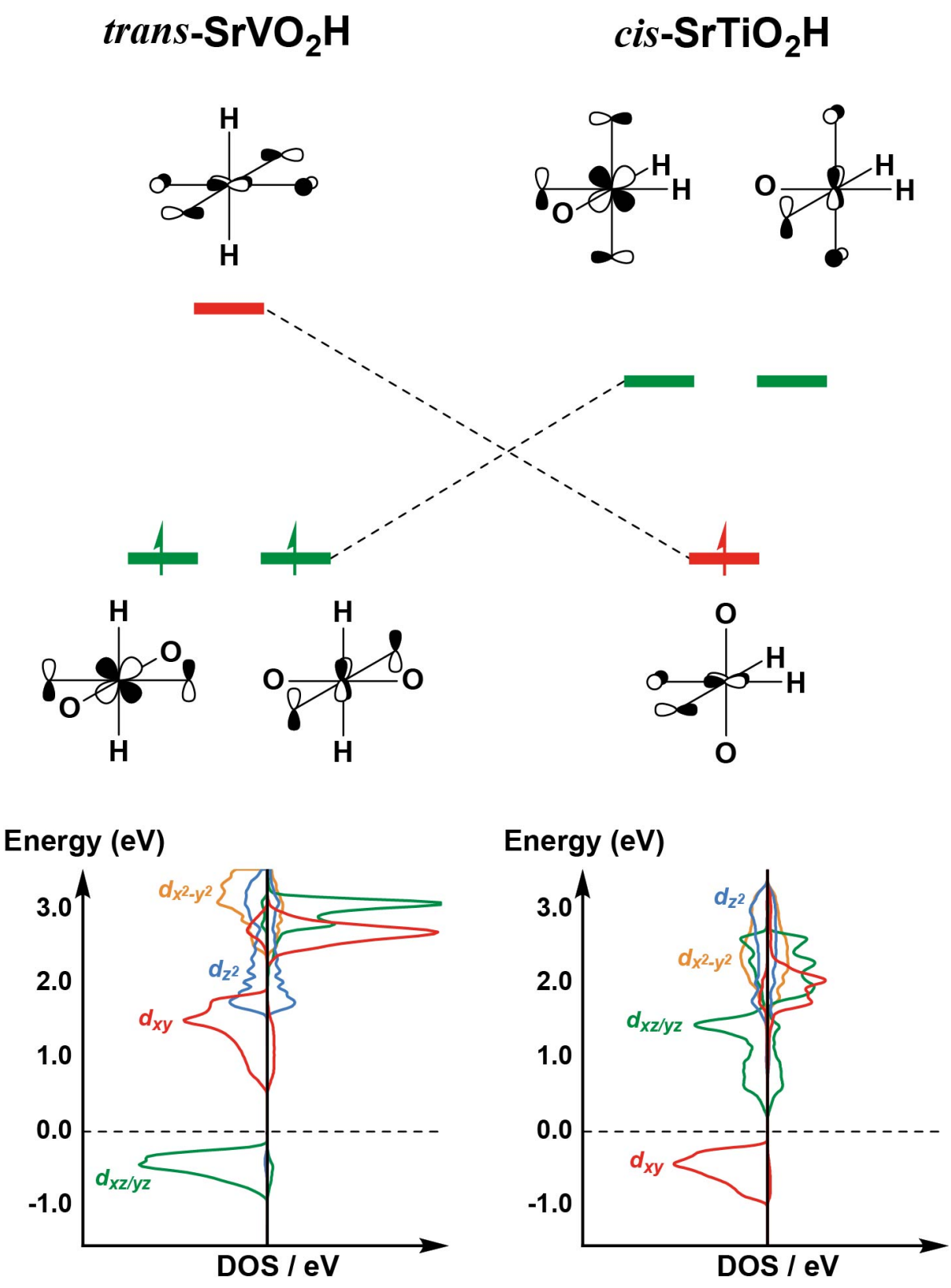


FIGURE 4.4: Orbital illustrations and PDOS of *trans*-$SrVO_2H$ and *cis*-$SrTiO_2H$

TABLE 4.3: Computed energy and lattice parameters of the *trans*- and *cis*-$SrCrO_2H$

System	Energy (eV)	a' (Å)	b' (Å)	c' (Å)
trans-$SrCrO_2H$	-129.283	5.628	5.628	7.171
cis-$SrCrO_2H$	-128.950	5.376	5.445	7.942

and $SrV_{0.75}Ti_{0.25}O_2H$ cases, the experimentally disordered structure of $SrCrO_2H$ has been modelled as *trans* and *cis* isomers as well, with the calculated energy collected in Table 4.3. The reason that we are investigating both of the *trans* and *cis* isomers for the $SrCrO_2H$ case here is different from that for the aforementioned three systems. For $SrVO_2H$, it is known for sure that the *trans* isomer is the ground state, and calculating the energy of the *cis* is to confirm the relative stability of the former through comparison. On the other hand, the $SrTiO_2H$ and $SrV_{0.75}Ti_{0.25}O_2H$ systems do not exist and the calculations are merely thought experiments. In contrast, $SrCrO_2H$ is known experimentally to be anion-disordered and therefore both of the *trans* and *cis* isomers may be present in the lattice. As can be seen from Table 4.3, the energy difference between the two isomers is the smallest among the four systems explored, with the *trans* structure slightly favoured (ΔE = +0.083 eV per formula unit). This indicates energetically the two isomers can hardly be distinguished, resulting in an overall disordered structure.

The calculated PDOS plots of $SrCrO_2H$ (Figure 4.5) confirm the picture of d^3 Cr^{3+} centres with the electronic configurations of $(d_{xz/yz})^2(d_{xy})^1(d_{z^2})^0(d_{x^2-y^2})^0$ and $(d_{xy})^1(d_{xz/yz})^2(d_{x^2-y^2})^0(d_{z^2})^0$ for the *trans* and *cis* isomers, respectively. Similar to what has been discussed before, the reversed order of the $d_{xz/yz}/d_{xy}$ and $d_{z^2}/d_{x^2-y^2}$ orbitals for these two structures originates from the position of the O^{2-} and H^- anions. For the *trans* arrangement, the oxides accumulate in the *ab*-plane, pushing the d_{xy} and $d_{x^2-y^2}$ orbitals to higher energy. While for the *cis* arrangement, the oxides gather along the *c*-axis and the repulsion from these ligands makes the $d_{xz/yz}$ and d_{z^2} orbitals less stable thus higher in energy.

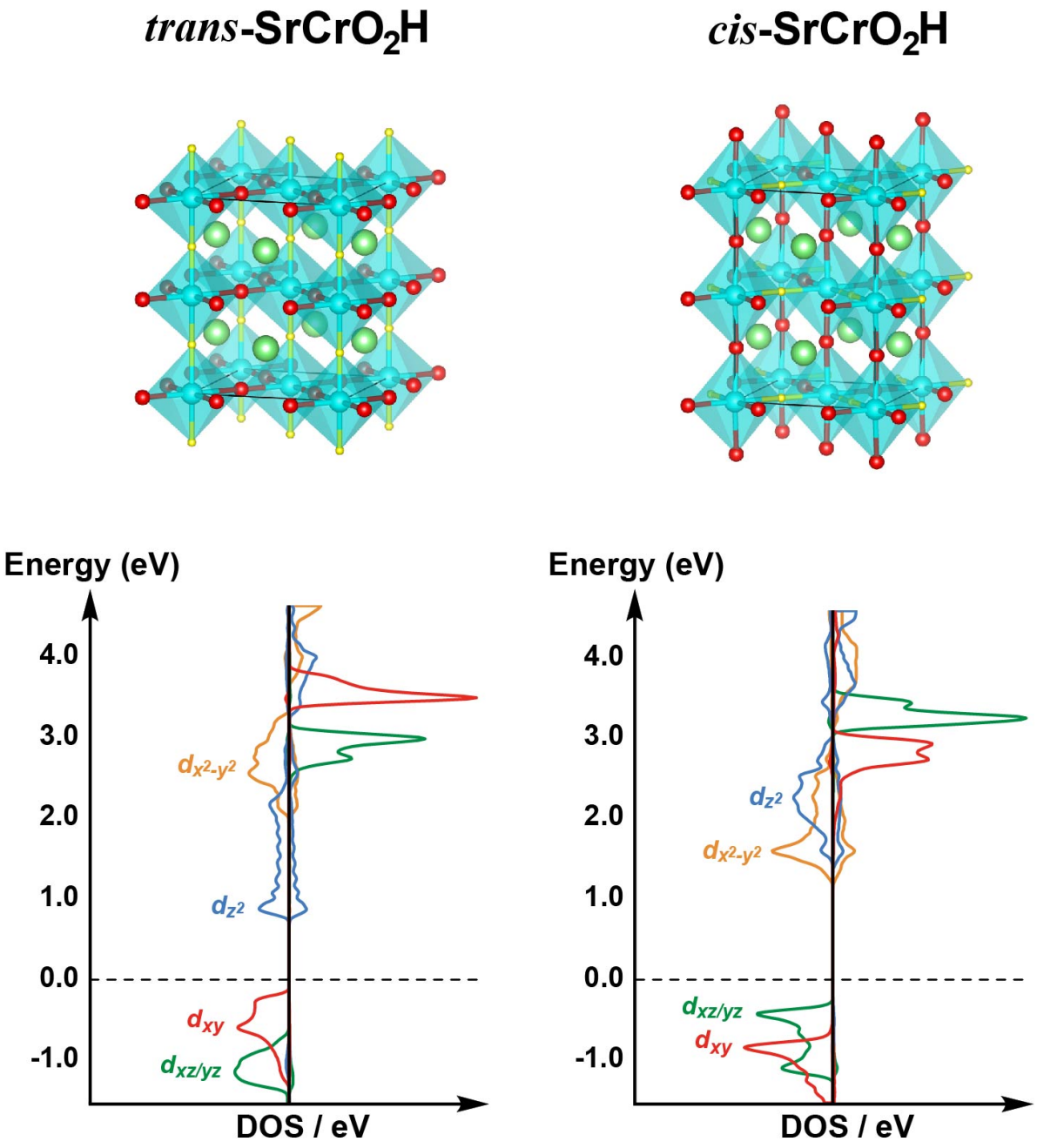


FIGURE 4.5: Structures and PDOS of *trans*- and *cis*-$SrCrO_2H$

4.5 Discussion

The differences in electronic structure between $SrVO_2H$, $SrTiO_2H$ and $SrCrO_2H$ systems can be analysed in terms of two competing factors, the first of which is the strong *trans* influence of the H^- ligand, which will in general disfavour mutually *trans* arrangements of these anions. This effect is mediated by the σ framework and stems from the fact that only a single metal d orbital can participate in both of the metal-hydride σ-bonds when the ligands are *trans* to each other. Superimposed upon this are striking differences in the π character of the two ligands: H^- is a pure σ-donor, while O^{2-} is a strong π-donor, and there is a significant driving force to accumulate the latter in the same plane as the vacant metal-based orbitals with d_π character. In the $SrVO_2H$ system, with a d^2 electronic configuration at the metal centre, these two competing factors are diametrically opposed: the presence of a single vacant d_π orbital (d_{xy}) means that the V-O π-bonding is optimal in the tetragonal phase, where all four O^{2-} anions are aligned in a single plane, but this necessarily forces the two H^- anions into a mutually *trans* arrangement. The observed preference for the tetragonal phase therefore indicates that in this case the enhanced π-donation from O^{2-} is the dominant factor. For the case of $SrTiO_2H$ with a d^1 electronic configuration at Ti^{3+}, in contrast, the presence of two vacant d_π orbitals allows effective Ti-O π-bonding in either *cis* or *trans* arrangements, thus the σ effect (*trans* influence) dominates, imposing a preference for the *cis* arrangement of H^- ligands. In the $SrV_{0.75}Ti_{0.25}O_2H$ system, the arrangement of anions necessarily represents a compromise because it is not possible to simultaneously satisfy the geometric preferences of V^{3+} (*trans*) and Ti^{3+} (*cis*) in a single lattice. Experimentally, this compromise in structure alone is not able to deliver a system that is sufficiently stable. Therefore, on doping $SrVO_2H$ with Ti^{3+}, the thermodynamics of the reaction process is altered, resulting in the formation of the cation- and anion-disordered phase $SrV_{0.95}Ti_{0.05}O_{1.5}H_{1.5}$. As for $SrCrO_2H$, the experimental anion-disordered structure

indicates that the system shows no (or very little) preference for the *cis* or *trans* arrangements. In terms of the electronic structure, the underlying dominant effect is somewhat similar to that of $SrTiO_2H$ but in an opposite way: for the d^3 Cr^{3+} centre in this case, the fact that all three d_π orbitals are half-filled does not allow effective Ti-O π-bonding in either *cis* or *trans* arrangements, therefore the positions of O^{2-} anions make no difference to the overall stability. On the other hand, the collection of the three singly-filled t_{2g} orbitals can be regarded as a sphere of electron density, with the two empty e_g orbitals d_{z^2} and $d_{x^2-y^2}$ lying in higher energy above them. Because of this spherical symmetry, again it makes no difference whether the H^- anions are in the equatorial or axial positions and as a result, the overall structure for $SrCrO_2H$ is anion-disordered. As a final note, experiments and calculations have shown that doping $SrVO_2H$ with Ti^{3+} cations (decreasing the number of *d* electrons) reduces the stability of the tetragonal phase, and attempts to synthesise the Cr^{3+}-centred oxyhydride phase have resulted in an anion-disordered cubic structure. Therefore, we concluded that the presence of a stable, anion-ordered tetragonal phase is uniquely associated with a d^2 configuration, and it is rapidly destabilised for even very small donations to either side of this limit, $d^{2\pm x}$.

Chapter 5

$LaSrNiRuO_4$ and $LaSr_3NiRuO_4H_4$: Reduced Perovskite Oxide and Oxyhydride Containing Ru^{2+}

5.1 Introduction

We have seen a number of examples of double perovskite oxides in Chapter 2, such as the Sr_2FeMoO_6 phase containing 3*d* Fe^{3+} and 4*d* Mo^{5+} centres. Systems with such mixtures of metal cations are not rare, since the structural framework of perovskite oxides are famously robust, and examples containing both 3*d* and 5*d* transition metal cations, such as Sr_2FeIrO_6[103], are well-known. However, for the reduced perovskite oxides with square-planar metal centres, systems with a mixture of transition-metal cations from different periods are more difficult to synthesise, simply because the two-dimensional framework is structurally less stable than the three-dimensional one found in the original perovskite phase. Despite that, it has recently been shown that, when contained within a suitable stabilising lattice, 4*d* transition metals can be incorporated into the reduced oxides. For example, the B-site disordered double perovskite $SrFe_{0.5}Ru_{0.5}O_3$ can be reduced to form $SrFe_{0.5}Ru_{0.5}O_2$[104], which is the first

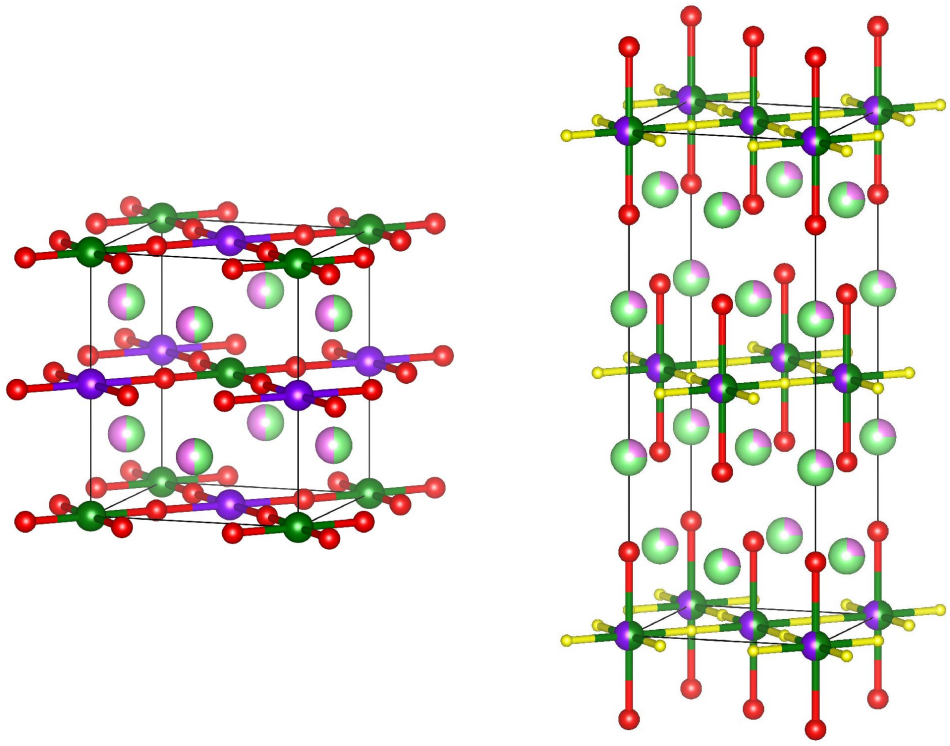


FIGURE 5.1: Crystal structures of $LaSrNiRuO_4$ and $LaSr_3NiRuO_4H_4$ (La: pink; Sr: light green; Ni: dark green; Ru: purple; O: red; H: yellow)

reported extended oxide phase containing Ru^{2+}. However, the disordered arrangement of Fe^{2+} and Ru^{2+} cations result in magnetic frustration and hence a spin glass, which prevents further exploration of the interaction between the 3*d* and 4*d* electronic states. In this chapter, the properties of the B-site ordered reduced perovskite $LaSrNiRuO_4$ (Figure 5.1) are described, where the electronic couplings between low-valent (electron-rich) 3*d* and 4*d* cations are studied for the first time in an extended oxide phase. Apart from this reduced double-perovskite-oxide system $LaSrNiRuO_4$, the coexistence of Ni^{+} and Ru^{2+} cations in the same lattice has also been observed in a reduced Ruddlesden-Popper phase, $LaSr_3NiRuO_4H_4$ (Figure 5.1). The most notable difference between these two phases is that $LaSr_3NiRuO_4H_4$ contains H^{-} anions, which, unlike those in $SrVO_2H$ that align along the *c*-axis, accumulate in the *ab*-plane. In fact, $LaSr_3NiRuO_4H_4$ is the first reported example of a reduced perovskite oxide phase containing both 4*d* transition metals and hydrides, with the 1:1

ratio of H^- to O^{2-} the highest reported so far.

The systems discussed previously, $SrVO_2H$ (Chapter 3) and Ti-doped $SrVO_2H$ (Chapter 4), both feature square-planar environment at the transition metal centre with long M-H bonds along the *c*-axis. In terms of electronic structure, the metal centres V^{3+} and Ti^{3+} share the same coordination geometry and differ only in their *d*-electron count. Therefore, the comparison between these systems can not reveal the relationship between different coordination environment and the corresponding electronic structure. Of the two systems covered in this chapter, $LaSrNiRuO_4$ contains square-planar metal cations and $LaSr_3NiRuO_4H_4$ features octahedral coordination environment due to the accumulation of H^- anions in the *ab*-plane that forces the O^{2-} anions to take positions along the *c*-axis. This significant difference in coordination geometry between these two systems both containing Ni^+ and Ru^{2+} cations, allows the relationship between coordination environment and electronic structure to be studied.

The results of these two projects have been published in *Inorg. Chem.*, 2016, **55**, 9012 and *Angew. Chem. Int. Ed.*, 2018, **57**, 5025.

5.2 $LaSrNiRuO_4$

We start with the discussion on the pure oxide $LaSrNiRuO_4$. The relevant experiments were conducted by Amano Patino *et al.*[105] from University of Oxford, UK.

5.2.1 Summary of Experimental Data

The monoclinic phase $LaSrNiRuO_4$ (a = 5.652 Å, b = 5.652 Å, c = 6.915 Å, γ = 90.54°) is synthesised through the reduction of the parent perovskite oxide $LaSrNiRuO_6$ with CaH_2, with the lattice parameters and bond lengths measured at 300 K (Figure 5.2a). The unit cell of the reduced phase is closely related to that of the parent

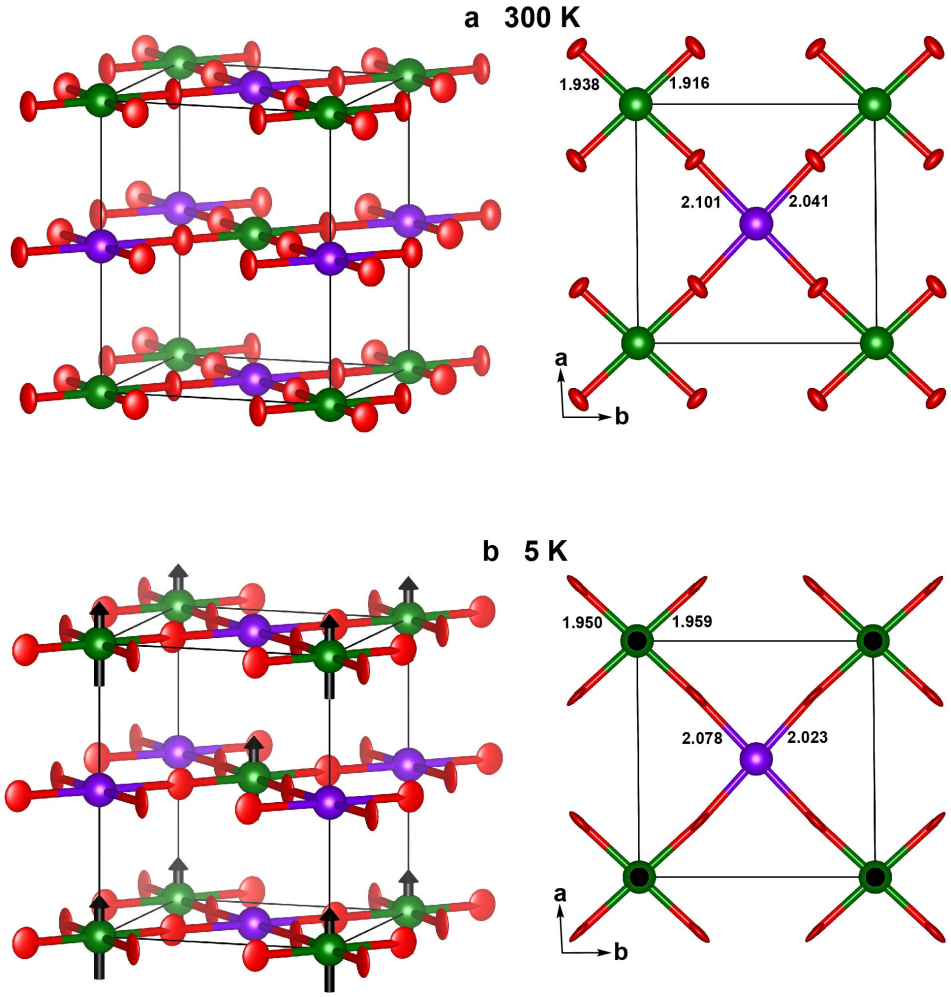


FIGURE 5.2: Magnetic moments (black arrows) and bond lengths (units in Å) of $LaSrNiRuO_4$ at 300 K and 5 K (La^{3+}/Sr^{2+} cations are omitted and O^{2-} anions are shown as displacement ellipsoids)

oxide, $LaSrNiRuO_6$ (a = 5.579 Å, b = 5.546 Å, c = 7.855 Å, β = 89.98°), but with a smaller lattice constant along the c-axis, which results in an infinite-layer structure similar to those of $SrFeO_2$, $SrFe_{0.5}Ru_{0.5}O_2$ and $LaNiO_2$[106]. Within the structure of $LaSrNiRuO_4$, the B-site $Ni^{+}O_4$ and $Ru^{2+}O_4$ squares adopt a "checkerboard" ordered arrangement (Figure 5.1), similar to that in the double perovskite oxide Sr_2FeMoO_6. Upon cooling to 5 K, the system takes a slightly different geometry (a = 5.660 Å, b = 5.658 Å, c = 6.901 Å, γ = 90.70°) (Figure 5.2b), with an unusual expansion of the total volume (220.97 $Å^3$ at 5 K *vs.* 220.89 $Å^3$ at 300 K). The Ni-O and Ru-O bond lengths

are more symmetrical at 5 K (1.950/1.959 Å and 2.078/2.023 Å, respectively) than those at 300 K (1.938/1.916 Å and 2.101/2.041 Å, respectively).

The magnetic susceptibility of $LaSrNiRuO_4$ has been measured at 300 K, and is consistent with a paramagnetic system with a combination of d^9 Ni^+ ($S = \frac{1}{2}$) and d^6 Ru^{2+} centres with two unpaired electrons ($S = 1$), of which the latter has been observed previously in $SrFe_{0.5}Ru_{0.5}O_2$. Apart from this magnetic data, the assignment of the oxidation states of Ni^+ and Ru^{2+} is as well supported through comparison of the local coordination environments of the B-site metal centres in $LaSrNiRuO_4$ with those in other infinite-layer oxide phases. The Ni-O bond lengths in $LaSrNiRuO_4$ (Figure 5.2a) are similar to but somewhat smaller than those in $LaNiO_2$ (1.979 Å), consistent with a d^9 electronic configuration for the former, while the contraction suggests that the $NiRuO_4$ plane is under compression. For the Ru-O bond lengths, a direct comparison between $LaSrNiRuO_4$ and $SrFe_{0.5}Ru_{0.5}O_2$ is rather difficult, because the B-site cations for the latter are disordered and the observed M-O bonds lengths are average values of the Fe-O and Ru-O bonds. This average bond length (1.998 Å) is, however, almost identical to that in $LaSrNiRuO_4$ (1.999 Å), giving some strong evidence for d^6 Ru^{2+} centres. On cooling the system to 5 K, the magnetic data suggest ferromagnetic order for the Ni^+ centres, and the Ru^{2+} centres become diamagnetic (Figure 5.2b), which is a dramatic and non-trivial change in the electronic state.

5.2.2 Methodology

All calculations were performed at the PBE+U level using the plane-wave basis code Vienna Ab initio Simulation Package (VASP 5.3.2)[87]. A plane-wave energy cut-off of 600 eV was imposed and the Γ-centred **k**-point grids of $9 \times 9 \times 9$ was used to sample the first Brillouin zone. The optimisations were done with all the geometrical constraints released, so the ions were allowed to move freely. For DOS calculations,

TABLE 5.1: Test of U_{eff} on Ni and Ru based on the F configuration

U_{eff}(Ni/Ru)	a (Å)	b (Å)	c (Å)	γ (°)	Ni-O (Å)	Ru-O (Å)	Spin (Ni/Ru)
1.0/1.0	5.671	5.670	6.926	92.94	1.95/2.05	1.95/2.07	1.10/1.50
2.0/1.0	5.676	5.674	6.912	92.86	1.96/2.05	1.95/2.06	1.10/1.51
3.0/1.0	5.680	5.684	6.909	92.81	1.97/2.05	1.95/2.06	1.11/1.52
4.0/1.0	5.688	5.685	6.897	92.67	1.98/2.05	1.95/2.06	1.11/1.53
5.0/1.0	5.695	5.693	6.890	92.64	1.99/2.06	1.95/2.06	1.11/1.54
6.0/1.0	5.703	5.706	6.889	92.64	1.99/2.07	1.94/2.06	1.10/1.54
7.0/1.0	5.710	5.713	6.883	92.62	2.00/2.07	1.94/2.06	1.09/1.55
8.0/1.0	5.718	5.720	6.873	92.57	2.01/2.08	1.94/2.06	1.08/1.55
9.0/1.0	5.724	5.730	6.867	92.53	2.02/2.08	1.94/2.06	1.07/1.56
1.0/2.0	5.679	5.669	6.917	92.57	1.96/2.04	1.96/2.07	1.06/1.59
2.0/2.0	5.685	5.676	6.907	92.60	1.97/2.04	1.96/2.07	1.07/1.59
3.0/2.0	5.688	5.682	6.892	92.58	1.98/2.05	1.95/2.06	1.08/1.60
4.0/2.0	5.697	5.692	6.891	92.53	1.99/2.05	1.95/2.06	1.09/1.61
5.0/2.0	5.705	5.705	6.887	92.59	1.99/2.06	1.95/2.06	1.09/1.61
6.0/2.0	5.711	5.707	6.877	92.48	2.00/2.06	1.95/2.06	1.09/1.62
7.0/2.0	5.718	5.714	6.868	92.42	2.01/2.07	1.95/2.06	1.08/1.62
8.0/2.0	5.726	5.721	6.860	92.38	2.02/2.07	1.94/2.06	1.07/1.62
9.0/2.0	5.731	5.733	6.856	92.42	2.02/2.08	1.94/2.06	1.06/1.62
1.0/3.0	5.687	5.675	6.906	92.50	1.97/2.03	1.96/2.07	1.03/1.67
2.0/3.0	5.702	5.687	6.906	92.40	1.98/2.04	1.96/2.07	1.05/1.68
3.0/3.0	5.702	5.689	6.891	92.38	1.99/2.04	1.96/2.07	1.06/1.68
4.0/3.0	5.712	5.693	6.880	92.31	1.99/2.05	1.96/2.06	1.07/1.69
5.0/3.0	5.721	5.700	6.869	92.26	2.00/2.05	1.96/2.06	1.07/1.69
6.0/3.0	5.724	5.716	6.881	92.41	2.01/2.06	1.95/2.06	1.07/1.69
7.0/3.0	5.738	5.715	6.852	92.16	2.02/2.06	1.96/2.06	1.06/1.69
8.0/3.0	5.740	5.723	6.860	92.19	2.02/2.07	1.95/2.06	1.06/1.69
9.0/3.0	5.746	5.732	6.845	92.29	2.03/2.08	1.95/2.06	1.05/1.69
1.0/4.0	5.695	5.683	6.894	92.09	1.99/2.03	1.96/2.07	1.00/1.76
2.0/4.0	5.706	5.693	6.888	92.18	1.99/2.04	1.96/2.07	1.03/1.76
3.0/4.0	5.745	5.675	6.879	91.90	2.00/2.04	1.97/2.06	1.04/1.76
4.0/4.0	5.720	5.701	6.873	92.21	2.00/2.05	1.96/2.07	1.05/1.75
5.0/4.0	5.733	5.713	6.869	92.08	2.01/2.05	1.96/2.07	1.06/1.76
6.0/4.0	5.735	5.714	6.859	92.07	2.01/2.05	1.96/2.06	1.06/1.75
7.0/4.0	5.747	5.721	6.855	92.06	2.02/2.07	1.96/2.06	1.05/1.75
8.0/4.0	5.754	5.727	6.849	92.01	2.03/2.07	1.96/2.06	1.05/1.75
9.0/4.0	5.763	5.737	6.842	91.95	2.03/2.07	1.96/2.06	1.04/1.75
1.0/5.0	5.707	5.704	6.875	90.60	2.00/2.02	2.01/2.04	0.99/2.81
2.0/5.0	5.714	5.711	6.869	90.61	2.01/2.03	2.01/2.04	1.01/1.81
3.0/5.0	5.723	5.720	6.864	90.60	2.01/2.03	2.01/2.04	1.03/1.80
4.0/5.0	5.725	5.722	6.846	90.61	2.02/2.04	2.00/2.04	1.04/1.80
5.0/5.0	5.733	5.730	6.843	90.62	2.02/2.04	2.00/2.04	1.05/1.80
6.0/5.0	5.747	5.742	6.845	90.64	2.03/2.05	2.00/2.04	1.05/1.80
7.0/5.0	5.749	5.744	6.830	90.66	2.03/2.06	2.00/2.04	1.05/1.80
8.0/5.0	5.756	5.750	6.825	90.66	2.04/2.06	2.00/2.04	1.05/1.80
9.0/5.0	5.721	5.791	6.802	90.02	2.03/2.03	2.05/2.05	1.42/1.52

a $17 \times 16 \times 15$ **k**-point sampling was used to improve the quality of the plots. The U_{eff} value was fixed at 6.0 eV for Ni^{+} and 3.0 eV for Ru^{2+} centres.

The value of U_{eff} is commonly known to be large for first-row late transition metals with compact 3*d* orbitals and smaller for second-row metals with 4*d* orbitals that are more diffuse. Typical values in the literature are 6.0 eV for Ni and 3.0 eV for Ru, which have been adopted in the calculations discussed in this chapter. However, the metal centres in $LaSrNiRuO_4$, Ni^{+} and Ru^{2+}, exhibit unusually low oxidation state thus might deviate from the traditional trend for U_{eff}. We therefore perform a series of tests for the values of U_{eff} based on the F configuration of $LaSrNiRuO_4$. This is not the true magnetic ground state ($S = \frac{1}{2}$ Ni^{+} and $S = 0$ Ru^{2+}, which we were not able to locate), but the test should still give us some hint on how U_{eff} affects the electronic structure. The dependence of the computational results on U_{eff} has been tested across a broad range: the values of U_{eff} were adjusted step-wisely for each test calculation, ranging from 1.0 to 9.0 eV for Ni^{+} and 1.0 to 5.0 eV for Ru^{2+}, respectively (Table 5.1). From the trend shown in the table we can see that the lattice parameters, Ni-O bond lengths and values of spin density are largely independent of the choice of U_{eff} for Ni^{+}. In contrast, for Ru^{2+}, increasing U_{eff} significantly increases the spin density ($\sim$1.50 for U_{eff} = 1.0 eV and $\sim$1.80 for U_{eff} = 5.0 eV). Apart from this, the lattice angle γ decreases to $\sim$90.6° and the Ru-O bond lengths become much more similar ($\sim$1.95/2.06 Å for U_{eff} = 1.0 eV and $\sim$2.00/2.04 Å for U_{eff} = 5.0 eV). Despite these observations, the change in U_{eff} does not make a huge difference on the geometry or electronic structure of $LaSrNiRuO_4$. At the generally accepted U_{eff} values of 6.0 eV for Ni and 3.0 eV for Ru, the calculated lattice parameters are consistent with the experimental ones and the spin density on the metal centres are reasonable, thus we adopted this setting.

5.2.3 Computational Results

For the $LaSrNiRuO_4$ system, we have explored a number of alignments of the spin moments on the two B-site metals (Figure 5.3), and the ferromagnetic state (F) proves to be the most stable (Table 5.2). The values of spin density of +1.07 and +1.69 on Ni and Ru, respectively, support the previous assignments of oxidation states as Ni^{+} and Ru^{2+}. The calculated values of energy for the F, C and A configurations can be mapped onto the diagonal elements of the Heisenberg spin Hamiltonian (Equation 3.4) to extract magnetic coupling constants. In the unit cells shown in Figure 5.3 we can identify two symmetry-distinct exchange coupling pathways, J_1 and J_2, where the former corresponds to the nearest neighbour intra-plane Ni-O-Ru coupling while the latter is the nearest neighbour inter-plane Ni-Ru coupling. Following the process discussed in Chapter 3, a similar matrix equation can be obtained:

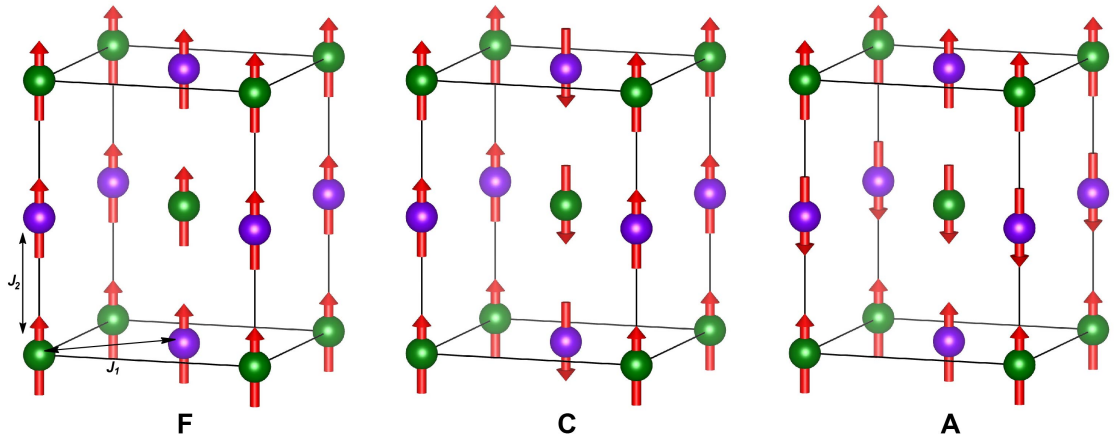


FIGURE 5.3: F, C and A magnetic configurations of $LaSrNiRuO_4$

$$\begin{bmatrix} 8 & 4 \\ -8 & 4 \\ 8 & -4 \end{bmatrix} \begin{bmatrix} J_1 \\ J_2 \end{bmatrix} = \begin{bmatrix} E_F + \Delta \\ E_C + \Delta \\ E_A + \Delta \end{bmatrix} \tag{5.1}$$

Then taking the differences between each pair of the three linear equations and substituting the energy differences obtained from Table 5.2 into the right-hand side lead

to:

$$\begin{bmatrix} 16 & 0 \\ 0 & 8 \end{bmatrix} \begin{bmatrix} J_1 \\ J_2 \end{bmatrix} = \begin{bmatrix} -0.14677 \\ -0.00569 \end{bmatrix} \tag{5.2}$$

Solving this system of linear equations yields J_1 = -9.2 meV and J_2 = 0.7 meV, which indicates relatively strong intra-plane ferromagnetic and weak inter-plane antiferromagnetic interactions between Ni^+ and Ru^{2+} centres.

TABLE 5.2: Computed energy of the F, C and A configurations

Configuration	Energy (eV)
F	-101.18650
C	-101.03973
A	-101.18081

The optimised lattice of $LaSrNiRuO_4$ is monoclinic, with a = 5.724 Å, b = 5.716 Å and c = 6.881 Å, in good agreement with the available crystallographic data. The optimised angle, $\gamma = 92.41^\circ$, is, however, somewhat larger than the experimental values (90.54° at 300 K and 90.70° at 5 K), with the result that the degree of asymmetry in the Ni-O and Ru-O bond lengths is overestimated (Figure 5.4, Ni-O: 2.01/2.06 Å; Ru-O: 1.95/2.06 Å). The value of γ, and hence the degree of asymmetry, is, however, strongly dependent on the chosen value of the U_{eff} parameter for Ru, with values of 5.0 eV giving an almost perfectly tetragonal lattice (Table 5.1). The shift toward more tetragonal structures is commensurate with an increase in the spin density at Ru (+1.80 for U_{eff} = 5.0 eV), which in turn suggests that the lower covalency of the Ru-O bond plays an important role in the magnitude of the distortion.

The PDOS of $LaSrNiRuO_4$ is shown in Figure 5.5. For Ni^+, only the spin-β component of the d_{xy} orbital lies above the Fermi level (note the axes for orbitals are defined such that a and b bisect the O-M-O angles), while the d_{z^2} orbital is doubly-occupied, giving a local configuration of $(d_{z^2})^2(d_{xz/yz})^4(d_{x^2-y^2})^2(d_{xy})^1$ and spin moment $S = \frac{1}{2}$. In the Ru^{2+} case, both components of the d_{xy} orbital lie above E_f, as do the spin-β components of $d_{x^2-y^2}$ and one linear combination of $d_{xz/yz}$ $(d_{xz} - d_{yz})$, giving a

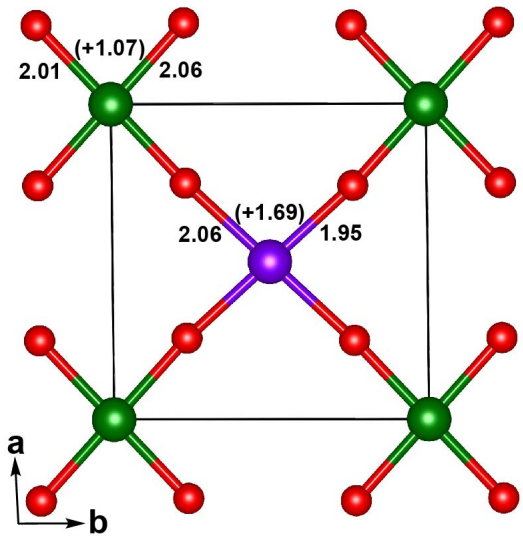


FIGURE 5.4: Computed spin density (in brackets) and bond lengths for the F configuration of $LaSrNiRuO_4$

$(d_{z^2})^2(d_{xz/yz})^3(d_{x^2-y^2})^1(d_{xy})^0$ configuration. The double occupation of the d_{z^2} orbital in Ru was also observed to be a feature of the electronic structure of $SrFe_{0.5}Ru_{0.5}O_2$ and indeed in other low-valent oxides in square-planar square-planar environments such as the $SrFeO_2$ archetype mentioned in Chapter 2.

5.2.4 Discussion

The magnetisation and neutron diffraction data indicate that $LaSrNiRuO_4$ appears to exist in two different electronic states. At a temperature of 300 K, the data are consistent with a paramagnetic state with localised $S = \frac{1}{2}$ Ni^+ and $S = 1$ Ru^{2+}, but upon cooling the system appears to undergo a cooperative ordering transition leading to a ferromagnetic alignment of the Ni^+ spins and a concomitant loss of spin moment at Ru^{2+}. Some insight into this highly unusual phase transition can be gained by examining the low-temperature crystal structure of $LaSrNiRuO_4$. The first striking feature is that, while the unit cell contracts parallel to the *c*-axis upon cooling, this is counteracted by an expansion in the *ab*-plane, leading to a larger unit cell volume at 5 K than 300 K. The data in Figure 5.2 confirm that the Ni-O and

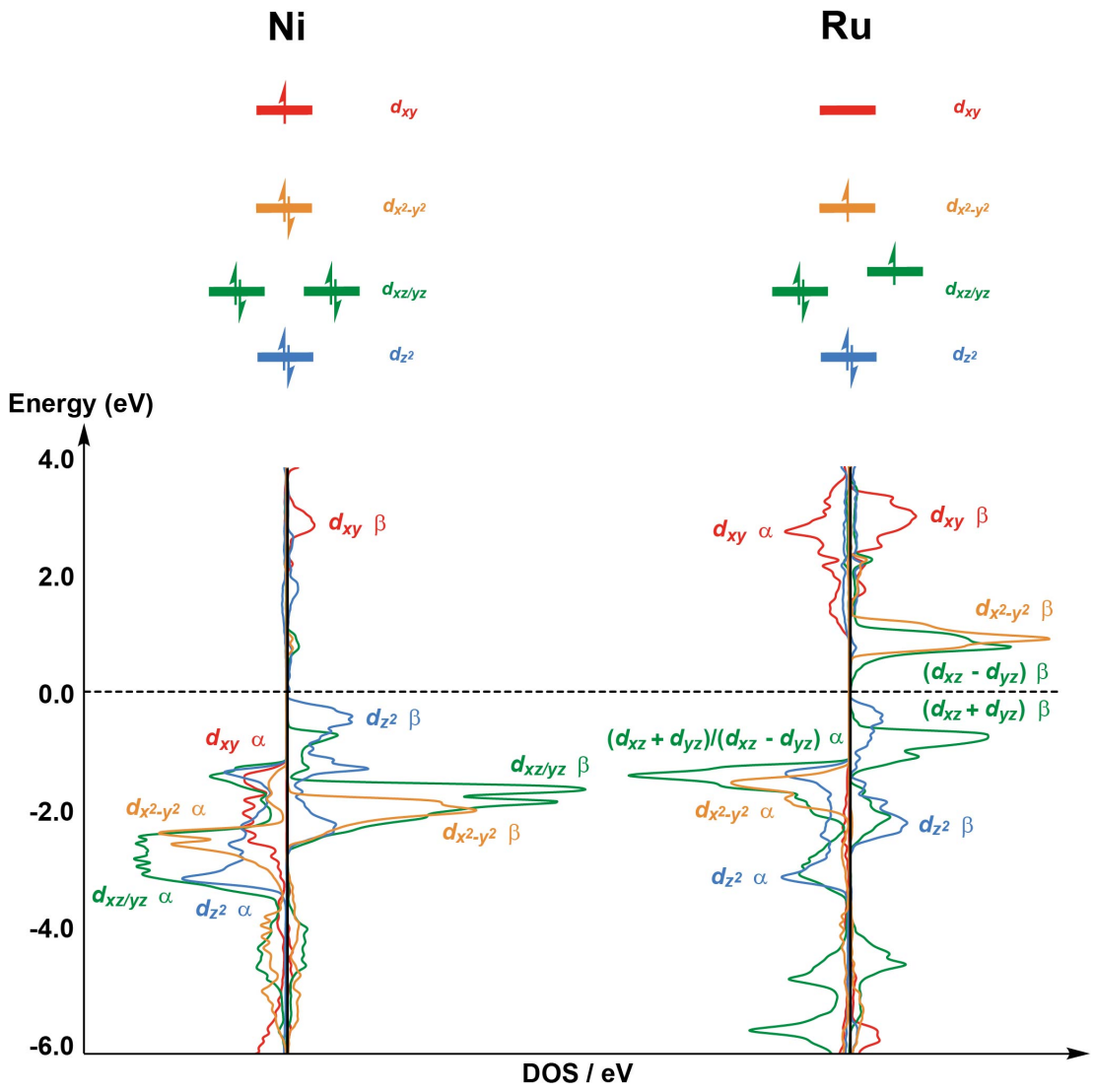


FIGURE 5.5: PDOS and electronic configurations for $LaSrNiRuO_4$

Ru-O bonds are longer and shorter, respectively, in the 5 K structure compared to the 300 K structure. This equalisation of the Ni-O and Ru-O bond lengths upon cooling is commensurate with a change in the O^{2-} displacement parameters. The displacement ellipsoids of the two crystallographically distinct O^{2-} anions in the 300 K structure have their largest values perpendicular to the Ni-O-Ru bond vector, a feature which is consistent with the general observation that the lowest energy vibrational displacement is perpendicular to the bond vector. In contrast, the largest displacement of the O^{2-} anions in the 5 K structure is approximately parallel to the

Ni-O-Ru bond vector. This behaviour is inconsistent with a vibrational displacement and instead suggests a disordered static displacement of the O^{2-} anions. A d^6 Ru^{2+} ion in a square-planar environment will inevitably be either orbitally degenerate or very nearly so, leading to Jahn-Teller instabilities. The observed changes to the Ru-O and Ni-O bond lengths at low temperature, and the appearance of static disorder in the Ni-O-Ru planes, are certainly consistent with a local lowering of symmetry associated with the low-temperature electronic state of $LaSrNiRuO_4$.

The picture of the electronic structure summarised in Figure 5.5 is entirely consistent with the high-temperature data, as the combination of a singly occupied d_{xy} orbital on Ni^+ and a vacant d_{xy} orbital on Ru^{2+} provides a ferromagnetic superexchange coupling pathway, and the partial occupation of the $d_{xz/yz}$ manifold on Ru^{2+} presents a clear driving force for the distortion from perfect tetragonal symmetry. The low-temperature data, and in particular the apparent absence of a paramagnetic moment at the Ru^{2+} centre, is less easy to rationalise. One possibility is that a more pronounced Jahn-Teller distortion would split the $d_{xz/yz}$ to an even greater degree and induce spin pairing at the Ru^{2+} centre, giving $(d_{z^2})^2(d_{xz}+d_{yz})^2(d_{x^2-y^2})^2(d_{xz}-d_{yz})^0(d_{xy})^0$. We have tried to locate a stable minimum corresponding to such a state by initialising calculations from a range of highly distorted structures, but the system invariably returns to the monoclinic, moderately distorted structure with two unpaired electrons on Ru^{2+}. Therefore, we find no evidence for this type of extreme Jahn-Teller distortion, although we note that an ordered arrangement of the local Jahn-Teller distortions of the Ru^{2+} centres (analogous to the orbital order observed in $LaMnO_3$[107], for example) could in principle stabilise a sufficiently large structural distortion to support a transition to a diamagnetic state. The average structure observed by diffraction provides no information on the presence or nature of such ordering, and it is intrinsically beyond the limits of the small model unit cell used in our calculations.

5.3 $LaSr_3NiRuO_4H_4$

Now we move to look at the $LaSr_3NiRuO_4H_4$ system. The relevant experiments were conducted by Jin *et al*.[108] from University of Oxford, UK.

5.3.1 Summary of Experimental Data

The tetragonal phase $LaSr_3NiRuO_4H_4$ ($a = b = 3.623$ Å, $c = 13.317$ Å) can be made through the reaction of the Ruddlesden-Popper phase $LaSr_3NiRuO_8$ ($a = b = 3.890$ Å, $c = 12.630$ Å) with CaH_2, a similar strategy as in the synthesis of $LaSrNiRuO_4$. Neutron powder diffraction data have revealed that the net result of the conversion of $LaSr_3NiRuO_8$ into $LaSr_3NiRuO_4H_4$ is to exchange the equatorial O^{2-} anions in the former phase for H^- anions. Unlike $LaSrNiRuO_4$ with Ni^+ and Ru^{2+} cation order, the B-site transition metals in $LaSr_3NiRuO_4H_4$ are completely disordered, a feature inherited from the parent phase $LaSr_3NiRuO_8$. It should be noticed that while for $LaSrNiRuO_4$ the a/b lattice parameters are larger than the parent oxide $LaSrNiRuO_6$ (5.652/5.652 Å *vs*. 5.579/5.546 Å), in the $LaSr_3NiRuO_4H_4$ case the order is reversed and the reduced phase has a smaller a (3.623 Å *vs*. 3.890 Å). This can be rationalised by first looking at the crystal structures of the two parent oxide phases $LaSrNiRuO_6$ and $LaSr_3NiRuO_8$ (Figure 5.6). Within the structure of the former double perovskite oxide, the $Ni^{2+}O_6$ and $Ru^{5+}O_6$ octahedra are distorted, indicating the system is under significant compression thus the Ni-Ru separations (∼3.91/∼3.95 Å) are contracted. The reduction of this phase into $LaSrNiRuO_4$, to some extent, releases this tension, leading to elongated Ni-Ru distances (3.978/4.015 Å), hence larger lattice parameters in the *ab*-plane. Reducing Ni^{2+}/Ru^{5+} to Ni^+/Ru^{2+} results in longer Ni-O/Ru-O bonds, which also contributes to the stretching of Ni-Ru separations in $LaSrNiRuO_4$. On the other hand, the $Ni^{2+}O_6/Ru^{5+}O_6$ octahedra in $LaSr_3NiRuO_8$ are not distorted, and nor are the $Ni^+O_2H_4/Ru^{2+}O_2H_4$ ones in $LaSr_3NiRuO_4H_4$. Therefore, the smaller lattice parameters in the *ab*-plane in the latter oxyhydride system

come from the much shorter Ni-H/Ru-H (1.811 Å) bonds compared to the Ni-O/Ru-O (1.945 Å) bonds in the parent oxide phase, simply because the H^- cations are naturally smaller than O^{2-}, and the reduction from Ni^{2+}/Ru^{5+} to Ni^+/Ru^{2+}, is unable to counteract the effect of the huge size difference between H^- and O^{2-} anions.

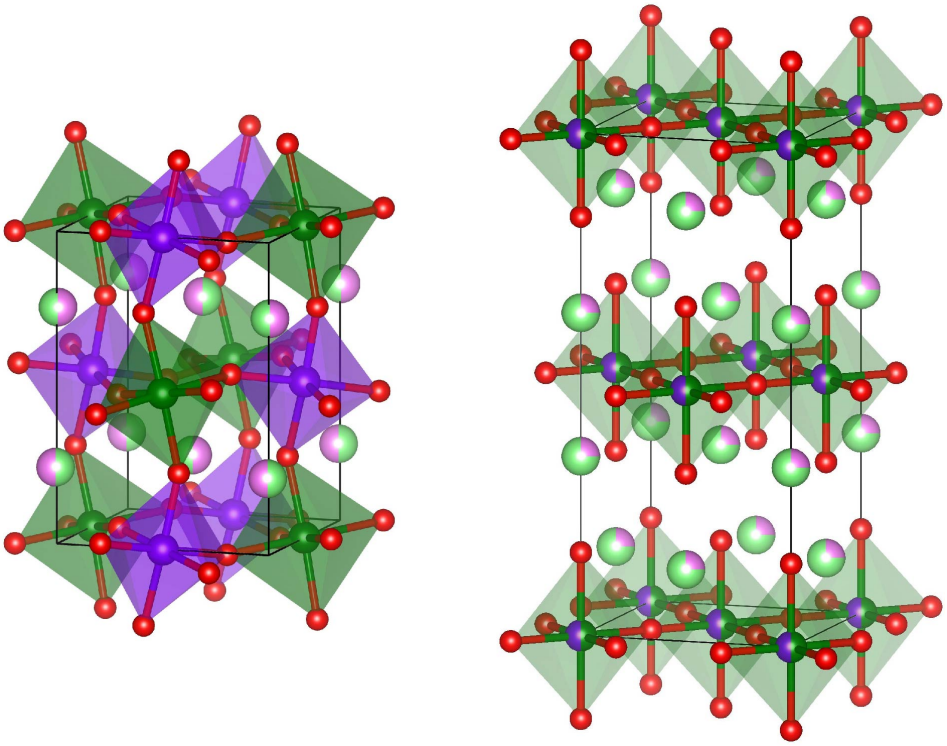


FIGURE 5.6: Crystal structures of $LaSrNiRuO_6$ and $LaSr_3NiRuO_8$

As for the magnetism of $LaSr_3NiRuO_4H_4$, in the temperature range of 10 to 300 K, the magnetic data are consistent with a $S = \frac{1}{2}$ Ni^+ and $S = 0$ Ru^{2+} electronic configuration. However, at a temperature as low as 2 K, Unlike the $LaSrNiRuO_4$ system, this oxyhydride phase shows no evidence of magnetic order. Experiments suggest that if $LaSr_3NiRuO_4H_4$ does adopt an antiferromagnetic ground state, the ordering temperature is extremely low.

5.3.2 Methodology

The methodology employed for the calculations of the $LaSr_3NiRuO_4H_4$ system are mostly the same as that for $LaSrNiRuO_4$, with the exception that the Γ-centred **k**-point grid of $5 \times 5 \times 3$ was used to sample the first Brillouin zone here. Because the oxidation states for Ni and Ru are the same for this two systems, again the U_{eff} values of 6.0 eV and 3.0 eV were used for these two metal centres, respectively.

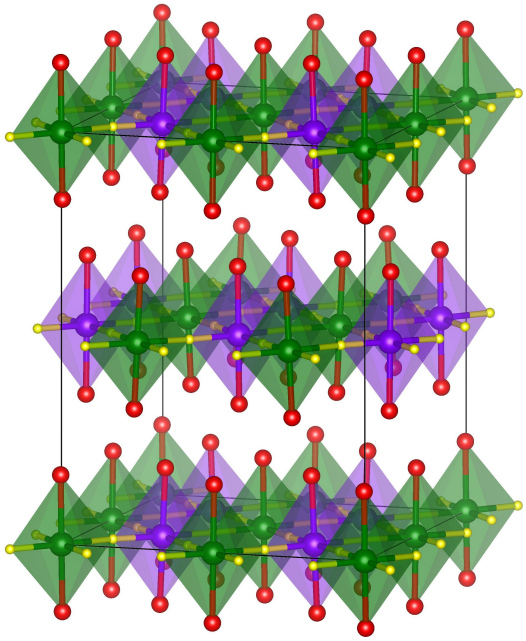


FIGURE 5.7: $2\sqrt{2} \times 2\sqrt{2} \times 1$ expansion of the primitive unit cell of $LaSr_3NiRuO_4H_4$ in "checkerboard" configuration (La^{3+} and Sr^{2+} cations are omitted)

The size of the unit cell for $LaSrNiRuO_4$ is sufficient for the investigation of its magnetic properties, because the Ni^{+} and Ru^{2+} cations are ordered within its lattice and each unit cell contains two formula units. In contrast, for $LaSr_3NiRuO_4H_4$, the metal centres are experimentally disordered and a single unit cell contains only one formula unit, therefore it is not big enough for the construction of different magnetic structures. To solve this problem, we have employed a $2\sqrt{2} \times 2\sqrt{2} \times 1$ expansion of the unit cell for the latter oxyhydride phase (Figure 5.7), which not only enables us to explore various magnetic configurations of the system, but also different possible

arrangements of the experimentally disordered Ni^+ and Ru^{2+} cations. For this issue of the Ni/Ru disorder, we have first used a "checkerboard" configuration as the ordered arrangement in $LaSrNiRuO_4$ for the analysis on structural and electronic properties of $LaSr_3NiRuO_4H_4$, with two more configurations as comparisons discussed in later sections.

5.3.3 Computational Results

For the $LaSr_3NiRuO_4H_4$ system, unlike the ferromagnetic $LaSrNiRuO_4$ at low temperature, the experiments suggest a very weak magnetic order with $S = \frac{1}{2}$ Ni^+ and $S = 0$ Ru^{2+}. Due to this weak magnetism, we did not calculate the coupling constants, but still construct four distinct magnetic configurations (Figure 5.8) to try to identify the magnetic ground state. The AF0 configuration is the most stable among these four (Table 5.3), with the F only slightly higher in energy (∼+0.001 eV), which indicates that the inter-layer interaction in this system is weak. The AF1 and AF2 configurations are much less stable (∼+9 eV) than the former two configurations, suggesting that the antiferromagnetic couplings through the Ni-O-Ru chain and the adjacent Ni-Ni interaction are significantly disfavoured. Furthermore, the energy of AF1 and AF2 being so close (∼0.06 eV) suggests that the intra-layer magnetic interactions are weak as well, which supports the experimental observation.

TABLE 5.3: Computed energy of the F, AF0, AF1 and AF2 configurations

Configuration	Energy (eV)
F	-595.38766
AF0	-595.38883
AF1	-586.32303
AF2	-586.26598

The optimised lattice of $LaSr_3NiRuO_4H_4$ is orthorhombic, with a' = 10.295 Å, b' = 10.275 Å and c = 13.418 Å, again in good agreement with the experimental data. It is noticeable that this geometry slightly deviates from the crystallographic tetragonal

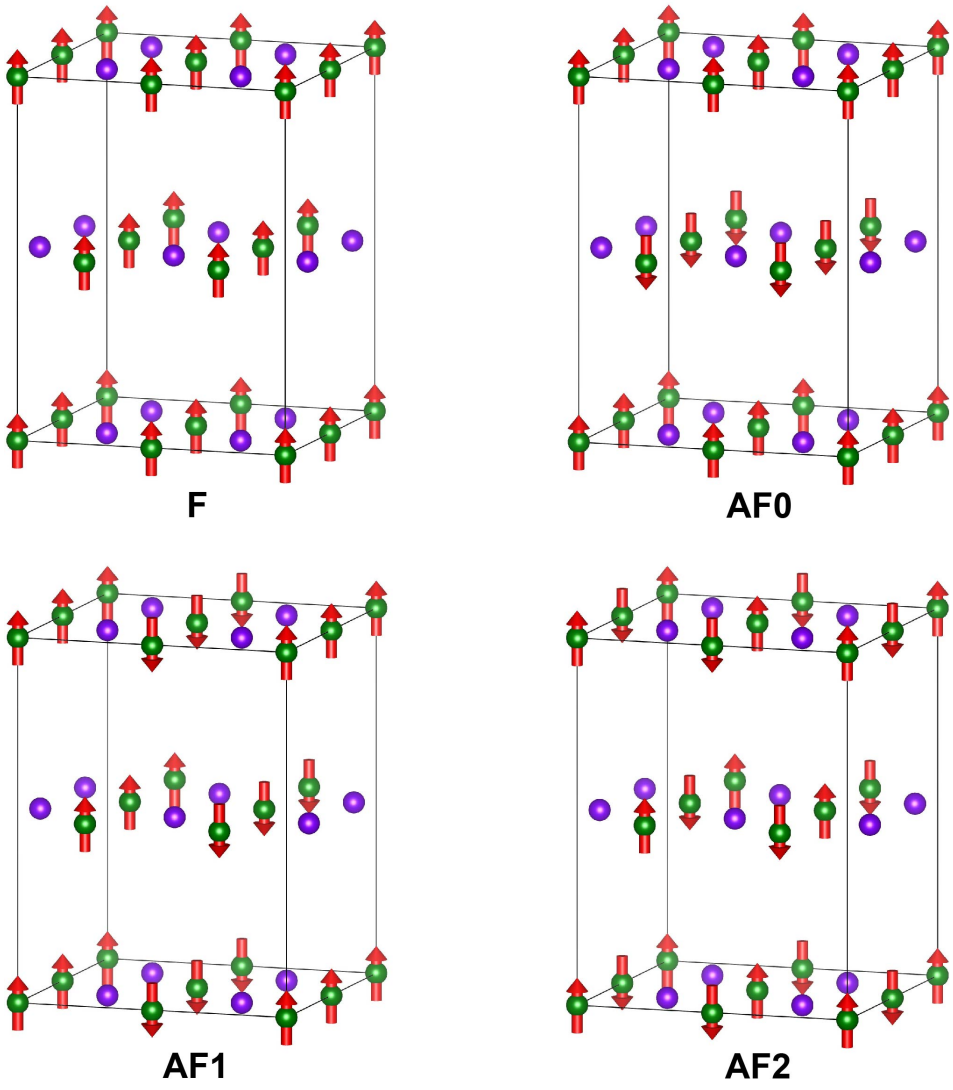


FIGURE 5.8: F, AF0, AF1 and AF2 configurations of $LaSr_3NiRuO_4H_4$

cell, probably because the Ni/Ru disorder is approximated as an ordered "checkerboard" arrangement here in the calculation.

The PDOS of $LaSr_3NiRuO_4H_4$ is shown in Figure 5.9. Even though the Ni^+ and Ru^{2+} are exactly the same as in the $LaSrNiRuO_4$ case in term of oxidation states, the electronic configurations of them are completely different. For Ni^+, the d_{z^2} orbital is only singly occupied, with the t_{2g} set of orbitals each filled with two electrons, leading to a $(d_{xz/yz})^4(d_{xy})^2(d_{x^2-y^2})^1(d_{z^2})^1$ electronic configuration. The strong splitting of the majority-spin and minority-spin components of the Ni bands is consistent with

the presence of a single unpaired electron on the Ni^+ centres (experimentally, ~0.91 μ_B) as well. As for Ru^{2+}, the contrast to that in $LaSrNiRuO_4$ is even more significant: here the six electrons are all paired in the $d_{xz/yz}$ and d_{xy} orbitals, resulting in a local electronic configuration of $(d_{xz/yz})^4(d_{xy})^2(d_{x^2-y^2})^0(d_{z^2})^0$ and overall diamagnetism. The PDOS for O^{2-} $2p$ and H^- $1s$ orbitals are plotted at the side as well, which shows that the interaction between the latter anions and the d orbitals (d_{z^2} in particular) of Ni^+ is weak, leading to a spiky peak of d_{z^2} α at ~-6.0 eV.

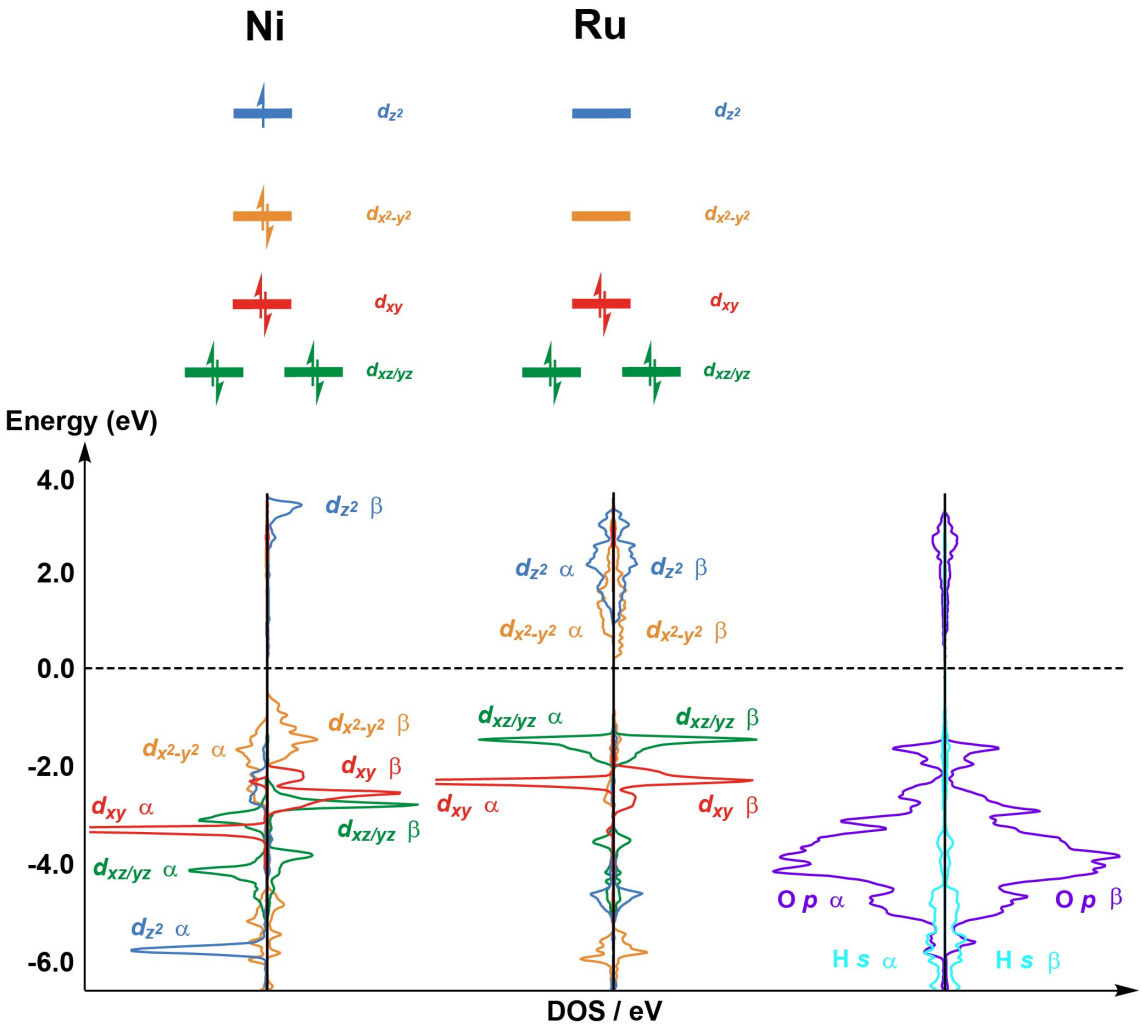


FIGURE 5.9: PDOS and electronic configurations for $LaSr_3NiRuO_4H_4$

As mentioned before, the arrangement of Ni^+/Ru^{2+} cations in $LaSrNiRuO_4$ is ordered, while that in $LaSr_3NiRuO_4H_4$ is not. In order to see how this disorder

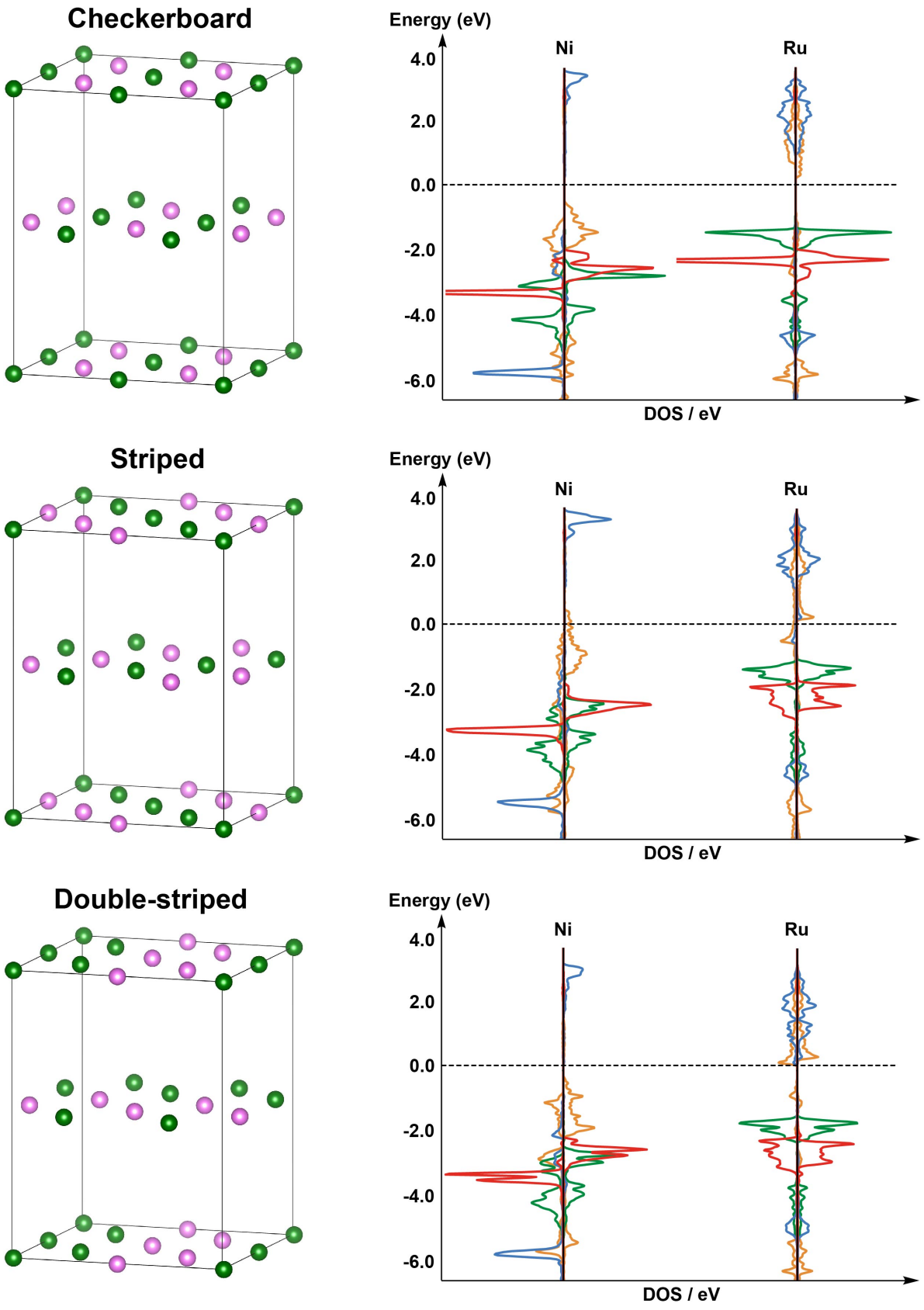


FIGURE 5.10: Structures and PDOS for the "checkerboard", "striped" and "double-striped" configurations of $LaSr_3NiRuO_4H_4$ (the labels of orbitals are omitted)

in the oxyhydride phase influences the electronic structure, on top of the previous "checkerboard" structure, we have constructed two more configurations, namely "striped" and "double-striped" (Figure 5.10). As can be seen from the PDOS plots, changing the relative position of the Ni^+ and Ru^{2+} cations in $LaSr_3NiRuO_4H_4$ does not have a dramatic effect on the electronic structure of the system. The calculated energy and lattice parameters for the three configurations are summarised in Table 5.4 as well, which do not show significant inconsistency between each other (differences < 1%), with the "checkerboard" the most stable among these three. Therefore, the ordered "checkerboard" configurations can be reasonably used as a typical representation of the disordered structure of $LaSr_3NiRuO_4H_4$.

TABLE 5.4: Computed energy and lattice parameters of the "checkerboard", "striped" and "double-striped" configurations of $LaSr_3NiRuO_4H_4$

Configuration	Energy (eV)	a' (Å)	b' (Å)	c (Å)	β (°)
Checkerboard	-595.38883	10.295	10.275	13.418	90.000
Striped	-592.89815	10.267	10.252	13.496	89.883
Double-striped	-593.57947	10.281	10.257	13.473	89.995

5.3.4 Discussion

The double occupation of the d_{z^2} orbital of the Ni^+ and Ru^{2+} cations in $LaSrNiRuO_4$ has been observed in the famous $SrFeO_2$ system mentioned in Chapter 2, which features d^6 Fe^{2+} centres with $S = 2$ in square-planar coordination environment. These two systems both feature two-dimensional structures, where the layers are separated by the A-site cations only. As in $SrFeO_2$, this type of structure lowers the energy of d_{z^2} orbitals and therefore allows extensive mixing with the 4*s* orbitals, resulting in the double occupation eventually. In contrast, for the $LaSr_3NiRuO_4H_4$ system, the equatorial O^{2-} are all substituted by H^-, leaving the axial O^{2-} anions untouched as in the parent oxide phase $LaSr_3NiRuO_8$. The H^- and O^{2-} ligands are well-known strong σ-donors and π-donors, respectively, therefore for the Ni^+ and Ru^{2+} in this

oxyhydride phase, the coordination environment is not square-planar but octahedral. As a result, there are no such energy-lowering effects for the d_{z^2} orbitals of the B-site transition-metal cations, thus they are singly-occupied. The PDOS plots of $LaSr_3NiRuO_4H_4$ (Figure 5.9) confirm the absence of significant H^- 1*s* character in the same energetic window as Ni^+ d_{z^2}, which also supports the weak magnetic order of the system: the magnetic orbitals, Ni^+ d_{z^2}, overlap only very weakly with the H^- 1*s* orbitals via the torus.

5.4 Generalisation

From the typical examples of $SrFeO_2$, and the systems containing Ni^+ and Ru^{2+} cations discussed above, we wish to provide a general observation of the electronic structure of these reduced perovskite oxide systems: for B-site metal centres with over half-occupied (but not fully-occupied) *d* orbitals (d^6 – d^9), if the coordination environment is square-planar (or pseudo-square-planar where the axial interaction is weak), the probability that the d_{z^2} orbitals are doubly-occupied is high. In other words, if the coordination geometry is so far away from a square plane that the axial interaction is strong, the d_{z^2} orbital tend to stay singly-occupied.

Concluding Remarks

In this thesis, several members of the family of transition metal oxide phases have been discussed: the $SrFeO_2$-analogue oxyhydride $SrVO_2H$, the Ti-doped structures of $SrVO_2H$, and the two Ru^{2+}-containing phases $LaSrNiRuO_4$ and $LaSr_3NiRuO_4H_4$. They can all be described as "low-valent" systems, in the sense that the central metal cations have relatively low oxidation states and thus high *d*-electron counts. The isolation of these low-valent phases originates from the low-temperature reduction strategy, which preserves the basic framework of the parent perovskite oxides. The number of *d* electrons is closely related to the local structure, in particular, the coordination geometry, of the metal centres. In the $SrVO_2H/SrV_{0.75}Ti_{0.25}O_2H/SrTiO_2H$ systems, we have seen that an anion-ordered tetragonal phase is uniquely associated with a d^2 electronic configuration, where the V^{3+}/Ti^{3+} cations are located in square planes. For the cases where the *d*-orbitals are over half-filled, using the two Ru^{2+}-containing phases as examples, we have shown that the occupation of d_{z^2} becomes the key issue: the doubly-occupied d_{z^2} is strongly associated with a square-planar coordination geometry. In fact, this double occupation of d_{z^2} orbitals has been observed and studied in the famous $SrFeO_2$ system, and it plays a key role in stabilising this structurally two-dimensional system where the intercalating O^{2-} anions along the *z*-direction have been removed.

By studying these systems, we hope to establish the basic features that underpin the structural and electronic properties of this family of transition metal oxide phases, which potentially exhibits fascinating physical and chemical properties. Based on the improved theories, we hope that more novel properties can be discovered and understood, more members from this family can be synthesised, and eventually lead to useful applications in the real world.

References

(1) R. V. Dronskowski, *Computational chemistry of solid state materials: a guide for material scientists, chemists, physicists and others*, Wiley-VCH, Weinheim, 2005.

(2) E. Schrödinger, *Ann. Phys.*, 1926, **79**, 361.

(3) W. Koch and M. C. Holthausen, *A chemist's guide to density functional theory*, Wiley-VCH, Weinheim, 2nd, 2001.

(4) A. Szabo and N. S. Ostlund, *Modern quantum chemistry: introduction to advanced electronic structure theory*, Dover, Mineola, 1996.

(5) T. A. Albright, J. K. Burdett and M.-H. Whangbo, *Orbital interactions in chemistry*, Wiley, Hoboken, 2nd, 2013.

(6) J. C. Slater, *Phys. Rev.*, 1930, **36**, 57.

(7) S. F. Boys, *Proc. Roy. Soc. London A*, 1950, **200**, 542.

(8) F. Jensen, *Introduction to computational chemistry*, John Wiley & Sons, Chichester, 2nd, 2007.

(9) E. R. Davidson and D. Feller, *Chem. Rev.*, 1986, **86**, 681.

(10) L. Pauling, *Chem. Rev.*, 1928, **5**, 173.

(11) J. E. Lennard-Jones, *Trans. Faraday Soc.*, 1929, **25**, 668.

(12) V. Fock, *Z. Phys.*, 1930, **61**, 126.

(13) V. Fock, *Z. Phys.*, 1930, **62**, 795.

(14) J. C. Slater, *Phys. Rev.*, 1930, **35**, 210.

(15) D. R. Hartree, *Proc. Cambr. Phil. Soc.*, 1929, **24**, 89.

(16) D. R. Hartree, *Proc. Cambr. Phil. Soc.*, 1929, **24**, 111.

(17) C. C. J. Roothaan, *Rev. Mod. Phys.*, 1951, **23**, 69.

(18) P.-O. Löwdin, *Adv. Chem. Phys.*, 1959, **2**, 207.

(19) L. H. Thomas, *Proc. Cambr. Phil. Soc.*, 1927, **23**, 542.

(20) E. Fermi, *Atti Accad. Naz. Lincei, Rend. Cl. Sci. Fis. Mat.*, 1927, **6**, 602.

(21) E. Fermi, *Atti Accad. Naz. Lincei, Rend. Cl. Sci. Fis. Mat.*, 1928, **7**, 342.

(22) E. Fermi, *Z. Phys.*, 1928, **48**, 73.

(23) J. C. Slater, *Phys. Rev.*, 1951, **81**, 385.

(24) P. Hohenberg and W. Kohn, *Phys. Rev.*, 1964, **136**, 864.

(25) W. Kohn and L. J. Sham, *Phys. Rev.*, 1965, **140**, 1133.

(26) A. D. Becke, *Phys. Rev. A*, 1988, **38**, 3098.

(27) J. P. Perdew, in *Electronic Structure of Solids* (P. Ziesche, H. Eschrig, Eds.), Akademie Verlag, Berlin, 1991.

(28) J. P. Perdew and Y. Wang, *Phys. Rev. B*, 1992, **45**, 13244.

(29) J. P. Perdew, S. Burke and M. Ernzerhof, *Phys. Rev. Lett.*, 1996, **77**, 3865.

(30) J. P. Perdew, *Phys. Rev. B*, 1986, **33**, 8822.

(31) J. P. Perdew, *Phys. Rev. B*, 1986, **34**, 7406.

(32) C. Lee, W. Yang and R. G. Parr, *Phys. Rev. B*, 1988, **37**, 785.

(33) P. J. Stephens, J. F. Devlin, D. F. Chabalowski and M. J. Frisch, *J. Phys. Chem.*, 1994, **98**, 11623.

(34) J. Heyd, G. E. Scuseria and M. Ernzerhof, *J. Chem. Phys.*, 2003, **118**, 8207.

(35) J. Paier, M. Marsman, K. Hummer, G. Kresse, I. C. Gerber and J. G. Angyan, *J. Chem. Phys.*, 2006, **124**, 154709.

(36) N. W. Ashcroft and N. D. Mermin, *Solid state physics*, Brooks/Cole, London, 1976.

(37) F. Bloch, *Z. Phys.*, 1928, **52**, 555.

(38) E. Wigner and F. Seitz, *Phys. Rev.*, 1933, **43**, 804.

(39) H. J. Kulik, N. Seelam, B. D. Mar and T. J. Martínez, *J. Phys. Chem. A*, 2016, **120**, 5939.

(40) M. Imada, A. Fujimori and Y. Tokura, *Rev. Mod. Phys.*, 1998, **70**, 1039.

(41) V. I. Anisimov, J. Zaanen and O. K. Andersen, *Phys. Rev. B*, 1991, **44**, 943.

(42) B. Brandow, *Adv. Phys.*, 1977, **26**, 651.

(43) N. F. Mott and Z. Zinamon, *Rep. Prog. Phys.*, 1970, **33**, 881.

(44) V. I. Anisimov and O. Gunnarsson, *Phys. Rev. B*, 1991, **43**, 7570.

(45) V. I. Anisimov, F. Aryasetiawan and A. I. Lichtenstein, *J. Phys. Condens. Matter*, 1997, **9**, 767.

(46) I. V. Solovyev, P. H. Dederichs and V. I. Anisimov, *Phys. Rev. B*, 1994, **50**, 16861.

(47) S. L. Dudarev, G. A. Botton, S. Y. Savrasov, C. J. Humphreys and A. P. Sutton, *Phys. Rev. B*, 1998, **57**, 1505.

(48) M. Cococcioni and S. de Gironcoli, *Phys. Rev. B*, 2005, **71**, 035105.

(49) L. Wang, T. Maxisch and G. Ceder, *Phys. Rev. B*, 2006, **73**, 195107.

(50) J. C. Slater, *Phys. Rev.*, 1937, **51**, 846.

(51) C. Herring, *Phys. Rev.*, 1940, **57**, 1169.

(52) E. Antoncik, *J. Phys, Chem. Solids*, 1959, **10**, 314.

(53) J. C. Phillips and L. Kleinman, *Phys. Rev.*, 1959, **116**, 287.

(54) D. R. Hamann, M. Schlüter and C. Chiang, *Phys. Rev. Lett.*, 1979, **43**, 1494.

(55) G. Kresse and D. Joubert, *Phys. Rev. B*, 1999, **59**, 1758.

(56) P. E. Blöchl, *Phys. Rev. B*, 1994, **50**, 17953.

(57) D. G. Marc and M. E. McHenry, *Structure of materials: an introduction to crystallography, diffraction and symmetry*, Cambridge University Press, Cambridge, 2007.

(58) J. F. Schooley, W. R. Hosler and M. L. Cohen, *Phys. Rev. Lett.*, 1964, **12**, 474.

(59) M. Azuma, W. T. Chen, H. Seki, M. Czapski, S. Olga, K. Oka, M. Mizumaki, T. Watanuki, N. Ishimatsu, N. Kawamura, S. Ishiwata, M. G. Tucker, Y. Shimakawa and J. P. Attfield, *Nat. Commun.*, 2011, **2**, 347.

(60) C. Eames, J. M. Frost, P. R. F. Barnes, B. C. O'Regan, A. Walsh and M. S. Islam, *Nat. Commun.*, 2015, **6**, 7497.

(61) K. L. Kobayashi, T. Kimura, H. Sawada, K. Terakura and Y. Tokura, *Nature*, 1998, **395**, 677.

(62) S. N. Ruddlesden and P. Popper, *Acta Cryst.*, 1957, **10**, 538.

(63) T. Williams, F. Lichtenberg, R. A. and B. G., *Mater. Res. Bull.*, 1991, **26**, 763.

(64) Y. Maeno, H. Hashimoto, K. Yoshida, S. Nishizaki, T. Fujita, J. G. Bednorz and F. Lichtenberg, *Nature*, 1994, **372**, 532.

(65) C. Lester, S. Ramos, R. S. Perry, T. P. Croft, R. I. Bewley, T. Guidi, P. Manuel, D. D. Khalyavin, F. E. M. and S. M. Hayden, *Nat. Mater.*, 2015, **14**, 373.

(66) M. A. Hayward and M. J. Rosseinsky, *Chem. Mater.*, 2000, **12**, 2182.

(67) M. A. Hayward, *Chem. Mater.*, 2006, **18**, 321.

(68) Y. Tsujimoto, C. Tassel, N. Hayashi, T. Watanabe, H. Kageyama, K. Yoshimura, M. Takano, M. Ceretti, C. Ritter and W. Paulus, *Nature*, 2007, **450**, 1062.

(69) T. Siegrist, S. M. Zahurak, D. W. Murphy and R. S Roth, *Nature*, 1988, **334**, 231.

(70) M. G. Smith, A. Manthiram, J. Zhou, J. B. Goodenough and J. T. Markert, *Nature*, 1991, **351**, 549.

(71) M. Azuma, Z. Hiroi, M. Takano, Y. Bando and Y. Takeda, *Nature*, 1992, **356**, 775.

(72) H. Kageyama, T. Watanabe, Y. Tsujimoto, A. Kitada, Y. Sumida, K. Kanamori, K. Yoshimura, N. Hayashi, S. Muranaka, M. Takano, M. Ceretti, W. Paulus, C. Ritter and G. André, *Angew. Chem. Int. Ed.*, 2008, **47**, 5740.

(73) M. A. Hayward, E. J. Cussen, J. B. Claridge, M. Bieringer, M. J. Rosseinsky, C. J. Kiely, S. J. Blundell, I. M. Marshall and F. L. Pratt, *Science*, 2002, **295**, 1882.

(74) R. M. Helps, N. H. Rees and M. A. Hayward, *Inorg. Chem.*, 2010, **49**, 11062.

(75) Y. Kobayashi, O. J. Hernandez, T. Sakaguchi, T. Yajima, T. Roisnel, Y. Tsujimoto, M. Morita, Y. Noda, Y. Mogami, A. Kitada, M. Ohkura, S. Hosokawa, Z. F. Li, K. Hayashi, Y. Kusano, J. E. Kim, N. Tsuji, A. Fujiwara, Y. Matsushita, K. Yoshimura, K. Takegoshi, M. Inoue, M. Takano and H. Kageyama, *Nat. Mater.*, 2012, **11**, 507.

(76) C. Tassel, Y. Goto, Y. Kuno, J. Hester, M. Green, Y. Kobayashi and H. Kageyama, *Angew. Chem. Int. Ed.*, 2014, **53**, 10377.

(77) F. D. Romero, A. Leach, J. S. Moller, F. Foronda, S. J. Blundell and M. A. Hayward, *Angew. Chem. Int. Ed.*, 2014, **53**, 7556.

(78) J. M. Pruneda, J. Iniguez, E. Canadell, H. Kageyama and M. Takano, *Phys. Rev. B*, 2008, **78**, 115101.

(79) H. J. Xiang, S. H. Wei and M. H. Whangbo, *Phys. Rev. Lett.*, 2008, **100**, 167207.

(80) J. B. Goodenough, *Magnetism and the chemical bond*, Interscience, London, 1963.

(81) T. Katayama, A. Chikamatsu, K. Yamada, K. Shigematsu, T. Onozuka, M. Minohara, H. Kumigashira, E. Ikenaga and T. Hasegawa, *J. Appl. Phys.*, 2016, **120**, 085305.

(82) Y. Wei, H. Gui, X. Li, Z. Zhao, Y. H. Zhao and W. Xie, *J. Phys. Condens. Matter*, 2015, **27**, 206001.

(83) K. Liu, Y. S. Hou, X. G. Gong and H. J. Xiang, *Sci. Rep.*, 2016, **6**, 19653.

(84) T. Kawakami, Y. Tsujimoto, H. Kageyama, X. Q. Chen, C. L. Fu, C. Tassel, A. Kitada, S. Suto, K. Hirama, Y. Sekiya, Y. Makino, T. Okada, T. Yagi, N. Hayashi, K. Yoshimura, S. Nasu, R. Podloucky and M. Takano, *Nat. Chem.*, 2009, **1**, 371.

(85) T. Yamamoto, D. Zeng, T. Kawakami, V. Arcisauskaite, K. Yata, M. A. Patino, N. Izumo, J. E. McGrady, H. Kageyama and M. A. Hayward, *Nat. Commun.*, 2017, **8**, 1217.

(86) R. J. Angel, *Rev. Mineral. Geochem.*, 2000, **41**, 35.

(87) G. Kresse and J. Furthmüller, *Phys. Rev. B*, 1996, **54**, 11169.

(88) A. V. Krukau, O. A. Vydrov, A. F. Izmaylov and G. E. Scuseria, *J. Chem. Phys.*, 2006, **125**, 224106.

(89) M. Brandbyge, J. L. Mozos, P. Ordejon, J. Taylor and K. Stokbro, *Phys. Rev. B*, 2002, **65**, 165401.

(90) J. Taylor, H. Guo and J. Wang, *Phys. Rev. B*, 2001, **63**, 245407.

(91) J. Wei, H. Ji, W. H. Guo, A. H. Nevidomskyy and D. Natelson, *Nat. Nanotechnol.*, 2012, **7**, 357.

(92) T. J. Huffman, P. Xu, M. M. Qazilbash, E. J. Walter, H. Krakauer, J. Wei, D. H. Cobden, H. A. Bechtel, M. C. Martin, G. L. Carr and D. N. Basov, *Phys. Rev. B*, 2013, **87**, 115121.

(93) C. A. Bridges, G. R. Darling, M. A. Hayward and M. J. Rosseinsky, *J. Am. Chem. Soc.*, 2005, **127**, 5996.

(94) M. Rahman, Y. Z. Nie and G. H. Guo, *Inorg. Chem.*, 2013, **52**, 12529.

(95) R. E. Schaak and T. E. Mallouk, *Chem. Mater.*, 2002, **14**, 1455.

(96) J. Gopalakrishnan, *Chem. Mater.*, 1995, **7**, 1265.

(97) J. B. Goodenough, *Localised to itinerant electronic transition in perovskite oxides*, Springer-Verlag, Berlin, 2001.

(98) J. G. Bednorz and K. A. Muller, *Z. Phys. B: Condens. Matter*, 1986, **64**, 189.

(99) J. B. MacChesney, H. J. Williams, J. F. Potter and R. C. Sherwood, *Phys. Rev.*, 1967, **164**, 779.

(100) G. Matsumoto, *J. Phys. Soc. Jpn.*, 1970, **29**, 606.

(101) P. Schiffer, A. P. Ramirez, W. Bao and S. W. Cheong, *Phys. Rev. Lett.*, 1995, **75**, 3336.

(102) M. A. Patino, D. Zeng, S. J. Blundell, J. E. McGrady and M. A. Hayward, *Inorg. Chem.*, 2018, **57**, 2890.

(103) P. D. Battle, G. R. Blake, T. C. Gibb and J. F. Vente, *J. Solid State Chem.*, 1999, **145**, 541.

(104) F. Denis Romero, S. J. Burr, J. E. McGrady, D. Gianolio, G. Cibin and M. A., *J. Am. Chem. Soc.*, 2013, **135**, 1838.

(105) M. A. Patino, D. Zeng, R. Bower, J. E. McGrady and M. A. Hayward, *Inorg. Chem.*, 2016, **55**, 9012.

(106) M. A. Hayward, M. A. Green, M. J. Rosseinsky and J. Sloan, *J. Am. Chem. Soc.*, 1999, **121**, 8843.

(107) J. Rodríguez-Carvajal, M. Hennion, F. Moussa, A. H. Moudden, L. Pinsard and A. Revcolevschi, *Phys. Rev. B*, 1998, **57**, R3189.

(108) L. Jin, M. Lane, D. Zeng, F. K. K. Kirschner, F. Lang, P. Manuel, S. J. Blundell, J. E. McGrady and M. A. Hayward, *Angew. Chem. Int. Ed.*, 2018, **57**, 5025.

List of Publications

The papers that have been published during my D.Phil study at University of Oxford are listed and attached here, in the order that they are discussed in the thesis. Apart from these publications on solid-state topics, there is another paper on molecular systems published, in collaboration with Dr. Chris Russell's group from University of Bristol.

- T. Yamamoto*, D. Zeng*, T. Kawakami, V. Arcisauskaite, K. Yata, M. A. Patino, N. Izumo, J. E. McGrady, H. Kageyama and M. A. Hayward, *Nat. Commun.*, 2017, **8**, 1217.
- M. A. Patino, D. Zeng, S. J. Blundell, J. E. McGrady and M. A. Hayward, *Inorg. Chem.*, 2018, **57**, 2890.
- M. A. Patino, D. Zeng, R. Bower, J. E. McGrady and M. A. Hayward, *Inorg. Chem.*, 2016, **55**, 9012.
- L. Jin, M. Lane, D. Zeng, F. K. K. Kirschner, F. Lang, P. Manuel, S. J. Blundell, J. E. McGrady and M. A. Hayward, *Angew. Chem. Int. Ed.*, 2018, **57**, 5025.
- L. C. Forfar, D. Zeng, M. Green, J. E. McGrady and C. A. Russell, *Chem. Eur. J.*, 2016, **22**, 5397.

nature COMMUNICATIONS

ARTICLE

DOI: 10.1038/s41467-017-01301-0 OPEN

The role of π-blocking hydride ligands in a pressure-induced insulator-to-metal phase transition in $SrVO_2H$

Takafumi Yamamoto [1], Dihao Zeng[2], Takateru Kawakami[3], Vaida Arcisauskaite[2], Kanami Yata[3], Midori Amano Patino[2], Nana Izumo[1], John E. McGrady[2], Hiroshi Kageyama [1,4] & Michael A. Hayward[2]

Transition-metal oxyhydrides are of considerable current interest due to the unique features of the hydride anion, most notably the absence of valence *p* orbitals. This feature distinguishes hydrides from all other anions, and gives rise to unprecedented properties in this new class of materials. Here we show via a high-pressure study of anion-ordered strontium vanadium oxyhydride $SrVO_2H$ that H^- is extraordinarily compressible, and that pressure drives a transition from a Mott insulator to a metal at ~ 50 GPa. Density functional theory suggests that the band gap in the insulating state is reduced by pressure as a result of increased dispersion in the *ab*-plane due to enhanced $V_{d\pi}$-$O_{p\pi}$-$V_{d\pi}$ overlap. Remarkably, dispersion along *c* is limited by the orthogonal $V_{d\pi}$-H_{1s}-$V_{d\pi}$ arrangement despite the greater *c*-axis compressibility, suggesting that the hydride anions act as π-blockers. The wider family of oxyhydrides may therefore give access to dimensionally reduced structures with novel electronic properties.

[1] Department of Energy and Hydrocarbon Chemistry, Graduate School of Engineering, Kyoto University, Nishikyo-ku, Kyoto 615-8510, Japan. [2] Department of Chemistry, University of Oxford, South Parks Road, Oxford OX1 3QR, UK. [3] Department of Physics, College of Humanities and Sciences, Nihon University, Setagaya, Tokyo 156-8550, Japan. [4] CREST, Japan Science and Technology Agency, 7-3-1 Hongo, Bunkyo-ku, Tokyo 113-0033, Japan. Takafumi Yamamoto and Dihao Zeng contributed equally to this work. Correspondence and requests for materials should be addressed to J.E.M. (email: john.mcgrady@chem.ox.ac.uk) or to H.K. (email: kage@scl.kyoto-u.ac.jp) or to M.A.H. (email: michael.hayward@chem.ox.ac.uk)

Transition-metal perovskite oxides, ABO_3, have been the subject of intense study, primarily due to their flexible chemistry which allows a wide variety of different metal cations to be incorporated within the same architecture. This fact, combined with the strong inter-cation electronic and magnetic coupling transmitted via O 2*p* orbitals, makes the perovskite oxides ideal playgrounds to explore physical and chemical phenomena in transition-metal oxides[1–5]. The most common approach employed to tune the behavior and properties of perovskite oxides is chemical substitution, which typically involves cation substitutions on the A- or B-sites of the ABO_3 framework[6, 7]. However, modification of the anion lattice, either through the introduction of anion vacancies[8, 9], or by substituting non-oxide hetero-anions[10–12], provides further opportunities to make dramatic changes to their physical behavior. For example, aliovalent anion doping allows the adjustment of metal oxidation states, the modification of the on-site electronic configuration of transition-metal centers and the tuning of inter-cation couplings, all of which can lead to the realization of novel electronic states.

Binary metal hydrides (e.g., NaH and CaH_2) have proven particularly powerful reagents for modifying the anion lattice because they facilitate the de-intercalation of oxide anions. These low-temperature topochemical reactions[13, 14] give access to metastable, oxygen-deficient phases that contain transition-metal cations in extremely low oxidation states (e.g., Ni^{I}, Co^{I}, Mn^{I}, and Ru^{II})[15–18] and/or highly unusual local coordination geometries (e.g., the square-planar $Fe^{II}O_4$ units observed in the widely studied infinite-layer phase, $SrFeO_2$)[19]. Reduction with metal hydrides can also bring about hydride-for-oxide anion exchange, yielding air-stable transition-metal oxyhydride phases, first observed during the conversion of $LaSrCoO_4$ and $Sr_3Co_2O_{7-x}$ into $LaSrCoO_3H_{0.7}$ and $Sr_3Co_2O_{4.33}H_{0.84}$, respectively[20, 21], and subsequently utilized to prepare $ATiO_{3-x}H_x$ (A = Ba, Sr, Ca)[22, 23] and $Sr_{n+1}V_nO_{2n+1}H_n$ ($n = 1, 2, \infty$)[24]. Further transition-metal oxyhydride phases, such as $SrCrO_2H$ and $LaSrMnO_{3.3}H_{0.7}$[25–27], have been prepared via high-pressure synthesis routes.

The incorporation of hydride anions into extended oxide phases can modify the properties of host phases dramatically due to the strongly contrasting features of oxide and hydride anions, the most obvious of which is the charge. For example, hydride-for-oxide substitution leads to reduction of the metal and induces metallic conductivity in insulating $A^{II}TiO_3$ phases[28, 29]. In addition, the lower electronegativity of hydride compared to oxide means a higher degree of covalency in M–H bonds compared to M–O, leading, for example, to strong Co–H–Co coupling via the σ framework in $LaSrCoO_3H_{0.7}$, and hence to a high magnetic ordering temperature[20, 30]. The labile nature of H^- in mixed oxide/hydride lattices also allows for facile anion-exchange reactions with nitride sources (NH_3, for example), yielding mixed oxide-nitrides such as $BaTiO_{3-x}N_{2x/3}$[31, 32]. In the context of the present paper, however, the most significant difference between the hydride and oxide anions (or indeed any other anion) is the absence of filled valence orbitals with π-symmetry. As a result, when hydride is substituted for oxide in an extended solid, exchange pathways of π-symmetry are effectively blocked, changing the orbital connectivity of a phase quite dramatically, particularly when the anions are in an ordered arrangement. Hydride-for-oxide anion substitution, along with a resultant anion order, therefore offers the intriguing prospect of preparing phases with electronic configurations and properties that contrast strongly with the parent oxide phases.

Reaction of cubic $SrVO_3$ with CaH_2 yields tetragonal $SrVO_2H$, an oxide-hydride phase which adopts an anion-ordered, layered structure consisting of planes of vertex-linked $V^{III}O_4$ units separated by ordered SrH layers[24]. This hydride-for-oxide anion exchange converts the apex-linked $V^{IV}O_6$ units in $SrVO_3$ into *trans*-$V^{III}O_4H_2$ centers in $SrVO_2H$, lifting the degeneracy of the vanadium 3*d* t_{2g} orbitals[24]. On-site electron–electron repulsion further splits the half-filled $d_{xz/yz}$ orbitals, leading to an insulating ground state that has been observed in photoemission and X-ray absorption spectroscopy measurements on thin film samples[33]. Neutron diffraction measurements reveal *G*-type antiferromagnetic order at relatively high temperature ($T_N > 300$ K), indicating the presence of strong antiferromagnetic interactions. The strong super-exchange coupling via the oxide ligands (J_1) is unremarkable, and has been confirmed by recent computational studies from Wei et al. and Liu et al. ($J_1 = 42.7$ meV and 23.5 meV, respectively)[34, 35]. In the absence of π-symmetry orbitals on the H^- bridging ligands, inter-layer coupling (J_2) might be expected to be very small. The computational work by both Wei and Liu noted above confirms that the inter-layer coupling is indeed substantially less than its intra-layer counterpart, although it is not negligible ($J_2 = 5.7$ meV and 1.9 meV, respectively). $SrVO_2H$ can therefore be viewed as a strongly correlated quasi-two-dimensional Mott insulator.

In this paper, we show how pressure can be used as a probe to investigate the structural and electronic properties of $SrVO_2H$. In the structurally related perovskite phase, $SrFeO_2$, an antiferromagnetically ordered Mott insulator at ambient pressure[19], the application of external pressure enhances the interactions between the FeO_2 layers, ultimately leading to a spin-state transition accompanied by antiferromagnetic-to-ferromagnetic and insulator-to-metal transitions[36]. Our motivation here is to establish how the presence of hydride ligands along the *c*-axis in $SrVO_2H$ influences the pressure dependence of the structural and electronic properties of the perovskite lattice.

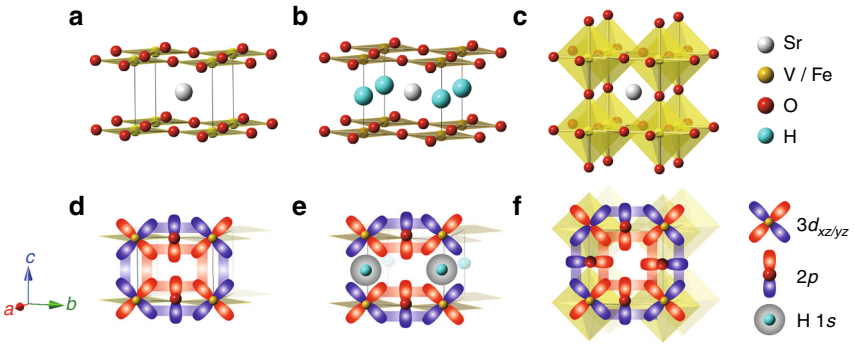


Fig. 1 Crystal structures of perovskite related materials. **a** $SrFeO_2$, **b** $SrVO_2H$, and **c** $SrVO_3$. White, yellow, red, and sky blue spheres, respectively, denote Sr, transition metal, O and H atoms. **d**–**f** represent the inter- and intra-layer orbital connectivity

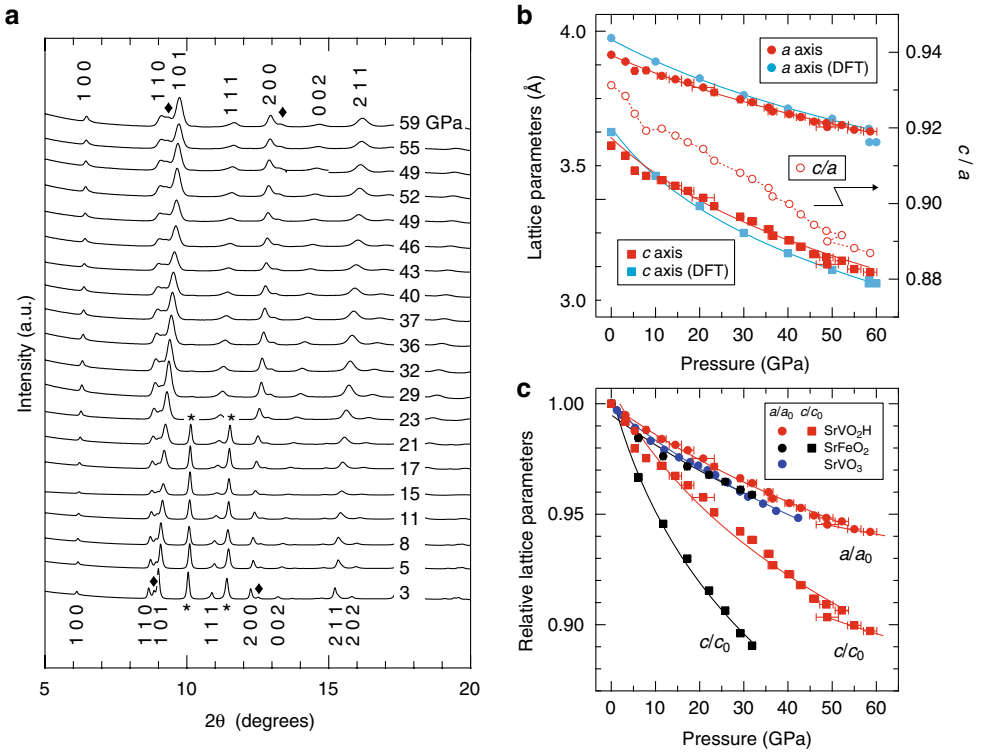


Fig. 2 High-pressure behavior of $SrVO_2H$ and $SrFeO_2$. **a** Powder synchrotron XRD patterns of $SrVO_2H$ (sample $SrVO_2H$-A) under various pressures at room temperature. All the patterns are indexed on the basis of a tetragonal unit cell. The filled diamond and asterisk symbols correspond to $SrVO_3$ and rhenium from the gasket, respectively. **b** Pressure dependence of lattice parameters for the experimental (red) and the DFT-computed (sky blue) values of $SrVO_2H$ – note that some error bars are smaller than the width of the symbols. The decrease in pressure from 52 GPa to 49 GPa as the cell volume decreases suggests a phase transition to a denser phase. **c** Relative lattice parameters, a/a_0 and c/c_0, of $SrVO_2H$ (red), $SrFeO_2$ (black), and $SrVO_3$ (dark blue) as a function of pressure. Circles and squares correspond to the *a* and *c* axes, respectively. Solid lines in **b** and **c** represent linearized Birch-Murnaghan fits to the data

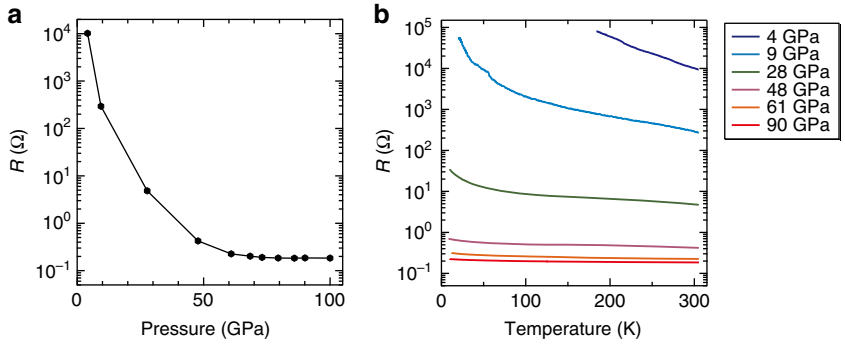


Fig. 3 Electrical resistance for $SrVO_2H$ under pressure. **a** Pressure dependence of resistance *R* at 300 K (sample $SrVO_2H$-B). **b** Temperature dependence of resistance *R* at various pressures

Results

Pressure-dependent structural studies of $SrVO_2H$. $SrVO_2H$ (Fig. 1b) was obtained from $SrVO_3$ (Fig. 1c) by using a CaH_2 reduction method. Powder synchrotron X-ray diffraction (XRD) data collected for $SrVO_2H$ (sample $SrVO_2H$-A; Supplementary Note 1) at room temperature and a variety of applied pressures (Fig. 2a) can be readily indexed on the basis of a tetragonal unit cell, with no evidence of a symmetry-breaking structural transition up to the highest pressure measured (59 GPa). After releasing pressure, the pattern returned to the original ambient-pressure form with only slight peak broadening (Supplementary Fig. 2). The pressure dependence of the lattice parameters of $SrVO_2H$ is shown in Fig. 2b and 2c, where the analogous data collected from $SrFeO_2$[36] and $SrVO_3$ (Supplementary Fig. 3) are also shown for comparison. Linearized Birch-Murnaghan fits[37] to these data allow the zero-pressure linear compressibility β of the *a* and *c* lattice parameters to be estimated (Supplementary Note 2). Fits to the data along *a*, which correspond to the compressibility of in-plane M–O bonds, yield similar β_a values of $1.47(4) \times 10^{-3}$ Pa^{-1} and $1.5(1) \times 10^{-3}$ GPa^{-1}, respectively, for $SrVO_2H$ and $SrFeO_2$. These values are also similar to the isotropic compressibility of $1.72(4) \times 10^{-3}$ GPa^{-1} for $SrVO_3$, indicating an approximately equal M–O bond stiffness in all three phases. In contrast, the *c*-axis compressibility of $\beta_c = 3.7(2) \times 10^{-3}$ GPa^{-1} for $SrVO_2H$, while substantially lower than $\beta_c = 5.0(2) \times 10^{-3}$ GPa^{-1} for $SrFeO_2$ where no ligand is present along the Fe–Fe vector

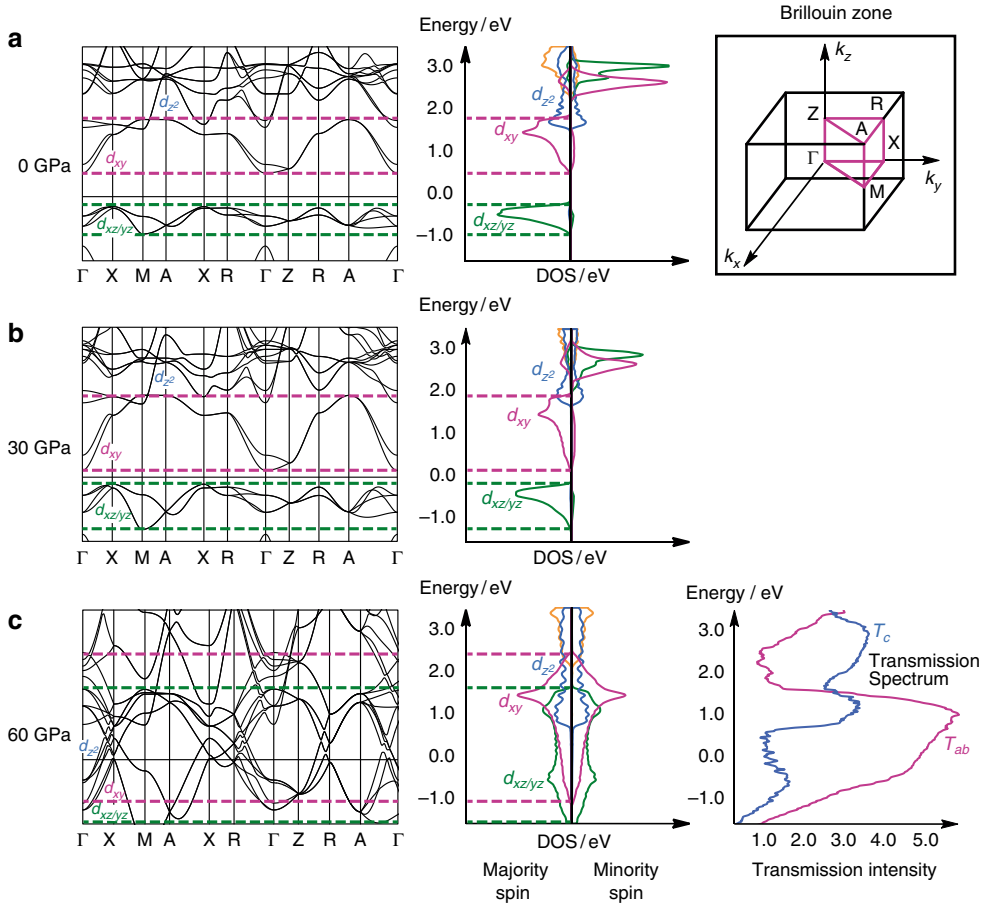


Fig. 4 Density functional theory for $SrVO_2H$. DOS and band structure, **a** at ambient pressure, **b** at 30 GPa, and **c** at 60 GPa. The transmission spectrum along the *c*-axis (T_c, blue line) and along the V–O–V bisector (T_{ab}, purple) is also shown in plot **c** for the high-pressure state. Majority- and minority-spin states in the DOS are shown to the left and right of the axis, respectively. The first Brillouin zone for the tetragonal lattice is shown in the inset

(Fig. 1a), is far larger than any of the values of β noted above, indicating that the V–H bonds in this phase are almost twice as compressible as the V–O bonds.

A pressure-induced insulator-to-metal transition in $SrVO_2H$. Figure 3 shows the resistivity of $SrVO_2H$ (sample $SrVO_2H$-B; Supplementary Note 1) as a function of applied pressure. The observed resistivity of ~ 300 Ω•cm at ambient pressure and 300 K is typical of a semiconductor and consistent with the Mott insulating picture proposed previously[24]. Application of up to 50 GPa pressure leads to a drop of four orders of magnitude in the resistivity of $SrVO_2H$ at 300 K, and a change in the temperature dependence, $\Delta R/\Delta T$, such that the resistance becomes essentially independent of temperature at this pressure (Supplementary Fig. 4), indicating an insulator-to-metal transition. This behavior is reproducible across different samples (Supplementary Fig. 5). We note that $\Delta R/\Delta T$ does not become positive even at 90 GPa, as might be expected for a metallic phase. However, our measurements were performed on a non-sintered powder sample rather than a single crystal, so conduction across grain boundaries is likely to mask the metallic character. Similar features have been reported in previous studies[36, 38]. It should be noted that the absolute value of the resistivity is affected by the presence of impurities in the sample (such as $SrVO_{3-x}$), but the essential features of the insulator-to-metal transition can be identified in all cases (Supplementary Fig. 6). The precise value of the critical pressure, P_c, of the insulator-to-metal transition is not immediately obvious from the resistivity data, but a small but distinct anomaly is observed in the plot of lattice parameters vs. pressure just below 50 GPa (Fig. 2b, 2c). The discontinuity in the plot arises because at this point a reduction in the volume of the sample space causes a decrease in the measured pressure, an observation that is consistent with a phase transition to a denser state (details in Supplementary Note 3). Our analysis of the electronic structure to be discussed in the next section suggests that this denser state may indeed be metallic.

Ambient pressure electronic structure of $SrVO_2H$. In order to explore the underlying origins of the physical measurements detailed above, we have turned to density functional theory. All calculations were performed at the PBE + U level, with a $\sqrt{2}\times\sqrt{2}\times 2$ expansion of the unit cell as shown in Supplementary Fig. 8. We adopt a value of $U_{\mathrm{eff}} = 2.0$ eV for the Hubbard U parameter of vanadium, typical of similar calculations in the literature[39–41]. A full discussion of the influence of U_{eff} on magnetic and structural properties, along with comparative data generated with the hybrid HSE06 functional, is presented in Supplementary Note 4, but our results are not strongly dependent on the chosen value, a point also noted by Wei et al. in their work[34]. The optimized cell parameters of the primitive unit cell at ambient pressure are $a = b = 3.98$ Å and $c = 3.69$ Å, in good agreement with the measured values of 3.93 Å and 3.67 Å. The spin densities on the vanadium centers confirm strong localization of the valence electrons, with $\rho(\mathrm{V}) = \pm 1.73$ being typical of a formally d^2 ion in an oxide lattice. The density of states (DOS) at ambient pressure and its projection onto selected valence orbitals is shown

in Fig. 4a. The high spin moment on each metal center means that each of the metal 3*d* bands in the projected DOS (PDOS) is split into majority- and minority-spin components (shown to the left and right of the *y*-axes in Fig. 4, respectively). Of the vanadium-based 3*d* manifold, only the majority-spin $3d_{xz/yz}$ orbitals lie below the Fermi level, E_f, with their minority-spin counterparts being located ~ 3 eV above it. The strong splitting of the octahedral t_{2g} manifold arises because whilst the $3d_{xz}$ and $3d_{yz}$ orbitals are destabilized by only two in-plane V–O π^* interactions, $3d_{xy}$ is destabilized by four, and this anisotropy, combined with the finite U_{eff}, leads to the emergence of a band gap and hence to the semiconducting properties of $SrVO_2H$ at ambient pressure. The band structure plot (Fig. 4a) highlights one further point that becomes significant in the context of the pressure-dependent properties: the dispersion of the bands just above and below E_f ($d_{xz/yz}$ and d_{xy}) is more prominent in the *ab*-plane (Γ→X→M, Z→R→A) than along the *c*-axis (M→A, X→R, Γ→Z). In direct contrast, the d_{z^2} band is more strongly dispersed along *c* due to σ-type interaction *via* hydride ligands, but the bottom of this band lies ~ 1.6 eV above E_f.

Pressure dependence of the electronic structure. The variation of optimized lattice parameters as a function of applied external pressure is displayed alongside the experimental data in Fig. 2b (sky blue lines). Whilst the computed lattice parameters are marginally more sensitive to pressure than those measured experimentally, the agreement between experiment and theory is striking, both in terms of the absolute values and in the differentiation between *a* and *c*, where the compressibility along the latter is approximately double that along the former. The corresponding PDOS plots and band structure diagrams for selected pressures are summarized in Fig. 4b (30 GPa) and Fig. 4c (60 GPa). As the pressure increases to 30 GPa, the most conspicuous change in the DOS is that the vacant majority-spin d_{xy} band broadens substantially (the dashed purple lines in Fig. 4 mark the upper and lower limits of this band), and the corresponding band structure confirms that this arises primarily due to increased dispersion in the *ab*-plane (Γ→X→M, Z→R→A). The occupied $d_{xz/yz}$ band also broadens, albeit to a lesser extent, and again this can be traced to greater dispersion in the *ab*-plane rather than along *c* (compare changes in dispersion along X→M vs. Γ→Z). At 60 GPa, the broadening is sufficient to induce overlap between the occupied $d_{xz/yz}$ and unoccupied d_{xy} bands, resulting in the complete loss of spin density and the emergence of a metallic state with an associated discontinuity in the optimized lattice parameters, consistent with the features observed in the crystallographic and resistivity data around 50 GPa. Even at 60 GPa, it is clear that it is the dispersion in the *ab*-plane, and not along *c*, which is the driving force for the transition to a metallic state: a clear band gap is maintained along Γ→Z and M→A. To reinforce this point, we have mimicked the effects of an anisotropic pressure source by varying either *a* or *c* while keeping the other constant (see Supplementary Fig. 11). If we maintain *a* at its ambient pressure value of 3.93 Å but reduce *c* to its 60 GPa-optimized value of 3.29 Å, we note that the dispersion of the $d_{xz/yz}$ band increases, but critically not to the extent that the band gap closes: the system remains an insulator. Conversely if we maintain *c* at its ambient-pressure value of 3.69 Å but contract *a* to its 60 GPa value of 3.67 Å, the band gap closes and a metallic state does emerge. From this, we conclude that it is the contraction in the *ab*-plane and not along *c* that drives the formation of the metallic state, despite the fact that the magnitude of the contraction in *ab* is smaller in absolute terms. To reinforce this point, we have explicitly computed the energy-dependent transmission spectrum for current flow both along the *c*-axis and in the *ab*-plane for the 60 GPa structure (Fig. 4c, right). The major peak in T_{ab} is coincident with the broad d_{xy} band that spans the Fermi level, while transmission along *c* (T_c) becomes significant only above ~ 0.8 eV, coincident with the bottom of the d_{z^2} band. As a result, transmission at the Fermi level is approximately five times stronger in the *ab*-plane than along *c*, indicating that the metallic behavior is strongly two-dimensional. In summary, the emergence of metallic behavior appears not to be connected directly to the very substantial compression along *c*, which simply reflects the intrinsically higher compressibility of the hydride ion vs. oxide, rather than any increased delocalization of itinerant electrons along this axis. The high-pressure metallic state can instead be considered as a quasi-two-dimensional metal with a conduction band made up mainly of the overlapping $d_{xz/yz}$ and d_{xy} bands with substantial dispersion only in the *ab*-plane. Finally we note that the precise window in which the insulator-to-metal transition is predicted to take place is strongly dependent on chosen methodology: a higher value of U_{eff} pushes the transition to higher pressures, as does the hybrid HSE06 functional (see Supplementary Note 4 for a full discussion). We do not, therefore, claim to be able to pinpoint the critical pressure exactly, but rather note that the pressure-induced dispersion of the d_{xy} band is the driving force in all cases. Thus unlike the absolute value of the critical pressure, our conclusions regarding the dimensionality of the metallic behavior are not strongly dependent on the chosen methodology.

Discussion

At first sight the pressure-induced insulator-metal transition in $SrVO_2H$ appears remarkably similar to that in $SrFeO_2$ previously reported by some of us[36] – both phases are antiferromagnetic insulators at ambient pressure, both undergo strongly anisotropic lattice contractions on the application of pressure ($\Delta c > \Delta a$) and both eventually become metallic, at 34 GPa and 50 GPa, respectively. A closer inspection however reveals profound differences between the two systems. In the case of $SrFeO_2$, the transition from insulating to metallic behavior is intimately connected to a change in spin state from $S = 2$ at ambient pressure to $S = 1$ above the critical pressure. The ambient-pressure electronic structure has been discussed at some length, and it is the d_{z^2} orbital of Fe that is doubly occupied ($(d_{z^2})^2(d_{xz/yz})^2(d_{xy})^1(d_{x^2-y^2})^1$)[42, 43]. The band gap is primarily a consequence of the large spin polarization that splits the majority- and minority-spin manifolds. Above P_c (34 GPa) however, the relative destabilization of the Fe–O σ^* $3d_{x^2-y^2}$ orbital as the Fe–O bond lengths are compressed leads to a local $(d_{z^2})^2(d_{xz/yz})^3(d_{xy})^1(d_{x^2-y^2})^0$ configuration ($S = 1$)[44]. At even higher pressures, the compression along *c* leads to repulsions between the d_{z^2} orbitals in adjacent layers, causing a partial transfer of electron density out of the d_{z^2} band into d_{xy}, and therefore to a substantial increase in the DOS at E_f. The result is a metallic state where the electron density distribution is approximately isotropic[36]. In contrast, our calculations on the $SrVO_2H$ system suggest that the greater compressibility along the *c*-axis is not directly related to the emergence of metallic behavior: even at the high-pressure limit the inter-layer V–V separation is too large to afford significant direct $V_{d\pi}$–$V_{d\pi}$ overlap. The very different behavior of $SrFeO_2$ and $SrVO_2H$ arises simply because the electronic configuration is very different (d^6 vs. d^2) and the band gap in the latter is determined by the different number of $V_{d\pi}$–$O_{2p\pi}$–$V_{d\pi}$ interactions experienced by the $3d_{xy}$ and $3d_{xz/yz}$ orbitals (four and two, respectively). The hydride ions in $SrVO_2H$ can therefore be viewed as π-orbital blockers in the sense that they have no π-symmetry valence orbitals to interact with the vanadium π-symmetry *d*-orbitals, $3d_{xz/yz}$. The metallic behavior

then emerges because the compression in the *ab*-plane, although smaller in magnitude than that along the *c*-axis, increases the $V_{d\pi}$–$O_{2p\pi}$–$V_{d\pi}$ interactions and hence the dispersion of the $3d_{xz/yz}$ and the $3d_{xy}$ bands, to the extent that they overlap and form a single continuous band. Schematic orbital connectivities for $SrFeO_2$, $SrVO_2H$ and $SrVO_3$ are shown in Fig. 2d–f. In short, when $SrVO_3$ is converted to $SrVO_2H$, the 3-dimensional $V_{d\pi}$–$O_{2p\pi}$–$V_{d\pi}$ network is reduced to two dimensions as a result of the π-blocking SrH layer, with dramatic consequences for the physical properties simply because the band gap falls in the middle of the $V_{d\pi}$ band.

Insulator-to-metal transitions in strongly correlated systems have been a central subject in condensed matter physics for many decades, and the transitions of a large number of oxides with different *d*-electron counts have been studied in some detail[45]. The physics of low *d*-electron count systems (d^1 or d^2 systems such as VO_2, V_2O_3, Ti_2O_3, and $REVO_3$ where RE = rare earth, for example) is, however, complicated because the splitting of the $M_{d\pi}$ manifold is very sensitive to the subtle details of the distortions and tilting of the MO_6 octahedra. In contrast, the highly anisotropic coordination environment of vanadium in $SrVO_2H$ simplifies the problem by causing a substantial zeroth-order splitting of this manifold, and the unusual pressure-dependent electronic properties of $SrVO_2H$ highlight the importance of the π-blocking nature of the hydride anion. We note that the use of π-blockers differs markedly from conventional strategies for reducing dimensionality, where bulky blocking layers are typically used to separate (super)conducting layers. These observations provide a strong motivation for the synthesis of new transition-metal oxyhydride phases with novel and elaborate anion-ordering schemes. Some closely related phases such as Sr_2VO_3H and $Sr_3V_2O_5H_2$ (Supplementary Fig. 14) are already known[24, 27], and similar pressure-induced insulator-to-metal transitions might be anticipated in these $S = 1$ chains and ladders. Wider studies of the oxyhydride family will undoubtedly increase our ability to control π-orbital connectivity, in reduced phases and hence engineer materials with novel properties.

Methods

Sample preparation. Powder samples of $SrVO_3$ were obtained by hydrogen reduction from $Sr_2V_2O_7$, as described previously[46]. Two powder samples of $SrVO_2H$ (referred to as $SrVO_2H$-A and $SrVO_2H$-B) were synthesized by a topochemical reaction between $SrVO_3$ and CaH_2, as reported previously[24]. The principal difference between the two reduced samples is that $SrVO_2H$-A contains small amounts of $SrVO_{3-x}$ which were observed to adversely affect the resistance measurements. A detailed discussion of samples $SrVO_2H$-A and $SrVO_2H$-B is presented in Supplementary Note 1.

High-pressure X-ray diffraction. Powder synchrotron XRD experiments for $SrVO_2H$-A under high pressures were performed at room temperature using the NE1A synchrotron beam line of the Photon Factory–Advanced Ring for Pulse X-rays (PF–AR) at the High Energy Accelerator Research Organization (KEK). Powder samples were loaded into a 100 μm hole of pre-indented rhenium gasket of the diamond anvil cell. Daphne oil 7373 was used as a pressure transmitting medium. The volume of the sample space was varied using a screw. At each volume, the fluorescence shift of ruby chips was used to measure the pressure. To estimate the pressure distribution along the sample, several ruby chips were placed inside the hole at different distances from its center. The pressure gradient increased with pressure, but did not exceed ±3 GPa at 59 GPa. The incident X-ray beam was monochromatized to a wavelength of 0.4173 Å. The beam was collimated to a diameter of about 50 μm at 0–21 GPa and 30 μm at 23–59 GPa. Due to the relatively large size of beam, peaks from the rhenium gasket were obvious in the pressure range 0–21 GPa. High-pressure experiments on $SrVO_3$ were conducted in the same manner, with a wavelength of 0.4186 Å and a beam collimated to 50 μm in diameter.

High-pressure resistivity. Four-probe ac resistance measurements were carried out using Pt electrodes. Three measurements were done on sample $SrVO_2H$-A up to 50 GPa and on sample $SrVO_2H$-B up to 100 GPa, all in the temperature range 8 K < *T* < 300 K. NaCl was used as a pressure transmitting medium. The sample-gasket cavity was coated with an insulating anhydrous gypsum ($CaSO_4$) with epoxy. The initial sectional area and the distance between probes were about 40 × 40 μm^2 and 30 μm, respectively. The applied pressure was calibrated with fluorescence manometer on ruby chips placed around the sample.

Density functional theory. The geometry optimizations described here were performed using the VASP software package (VASP 5.3)[47], with the PBE density functional. In order to investigate different magnetic configurations it proved necessary to consider a $\sqrt{2} \times \sqrt{2} \times 2$ expansion of the primitive unit cell (Supplementary Fig. 8). A plane-wave cutoff of 600 eV was used and the Brillouin zone was sampled on an 8 × 8 × 7 Γ-centered grid. The effect of strong correlations is typically introduced through the effective Hubbard *U* value (U_{eff}). A survey of the literature indicates that U_{eff} values up to 5.0 eV have been adopted for vanadium[39–41]. In the present study, we adopt a value of $U_{eff} = 2.0$ eV, although the dependence of the optimized lattice parameters on U_{eff} is weak (Supplementary Table 2). The potential pressure dependence of U_{eff} in $SrFeO_2$ has been discussed, and Rahman et al. have suggested that its value should decrease approximately linearly with pressure from its ambient-pressure value[44]. Whilst systematic reduction of our chosen value of 2.0 eV to 0.0 eV in the present case reduces the absolute value of the critical pressure of insulator-to-metal transition, it does not influence the underlying physics in any substantial way. We have also considered the hybrid HSE06 functional[48] with 25% Hartree-Fock exchange and a range constant, ω, of 0.2. These calculations were done as single points using the geometries optimized at the PBE + *U* ($U_{eff} = 2.0$ eV) level. An insulating state is retained with HSE06 even at a structure optimized under 90 GPa of pressure, but the closing of the band gap due to broadening of the d_{xy} conduction band is clearly discernable. Transport analysis was performed using the ATK software package (ATK 2016.4)[49, 50] with the same PBE density functional and $U_{eff} = 2.0$ eV used in the VASP calculations. A localized double-ζ basis set, extended with single polarization function (DZP) was used to describe all atoms. The Brillouin zone was sampled on a 21 × 21 × 21 Monkhorst-Pack grid.

Data availability. The data that support the findings of this study are available from the corresponding author upon reasonable request.

Received: 14 March 2017 Accepted: 7 September 2017
Published online: 31 October 2017

References

1. Schooley, J. F., Hosler, W. R. & Cohen, M. L. Superconductivity in semiconducting $SrTiO_3$. *Phys. Rev. Lett.* **12**, 474–475 (1964).
2. Moritomo, Y., Asamitsu, A., Kuwahara, H. & Tokura, Y. Giant magnetoresistance of manganese oxides with a layered perovskite structure. *Nature* **380**, 141–144 (1996).
3. Kobayashi, K. I., Kimura, T., Sawada, H., Terakura, K. & Tokura, Y. Room-temperature magnetoresistance in an oxide material with an ordered double-perovskite structure. *Nature* **395**, 677–680 (1998).
4. Azuma, M. et al. Colossal negative thermal expansion in $BiNiO_3$ induced by intermetallic charge transfer. *Nat. Commun.* **2**, 347 (2011).
5. Boris, A. V. et al. Dimensionality control of electronic phase transitions in nickel-oxide superlattices. *Science* **332**, 937–940 (2011).
6. Sleight, A. W., Gillson, J. L. & Bierstedt, P. E. High-temperature superconductivity in $BaPb_{1-x}Bi_xO_3$ system. *Solid State Commun.* **17**, 27–28 (1975).
7. Alonso, J. A., Martínez-Lope, M. J., Casais, M. T., Aranda, M. A. G. & Fernández-Díaz, M. T. Metal-insulator transitions, structural and microstructural evolution of $RNiO_3$ (*R* = Sm, Eu, Gd, Dy, Ho, Y) Perovskites: evidence for room-temperature charge disproportionation in monoclinic $HoNiO_3$ and $YNiO_3$. *J. Am. Chem. Soc.* **121**, 4754–4762 (1999).
8. Hiroi, Z. & Takano, M. Absence of superconductivity in the doped antiferromagnetic spin-ladder compound $(La,Sr)CuO_{2.5}$. *Nature* **377**, 41–43 (1995).
9. Le Toquin, R., Paulus, W., Cousson, A., Prestipino, C. & Lamberti, C. Time-resolved in situ studies of oxygen intercalation into $SrCoO_{2.5}$, performed by neutron diffraction and X-ray absorption spectroscopy. *J. Am. Chem. Soc.* **128**, 13161–13174 (2006).
10. Jansen, M. & Letschert, H. Inorganic yellow-red pigments without toxic metals. *Nature* **404**, 980–982 (2000).
11. Kobayashi, Y., Tian, M., Eguchi, M. & Mallouk, T. E. Ion-exchangeable, electronically conducting layered perovskite oxyfluorides. *J. Am. Chem. Soc.* **131**, 9849–9855 (2009).
12. Tsujimoto, Y., Sathish, C., Matsushita, Y., Yamaura, K. & Uchikoshi, T. New members of layered oxychloride perovskites with square planar coordination: $Sr_2MO_2Cl_2$ (M = Mn, Ni) and $Ba_2PdO_2Cl_2$. *Chem. Commun.* **50**, 5915–5918 (2014).

13. Hayward, M. A., Green, M. A., Rosseinsky, M. J. & Sloan, J. Sodium hydride as a powerful reducing agent for topotactic oxide deintercalation: synthesis and characterization of the nickel(I) oxide $LaNiO_2$. *J. Am. Chem. Soc.* **121**, 8843–8854 (1999).
14. Yamamoto, T. & Kageyama, H. Hydride reductions of transition metal oxides. *Chem. Lett.* **42**, 946–953 (2013).
15. Hayward, M. & Rosseinsky, M. Synthesis of the infinite layer Ni(I) phase $NdNiO_{2+x}$ by low temperature reduction of $NdNiO_3$ with sodium hydride. *Solid State Sci.* **5**, 839–850 (2003).
16. Seddon, J., Suard, E. & Hayward, M. The topotactic reduction of $YBaCo_2O_5$ and $LaBaCo_2O_5$ – square-planar Co(I) in an extended oxide. *J. Am. Chem. Soc.* **132**, 2802–2810 (2010).
17. Dixon, E., Hadermann, J., Ramos, S., Goodwin, A. L. & Hayward, M. A. Mn(I) in an extended oxide - the synthesis and characterization of $La_{1-x}Ca_xMnO_{2+}d$ $(0.6 < x < 1)$. *J. Am. Chem. Soc.* **133**, 18397–18405 (2011).
18. Denis Romero, F. et al. $SrFe_{0.5}Ru_{0.5}O_2$: square-planar Ru^{2+} in an extended oxide. *J. Am. Chem. Soc.* **135**, 1838–1844 (2013).
19. Tsujimoto, Y. et al. Infinite-layer iron oxide with a square-planar coordination. *Nature* **450**, 1062–1065 (2007).
20. Hayward, M. A. et al. The hydride anion in an extended transition metal oxide array–$LaSrCoO_3H_{0.7}$. *Science* **295**, 1882–1884 (2002).
21. Helps, R., Rees, N. & Hayward, M. A. $Sr_3Co_2O_{4.33}H_{0.84}$ – an extended transition metal oxide-hydride. *Inorg. Chem.* **49**, 11062–11068 (2010).
22. Kobayashi, Y. et al. An oxyhydride of $BaTiO_3$ exhibiting hydride exchange and electronic conductivity. *Nat. Mater.* **11**, 507–511 (2012).
23. Sakaguchi, T. et al. Oxyhydrides of (Ca,Sr,Ba)TiO_3 perovskite solid solutions. *Inorg. Chem.* **51**, 11371–11376 (2012).
24. Denis Romero, F. et al. Strontium vanadium oxide-hydrides: 'square-planar' two-electron phases. *Angew. Chem. Int. Ed.* **53**, 7556–7559 (2014).
25. Tassel, C. et al. Direct synthesis of chromium perovskite oxyhydride with a high magnetic transition temperature. *Angew. Chem. Int. Ed.* **53**, 10377–10380 (2014).
26. Tassel, C. et al. High-pressure synthesis of manganese oxyhydride with partial anion order. *Angew. Chem. Int. Ed.* **55**, 9667–9670 (2016).
27. Bang, J. et al. Hydrogen ordering and new polymorph of layered perovskite oxyhydrides: $Sr_2VO_{4-x}H_x$. *J. Am. Chem. Soc.* **136**, 7221–7224 (2014).
28. Yajima, T. et al. Epitaxial thin films of $ATiO_{3-x}H_x$ (A = Ba, Sr, Ca) with metallic conductivity. *J. Am. Chem. Soc.* **134**, 8782–8785 (2012).
29. Bouilly, G. et al. Electrical properties of epitaxial thin films of oxyhydrides $ATiO_{3-x}H_x$ (A = Ba and Sr). *Chem. Mater.* **27**, 6354–6359 (2015).
30. Bridges, C. A., Darling, G. R., Hayward, M. A. & Rosseinsky, M. J. Electronic structure, magnetic ordering, and formation pathway of the transition metal oxide hydride $LaSrCoO_3H_{0.7}$. *J. Am. Chem. Soc.* **127**, 5996–6011 (2005).
31. Yajima, T. et al. A labile hydride strategy for the synthesis of heavily nitridized $BaTiO_3$. *Nat. Chem.* **7**, 1017–1023 (2015).
32. Masuda, N. et al. Hydride in $BaTiO_{2.5}H_{0.5}$: a labile ligand in solid state chemistry. *J. Am. Chem. Soc.* **137**, 15315–15321 (2015).
33. Katayama, T. et al. Epitaxial growth and electronic structure of oxyhydride $SrVO_2H$ thin films. *J. Appl. Phys.* **120**, 085305 (2016).
34. Wei, Y. et al. The effect of hydrogen ordering on the electronic and magnetic properties of the strontium vanadium oxyhydride. *J. Phys. Condens. Matter* **27**, 206001 (2015).
35. Liu, K., Hou, Y. S., Gong, X. G. & Xiang, H. J. Orbital delocalization and enhancement of magnetic interactions in perovskite oxyhydrides. *Sci. Rep.* **6**, 19653 (2016).
36. Kawakami, T. et al. Spin transition in a four-coordinate iron oxide. *Nat. Chem.* **1**, 371–376 (2009).
37. Hazen, R. M. & Downs, R. T. *High-Temperature and High-Pressure Crystal Chemistry* (Reviews in Mineralogy & Geochemistry Vol. 41) Part I, Chapter 2, 35-60 (Mineralogical Society of America / Geochemical Society, 2001).
38. Yamamoto, T. et al. Pressure-induced structural, magnetic, and transport transitions in the two-legged ladder $Sr_3Fe_2O_5$. *J. Am. Chem. Soc.* **133**, 6036–6043 (2011).
39. Wang, L., Maxisch, T. & Ceder, G. Oxidation energies of transition metal oxides within the GGA + U framework. *Phys. Rev. B* **73**, 195107 (2006).
40. Wei, J., Ji, H., Guo, W. H., Nevidomskyy, A. H. & Natelson, D. Hydrogen stabilization of metallic vanadium dioxide in single-crystal nanobeams. *Nat. Nanotechnol.* **7**, 357–362 (2012).
41. Huffman, T. J. et al. Anisotropic infrared response of vanadium dioxide microcrystals. *Phys. Rev. B* **87**, 115121 (2013).
42. Pruneda, J. M., Íñiguez, J., Canadell, E., Kageyama, H. & Takano, M. Structural and electronic properties of $SrFeO_2$ from first principles. *Phys. Rev. B* **78**, 115101 (2008).
43. Xiang, H. J., Wei, S. –H. & Whangbo, M.–H. Origin of the structural and magnetic anomalies of the layered compound $SrFeO_2$: a density functional investigation. *Phys. Rev. Lett.* **100**, 167207 (2008).
44. Rahman, M., Nie, Y. Z. & Guo, G. H. Electronic structures and magnetism of $SrFeO_2$ under pressure: a first-principles study. *Inorg. Chem.* **52**, 12529–12534 (2013).
45. Imada, M., Fujimori, A. & Tokura, Y. Metal-insulator transitions. *Rev. Mod. Phys.* **70**, 1039–1263 (1998).
46. Rey, M. J. et al. Preparation and structure of the compounds $SrVO_3$ and Sr_2VO_4. *J. Solid State Chem.* **86**, 101–108 (1990).
47. Kresse, G. & Furthmuller, J. Efficient iterative schemes for *ab initio* total-energy calculations using a plane-wave basis set. *Phys. Rev. B* **54**, 11169–11186 (1996).
48. Krukau, A., Vydrov, O., Izmaylov, A. & Scuseria, G. Influence of the exchange screening parameter on the performance of screened hybrid functionals. *J. Chem. Phys.* **125**, 224106 (2006).
49. Brandbyge, M., Mozos, J.-L., Ordejon, P., Taylor, J. & Stokbro, K. Density-functional method for nonequilibrium electron transport. *Phys. Rev. B* **65**, 165401 (2002).
50. Taylor, J., Guo, H. & Wang, J. Ab initio modeling of quantum transport properties of molecular electronic devices. *Phys. Rev. B* **63**, 245407 (2001).

Acknowledgements

The work was supported by CREST and JSPS KAKENHI (JP16H06438, JP16H6439, JP16H6440, JP16K21724, and JP16H06033). High-pressure synchrotron radiation experiments were performed under the approval of the Photon Factory Program Advisory Committee (No. 2015G012). We thank Taku Okada and Takumi Kikegawa for their support of the high-pressure XRD measurement. MAP thanks CONACYT and the Balliol College, Oxford for a scholarship. J.E.M. and V.A. acknowledge financial support from the EPSRC (EP/K021435/1).

Author contributions

T.Y., D.Z., J.E.M., H.K., and M.A.H. designed the research. M.A.P. and N.I. synthesized the material. T.Y. collected high-pressure XRD data and analyzed. T.K. and K.Y. measured the high-pressure resistivity. D.Z. and V.A. performed the electronic structure analysis. All the authors discussed the results. T.Y., D.Z., H.K., J.E.M., and M.A.H. wrote the manuscript, with comments from all the authors.

Additional information

Supplementary Information accompanies this paper at doi:10.1038/s41467-017-01301-0.

Competing interests: The authors declare no competing financial interests.

Reprints and permission information is available online at http://npg.nature.com/reprintsandpermissions/

Publisher's note: Springer Nature remains neutral with regard to jurisdictional claims in published maps and institutional affiliations.

Open Access This article is licensed under a Creative Commons Attribution 4.0 International License, which permits use, sharing, adaptation, distribution and reproduction in any medium or format, as long as you give appropriate credit to the original author(s) and the source, provide a link to the Creative Commons license, and indicate if changes were made. The images or other third party material in this article are included in the article's Creative Commons license, unless indicated otherwise in a credit line to the material. If material is not included in the article's Creative Commons license and your intended use is not permitted by statutory regulation or exceeds the permitted use, you will need to obtain permission directly from the copyright holder. To view a copy of this license, visit http://creativecommons.org/licenses/by/4.0/.

© The Author(s) 2017

Extreme Sensitivity of a Topochemical Reaction to Cation Substitution: $SrVO_2H$ vs $SrV_{1-x}Ti_xO_{1.5}H_{1.5}$.

Midori Amano Patino [†], Dihao Zeng [†], Stephen J. Blundell [‡], John E. McGrady [†] and Michael A. Hayward [†]*.

[†] Department of Chemistry, University of Oxford, Inorganic Chemistry Laboratory, South Parks Road, Oxford, OX1 3QR, United Kingdom.

[‡] Department of Physics, Clarendon Laboratory, University of Oxford, Parks Road, Oxford, OX1 3PU, UK.

Supporting Information Placeholder

ABSTRACT: The anion-ordered oxide-hydride $SrVO_2H$ is an antiferromagnetic insulator due to strong correlations between vanadium d-electrons. In an attempt to hole-dope $SrVO_2H$ into a metallic state, a strategy of first preparing $SrV_{1-x}Ti_xO_3$ phases and then converting them to the corresponding $SrV_{1-x}Ti_xO_2H$ phases *via* reaction with CaH_2 was followed. This revealed that the solid-solution between $SrVO_3$ and $SrTiO_3$ is only stable at high temperature. In addition reactions between $SrV_{0.95}Ti_{0.05}O_3$ and CaH_2 were observed to yield $SrV_{0.95}Ti_{0.05}O_{1.5}H_{1.5}$ not $SrV_{0.95}Ti_{0.05}O_2H$. This dramatic change in reactivity for a very modest change in initial chemical composition is attributed to an electronic destabilization of $SrVO_2H$ on titanium substitution. DFT calculations indicate that the presence of an anion-ordered, tetragonal $SrMO_2H$ phase is uniquely associated with a d^2 electron count, and that titanium substitution leads to an electronic destabilization of $SrV_{1-x}Ti_xO_2H$ phases which, ultimately, drives further reaction of $SrV_{1-x}Ti_xO_2H$ to $SrV_{1-x}Ti_xO_{1.5}H_{1.5}$. The observed sensitivity of the reaction products to the chemical composition of initial phases highlights some of the difficulties associated with electronically doping metastable materials prepared by topochemical reactions.

Introduction

Low-temperature, structure-conserving reactions can be used to manipulate the anion lattices of complex transition-metal oxides, offering routes to highly metastable phases which cannot be readily prepared via conventional high-temperature synthesis. 'Topochemical' reactions of this type have been used to generate extended solids containing arrays of transition-metal cations in highly unusual oxidation-state/coordination-geometry combinations.[1-3] For example, by utilising binary metal hydrides such as NaH, LiH or CaH_2 as reducing agents,[4] it has proved possible to deintercalate oxide ions from transition-metal oxide perovskites to yield phases containing square-planar Fe^{2+}, Co^{1+}, Ni^{1+} or Ru^{2+} cations.[5-8] In addition hydride-for-oxide anion exchange reactions can also occur, leading to the formation of transition-metal oxide-hydride phases such as $LaSrCoO_3H_{0.7}$, $Sr_3Co_2O_{4.33}H_{0.84}$, $A^{II}TiO_{3-x}H_y$ and the $Sr_{n+1}V_nO_{2n+1}H_n$ series,[9-12] all of which contain reduced transition-metal cations in oxide-hydride coordination spheres. The very unusual electronic structures of these metastable solid-state compounds mean that they are of intrinsic chemical interest, but their electronic and magnetic properties, which arise from the cooperative interactions between the paramagnetic centres, also offer the potential for novel materials properties. Unfortunately, the majority of the reported anion-vacancy ordered reduced oxides and oxide-hydrides prove to be antiferromagnetic insulators, simply because large on-site electron-electron repulsion terms (U) tend to localize the unpaired metal d-electrons on discrete metal cation sites. Valence-electron localization of this type is frequently observed in transition metal oxide phases – even those prepared *via* high-temperature routes – and is particularly common in systems containing 3d transition metal cations in integer oxidation states.[13] Itinerant electrons can, however, be generated *via* chemical 'doping', which drives the transition-metal ions into non-integer or mixed valent states. A classic example is the Cu^{2+} phase La_2CuO_4 which is a simple antiferromagnetic insulator in its pure form. However, doping the system, *via* barium-for-lanthanum substitution leads to a mixed valent $Cu^{2+/3+}$ state which exhibits both metallic conductivity and superconductivity.[14] Likewise the Mn^{3+} and Mn^{4+} phases, $LaMnO_3$ and $CaMnO_3$, are both antiferromagnetic insulators,[15-16] but mixed valent $Mn^{3+/4+}$ members of the $La_{1-x}Ca_xMnO_3$ solid solution exhibit metal-insulator transitions and large magnetoresistive ratios.[17]

The remarkable differences in physical properties of the doped and undoped oxides provide strong motivation to explore the effects of doping on topochemically prepared phases. The oxide-hydride $SrVO_2H$ is an ideal candidate in this respect.[12] As shown in Figure 1, $SrVO_2H$ adopts an anion-ordered structure in which the V^{3+} cations reside within *trans*-VO_4H_2 local coordination sites which then share corners to form a 3D network. The ordered arrangement of oxide and hydride anions lifts the degeneracy of the π-symmetry vanadium d-orbitals (d_{xz}, d_{yz}, d_{xy}), giving a local $(d_{xz/yz})^2(d_{xy})^0(d_{z^2})^0(d_{x^2-y^2})^0$ configuration. Substantial on-site repulsions split the half-filled $d_{xz/yz}$ band, leading to a Mott-Hubbard insulating state.[12, 18-19] In very recent work we have demonstrated that $SrVO_2H$ undergoes a pressure induced insulator-to-metal transition at ~50 GPa.[20] The resulting metallic state exhibits a significant 2-dimensional character because the hydride ions block dispersion along the z-axis of the π-symmetry bands which span the Fermi level. A detailed study of this pressure-induced metallic state is, unfortunately, experimentally very challenging and so we hope to gain an alternative perspective on this material *via* hole-doping with Ti, which should partially depopulate the $d_{xz/yz}$ band and hence generate a metallic state at ambient pressure. Here we describe our attempts to hole-dope $SrVO_2H$, first by preparing samples of titanium-substituted $SrV_{1-x}Ti_xO_3$, and then reducing them to form oxide-hydride phases. In the course of these studies we observed that the low-temperature anion-exchange reaction which forms the oxide-hydride phases is

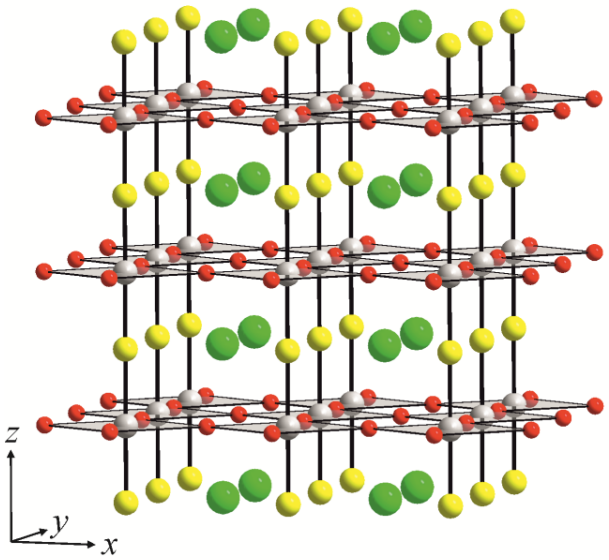


Figure 1 The crystal structure of $SrVO_2H$. Green, grey, red and yellow spheres represent Sr, V, O and H respectively.

extremely sensitive to even very small changes in the composition of the 'parent' oxide. The Ti-doped analogue of $SrVO_2H$, $SrV_{1-x}Ti_xO_2H$, is only transiently stable, reacting further to form $SrV_{1-x}Ti_xO_{1.5}H_{1.5}$, the doped analogue of the inaccessible $SrVO_{1.5}H_{1.5}$ phase. This extreme sensitivity to chemical substitution has important implications for doping strategies of other topochemically prepared materials.

Experimental

Synthesis of $SrV_{1-x}Ti_xO_3$. The synthesis of $SrV_{1-x}Ti_xO_3$ samples was attempted in two different ways, a 'ceramic' synthesis route and an 'arc-melt' route. The ceramic synthesis of $SrV_{1-x}Ti_xO_3$ utilized a modified version of the procedure previously described to prepare $SrVO_3$.[21] Suitable ratios of $SrCO_3$ (99.99%), V_2O_5 (99.99%) and TiO_2 (99.995%, previously dried at 900 °C) were ground together and then heated in air at 900 °C for 12 h to decompose the carbonate and prepare $Sr_2V_{2-2x}Ti_{2x}O_{7-\delta}$, as confirmed by powder X-ray diffraction. Samples were then heated at 1075 °C, under flowing H_2 (100%), for multiple periods of 12 h with intermediate grinding, until no further changes were observed in X-ray powder diffraction patterns. $SrV_{1-x}Ti_xO_3$ samples were also prepared *via* arc-melting. Suitable stoichiometric ratios of SrO (prepared by heating $SrCO_3$ under vacuum at 1100 °C), V_2O_3 (99.7%), and TiO_2 were thoroughly mixed inside an argon filled glovebox, pressed into pellets and transferred to the arc-melt furnace without being exposed to air. The furnace was purged with argon and the pellets were melted a total of four times in an electrical discharge arc, on a water-cooled copper hearth, with each pellet being turned between heatings. Samples were allowed to cool for 15 minutes inside the furnace under flowing argon before immediately being transferred to an argon filled glovebox.

Reduction of $SrV_{1-x}Ti_xO_3$. Samples of $SrV_{1-x}Ti_xO_3$ were reacted with CaH_2 as described previously for the synthesis of $SrVO_2H$ from $SrVO_3$.[12] Powder samples of $SrV_{1-x}Ti_xO_3$ were ground together with 2 mole equivalents of CaH_2 in an argon-filled glove box and then sealed under vacuum in amorphous-silica ampoules. Samples were then heated at 610 °C for multiple 2 day periods (as described in the text below) with regrinding between heating periods. Reaction products were washed, under an inert atmosphere, with 4 x 100 ml of a 0.1 M solution of NH_4Cl in methanol, followed by 4 x 100 ml of clean methanol in order to remove unreacted CaH_2 and reaction by-products (CaO).

Characterization. X-ray powder diffraction data were collected from samples sealed under argon in gas-tight sample holders using a PANalytical X'Pert diffractometer incorporating an X'celerator position sensitive detector (monochromatic Cu $K_{\alpha 1}$ radiation). High-resolution synchrotron X-ray powder diffraction data were collected using instrument I11 at the Diamond Light Source Ltd. Diffraction patterns were collected using Si-calibrated X-rays with an approximate wavelength 0.825 Å, from samples sealed in 0.5mm diameter borosilicate glass capillaries. All samples were diluted with an equal volume of amorphous boron to limit absorption. Rietveld profile refinements were performed using the GSAS suite of programs.[22] Magnetization data were collected using a Quantum Design MPMS SQUID magnetometer. The μ^+SR experiments were carried out at the Swiss Muon Source, PSI, Switzerland. In a μ^+SR experiment, spin-polarized muons were implanted in the bulk of a material and the time-dependence of their polarization monitored by recording the angular distribution of the subsequent positron decay. Thermogravimetric measurements were performed by heating powder samples at a rate of 5 °C·min^{-1} under an oxygen atmosphere, using a Mettler-Toledo MX1 thermogravimetric microbalance. Manganometric titrations were performed by dissolving samples in 5M H_2SO_4 and then titrating the resulting solution against $KMnO_4$.

DFT calculations. All density functional calculations were performed using the VASP software package (VASP 5.3),[23] with the PBE density functional[24] and an effective Hubbard U (U_{eff}) of 2.0 eV on Ti and V centers was used to describe the effect of strong correlations. A plane-wave cutoff of 600 eV was imposed in all cases and the Brillouin zone was sampled on an 8 × 8 × 7 Γ-centered grid. In order to investigate different models of anion disorder in $SrTiO_2H$, we consider a $\sqrt{2} \times \sqrt{2} \times 2$ expansion of the primitive unit cell which contains four transition metal centers (Figure 6). All the configurations were modelled as G-type antiferromagnets.

Results

$SrVO_3$-$SrTiO_3$ solubility. X-ray powder diffraction data collected from $SrV_{1-x}Ti_xO_3$ (x = 0.05, 0.4, 0.5) samples prepared by the ceramic route (Figures 2 and S1) could be indexed on the basis of two primitive cubic phases with lattice parameters in close agreement to the reported parameters of $SrVO_3$ (3.840 Å)[21] and $SrTiO_3$ (3.905 Å)[25]. Thus 2-phase models based on the structures of $SrVO_3$ and $SrTiO_3$ were refined against the data to yield lattice parameters and phase fractions listed in Table 1 (top). The very close correspondence between the lattice parameters of the two phases with those of $SrVO_3$ and $SrTiO_3$, combined with correspondence between the fraction of phase 2 ($SrTiO_3$) and the Ti content of the original mixture, suggests that there is almost no solubility between $SrVO_3$ and $SrTiO_3$ under these 'ceramic' synthesis conditions.

X-ray powder diffraction data collected from $SrV_{1-x}Ti_xO_3$ samples prepared by the arc-melt route are shown in Figures 2 and S1. Two primitive cubic phases are again required to model the data, but the refined lattice parameters (listed in Table 1) do not correspond to either $SrVO_3$ or $SrTiO_3$. Moreover, unlike the phases generated by ceramic synthesis, the refined lattice parameters are dependent on sample composition. Finally, the fractions of the two phases do not correlate with the Ti content of the samples as closely as those from the ceramic route. This accumulated evidence indicates that while perfect, single-phased solid-solutions were not prepared *via* the arc-melt route, there is some solubility between $SrVO_3$ and $SrTiO_3$ under the arc-melt conditions and that the sample of nominal composition $SrV_{0.95}Ti_{0.05}O_3$ (*i.e.* that formed from 5% Ti content in the starting material) does contain some titanium dissolved in the majority phase. For the sake of simplicity, this majority phase will henceforth be referred to as

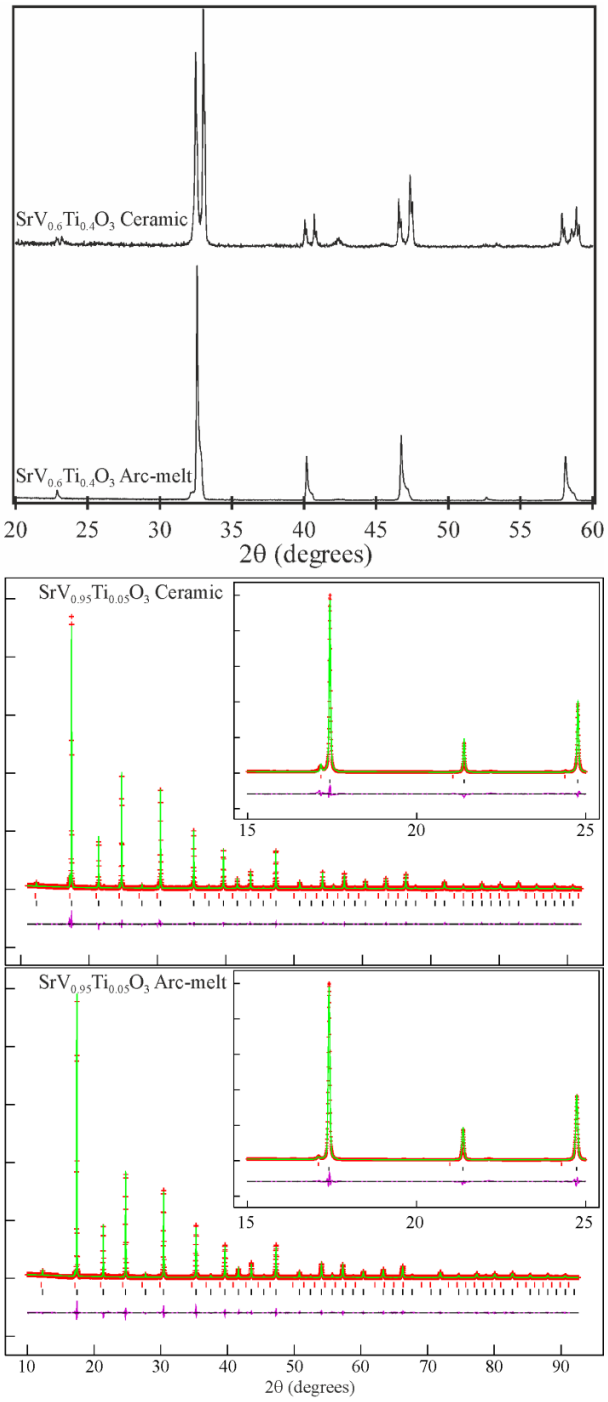


Figure 2. (top) X-ray powder diffraction data collected from samples of nominal composition $SrV_{0.6}Ti_{0.4}O_3$ prepared by ceramic and arc-melt routes. (bottom) Observed, calculated and difference plots from the 2-phase refinements against synchrotron X-ray powder diffraction data of samples of nominal composition $SrV_{0.95}Ti_{0.05}O_3$ prepared by ceramic and arc-melt routes.

'$SrV_{0.95}Ti_{0.05}O_3$', although the titanium content is lower than this formula indicates.

To investigate the stability of these $SrV_{1-x}Ti_xO_3$ solid-solutions, 2 aliquots of the arc-melt prepared $SrV_{0.95}Ti_{0.05}O_3$ sample were sealed in evacuated amorphous-silica ampoules and then heated,

Ceramic Samples				
	Phase 1		Phase 2	
Ti content (%)	*a* (Å)	fraction (%)	*a* (Å)	fraction (%)
5	3.8471(1)	95.5(3)	3.9063(1)	4.5(3)
40	3.8439(2)	57.2(5)	3.9041(2)	42.8(5)
50	3.8463(1)	48.3(4)	3.9035(1)	51.7(4)
Arc-melt Samples				
	Phase 1		Phase 2	
Ti content (%)	*a* (Å)	fraction (%)	*a* (Å)	fraction (%)
5	3.8513(1)	97.3(1)	3.9214(1)	2.7(1)
40	3.8610(1)	38.1(3)	3.8832(1)	61.9(3)
50	3.8742(1)	37.9(4)	3.8900(1)	62.1(4)
5 (annealed 600 °C)	3.8510(1)	97.2(1)	3.9210(1)	2.8(1)
5 (annealed 1100 °C)	3.8432(1)	94.7(2)	3.9020(1)	5.3(2)

Table 1. Lattice parameters and phase fractions from the structural refinement of $SrV_{1-x}Ti_xO_3$ samples prepared by ceramic and arc-melt routes.

one at 600 °C and the other at 1200 °C, for 7 days and then cooled at 2 °C·min^{-1} to ambient temperature. Refinement of the X-ray powder diffraction data from the annealed samples shows that the solid solution is stable at 600 °C but not at 1100°C, where it reverts to a mixture of $SrVO_3$ and $SrTiO_3$ (as indicated by the parameters in Table 1).

Topochemical reduction of '$SrV_{0.95}Ti_{0.05}O_3$'. Samples of '$SrV_{0.95}Ti_{0.05}O_3$' prepared *via* both ceramic and arc-melt routes were reacted with CaH_2 as described above. Figure 3 (top) shows a series of X-ray powder diffraction patterns collected from the products of reaction between the ceramic sample and CaH_2 as a function of reaction time. These data are consistent with the ceramic sample of $SrV_{0.95}Ti_{0.05}O_3$ being a simple mixture of $SrVO_3$ and $SrTiO_3$ which is transformed by the action of CaH_2 into a mixture of $SrVO_2H$ (marked in red) and a small amount of $SrTiO_{3-x}H_x$ (black), precisely as would be expected from previous studies of these perovskite phases in isolation.[12, 26] Synchrotron X-ray powder diffraction data collected from the washed reaction products after 10 days heating confirm these are the reaction products (Figure S2 and Table S1 in the Supporting Information). Thermogravimetric re-oxidation of this sample under flowing oxygen resulted in a 14.5% gain in mass (Figure S3), consistent with the composition detailed in Table S1 (full details of the experiment are described in the Supporting information).

Figure 3 also shows diffraction data collected from the products of reaction between arc-melt prepared $SrV_{0.95}Ti_{0.05}O_3$ and CaH_2. The diffraction pattern taken after 4 days heating looks very similar to the analogous data from the ceramic $SrV_{0.95}Ti_{0.05}O_3$ sample, containing a mixture of CaO, CaH_2, unreacted cubic $SrV_{0.95}Ti_{0.05}O_3$ along with a small amount of a new tetragonal phase which we formulate as '$SrV_{0.95}Ti_{0.05}O_2H$' (red). The *a* lattice parameter of this new phase is very similar to that of undoped $SrVO_2H$ (3.929(1) Å vs 3.92331(3) Å), but a distinct elongation along *c*, the V-H-V axis, is apparent (3.738(4) Å vs 3.6671(3) Å). After 8 days of heating, the peaks due to the tetragonal phase

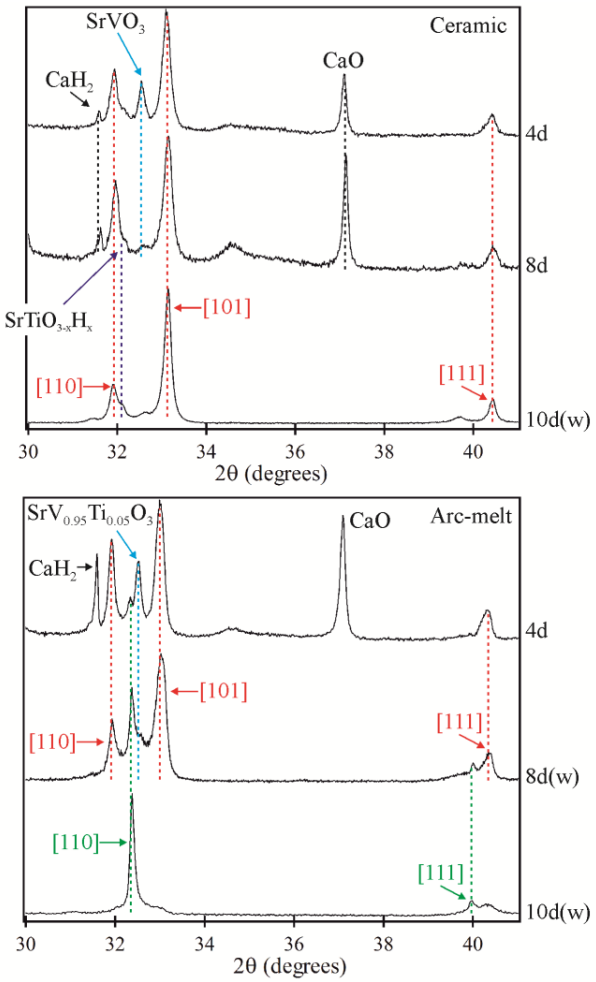


Figure 3. X-ray powder diffraction data collected during the reaction between CaH_2 and $SrV_{0.95}Ti_{0.05}O_3$ prepared by ceramic (top) and arc-melt (bottom) routes. Red symbols indicate positions and Miller indices of tetragonal 'Sr(V/Ti)O_2H' phases, green symbols indicate positions and Miller indices of cubic Sr(V/Ti)$O_{1.5}H_{1.5}$. Data sets marked with a (w) have been washed to remove CaH_2 and CaO.

reduce in intensity and are replaced by a new cubic phase (a = 3.888(1) Å) (green) which eventually becomes dominant after 10 days. Synchrotron X-ray powder diffraction data collected from a sample after 10 days of heating, washed to remove CaH_2 and CaO (Figure 4), can be fitted by a 3-phase model consisting of the dominant cubic phase ($SrV_{0.95}Ti_{0.05}O_xH_y$, 84.3(2)%), a tetragonal phase ($SrV_{0.95}Ti_{0.05}O_2H$, 9.7(4)%) and a minor vanadium metal impurity (5.6(4)%) (Table 2). Thermogravimetric re-oxidation of this sample under flowing oxygen resulted in a 17.2% gain in mass (Figure S4), consistent with a composition of $SrV_{0.95}Ti_{0.05}O_{1.5}H_y$ for the majority cubic phase, as described in detail in the Supporting information. Manganometric titrations indicate an average vanadium/titanium oxidation state of +2.12(3) for the sample (Table S2). When the presence of $SrV_{0.95}Ti_{0.05}O_2H$ and vanadium metal are taken into account, this indicates that the average vanadium/titanium oxidation state in $SrV_{0.95}Ti_{0.05}O_xH_y$ is +2.47(4), consistent with a composition for the majority cubic phase of $SrV_{0.95}Ti_{0.05}O_{1.5}H_{1.5}$ and indicating reduction substantially beyond the V^{3+} level.

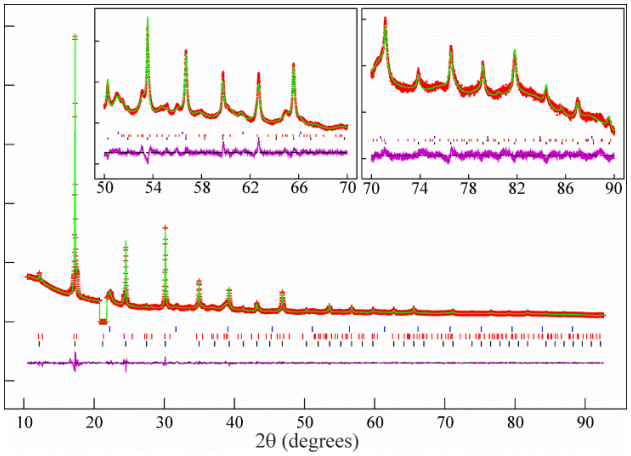


Figure 4. Observed calculated and difference plots from the refinement of $SrV_{0.95}Ti_{0.05}O_{1.5}H_{1.5}$ against synchrotron X-ray powder diffraction data. Lower tick marks indicate peak positions of the majority phase, middle tick marks $SrV_{0.95}Ti_{0.05}O_2H$, upper tick marks elemental vanadium. The excluded region removes a contribution from the 'amorphous' boron used to dilute the sample.

$SrV_{0.95}Ti_{0.05}O_{1.5}H_{1.5}$					
Atom	x	y	z	Fraction	U_{iso} (Å^2)
Sr	½	½	½	1	0.0038(2)
V/Ti	0	0	0	0.95/0.05	0.0024(1)
O/H	½	0	0	0.5/0.5	0.0017(2)
$SrV_{0.95}Ti_{0.05}O_{1.5}H_{1.5}$: space group *Pm*-3*m* (#221) Formula weight : 163.90 g mol^{-1}, Z = 1 Mass Fraction: 84.3(2) % a = 3.888(1) Å					
$SrV_{0.95}Ti_{0.05}O_2H$					
Atom	x	y	z	Fraction	U_{iso} (Å^2)
Sr	½	½	½	1	0.0042(3)
V/Ti	0	0	0	0.95/0.05	0.0021(2)
O	½	0	0	1	0.0019(3)
H	0	0	½	1	0.002†
$SrV_{0.95}Ti_{0.05}O_2H$: space group *P*4/*mmm* (#123) Formula weight : 170.40 g mol^{-1}, Z = 1 Mass Fraction: 9.7(4) % a = 3.929(1) Å, c = 3.738(4) Å					
Vanadium					
V: space group *Im*-3*m* (#229) Formula weight : 50.94 g mol^{-1}, Z = 2 Mass Fraction: 5.6(4) % a = 3.032(3) Å					
Radiation source: Synchrotron X-ray, λ = 0.82626(1) Temperature: 298 K χ^2 = 9.625; *wRp*= 3.43 %; *Rp* = 2.31 %.					

Table 2. Structural details from the 3-phase refinement of $SrV_{0.95}Ti_{0.05}O_{1.5}H_{1.5}$ against synchrotron X-ray powder diffraction data. †Thermal parameter of hydride is set at 0.002 Å^2.

Physical characterization of $SrV_{0.95}Ti_{0.05}O_{1.5}H_{1.5}$. Zero-field cooled and field cooled magnetization data collected from $SrV_{0.95}Ti_{0.05}O_{1.5}H_{1.5}$ in an applied field of 100 Oe (Figure 5) can be fitted to the Curie-Weiss law ($\chi = C/(T-\theta) + K$) to yield values of $C = 1.99(3) \times 10^{-2}$ cm^3 K mol^{-1}, $\theta = 2.27(7)$ K, $K = 8.5(1) \times 10^{-4}$ cm^3 K mol^{-1}. The parameters indicate that the majority of the observed magnetization is temperature independent, with the value of the Curie constant corresponding to 0.2% of that expected for S = 1, V^{3+} centers. μ^+SR data collected from $SrV_{0.95}Ti_{0.05}O_{1.5}H_{1.5}$ (Figure S5) show only a relaxation of the polarization and no precession signal that would be associated with long range magnetic order (data collected from the reduced ceramic sample do show oscillations which are due to the presence of magnetically ordered $SrVO_2H$, as expected from previous studies of this material).[12] This combination of physical data indicates that while no local paramagnetic moment can be observed for the vanadium centers, there is no indication of long range magnetic order in $SrV_{0.95}Ti_{0.05}O_{1.5}H_{1.5}$. Transport measurements performed on cold-pressed powder samples of $SrV_{0.95}Ti_{0.05}O_{1.5}H_{1.5}$ indicate that it is insulating.

Discussion

$SrVO_3$-$SrTiO_3$ solubility. The lack of solubility between $SrVO_3$ and $SrTiO_3$ under 'ceramic' conditions is surprising in light of previous reports in the literature describing the complete $SrV_{1-x}Ti_xO_3$ solid solution, studied both as powder and single crystal samples.[27-28] In the former study, powder samples were prepared at higher temperatures than employed under our 'ceramic' conditions (1500 °C, 10% H_2 in argon). However, when we attempted to replicate these high temperature conditions the samples prepared contained large quantities of $SrV_{10}O_{15}$, presumably due to Sr volatility, and so were unsuitable for topochemical reduction studies. In the arc-melting route used here, high temperatures (T > 2000 °C) are applied only for a brief time, and as a result reagent volatility is less of a problem. The increased $SrVO_3$-$SrTiO_3$ solubility observed in samples prepared by arc-melting, in combination with the previous high-temperature synthesis reports, suggests that the $SrV_{1-x}Ti_xO_3$ solid solution is only stable at high temperature, but can be partially quenched as a metastable phase by rapid cooling. This low-temperature meta-stability is confirmed by the observation that when annealed at 1100 °C, 'quenched' $SrV_{1-x}Ti_xO_3$ samples completely separate into simple mixtures of $SrVO_3$ and $SrTiO_3$. As noted above, the arc-melted $SrV_{1-x}Ti_xO_3$ solid solutions still exhibit a degree of phase separation. We attribute the multiphase nature of the arc-melted samples to the limited cooling rate which can be achieved in the arc furnace, which allows for a degree of phase separation on cooling. Despite this partial phase separation, it is clear that in the arc-melted $SrV_{0.95}Ti_{0.05}O_3$ sample, the majority cubic '$SrVO_3$' phase contains some dissolved titanium. Furthermore, annealing studies show that the $SrV_{0.95}Ti_{0.05}O_3$ solid solution is kinetically stable at 600 °C, so the topochemical reduction/anion exchange of $SrV_{1-x}Ti_xO_3$ phases can be studied.

Influence of doping on reaction products. The change in reactivity between $SrVO_3$ and CaH_2 on titanium doping is striking. Unsubstituted $SrVO_3$ reacts readily with CaH_2 to yield $SrVO_2H$, but attempts to advance this reaction further by raising the reaction temperature lead to non-topochemical reactions and, ultimately, to the formation of SrO and metallic vanadium. In contrast, the reaction between CaH_2 and the arc-melted sample of nominal composition $SrV_{0.95}Ti_{0.05}O_3$ proceeds all the way to cubic $SrV_{0.95}Ti_{0.05}O_{1.5}H_{1.5}$, with the direct analogue of $SrVO_2H$, tetragonal '$SrV_{0.95}Ti_{0.05}O_2H$', appearing only transiently as an intermediate phase. These very different reaction outcomes suggest that the presence of even small amounts of titanium dopant destabilizes $SrV_{0.95}Ti_{0.05}O_2H$ in some way, allowing it to react further. Whilst the different reactivity patterns have frustrated our initial goal of

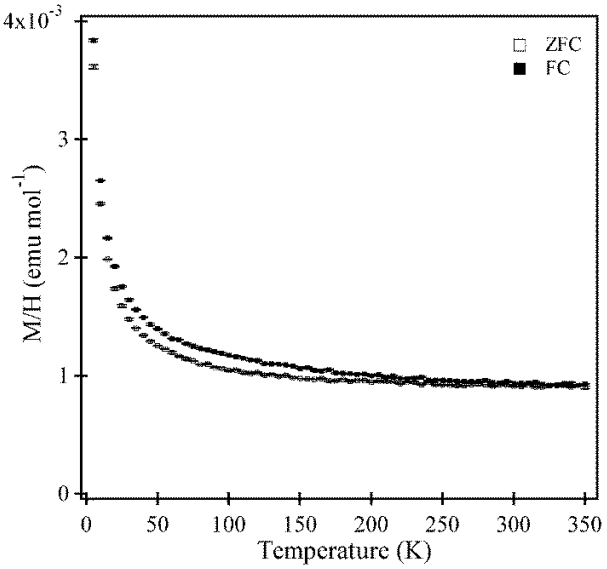


Figure 5. Zero-field cooled and field cooled magnetization data collected from $SrV_{0.95}Ti_{0.05}O_{1.5}H_{1.5}$ in an applied field of 100 Oe.

forming stable hole-doped analogues of $SrVO_2H$, they raise some important questions about the origin of stability in these mixed anion lattices. The lattice parameters of the '$SrV_{0.95}Ti_{0.05}O_2H$' intermediate phase offer some clues to the origin of its relative instability. We noted above that whilst the lattice parameter *a* is marginally shorter than that in unsubstituted $SrVO_2H$ (3.929(1) Å *vs* 3.9331(4) Å), *c* is significantly elongated (3.738(4) Å *vs* 3.6671(3) Å).[12] These changes are consistent with a degree of anion disorder in the Ti-containing phase, with small concentrations of oxide ions along *c* and hydride ions in the *ab* plane causing elongation and contraction, respectively. We note in this context that $SrCrO_2H$ adopts a cubic, anion-disordered structure quite different from that of $SrVO_2H$,[29] suggesting that the anion-ordered tetragonal phase is uniquely stable for a d^2 electronic configuration: deviations to either lower ($SrV_{0.95}Ti_{0.05}O_2H$, $d^{1.95}$) or higher ($SrCrO_2H$, d^3) electron counts appear to drive the system into alternative anion-disordered phases. The partial disordering of the anion lattice adds a large degree of strain to the framework because V-O-V connections are inserted into a lattice optimized for V-H-V links, and *vice versa*, which significantly destabilizes $SrV_{0.95}Ti_{0.05}O_2H$ with respect to anion-ordered $SrVO_2H$.

These observations are supported by a series of DFT calculations performed on the $\sqrt{2} \times \sqrt{2} \times 2$ expanded unit cells shown in Figure 6, each of which contains four transition metal centers. We have studied the two limiting stoichiometries, $SrVO_2H$ and $SrTiO_2H$, as well as $SrV_{0.75}Ti_{0.25}O_2H$, the closest model to the $SrV_{0.95}Ti_{0.05}O_2H$ phase that is accessible within a unit cell of these dimensions. In the *trans* unit cell, the anions are arranged in the same ordered array found in native $SrVO_2H$: *i.e.* with the two hydrides aligned mutually *trans* along the *c* direction. In the *cis* isomer, the hydrides are moved into the *ab* plane and, in the arrangement shown in Figure 6, they are eclipsed in successive *ab* planes. The alternative where the hydrides are staggered in successive planes is computed to be higher in energy in all cases, and is not considered further here. We acknowledge that the *cis* arrangement represents only one possible arrangement amongst the many that could contribute to the anion-disordered cubic phase, but nevertheless a comparison of the two unit cells allows us to assess the energetic cost of moving the hydrides around the lattice. In the case of $SrVO_2H$, the *trans* arrangement of hydride ligands proves to be substantially more stable than the *cis* alternative ($\Delta E = +0.26$ eV per formula unit), consistent with its

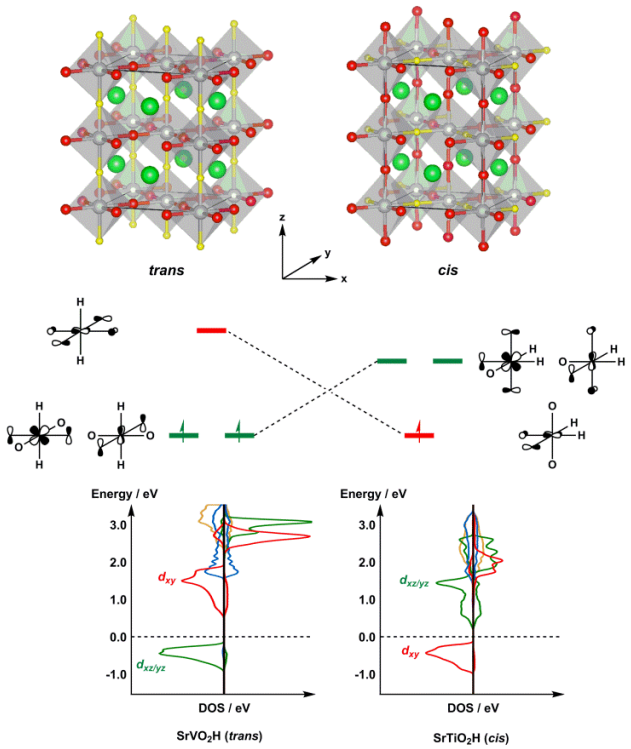


Figure 6. (top) *Trans* and *cis* unit cells used in the computational study. Sr, V, O and H are in dictated by green, grey, red and yellow spheres respectively. (bottom) The calculated density of states for *trans*-$SrVO_2H$ and *cis*-$SrTiO_2H$.

established preference for the tetragonal phase. In $SrTiO_2H$, in contrast, the order is reversed, with a strong preference for the *cis* arrangement over *trans* (ΔE = -0.21 eV). The mixed metal system $SrV_{0.75}Ti_{0.25}O_2H$ is intermediate between these two limits, with the *trans* structure being favored, but to a much lesser degree than in the all-vanadium analogue (ΔE = +0.09 eV). The calculations therefore indicate that the *trans* arrangement is optimal for the d^2 configuration of V^{3+}, and is progressively destabilized relative to its *cis* analogue as the concentration of Ti^{3+} is increased. We can analyze these differences in terms of two competing factors, the first of which is the strong *trans* influence of the hydride ligand which will in general disfavor mutually *trans* arrangements of hydride ligands. This effect is mediated by the σ framework, and stems from the fact that only a single metal d orbital can participate in both metal-hydride σ bonds when the ligands are *trans* to each other. Superimposed upon this are striking differences in the π character of the two ligands: a hydride is a pure σ donor while an oxide is also a strong π donor, and there is a strong driving force to accumulate oxide ligands in the same plane as vacant metal-based orbitals with dπ character. In the case of $SrVO_2H$, with a d^2 configuration at the metal, these two competing factors are diametrically opposed: the presence of a single vacant dπ orbital (d_{xy}) means that the O-V π bonding is optimal in the tetragonal phase, where all four oxides are aligned in a single plane, but this necessarily forces the two hydrides into a mutually *trans* arrangement. The observed preference for the tetragonal phase indicates that in this case the enhanced π donation from the oxides is the dominant factor. For a d^1 configuration, in contrast, the presence of two vacant dπ orbitals allows for effective O-Ti π bonding in either *cis* or *trans* arrangements, and the σ effects (the *trans* influence) then dominate, imposing a preference for the *cis* arrangement of hydrides. In the $SrV_{0.75}Ti_{0.25}O_2H$ system the

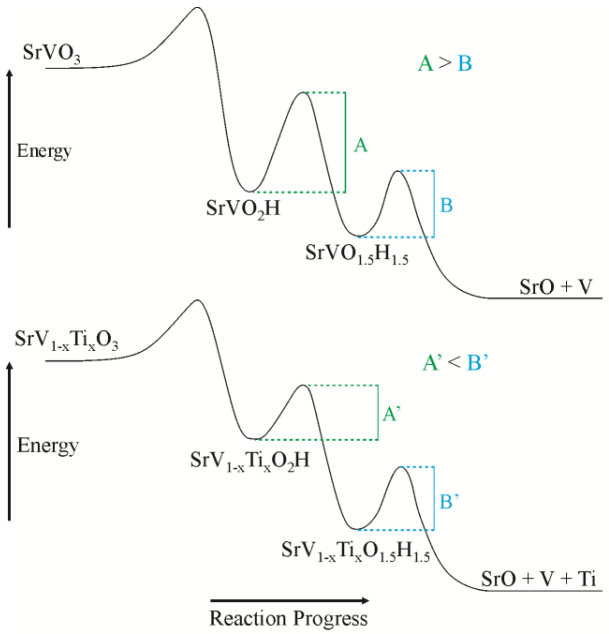


Figure 7. Schematic diagram showing the difference in activation energies for the reduction of $SrVO_3$ and $SrV_{1-x}Ti_xO_3$.

arrangement of anions necessarily represents a compromise because it is not possible to simultaneously satisfy the geometric preferences of V (*trans*) and Ti (*cis*) in a single lattice.

The tendency of increasing quantities of Ti in the lattice to reduce the stability of the tetragonal phase suggests that the presence of a stable, anion-ordered tetragonal phase is uniquely associated with a d^2 configuration. Moreover, the properties of the $SrV_{0.95}Ti_{0.05}O_2H$ phase indicate that even a relatively small depletion of the electron density in the dπ band is sufficient to tip the balance in favor of anion disorder. This provides a framework for understanding the different paths followed by the topochemical reactions of CaH_2 with $SrVO_3$ and $SrV_{1-x}Ti_xO_3$. Figure 7 shows schematic reaction-energy profiles for the two cases, where the key difference is that the tetragonal $SrVO_2H$ phase lies in a deeper well on the potential energy surface than the corresponding tetragonal phase for $SrV_{1-x}Ti_xO_2H$. This in turn raises the activation energy for the topochemical reaction that converts $SrVO_2H$ into $SrVO_{1.5}H_{1.5}$, allowing the former to be trapped as a stable species while $SrV_{1-x}Ti_xO_2H$ is only a transiently stable intermediate. Indeed, the absence of detectable amounts of $SrVO_{1.5}H_{1.5}$ indicates that the activation energy for the formation of this compound from $SrVO_2H$ is greater than that for its subsequent decomposition to SrO and metallic V. Even small amounts of titanium substitution significantly degrade the special stability of $SrVO_2H$, making the system more reactive and leading to the observed changes in reaction outcome.

Attempts to dope other phases prepared *via* topochemical reactions have revealed similar but less dramatic responses to cation substitution. For example, attempts to electron dope the Fe^{2+} phase $SrFeO_2$ *via* rare earth substitution for strontium reveal that $RE_xSr_{1-x}FeO_{3-\delta}$ is reduced to $RE_xSr_{1-x}FeO_{2+x/2}$, maintaining an oxidation state of Fe^{2+} in the reduced phase.[30] However, it should also be noted that the sensitivity to cation substitution observed for $SrVO_2H$ and $SrFeO_2$ is not universal in topochemical reduction reactions. For example the conversion of $La_{1-x}A_xMnO_3$ (A = Ba, Sr, Ca) perovskites to $La_{1-x}A_xMnO_{2.5}$ brownmillerite phases containing mixtures of $Mn^{2+/3+}$, is tolerant of a range of A-site compositions and can be readily achieved for $0.15 < x < 0.5$ for A = Sr and $0.22 < x < 0.5$ for A = Ca.[31]

Conclusions

Topochemical reduction of $SrVO_3$ yields the anion-ordered, tetragonal phase $SrVO_2H$. However the analogous reaction conditions applied to hole-doped $SrV_{0.95}Ti_{0.05}O_3$ yields cubic $SrV_{0.95}Ti_{0.05}O_{1.5}H_{1.5}$ not tetragonal $SrV_{0.95}Ti_{0.05}O_2H$. This product, $SrV_{0.95}Ti_{0.05}O_{1.5}H_{1.5}$ is an insulating mixed valent $V^{2+/3+}$ phase, suggesting that the O^{2-}/H^- disorder acts to localize the vanadium d-electrons. Magnetization and μ^+SR data show respectively that the vanadium centers exhibit no local magnetic moment and that there is no indication of (antiferro)magnetic order. This unusual combination of transport and magnetic properties leads us to suggest the system may adopt a network of V-V bonds, although further characterization will be required to rigorously demonstrate this.

Whilst the hole doping of $SrVO_3$ did not, ultimately, achieve the initially intended outcome of producing hole-doped analogues of $SrVO_2H$, the dramatic differences in reactivity in response to seemingly minor changes in composition have encouraged us to consider the factors that determine the outcome of reactions in the solid state. Under typical high-temperature synthetic conditions the products of a reaction are determined by thermodynamic stability and small compositional changes tend not to change the thermodynamic parameters to the extent that some other competing phase becomes more stable. As a result it is generally possible to make small compositional changes to solid phases to tune their physical and chemical behaviour – that is to say these phases are generally 'dopable'. In contrast the products of low-temperature topochemical reactions are selected under kinetic control – the product phase is the one which forms fastest, and is not necessarily the most thermodynamically stable. As a result the products of such reactions depend sensitively on the microscopic mechanism followed by a reaction. The change in reaction product from $SrVO_2H$ to $SrV_{1-x}Ti_xO_{1.5}H_{1.5}$ upon substituting ~5% of the vandium in $SrVO_3$ for titanium shows that even small changes in composition can dramatically alter the relative rates of the competing pathways which exist under low-temperature conditions. Given that this observed sensitivity of the reaction mechansim to chemical compostion is likely to be a general feature of topochemical reactions, we must conclude that a large number of the metastable phases prepared *via* topochemical reactions will, ultimately, prove not to be dopable.

ASSOCIATED CONTENT

Supporting Information

X-ray powder diffraction data from $SrV_{0.5}Ti_{0.5}O_3$ samples. Structural, compositional and μ^+SR characterization of 'reduced' ceramic $SrV_{0.95}Ti_{0.05}O_3$ and $SrV_{0.95}Ti_{0.05}O_{1.5}H_{1.5}$. Details of DFT calculations.

AUTHOR INFORMATION

Corresponding Author

michael.hayward@chem.ox.ac.uk

Author Contributions

The manuscript was written through contributions of all authors. The authors declare no competing financial interests.

ACKNOWLEDGMENT

MAP thanks CONACYT and the Balliol College, Oxford for a scholarship. Experiments at the Diamond Light Source were performed as part of the Block Allocation Group award "Oxford Solid State Chemistry BAG to probe composition-structure-property relationships in solids" (EE13284). Part of this work was carried out at the Swiss Muon Source (SμS), Paul Scherrer Institut, Villigen, Switzerland

REFERENCES

1. Hayward, M. A., Soft chemistry synthesis of oxides. In *Comprehensive Inorganic Chemistry II*, Reedijk, J.; Poeppelmeier, K. R., Eds. Elsevier: Oxford, 2013; Vol. 2, pp 417-453.
2. Schaak, R. E.; Mallouk, T. E., Perovskites by design: A toolbox of solid-state reactions. *Chem. Mater.* **2002,** *14*, 1455-1471.
3. Gopalakrishnan, J., Chimie douce approaches to the synthesis of metastable oxide materials. *Chem. Mater.* **1995,** *7*, 1265-1275.
4. Yamamoto, T.; Kageyama, H., Hydride reduction of transition metal oxides. *Chem. Lett.* **2013,** *42*, 946.
5. Tsujimoto, Y.; Tassel, C.; Hayashi, N.; Watanabe, T.; Kageyama, H.; Yoshimura, K.; Takano, M.; Ceretti, M.; Ritter, C.; Paulus, W., Infinite-layer iron oxide with a square-plannar coordination. *Nature* **2007,** *450*, 1062-1065.
6. Seddon, J.; Suard, E.; Hayward, M., Topotactic reduction of $YBaCo_2O_5$ and $LaBaCo_2O_5$: square-planar Co(I) in an extended oxide. *J. Am. Chem. Soc.* **2010,** *132*, 2802-2810.
7. Hayward, M. A.; Green, M. A.; Rosseinsky, M. J.; Sloan, J., Sodium hydride as a powerful reducing agent for topotactic oxide deintercalation: synthesis and characterisation of the nickel (I) oxide $LaNiO_2$. *J. Am. Chem. Soc.* **1999,** *121*, 8843-8854.
8. Denis Romero, F.; Burr, S. J.; McGrady, J. E.; Gianolio, D.; Cibin, G.; Hayward, M. A., $SrFe_{0.5}Ru_{0.5}O_2$: sqaure-planar Ru^{2+} in an extended oxide. *J. Am. Chem. Soc.* **2013,** *135*, 1838-1844.
9. Hayward, M. A.; Cussen, E. J.; Claridge, J. B.; Bieringer, M.; Rosseinsky, M. J.; Kiely, C. J.; Blundell, S. J.; Marshall, I. M.; Pratt, F. L., The hydride anion in an extended transition metal oxide array - $LaSrCoO_3H$. *Science* **2002,** *295*, 1882.
10. Helps, R.; Rees, N.; Hayward, M., $Sr_3Co_2O_{4.33}H_{0.84}$: An extended transition metal oxide-hydride. *Inorg. Chem.* **2010,** *49*, 11062-11068.
11. Kobayashi, Y.; Hernandez, O. J.; Sakaguchi, T.; Yajima, T.; Roisnel, T.; Tsujimoto, Y.; Morita, M.; Noda, Y.; Mogami, Y.; Kitada, A.; Ohkura, M.; Hosokawa, S.; Li, Z. F.; Hayashi, K.; Kusano, Y.; Kim, J. E.; Tsuji, N.; Fujiwara, A.; Matsushita, Y.; Yoshimura, K.; Takegoshi, K.; Inoue, M.; Takano, M.; Kageyama, H., An oxyhydride of $BaTiO_3$ exhibiting hydride exchange and electronic conductivity. *Nat. Mater.* **2012,** *11*, 507-511.
12. Denis Romero, F.; Leach, A.; Moller, J. S.; Foronda, F.; Blundell, S.; Hayward, M. A., Strontium vanadium oxide-hydrides: 'square-planar' two-electron phases. *Angew. Chem., Int. Ed.* **2014,** *53*, 7556-7559.
13. Goodenough, J. B., *Localized to itinerant electronic transition in perovskite oxides*. Springer-Verlag: Berlin, 2001.
14. Bednorz, J. G.; Muller, K. A., Possible high-Tc superconductivity in the Ba-La-Cu-O system. *Z. Phys. B* **1986,** *64*, 189-193.
15. MacChesney, J. B.; Williams, H. J.; Potter, J. F.; Sherwood, R. C., Magnetic study of manganate phases - $CaMnO_3$ $Ca4Mn_3O_{10}$ $Ca_3Mn_2O_7$ Ca_2MnO_4. *Phys. Rev.* **1967,** *164*, 779-&.
16. Matsumot.G, Study of $(La_{1-x}Ca_x)MnO_{3.1}$ magnetic strucutre of $LaMnO_3$. *J. Phys. Soc. Jpn.* **1970,** *29*, 606-&.
17. Schiffer, P.; Ramirez, A. P.; Bao, W.; Cheong, S. W., Low-temperature magnetoresistance and the magnetic phase-diagram of $La_{1-x}Ca_xMnO_3$. *Phys. Rev. Lett.* **1995,** *75*, 3336-3339.
18. Liu, K.; Hou, Y. S.; Gong, X. G.; Xiang, H. J., Orbital delocalization and enhancement of magnetic interactions in perovskite oxyhydrides. *Scientific Reports* **2016,** *6*.
19. Wei, Y. F.; Gui, H.; Li, X.; Zhao, Z. J.; Zhao, Y. H.; Xie, W. H., The effect of hydrogen ordering on the electronic and magnetic properties of the strontium vanadium oxyhydride. *J. Phys.:Condens. Matter* **2015,** *27*.
20. Yamamoto, T.; Zeng, D.; Kawakami, T.; Arcisauskaite, V.; Yata, K.; Patino, M. A.; Izumo, N.; McGrady, J. E.; Kageyama, H.; Hayward, M. A., The role of π-blocking hydride ligands in a pressure-induced insulator-to-metal phase transition in $SrVO_2H$. *Nature Communications* **2017,** *8*, 1217.
21. Rey, M. J.; Dehaudt, P.; Joubert, J. C.; Lambertandron, B.; Cyrot, M.; Cyrotlackmann, F., Preparation and structure of the compounds $SrVO_3$ and Sr_2VO_4. *J. Solid State Chem.* **1990,** *86*, 101-108.

22. Larson, A. C.; Von Dreele, R. B. *General Structure Analysis System*, Los Alamos National Laboratory Report LAUR 86-748: 2000.

23. Kresse, G.; Furthmuller, J., Efficient iterative schemes for ab initio total-energy calculations using a plane-wave basis set. *Phys. Rev. B* **1996,** *54*, 11169-11186.

24. Perdew, J. P.; Burke, K.; Wang, Y., Generalized gradient approximation for the exchange-correlation hole of a many-electron system. *Phys. Rev. B* **1996,** *54*, 16533-16539.

25. Schmidbauer, M.; Kwasniewski, A.; Schwarzkopf, J., High-precision absolute lattice parameter determination of $SrTiO_3$, $DyScO_3$ and $NdGaO_3$ single crystals. *Acta Crystallographica Section B-Structural Science Crystal Engineering and Materials* **2012,** *68*, 8-14.

26. Sakaguchi, T.; Kobayashi, Y.; Yajima, T.; Ohkura, M.; Tassel, C.; Takeiri, F.; Mitsuoka, S.; Ohkubo, H.; Yamamoto, T.; Kim, J. E.; Tsuji, N.; Fujihara, A.; Matsushita, Y.; Hester, J.; Avdeev, M.; Ohoyama, K.; Kageyama, H., Oxyhydrides of (Ca,Sr,Ba)TiO_3 perovskite solid solutions. *Inorg. Chem.* **2012,** *51*, 11371-11376.

27. Hong, K. Y.; Kim, S. H.; Heo, Y. J.; Kwon, Y. U., Metal-insulator transitions of $SrTi_{1-x}V_xO3$ solid solution system. *Solid State Comm.* **2002,** *123*, 305-310.

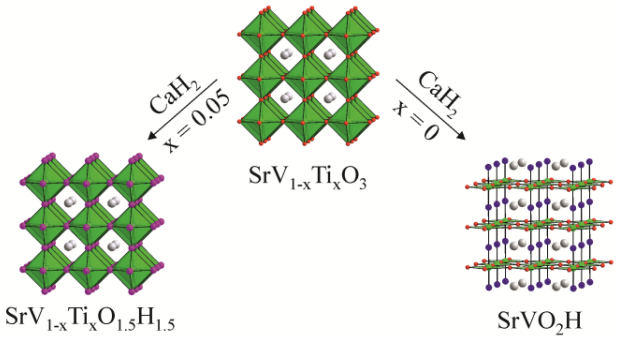
28. Tsuiki, H.; Kitazawa, K.; Fueki, K., The donor level of V^{4+} and the metal-nonmetal transtion in $SrTi_{1-x}V_xO_3$. *Japanese Journal of Applied Physics Part 1-Regular Papers Brief Communications & Review Papers* **1983,** *22*, 590-596.

29. Tassel, C.; Goto, Y.; Kuno, Y.; Hester, J.; Green, M.; Kobayashi, Y.; Kageyama, H., Direct synthesis of chromium perovskite oxyhydride with a high magnetic-transition temperature. *Angew. Chem., Int. Ed.* **2014,** *53*, 10377-10380.

30. Yamamoto, T.; Ohkubo, H.; Tassel, C.; Hayashi, N.; Kawasaki, S.; Okada, T.; Yagi, T.; Hester, J.; Avdeev, M.; Kobayashi, Y.; Kageyama, H., Impact of lanthanoid substitution on the structural and physical properties of an infinite-layer iron oxide. *Inorg. Chem.* **2016,** *55*, 12093-12099.

31. Parsons, T. G.; D'Hondt, H.; Hadermann, J.; Hayward, M. A., The synthesis and structural characterisation of of $La_{1-x}A_xMnO_{2.5}$ (A = Ba, Sr, Ca) phases – mapping the variants of the brownmillerite structure. . *Chem. Mater.* **2009,** *21*, 5527.

SYNOPSIS TOC Titanium substitution dramatically changes the outcome of the anion exchange of $SrVO_3$, yielding $SrV_{1-x}TiO_{1.5}H_{1.5}$, not $SrV_{1-x}TiO_2H$. This dramatic change in reactivity is attributed to an electronic destabilization of $SrVO_2H$ on titanium substitution. DFT calculations indicate that the presence of an anion-ordered, tetragonal $SrMO_2H$ phase is uniquely associated with a d^2 electron count, and that titanium substitution leads to an electronic destabilization of $SrV_{1-x}Ti_xO_2H$ phases which, ultimately, drives further reaction of $SrV_{1-x}Ti_xO_2H$ to $SrV_{1-x}Ti_xO_{1.5}H_{1.5}$.



A Coupled Electronic and Magnetic Phase Transition in the Infinite-Layer Phase $LaSrNiRuO_4$

Midori Amano Patino, Dihao Zeng, Ryan Bower, John E. McGrady, and Michael A. Hayward*

Department of Chemistry, University of Oxford, Inorganic Chemistry Laboratory, South Parks Road, Oxford, OX1 3QR, UK.

Supporting Information Placeholder

ABSTRACT: Topochemical reduction of the ordered double perovskite $LaSrNiRuO_6$ with CaH_2 yields $LaSrNiRuO_4$ – an extended oxide phase containing infinite sheets of apex-linked, square-planar $Ni^{1+}O_4$ and $Ru^{2+}O_4$ units ordered in a checkerboard arrangement. At room temperature the localized Ni^{1+} (d^9, S = ½) and Ru^{2+} (d^6, S = 1) centers behave paramagnetically. However on cooling below 250 K the system undergoes a cooperative phase transition in which the nickel spins align ferromagnetically, while the ruthenium cations appear to undergo a change in spin configuration to a diamagnetic spin state. Features of the low-temperature crystal structure suggest a symmetry lowering Jahn-Teller distortion could be responsible for the observed diamagnetism of the ruthenium centers.

Introduction

Transition metal oxides have been the subject of prolonged and intense study due to the wide variety of electronic properties they can exhibit. This complex behavior arises because unpaired electrons, originally located within the metal *d*-orbitals, can interact strongly with each other through a variety of coupling mechanisms (orbital, lattice, spin) to yield collective, correlated electronic states. As a result, the electronic structure of such systems is a strong function of the transition metal oxidation state (electron count), local structure (metal coordination geometry) and the long range lattice connectivity. Low-temperature topochemical synthesis routes offer many attractive opportunities to prepare novel extended oxide phases containing arrays of transition metal cations. In particular, they provide access to unusual oxidation states and/or local coordination environments which cannot be readily prepared via high-temperature 'ceramic' synthesis approaches.[1] For example, the reductive deintercalation of oxide ions from transition metal perovskite oxide phases has allowed the preparation of compounds containing Mn^{1+} centers $(La_{1-x}Ca_xMnO_2)$[2], square-planar Ni^{1+} ($LaNiO_2$), Co^{1+} ($LaBaCo_2O_{4.25}$) and Fe^{2+} centers $(SrFeO_2)$[3-5]. When combined with oxide-for-hydride anion exchange, similar protocols have generated V^{3+} ($SrVO_2H$) and Ti^{3+} centers $(BaTiO_{3-x}H_x)$.[6,7] In order to increase the chemical diversity of phases that can be prepared by this approach we have recently demonstrated that, when contained within a suitable stabilizing lattice, 4*d* transition metals such as ruthenium can be incorporated into topochemically reduced oxides. Thus the B-cation disordered perovskite $SrFe_{0.5}Ru_{0.5}O_3$ can be reduced to yield $SrFe_{0.5}Ru_{0.5}O_2$, the first reported example of Ru^{2+} in an extended oxide phase.[8] The disordered arrangement of Fe^{2+} and Ru^{2+} centers in $SrFe_{0.5}Ru_{0.5}O_2$ results in frustration of the magnetic couplings and spin glass behavior, preventing a detailed exploration of the interactions between the 3*d* and 4*d* electronic states. Here we describe the analogous reduction of the double perovskite $LaSrNiRuO_6$ in which the nickel and ruthenium cations adopt an ordered arrangement, allowing the electronic couplings between electron-rich 3*d* and 4*d* cations to be studied for the first time in an extended oxide phase.

Experimental

Synthesis of $LaSrNiRuO_6$. Samples of $LaSrNiRuO_6$ were prepared via a citrate gel method. Suitable stoichiometric ratios of La_2O_3 (99.999%), $SrCO_3$ (99.99%), Ni powder (99.996%), and RuO_2 (99.99% dried at 800°C) were dissolved in a minimum quantity of 6 M nitric acid. 3 mole equivalents of citric acid and 5 ml of analar ethylene glycol were added and the solution was heated with constant stirring. The gels thus formed were subsequently ground into a fine powder, placed in an alumina crucible and heated at 1 °C min^{-1} to 900 °C in air. The powders were then reground, pressed into 13 mm pellets and then heated at 1200ºC in air for 2 periods of 24 h. After the final heating period samples were rapidly quenched to room temperature. X-ray powder diffraction data collected from $LaSrNiRuO_6$ could be readily indexed using a monoclinic unit cell with lattice parameters a = 5.579(1) Å, b = 5.546(1) Å, c = 7.855(1) Å, β = 89.98(4) º in good agreement with literature values.[9]

Reduction of $LaSrNiRuO_6$. Samples of $LaSrNiRuO_{6-x}$ were prepared by reacting $LaSrNiRuO_6$ with 4 mole equivalents of CaH_2 at 360 ºC in a 'venting' apparatus described previously.[10] After reaction, calcium containing phases were removed from samples by washing with a 0.05 M solution of NH_4Cl in methanol and then a further 4 × 80 ml aliquots of clean methanol before being dried under vacuum.

Characterization. X-ray powder diffraction data were collected from samples contained in gas-tight sample holders using a PANalytical X'Pert diffractometer incorporating an X'celerator position sensitive detector (monochromatic Cu $K_{\alpha1}$ radiation). Neutron powder diffraction data were collected using the POLARIS instrument, at the ISIS neutron source, from samples contained within vanadium cans sealed under argon with indium washers. Rietveld profile refinements were performed using the GSAS suite of programs.[11] Magnetization data indicated that all the reduced samples contained small quantities of ferromagnetic elemental nickel, which masked the magnetic behavior of the bulk phases. The paramagnetic susceptibility and saturated ferromagnetic moment of samples were therefore measured using a 'ferromagnetic subtraction' technique described previously [12] and described fully in the Supporting Information. Thermogravimetric measurements were performed by heating powder samples at a rate of 5 ºC min^{-1} under a 10% H_2 in N_2 atmosphere, using a Mettler-Toledo MX1 thermogravimetric microbalance.

Calculations. All computations described above were performed using the VASP software package (VASP 5.3)[13], with the PBE density functional[14] and the PAW pseudopotentials.[15] A plane-wave cut off energy of 600 eV was used, along with a 9 × 9 × 9 Gamma-centred grid for sampling of the Brillouin zone. The effect of strong correlations is typically introduced through the effective Hubbard U (U_{eff}) value. In this work we have used U_{eff} = 6.0 eV for Ni and 3.0 eV for Ru unless stated otherwise. Geometry optimizations were performed with the unit cell volume constraint released and all ions are allowed to move freely.

Results and Discussion

Chemical and structural characterization of $LaSrNiRuO_4$. Reaction of the double perovskite, $LaSrNiRuO_6$, with CaH_2 at 360 ºC results in the formation of a new body-centred monoclinic phase (a = 5.652(3) Å, b = 5.652(3) Å, c = 6.9151(4) Å, γ = 90.54(1)º) shown to have a composition of $LaSrNiRuO_4$ by thermogravimetric analysis (SI, Figure S2). The unit cell of the reduced phase is closely related to that of $LaSrNiRuO_6$ but with a large contraction along the c-axis (6.9151(4) Å vs 7.855(1) Å), suggesting that $LaSrNiRuO_4$ adopts an infinite layer structure similar to those of $LaNiO_2$ and $SrFe_{0.5}Ru_{0.5}O_2$[3,5] whilst maintaining the Ni/Ru cation order of the $LaSrNiRuO_6$ parent phase. A crystallographic model of this type was constructed in space group *I112/m* and refined against neutron powder diffraction data collected from $LaSrNiRuO_4$ at 300 K. During the refinement all atomic positions were allowed to vary freely and all atoms were described using anisotropic displacement parameters. Close inspection of the data revealed contributions from elemental nickel (2.3 wt %) as well as La_2O_3 (0.3 wt %), so these were added to the model as secondary phases. The refinement converged readily to give a good statistical fit. Selected bond lengths and angles are summarized in Table 1 in the main text, with full details of the refined structure in Table S1. Figure 1 shows a representation of the refined structure of $LaSrNiRuO_4$ with plots of the observed and calculated diffraction data are shown in the Supporting information (Figure S3).

Figure 1 shows a representation of the structure of $LaSrNiRuO_4$, in which it can be seen that the ruthenium and nickel centers adopt square-planar local coordinations which share corners to form infinite sheets. As the Ni/Ru cation order of the parent $LaSrNiRuO_6$ phase is retained in the reduced product, the $Ni^{1+}O_4$ and $Ru^{2+}O_4$ squares adopt a checkerboard ordered arrangement, which, to the best of our knowledge, is the first example of a B-cation ordered infinite-layer oxide phase.

Comparison of the local coordination environments of the transition metals in $LaSrNiRuO_4$ with those in other infinite-layer oxide phases supports this assignment of the Ni^{1+} and Ru^{2+} oxidation states, although the Ni-O bond lengths (1.916(11) Å and 1.938(11) Å) are somewhat shorter than those in $LaNiO_2$ (1.979 Å)[3] suggesting that the $NiRuO_4$ plane is under significant compression. A direct comparison of the ruthenium coordination geometries in $LaSrNiRuO_4$ and $SrFe_{0.5}Ru_{0.5}O_2$ is complicated by the fact that the latter phase is B-cation disordered and thus the M-O bond lengths observed are an average of the Fe-O and Ru-O lengths. The average Fe/Ru-O length (1.998 Å)[8] is, however, almost identical to the average of the Ni-O and Ru-O lengths in $LaSrNiRuO_4$ (1.99 Å).

The stability of $LaSrNiRuO_4$ is remarkable in light of the fact that low temperature reduction of $SrRuO_3$ leads to decomposition and the formation of SrO and Ru, reflecting the very exoergic nature of the Ru^{2+}/Ru reduction couple (Ru^{2+}/Ru E° = +0.455 V).[16] The formation of $LaSrNiRuO_4$ via the reduction of $LaSrNiRuO_6$ demonstrates that, like the Sr-Fe-O lattice in $SrFe_{0.5}Ru_{0.5}O_2$[8] or the Na-La-Ti-O lattice in $Na_2La_2Ti_2RuO_8$,[17] the La-Sr-Ni-O lattice in $LaSrNiRuO_4$ is sufficiently robust to resist over-reduction/decomposition to metallic Ru along with Ni and the oxides La_2O_3 and SrO.

Cation	Anion	Bond length (Å)	
		300 K	5 K
Ni	O(1)	1.916(11) × 2	1.959(11)
	O(2)	1.938(11) × 2	1.950(11)
Ru	O(1)	2.041(12) × 2	2.023(12)
	O(2)	2.101(12) × 2	2.078(12)
		Bond angles (º)	
Ni-O(1)-Ru		176.5(3)	174.4(3)
Ni-O(2)-Ru		177.0(3)	176.3(3)

Table 1. Selected bond lengths and angles from the refined structures of $LaSrNiRuO_4$ at 300 K and 5K.

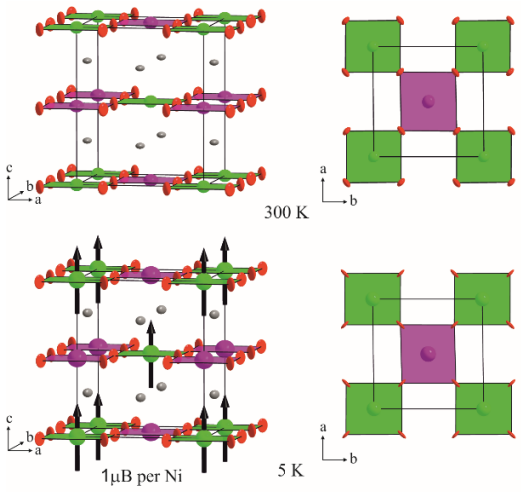


Figure 1. Representations of the crystal structure of LaSrNiRuO4 at 300 K and at 5 K. Grey, red, green and purple ellipsoids represent La3+/Sr2+, O2-, Ni1+ and Ru2+ positions respectively.

Magnetic Characterization of $LaSrNiRuO_4$. Magnetization data collected from $LaSrNiRuO_4$ using the "ferromagnetic subtraction" technique described in the SI, are shown in Figure 2. The paramagnetic susceptibility of $LaSrNiRuO_4$ can be fitted by the Curie-Weiss law ($\chi = C/(T-\theta)$) in the temperature range 250 < T/K < 300 to yield values of C = 1.395 cm^3 K mol^{-1} and θ = +192.7 K. The observed Curie constant is in good agreement with that expected for a combination of a d^9, S = ½ Ni^{1+} center and a d^6 Ru^{2+} centre with two unpaired electrons (S = 1), the latter having been observed previously in $SrFe_{0.5}Ru_{0.5}O_2$.[8]

On cooling below T ~ 250 K the paramagnetic susceptibility of $LaSrNiRuO_4$ goes through a local maximum before becoming essentially temperature independent below 150 K. This change is accompanied by a large increase in the saturated ferromagnetic moment of the sample (~1 μ_B in the low-temperature limit) consistent with a transition to a magnetically ordered state with a net spontaneous magnetic moment. Comparison of neutron powder diffraction data collected from $LaSrNiRuO_4$ at 300 K and 5 K reveals a subtle enhancement in the intensity of some of the diffraction peaks in the low temperature data set (Figure S4, Supporting Information), consistent with magnetic order at low temperature.

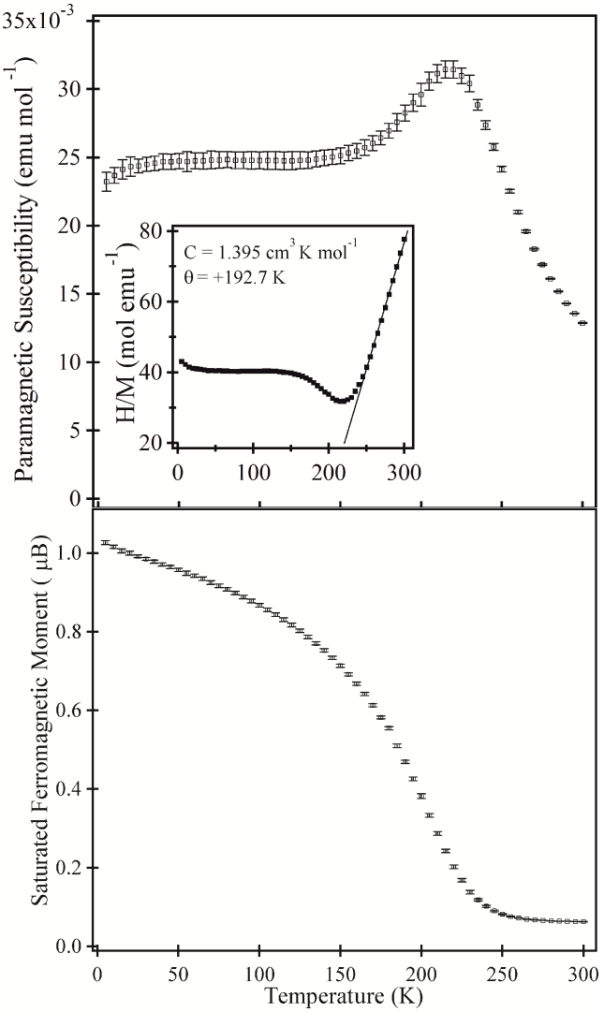


Figure 2. The paramagnetic susceptibility (top) and saturated ferromagnetic moment (bottom) of $LaSrNiRuO_4$ collected as a function of temperature. Inset in top panel shows fit to the Curie-Weiss law in the temperature range 250 < T/K < 300.

The magnetic scattering can be indexed using the body-centered crystallographic unit cell, implying that the ordered magnetic lattice is also body centered and therefore that all the nickel centers have the same ordered moment, as do all the ruthenium centers. Magnetic models were constructed on this basis, where the magnetic moments on the nickel and ruthenium centers were allowed to vary independently, and these where refined against the low-temperature diffraction data, in combination with the structural model developed above for the high-temperature diffraction data. The best fit to the data was achieved by aligning both the nickel and ruthenium moments parallel to the z-axis. Under this constraint the model refined to give a moment of 1.03(8) μ_B on the nickel site and 0.05(9) μ_B on the ruthenium site, with the two moments aligned parallel. The net moment of 1.08(17) μ_B is in good agreement with the saturated ferromagnetic moment of $LaSrNiRuO_4$ measured at 5 K.

An alternative ferrimagnetic structure in which a moment of 1 μ_B on the nickel centers is anti-aligned with 2 μ_B on the ruthenium sites would also yield a net moment of ~ 1 μ_B per formula unit, however this model gives a very poor fit to the data and rapidly converts to the ferromagnetic nickel model described above when the magnitude of the ordered moments is refined.

Other alternative models with antiferromagnetic couplings between Ni or Ru centers (either within the MO_2 planes and/or between metal centers in adjacent MO_2 planes) have magnetic scattering peaks which are not observed in the experimental data.

Full details of the crystal and magnetic structure of $LaSrNiRuO_4$ refined against the data collected at 5 K are given in Table S1 and Table S2 respectively, with selected bond lengths and angles given in Table 1 in the main text. Plots of the observed and calculated diffraction data are shown in Figure S4.

Electronic structure analysis. The magnetization and neutron diffraction data indicate that $LaSrNiRuO_4$ appears to exist in two different electronic states. At temperatures above T ~ 250 K, the data are consistent with a paramagnetic state with localized S = ½, Ni^{1+} and S = 1, Ru^{2+}, but on cooling the system appears to undergo a cooperative ordering transition leading to a ferromagnetic alignment of the nickel spins and a concomitant loss of spin moment at ruthenium. Some insight into this highly unusual phase transition can be gained by examining the low-temperature crystal structure of $LaSrNiRuO_4$. The first striking feature is that whilst the unit cell contracts parallel to the z-axis upon cooling, this is counteracted by an expansion in the xy-plane, leading to a larger unit cell volume at 5 K than 300 K (V = 220.97(17) $Å^3$ at 5 K *vs* 220.89(17) $Å^3$ at 300 K). The data in Table 1 confirm that the Ni-O and Ru-O bonds are longer and shorter, respectively, in the 5 K structure compared to the 300 K structure. This equalization of the Ni-O and Ru-O bond lengths upon cooling is commensurate with a change in the oxygen displacement parameters, shown in Figure 1. The displacement ellipsoids of the two crystallographically distinct oxide ions in the 300 K structure have their largest values perpendicular to the Ni-O-Ru bond vector – a feature which is consistent with the general observation that the lowest energy vibrational displacement is perpendicular to the bond vector. In contrast the largest displacement of the oxide ions in the 5 K structure is approximately parallel to the Ni-O-Ru bond vector. This behavior is inconsistent with a vibrational displacement and instead suggests a disordered static displacement of the oxide ions, consistent with the local lowering of symmetry.

A d^6 Ru^{2+} ion in a square-planar environment will inevitably be either orbitally degenerate or very nearly so, leading to Jahn-Teller instabilities. The observed changes to the Ru-O and Ni-O bond lengths at low temperature, and the appearance of static disorder in the Ni-Ru-O planes, are certainly consistent with a local lowering of symmetry associated with the low temperature electronic state of $LaSrNiRuO_4$. In order to explore the origins of the structural and magnetic features in more detail, we have performed a series of calculations on $LaSrNiRuO_4$ using density functional theory. We have explored a number of alignments of the spin moments on the two metals, and the ferromagnetic state

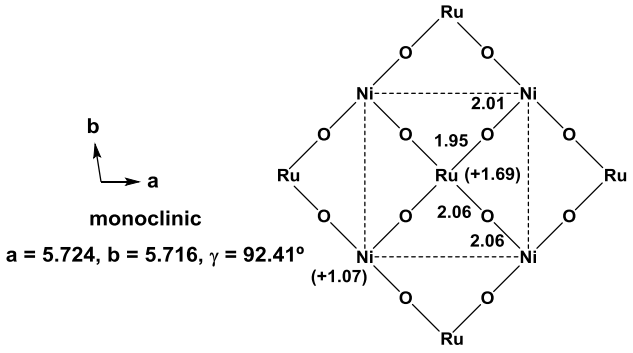


Figure 3. Optimised bond lengths and net spin densities (in brackets) for the monoclinic unit cell (dashed line).

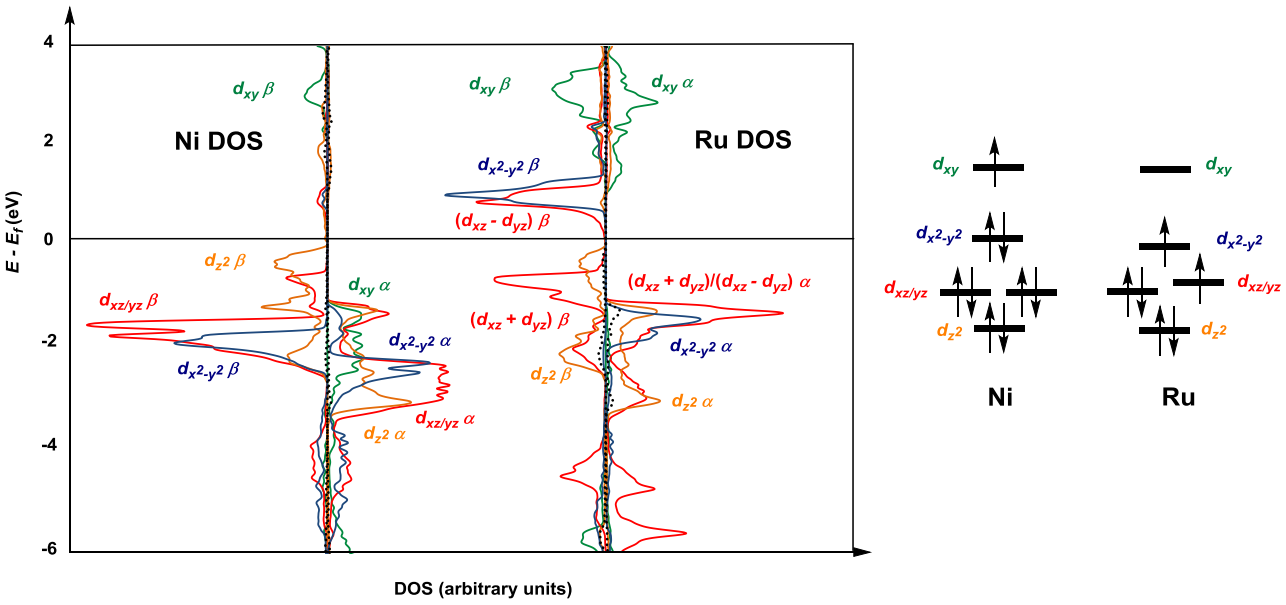


Figure 4 Spin-polarised projected density of states (Ni and Ru) for $LaSrNiRuO_4$ (U_{eff}(Ni) = 6.0 eV, U_{eff}(Ru) = 3.0 eV).

proves to be the most stable: spin densities of 1.07 and 1.69 on Ni and Ru, respectively, support the previous assignments of oxidation states as Ni^{1+} and Ru^{2+}.

The optimized lattice is monoclinic (Figure 3), with a = 5.724 Å, b = 5.716 Å and c = 6.881 Å, in good agreement with the available crystallographic data. The optimized angle, γ = 92.41°, is, however, somewhat larger than the experimental value of 90.69°, with the result that the degree of asymmetry in the Ni-O and Ru-O bond lengths is overestimated (Ni-O: 2.01/2.06 Å, Ru-O: 1.95/2.06 Å). The value of gamma, and hence the degree of asymmetry, is however strongly dependent on the chosen value of the Hubbard U parameter for Ru, with values of 5.0 eV and higher giving an almost perfectly tetragonal lattice. The shift towards more tetragonal structures is commensurate with an increase in the spin density at Ru (1.80 for U_{eff}*(Ru)* = 5.0 eV), which in turn suggests that the lower covalency of the Ru-O bond plays an important role in the magnitude of the distortion.

The density of states, projected onto the individual components of the d orbitals of both Ni and Ru is shown in Figure 4. For Ni, only the spin-□ component of the d_{xy} orbital lies above the Fermi level (note the axes are defined such that x and y bisect the O-M-O angles), while the d_{z^2} orbital is doubly occupied, giving a local configuration of $(d_{z^2})^2(d_{xz/yz})^4(d_{x^2-y^2})^2(d_{xy})^1$ and spin moment S = ½. In the Ru case, both components of the d_{xy} orbital lie above the Fermi level, as do the spin-β components of $d_{x^2-y^2}$ and one linear combination of $d_{xz/yz}$, giving a $(d_{z^2})^2(d_{xz/yz})^3(d_{x^2-y^2})^1(d_{xy})^0$ configuration. The double occupation of the d_{z^2} orbital in Ru was also observed to be a feature of the electronic structure of $SrFe_{0.5}Ru_{0.5}O_2$,[8] and indeed in many other low-valent oxides in square-planar or distorted square-planar environments ($Ca/SrFeO_2$, Sr_2FeRuO_4).[5,8,18,19] Canadell and co-workers have shown that it has its origins in strong s/d_{z^2} hybridization which allows the majority- and minority-spin components of the s/d_{z^2} orbital to differ spatially, reducing the repulsion between the formally paired electrons.[20] The significant Ru 5s character in the DOS (dashed black line) coincident with the prominent d_{z^2} features, confirms that similar hybridization is important in $LaSrNiRuO_4$.

The picture of the electronic structure summarized in Figure 4 is entirely consistent with the high-temperature data, in so much as the combination of a singly occupied d_{xy} orbital on Ni^{1+} and a vacant d_{xy} orbital on Ru^{2+} provides a ferromagnetic superexchange coupling pathway and the partial occupation of the $d_{xz/yz}$ manifold on Ru presents a clear driving force for the distortion from perfect tetragonal symmetry. The low-temperature data, and in particular the apparent absence of a paramagnetic moment at the ruthenium centre, is less easy to rationalise. The inclusion of spin-orbit coupling has only a very minor impact on the computed moment, consistent with earlier observations by Lee *et al*. on the double perovskite $SrCrRuO_6$.[21] A second possibility is that a more pronounced Jahn-Teller distortion would split the $d_{xz/yz}$ to an even greater degree and induce spin pairing at the Ru^{2+} centre ($(d_{z^2})^2(d_{xz}+d_{yz})^2(d_{x^2-y^2})^2(d_{xz}-d_{yz})^2$ $(d_{xy})^0$). We have tried to locate a stable minimum corresponding to such a state by initialising calculations from a range of highly distorted structures, but the system invariably returns to the monoclinic, moderately distorted structure with two unpaired electrons on Ru. Thus we find no evidence for this type of extreme Jahn-Teller distortion, although we note that an ordered arrangement of the local Jahn-Teller distortions of the Ru centres (analogous to the orbital order observed in $LaMnO_3$, for example)[22] could in principle stabilise a sufficiently large structural distortion to support a transition to a diamagnetic state. The average structure observed by diffraction provides no information on the presence or nature of such ordering, and it is intrinsically beyond the limits of the small model unit cell used in our calculations.

Conclusion

We report here the synthesis and characterisation of $LaSrNiRuO_4$, the first example of a B-cation ordered infinite layered oxide. The oxide layers support transition metal ions, Ni^{1+} and Ru^{2+} in remarkably low oxidation states, the thermodynamically favoured decomposition to elemental ruthenium and nickel being retarded by the integrity of the oxide lattice. Above 250 K the structure of $LaSrNiRuO_4$ is monoclinic and the metal ions behaving paramagnetically (weak ferromagnetic coupling), with local moments of S = 1 (Ru^{2+}) and S = ½ (Ni^{+}). These features are well reproduced by density functional theory, which predicts a triplet configuration at Ru with a Jahn-Teller distortion driven by an orbitally degenerate $(d_{z^2})^2(d_{xz/yz})^3(d_{x^2-y^2})^1(d_{xy})^0$ configuration. Below 250 K the magnetic susceptibility goes through a local maximum, indicative of the onset of ferromagnetic order,

with the saturated moment of 1 μB, observed at low temperature, localised entirely on the nickel centres, with the ruthenium ions becoming diamagnetic. An extreme Jahn-Teller distortion offers one potential explanation for this observation, although we have been unable to locate such a structure computationally.

ASSOCIATED CONTENT

Supporting Information

Description of the procedure used to measure magnetization data. Thermogravimetric data from the reduction of $LaSrNiRuO_4$. Full structural details and plots of the data from the nuclear and magnetic refinements of $LaSrNiRuO_4$ against neutron powder diffraction data. Details of the computational methodology used.

AUTHOR INFORMATION

Corresponding Author

michael.hayward@chem.ox.ac.uk

Author Contributions

The manuscript was written through contributions of all authors.

ACKNOWLEDGMENT

We thank R. Smith for assistance collecting the neutron diffraction data. Experiments at the ISIS pulsed neutron facility were supported by a beam time allocation from the STFC. MAP thanks CONACYT and the Balliol College, Oxford for a scholarship.

REFERENCES

(1) Hayward, M. A. In *Comprehensive Inorganic Chemistry II*; Reedijk, J., Poeppelmeier, K. R., Eds.; Elsevier: Oxford, 2013; Vol. 2, p 417.

(2) Dixon, E.; Hadermann, J.; Ramos, S.; Goodwin, A. L.; Hayward, M. A. *J. Am. Chem. Soc.* **2011**, *133*, 18397.

(3) Hayward, M. A.; Green, M. A.; Rosseinsky, M. J.; Sloan, J. *J. Am. Chem. Soc.* **1999**, *121*, 8843.

(4) Seddon, J.; Suard, E.; Hayward, M. A. *J. Am. Chem. Soc.* **2010**, *132*, 2802.

(5) Tsujimoto, Y.; Tassel, C.; Hayashi, N.; Watanabe, T.; Kageyama, H.; Yoshimura, K.; Takano, M.; Ceretti, M.; Ritter, C.; Paulus, W. *Nature* **2007**, *450*, 1062.

(6) Denis Romero, F.; Leach, A.; Moller, J. S.; Foronda, F.; Blundell, S.; Hayward, M. A. *Angew. Chem., Int. Ed.* **2014**, *53*, 7556.

(7) Kobayashi, Y.; Hernandez, O. J.; Sakaguchi, T.; Yajima, T.; Roisnel, T.; Tsujimoto, Y.; Morita, M.; Noda, Y.; Mogami, Y.; Kitada, A.; Ohkura, M.; Hosokawa, S.; Li, Z. F.; Hayashi, K.; Kusano, Y.; Kim, J. E.; Tsuji, N.; Fujiwara, A.; Matsushita, Y.; Yoshimura, K.; Takegoshi, K.; Inoue, M.; Takano, M.; Kageyama, H. *Nat. Mater.* **2012**, *11*, 507.

(8) Denis Romero, F.; Burr, S. J.; McGrady, J. E.; Gianolio, D.; Cibin, G.; Hayward, M. A. *J. Am. Chem. Soc.* **2013**, *135*, 1838.

(9) Gateshki, M.; Igartua, J. M. *Mater. Res. Bull.* **2003**, *38*, 1893.

(10) O'Malley, M.; Lockett, M. A.; Hayward, M. A. *J. Solid State Chem.* **2007**, *180*, 2851.

(11) Larson, A. C.; Von Dreele, R. B.; Los Alamos National Laboratory Report LAUR 86-748: 2000.

(12) Hayward, M. A.; Rosseinsky, M. J. *Chem. Mater.* **2000**, *12*, 2182.

(13) Kresse, G.; Furthmuller, J. *Phys. Rev. B* **1996**, *54*, 11169.

(14) Perdew, J. P.; Burke, K.; Ernzerhof, M. *Phys. Rev. Lett.* **1996**, *77*, 3865.

(15) Perdew, J. P.; Ruzsinszky, A.; Csonka, G. I.; Vydrov, O. A.; Scuseria, G. E.; Constantin, L. A.; Zhou, X. L.; Burke, K. *Phys. Rev. Lett.* **2008**, *100*.

(16) Greenwood, N. N.; Earnshaw, A. *Chemistry of the Elements*; Pergamon Press: Oxford, 1997.

(17) Pratt, J. A.; Shepherd, A. M.; Hayward, M. A. *Inorg. Chem.* **2015**, *54*, 10993.

(18) Tassel, C.; Pruneda, J. M.; Hayashi, N.; Watanabe, T.; Kitada, A.; Tsujimoto, Y.; Kageyama, H.; Yoshimura, K.; Takano, M.; Nishi, M.; Ohoyama, K.; Mizumaki, M.; Kawamura, N.; Iniguez, J.; Canadell, E. *J. Am. Chem. Soc.* **2009**, *131*, 221.

(19) Wen, X. D.; Cahill, T. J.; Gerovac, N. M.; Bucknum, M. J.; Hoffmann, R. *Inorg. Chem.* **2010**, *49*, 249.

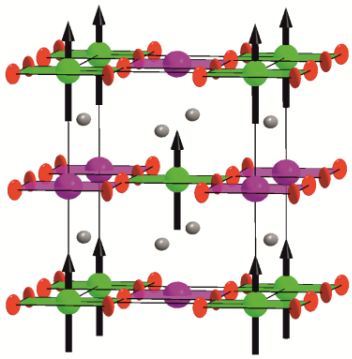
(20) Pruneda, J. M.; Iniguez, J.; Canadell, E.; Kageyama, H.; Takano, M. *Phys. Rev. B* **2008**, *78*.

(21) Lee, K. W.; Pickett, W. E. *Phys. Rev. B* **2008**, *77*.

(22) Rodriguez-Carvajal, J.; Hennion, M.; Moussa, F.; Moudden, A. H.; Pinsard, L.; Revcolevschi, A. *Phys. Rev. B* **1998**, *57*, R3189.

.

SYNOPSIS TOC (Word Style “SN_Synopsis_TOC”). If you are submitting your paper to a journal that requires a synopsis graphic and/or synopsis paragraph, see the Instructions for Authors on the journal’s homepage for a description of what needs to be provided and for the size requirements of the artwork.



$LaSr_3NiRuO_4H_4$: a 4d transition-metal oxide-hydride containing metal hydride sheets.

Lun Jin, Michael Lane, Dihao Zeng, Franziska K. K. Kirschner, Franz Lang, Pascal Manuel, Stephen J. Blundell, John E. McGrady and Michael A. Hayward*

Abstract: We report the synthesis of the first 4d transition metal oxide-hydride, $LaSr_3NiRuO_4H_4$, prepared *via* topochemical anion exchange. Neutron diffraction data show that the hydride ions occupy the equatorial anion sites in the host lattice and as a result the Ru and Ni cations are located in a plane containing only hydride ligands – a unique structural feature with obvious parallels to the CuO_2 sheets present in the superconducting cuprates. DFT calculations confirm the presence of S = ½ Ni^{1+} and S = 0, Ru^{2+} centres, but neutron diffraction and μSR data show no evidence for long-range magnetic order between the Ni centres down to 1.8 K. The observed weak inter-cation magnetic coupling can be attributed to poor overlap between Ni $3d_{z^2}$ and H 1*s* in the super-exchange pathways.

Complex transition metal oxides continue to be the subject of extensive study because they exhibit a wide variety of interesting physical and chemical properties. These range from magnetoresistance, high-temperature superconductivity and collective magnetism to ferroelectricity, ionic conductivity and unusual catalytic and photocatalytic behavior.[1] Typically the properties of complex oxides are tuned *via* cation substitutions, but modifications to the anion lattice, either by the introduction of anion vacancies or by substituting non-oxide hetero-anions, can also be used to modify the chemical and physical behavior of oxides. For example, 'anion doping' allows metal oxidation states to be adjusted, the on-site electronic configuration of transition metal centers to be modified (through ligand-field interactions) and inter-cation couplings to be tuned (though cation-anion-cation linkages), providing access to novel electronic states.

The contrasting features of oxide (O^{2-}) and hydride (H^-) anions offer many attractive opportunities to modify the electronic properties of 'host' oxide phases by anion substitution. The most obvious difference between oxide and hydride ions is their charge, as a result of which, hydride-for-oxide substitution necessarily involves reduction, allowing access to unusually low transition-metal oxidation states. The conversion of insulating $A^{II}TiO_3$ oxides into metallic $A^{II}TiO_{3-x}H_y$ oxide-hydrides is a classic example of the use of hydride-for-oxide substitution to modify materials properties.[2] The lower electronegativity of hydride compared to oxide also implies a higher degree of covalency and orbital mixing in M-H bonds compared to M-O analogues, and as a result the band structures of oxide-hydrides will be qualitatively different from their parent oxides. In addition, magnetic coupling strengths can be strongly enhanced in oxide-hydride phases, resulting in the high magnetic ordering temperatures observed for $LaSrCoO_3H_{0.7}$, $SrVO_2H$ and $SrCrO_2H$.[3] A final, more subtle difference between oxide and hydride ions is the absence of π-symmetry valence orbitals on the H^- anion. The 'orbital connectivity' of a phase can therefore be altered dramatically, especially if the oxide and hydride anions adopt an ordered arrangement. For example, the anion-ordered oxide-hydride $SrVO_2H$, where the hydride ions form V-H-V chains along the *z*-axis, is an antiferromagnetic insulator at ambient pressure, but undergoes a metal-to-insulator transition when pressurized to ~50 GPa.[4] The resulting metallic state exhibits significant 2-dimensional character because the hydride ions limit dispersion of the π-symmetry bands, which span the Fermi level, along the *z*-axis.

Despite their many attractive features, only a handful of transition-metal oxide-hydride phases have been prepared to date. The few reported systems can be separated into different groups on the basis of the mechanism by which the metastable oxide-hydride phase is stabilized with respect to decomposition to the elemental transition metal and water (AMO_xH_y => AO + M + H_2O), the thermodynamic sink in all cases. Early transition metal oxide-hydrides such as those containing titanium ($ATiO_xH_y$)[5] vanadium ($Sr_{n+1}V_nO_{3n-1}H_n$)[3b] and chromium ($SrCrO_2H$)[3c] can be thought of as ionically stabilized – these transition metals resist reduction due to their low electronegativities, and their high formal charges help to stabilize the H^- anion through columbic interactions. In contrast 'late' transition metals such as cobalt (as in $LaSrCo_3H_{0.7}$, $Sr_3Co_2O_{4.33}H_{0.84}$)[3a, 6] stabilize the oxide-hydride phases through strong Co_{3d}-H_{1s}-O_{2p} covalent interactions.[7] This covalent stabilization of cobalt oxide-hydrides has direct parallels to the strong σ-bonds observed in molecular hydride systems of late 4d and 5d transition metals such as Ru, Rh and Ir, suggesting that it should be possible to prepare covalently stabilized oxide-hydride phases based on the same metals. Following this logic, we have chosen to explore the reduction/anion-exchange chemistry of a number of complex oxides containing 4d transition metal cations using CaH_2 as a reductant and source of hydride ions. We have noted in previous work, however, that 4d transition-metal oxide perovskite and Ruddlesden-Popper phases tend to decompose to yield elemental metals on reaction with CaH_2 unless they are stabilized by the presence of a 3d transition metal ion.[8] For example, reaction of $SrRuO_3$ with CaH_2 yields SrO and Ru but $SrFe_{0.5}Ru_{0.5}O_3$ and $LaSrNiRuO_6$

[*] Miss L. Jin, Mr. M. Lane, Mr. D. Zeng, Professor J. E. McGrady, Professor M. A. Hayward.
Department of Chemistry, Inorganic Chemistry Laboratory, University of Oxford, South Parks Road, OX1 3QR, UK.
E-mail: michael.hayward@chem.ox.ac.uk
Ms F. K. K. Kirschner, Dr. F. Lang, Professor S. J. Blundell
Department of Physics, Clarendon Laboratory, University of Oxford, Parks Road, OX1 3PU, UK.
Dr. P. Manuel
ISIS Facility, Rutherford Appleton Laboratory, Chilton, Oxon OX11 0QX, UK.

[**] Experiments at the Diamond Light Source were performed as part of the Block Allocation Group award "Oxford Solid State Chemistry BAG to probe composition-structure-property relationships in solids" (EE13284). Experiments at the ISIS pulsed neutron facility were supported by a beam time allocation from the STFC. Part of this work was performed at the Swiss Muon Source

Supporting information for this article is given via a link at the end of the document.

ANUSCRIPT

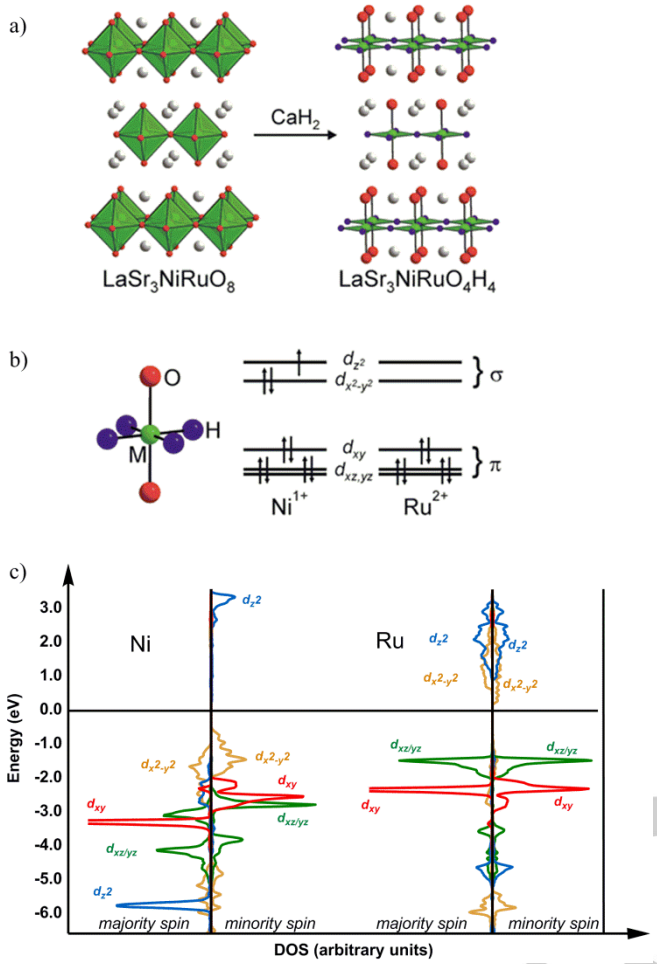


Figure 1. Crystal structure and transition-metal electronic configurations of $LaSr_3NiRuO_4H_4$ a) The Ruddlesden-Popper phase $LaSr_3NiRuO_8$ is transformed topochemically into the oxide-hydride $LaSrNiRuO_4H_4$ by the action of CaH_2 at 450 ºC. La/Sr, Ni/Ru, O and H are represented as grey, green, red and blue spheres respectively. b) The O_2H_4 coordination of Ni^{1+} and Ru^{2+} results in S = ½ and S = 0 spin states respectively. c) Spin-polarised projected density of states (Ni and Ru) for $LaSr_3NiRuO_4H_4$ (U_{eff}(Ni) = 3.0 eV, U_{eff}(Ru) = 1.0 eV). The Ni^{1+} ions are coupled ferromagnetically within the $NiRuH_2$ layers, but coupling between adjacent layers is antiferromagnetic. Majority- and minority-spin components are shown to left and right of the vertical axes, respectively. Complete DOS plots, including contributions from the oxide and hydride ligands are shown in supporting information, Figure S8)

yield $SrFe_{0.5}Ru_{0.5}O_2$ and $LaSrNiRuO_4$ respectively.[8a, 9] We have therefore focused our investigations on the anion exchange chemistry of the 3d/4d Ruddlesden-Popper oxide $LaSr_3NiRuO_8$ in which the combination of late-3d (Ni) and 4d (Ru) transition metal ions should both help to covalently stabilize any oxide-hydride phase formed.

Reaction between the Ruddlesden-Popper phase $LaSr_3NiRuO_8$ and CaH_2 proceeds initially via the topochemical deintercalation of oxide ions. Reaction at 400 ºC leads to the formation of the orthorhombic phase $LaSr_3NiRuO_7$ (a = 3.907 Å, b = 3.789 Å, c = 12.689 Å), which is then converted into $LaSr_3NiRuO_6$ (a = 3.853 Å, b = 3.593 Å, c = 13.011 Å) when the temperature is raised to 425 ºC, with CaO and H_2 being the other reaction products. On raising the temperature to 450 ºC, however, an anion exchange reaction occurs which converts orthorhombic $LaSr_3NiRuO_6$ into tetragonal $LaSr_3NiRuO_4H_4$ (a = 3.6226 Å, c = 13.317 Å) while CaH_2 is converted into CaO. Neutron powder diffraction data reveal that the net result of the conversion of $LaSr_3NiRuO_8$ into $LaSr_3NiRuO_4H_4$ is to exchange the 'equatorial' oxide ions in the former phase for hydride ions, as shown in Figure 1 (Full details of the structural refinement of $LaSr_3NiRuO_4H_4$ are given in the Supporting Information). The –(La/Sr)O–(Ni/Ru)O_2–(La/Sr)O– stacking sequence of the parent oxide is converted to a –(La/Sr)O–(Ni/Ru)H_2–(La/Sr)O– sequence in the oxide-hydride, with the Ru and Ni cations located in a plane containing only hydride ligands. The coordination spheres of the corner-linked square-planar MH_4 units in this plane are completed by two axial oxide ions that link the planes to the neighboring (La/Sr)O layers. To the best of our knowledge $LaSr_3NiRuO_4H_4$ is the first reported example of an oxide-hydride phase containing a 4d transition metal, and the 1:1 ratio of hydride to oxide is the highest yet reported. Moreover, the ordering of the anions generates a unique structural motif wherein the MH_2 planes containing the transition metals are completely devoid of oxide ions, with obvious parallels to the CuO_2 sheets present in the superconducting cuprates.

Magnetization data collected from $LaSr_3NiRuO_4H_4$ are consistent with the presence of a small amount (~ 2 mole %) of elemental nickel in the sample, although this could not be observed in diffraction data. As a result magnetization data were collected using a 'ferromagnetic subtraction' technique, described in the Supporting Information, which utilizes the fact that the magnetization of elemental nickel saturates in applied fields greater that 2T. Figure 2 shows a plot of the paramagnetic susceptibility of $LaSr_3NiRuO_4H_4$ as a function of temperature. These data can be fitted to the Curie-Weiss law ($\chi = C/(T-\theta)$) in the temperature range 10 < T/K < 300 to yield a Curie constant of 0.374(2) cm^3 K mol^{-1} consistent with a Ni^{1+} S = ½, Ru^{2+} S = 0 electronic configuration as shown in Figure 1. A complementary electronic structure investigation using density functional theory confirmed this simple picture. The density of states, projected onto the individual angular momentum components of the Ni and Ru d orbitals (Figure 1c), shows only the minority-spin component of Ni d_{z^2} above the Fermi level: the bands formed by the other 9 spin orbitals are occupied. The strong splitting of the majority- and minority-spin components of the Ni bands is consistent with the presence of a single unpaired electron on the Ni^+ centers (0.91 μ_B). The Ru centers, in contrast, are diamagnetic, with both the minority- and majority-spin components of $d_{xz/yz}$ and d_{xy} occupied in a typical low-spin t_{2g}^6 (Ru^{2+}) arrangement.

The paramagnetic susceptibility of $LaSr_3NiRuO_4H_4$ goes through a maximum at 10 K and this is accompanied by an increase in the saturated ferromagnetic moment of the sample (Figure 2). These data in combination suggest the onset of magnetic order. However, neutron powder diffraction data collected from $LaSr_3NiRuO_4H_4$ at 2 K show no additional diffraction features that would support the presence of a long-range magnetic ordered state, although we note that the relatively small size of the Ni moment (S = ½) could account for our failure to observe magnetic diffraction features in low-temperature neutron diffraction data. We have therefore collected μ^+SR data as an

independent probe of local magnetic order: μ⁺SR data collected from $LaSr_3NiRuO_4H_4$ are shown in Figure 3 and show no

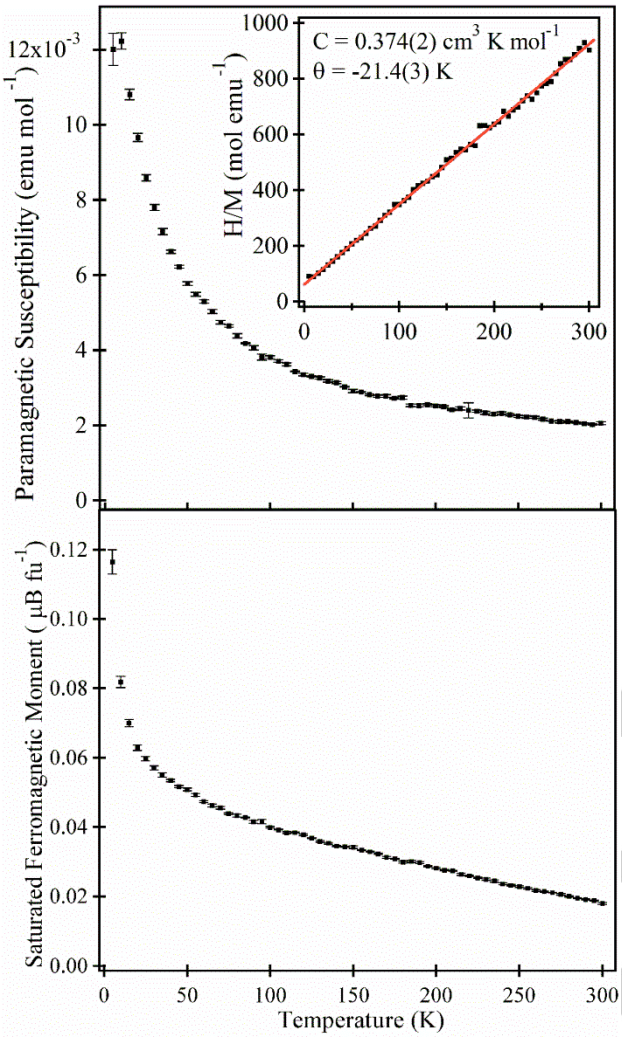


Figure 2. The paramagnetic susceptibility (top) and saturated ferromagnetic moment (bottom) of $LaSr_3NiRuO_4H_4$ collected as a function of temperature. The inset in the top panel shows the fit to the Curie-Weiss law in the temperature range 10 < T/K < 300.

evidence for magnetic order down to a temperature of 1.8 K, in agreement with the neutron powder diffraction data. The muon polarization simply relaxes with a rate which increases as the sample is cooled, consistent with fluctuations that slow down on cooling, but not to the point where long range order is obtained. This suggests that if $LaSr_3NiRuO_4H_4$ does adopt an antiferromagnetic ground state, the ordering temperature is extremely low. The apparent weakness of the magnetic coupling is consistent with orientation of the magnetic orbital, Ni^{1+} d_{z^2}, which overlaps only very weakly with the 1s orbitals of the hydride ligands *via* the torus. The complete density of states plot shown in Figure S8 confirms the absence of significant H 1s character in the same energetic window as Ni^{1+} d_{z^2}.

In conclusion, we have reported the synthesis of an anion-ordered mixed oxide/hydride phase, where the transition metals, Ni and Ru, reside in a tetragonal MO_2H_4 coordination environment. The presence of a plane that is entirely devoid of oxide ligands is, to the best of our knowledge, a unique feature in oxide-hydride chemistry, and provides an elegant comparison to the extensively studied $SrVO_2H$ phase, where the metal coordination is MO_4H_2. The measured structural and magnetic data, along with the computational study, are consistent with the presence of transition metal ions in remarkably low oxidation states, Ru^{2+} and Ni^{1+}, for an oxide lattice.

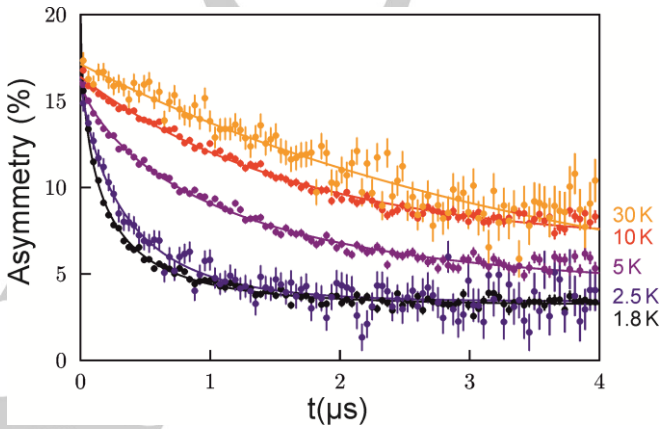


Figure 3. Plots of the asymmetry of μ⁺SR data collected from $LaSr_3NiRuO_4H_4$ at various temperatures.

Experimental Details

Samples of $LaSr_3NiRuO_8$ were prepared by a high-temperature ceramic method as described in the Supporting Information. $LaSr_3NiRuO_8$ was converted to $LaSr_3NiRuO_4H_4$ by grinding with CaH_2 in an argon filled glovebox, sealing the resulting powder mixture in an evacuated silica ampoule and then heating at 450 °C for 3 periods of 7 days, with the sample being reground between heating periods. Once the reaction was deemed complete, the reaction mixture was washed, under nitrogen, with 8 × 25 ml of 0.1 M NH_4Cl solution in methanol in order to remove the CaO, formed as a by-product of the reaction, and any unreacted CaH_2. This was then followed by washing with 5 × 25 ml of clean methanol to dissolve NH_4Cl residues. The sample was then dried under vacuum. Synchrotron X-ray powder diffraction data were collected from samples contained within 0.3mm capillaries, using the I11 diffractometer at the Diamond Light Source, UK. Time-of-flight neutron powder diffraction data were collected from $LaSr_3NiRuO_4H_4$ using the WISH diffractometer at the ISIS neutron source, UK. Details of the structural refinements of both $LaSr_3NiRuO_8$ and $LaSr_3NiRuO_4H_4$ are given in the Supporting Information. Magnetisation data were collected from powder samples using an Quantum Design SQUID magnetometer as described in the Supporting Information. The μ⁺SR experiments were carried out at the Swiss Muon Source, PSI, Switzerland. In a μ⁺SR experiment, spin-polarised muons were implanted in the bulk of a material and the time-dependence of their polarisation monitored by recording the angular distribution of the subsequent positron decay. All density functional calculations were performed using the VASP software package (VASP 5.3).[10] The PBE functional[11] was used, along with Hubbard *U* values (U_{eff}) of 3.0 eV on Ni and 1.0 eV on Ru to describe the effect of strong correlations. A plane-wave cut off of 600 eV was imposed in all cases,

and the Brillouin zone was sampled on an 8 × 8 × 7 *Γ*-centred grid. In order to investigate different patterns of exchange coupling between the paramagnetic centres we consider a 2 x 2 x 1 expansion of the primitive unit cell, which contains four formula units. The Ni and Ru ions are not distinguished in the diffraction study, so we have chosen a chequerboard arrangement where each Ni^{1+} ion is surrounded by four Ru^{2+} nearest neighbours and *vice versa*. Similarly, the positions of the La^{3+} and Sr^{2+} ions are not available from the diffraction data, so we have chosen to place the La^{3+} ions in the unit cell such that the distances between them, and hence the electrostatic repulsion, is minimised. This amounts to placing one La^{3+} in each of the four layers in the unit cell. Full details are given in the supporting information.

Keywords: oxide-hydride • neutron diffraction • density functional theory • transition metals

[1] a) P. Schiffer, A. P. Ramirez, W. Bao, S. W. Cheong, *Phys. Rev. Lett.* **1995**, *75*, 3336-3339; b) J. G. Bednorz, K. A. Muller, *Z. Phys. B* **1986**, *64*, 189-193; c) R. E. Cohen, *Nature* **1992**, *358*, 136-138; d) P. Lacorre, F. Goutenoire, O. Bohnke, R. Retoux, Y. Laligant, *Nature* **2000**, *404*, 856-858; e) R. Asahi, T. Morikawa, T. Ohwaki, K. Aoki, Y. Taga, *Science* **2001**, *293*, 269-271.

[2] a) G. Bouilly, T. Yajima, T. Terashima, W. Yoshimune, K. Nakano, C. Tassel, Y. Kususe, K. Fujita, K. Tanaka, T. Yamamoto, Y. Kobayashi, H. Kageyama, *Chem. Mater.* **2015**, *27*, 6354-6359; b) T. Yajima, A. Kitada, Y. Kobayashi, T. Sakaguchi, G. Bouilly, S. Kasahara, T. Terashima, M. Takano, H. Kageyama, *J. Am. Chem. Soc.* **2012**, *134*, 8782-8785.

[3] a) M. A. Hayward, E. J. Cussen, J. B. Claridge, M. Bieringer, M. J. Rosseinsky, C. J. Kiely, S. J. Blundell, I. M. Marshall, F. L. Pratt, *Science* **2002**, *295*, 1882; b) F. Denis Romero, A. Leach, J. S. Moller, F. Foronda, S. Blundell, M. A. Hayward, *Angew. Chem., Int. Ed.* **2014**, *53*, 7556-7559; c) C. Tassel, Y. Goto, Y. Kuno, J. Hester, M. Green, Y. Kobayashi, H. Kageyama, *Angew. Chem., Int. Ed.* **2014**, *53*, 10377-10380.

[4] T. Yamamoto, D. Zeng, T. Kawakami, V. Arcisauskaite, K. Yata, M. A. Patino, N. Izumo, J. E. McGrady, H. Kageyama, M. A. Hayward, *Nature Communications* **2017**, *8*, 1217.

[5] Y. Kobayashi, O. J. Hernandez, T. Sakaguchi, T. Yajima, T. Roisnel, Y. Tsujimoto, M. Morita, Y. Noda, Y. Mogami, A. Kitada, M. Ohkura, S. Hosokawa, Z. F. Li, K. Hayashi, Y. Kusano, J. E. Kim, N. Tsuji, A. Fujiwara, Y. Matsushita, K. Yoshimura, K. Takegoshi, M. Inoue, M. Takano, H. Kageyama, *Nat. Mater.* **2012**, *11*, 507-511.

[6] R. M. Helps, N. H. Rees, M. A. Hayward, *Inorg. Chem.* **2010**, *49*, 11062.

[7] C. A. Bridges, G. R. Darling, M. A. Hayward, M. J. Rosseinsky, *J. Am. Chem. Soc.* **2005**, *127*, 5996.

[8] a) F. Denis Romero, S. J. Burr, J. E. McGrady, D. Gianolio, G. Cibin, M. A. Hayward, *J. Am. Chem. Soc.* **2013**, *135*, 1838-1844; b) F. Denis Romero, D. Gianolio, G. Cibin, P. A. Bingham, J.-C. d'Hollander, S. D. Forder, M. A. Hayward, *Inorg. Chem.* **2013**, *52*, 10920-10928.

[9] M. Amano Patino, D. Zeng, R. Bower, J. E. McGrady, M. A. Hayward, *Inorg. Chem.* **2016**, *55*, 9012-9016.

[10] G. Kresse, J. Furthmüller, *Phys. Rev. B: Condens. Matter Mater. Phys.* **1996**, *54*, 11169– 11186.

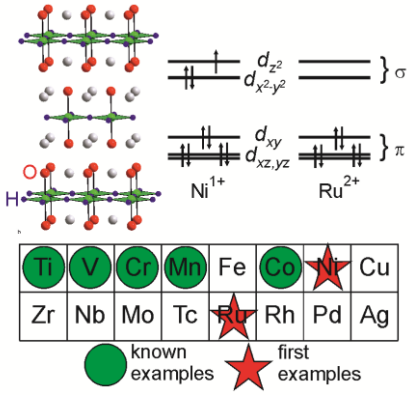
[11] J. P. Perdew, K. Burke, M. Ernzerhof, *Phys. Rev. Lett.* **1996**, *77*, 3865– 3868.

WILEY-VCH

Entry for the Table of Contents (Please choose one layout)

COMMUNICATION

A 4d transition-metal oxide-hydride, $LaSr_3NiRuO_4H_4$, is prepared *via* topochemical anion exchange. Hydride ions occupy equatorial anion sites in the lattice and as a result the Ru and Ni cations are located in a plane containing only hydride ligands.



*Lun Jin, Michael Lane, Dihao Zeng, Franziska K. K. Kirschner, Franz Lang, Pascal Manuel, Stephen J. Blundell, John E. McGrady and Michael A. Hayward**

Page No. – Page No.

$LaSr_3NiRuO_4H_4$: a 4d transition-metal oxide-hydride containing metal hydride sheets.

WILEY-VCH

Probing the Structure, Dynamics and Bonding of Coinage Metal Complexes of White Phosphorus

Laura C. Forfar,[a] Dihao Zeng,[b] Michael Green,[a] John E. McGrady*[b] and Christopher A. Russell*[a]

Abstract: A series of cationic white phosphorus complexes of the coinage metals Au and Cu have been synthesised and characterised both in the solid state and in solution. All complexes feature a P_4 unit coordinated through an edge P-P vector (i.e. η^2-like), although the degree of activation (as measured by the coordinated P–P bond length) is greater in the gold species. All the cations are fluxional on the NMR timescale at room temperature, but in the case of the gold systems fluxionality is frozen out at –90 °C. Electronic structure calculations suggest that this fluxionality proceeds *via* an η^1-coordinated M–P_4 intermediate.

Introduction

White phosphorus, P_4, represents the major industrial P-atom source for the production of organophosphorus compounds which are employed on a large scale in a wide range of technologies. The syntheses of these organophosphorus compounds involve a multistep process in which P_4 is first chlorinated or oxychlorinated to generate tri- and pentavalent phosphorus halides/oxohalides, which are subsequently functionalised by, for example, salt elimination reactions. Clearly this process is both hazardous and environmentally unfriendly. An alternative approach involving the controlled activation of P_4 leading to phosphorus-containing products without the need for direct halogenation is clearly desirable, but at the present time remains a target rather than a reality – the attainment of this goal will be underpinned by a deep understanding of the coordination chemistry of P_4.[1] Thus, despite the fact that P_4 is recognised as being a poor donor ligand, the coordination chemistry of white phosphorus in a wide variety of transition metal complexes has been studied.[2] Commonly, reactions of P_4 with transition metal fragments lead to decomposition of the tetrahedral P_4 molecule; however, coordination of the intact P_4 moiety has been observed in a number of cases, with binding either *via* an edge (*i.e.*, η^2) or a corner (*i.e.*, η^1), depending on the precise steric and electronic environment at the metal centre. In the electronically preferred η^2-mode, the resemblance between M–P_4 binding and M–alkene binding has been noted.[3]

Our own interest in this topic is part of our studies into the binding of small molecules at coinage metal centres. Thus we recently reported[4] that reactions of equimolar quantities of simple metal salts MX (M = Au, Cu, X = Cl; M = Ag, X = OTf) and $GaCl_3$ in CH_2Cl_2 with P_4 led to phosphorus ligating a cationic coinage metal centre. For Cu and Ag, ion-contacted coordination polymers are formed; for Au, an ion-separated complex is observed that features the $[Au(\eta^2\text{-}P_4)_2]^+$ cation. The observation of these different structures was rationalised using a simple thermodynamic cycle complemented by gas-phase quantum chemical studies which showed weak M–P_4 interactions. The formation of $[M(\eta^2\text{-}P_4)_2]^+$ is rather endothermic for M = Cu, Ag, allowing competitive formation of coordination polymers *via* M–Cl links. The nature of the M–P_4 bond in complexes of this type has been the matter of some discussion, dating back to Ginsberg and Welch's earliest discussions of the electronic structure of $RhCl(\eta^2\text{-}P_4)(PPh_3)_2$ using extended Hückel and SCF-X_α theory.[3, 5] The coordinated P–P bond in this case is significantly elongated from its equilibrium value in P_4 (2.4616(22) Å vs 2.1994(3) Å from gas-phase electron diffraction[6]). The synergic nature of the bonding (and hence the analogy to the familiar Dewar-Chatt-Duncanson binding model[7] for ethene) was noted at this point: donation of electron density from the P–P σ bond to the metal and back-donation of metal d electrons into P–P σ^* may both contribute to the overall stability of the complex. Following the report of the $[Ag(P_4)_2]^+$ cation,[8] Krossing and van Wüllen argued that the coordinated P–P bond length of 2.329(2) Å was in fact a truer signature of an η^2-P_4 coordination mode, and that the rhodium complex was better formulated as a κ^2-$[P_4]^{2-}$ complex of Rh(III).[2a] Subsequent calculations by Deubel confirmed the importance of back-bonding, even in the complex of Ag^+, but also suggested that the planar (D_{2h}) cordination geometry about Ag^+ was the result of inter- rather than intramolecular factors.[8] Despite the differences of opinion that have emerged in these papers, the synergic nature of the bonding is not in doubt, and it seems clear that all P_4 complexes that are bound *via* two phosphorus atoms lie comewhere on a continuum whose limits are M(I)(η^2-P_4) and M(III)(κ^2-P_4).

The rich coordination chemistry that has emerged in these apparently simple systems prompted us to seek a greater

[a] *Dr Laura C. Forfar, Prof.. Michael Green, Dr. Christopher A. Russell*
School of Chemistry
University of Bristol
Cantock's Close, Bristol, BS8 1TS, United Kingdom
E-mail: chris.russell@bristol.ac.uk
[b] *Dihao Zeng, Prof. John E. McGrady*
Department of Chemistry
University of Oxford
South Parks Road, OX1 3QZ, United Kingdom
E-mail: john.mcgrady@chem.ox.ac.uk

Supporting information for this article is available on the WWW under http://dx.doi.org/

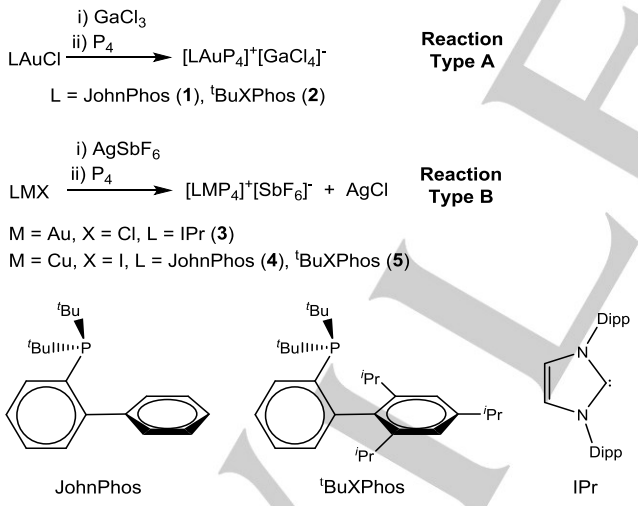
understanding of these M–P_4 interactions by introducing co-ligands at the metal centres. Herein we present a combined synthetic, solid-state, solution and computational analysis of these complexes.

Results and Discussion

Synthesis and structure

Our synthetic approaches towards these complexes are shown in Scheme 1 and involves the initial reaction of CH_2Cl_2 solutions of [LMX] with $GaCl_3$ or $AgSbF_6$ {L = P(^{t}Bu)$_2$(*o*-biphenyl) (JohnPhos), P(^{t}Bu)$_2$(2',4',6' -triisopropylbiphenyl) (^{t}BuXPhos) or 1,3-bis(2,6-diisopropylphenyl)-1,3-dihydro-2H-imidaz-ol-2-ylidene(IPr)} followed by the addition of one equivalent of white phosphorus.

The resulting solutions are, in the cases of the gold complexes **1**–**3** (Scheme 1), clear and colourless, which display broad $^{31}P\{^1H\}$ resonances (CD_2Cl_2, RT) for the P_4 moiety that are significantly downfield from that of free P_4 under the same conditions (**1**, δ ≈ –454 ppm; **2**, δ ≈ –455 ppm; **3**, δ ≈ –465 ppm; *cf.* free P_4 at δ ≈ –525 ppm). It is interesting to note that, for complex **1**, reactions with sub-stoichiometric equivalents of P_4 gave solutions which showed additional peaks in the $^{31}P\{^1H\}$ NMR spectrum which, although they cannot be definitively assigned, are suggestive of more complex coordination chemistry. Furthermore. reactions of Type A were attempted using Cu compounds; again $^{31}P\{^1H\}$ NMR was indicative of complexation of the P_4 unit but the samples coudl not be purified and no further chracteristaion was attempted.



Scheme 1. Reactions used to prepare **1**–**5**.

In contrast, the copper complexes **4** and **5** form intensely yellow coloured solutions that display $^{31}P\{^1H\}$ NMR signals (CD_2Cl_2, RT) for the P_4 moiety at δ ≈ –468 ppm (**4**) and δ ≈ –493 ppm (**5**) respectively. It is noteworthy that in all cases **1**–**5**, the room temperature NMR spectra gave chemical shifts characteristic of an intact P_4 cage, and that in each case only a solitary signal for the P_4 moiety was observed, suggesting that a dynamic process is occurring on the NMR timescale leading to the single time-averaged signal.

Crystals of **1**–**5** were grown that were suitable for analysis by single crystal X-ray diffraction experiments (molecular structures of the cations are shown in Figure 1; key bond dimensions are given in Table 1). The solid state structure of [{P^{t}Bu$_2$(*o*-biphenyl)}Au(η^2-P_4)][$GaCl_4$] (**1**) shows P_4 binding symmetrically to gold in an η^2-fashion with a coordinated P–P bond length of 2.341(3) Å, somewhat longer than that in free P_4 (2.20 Å) but shorter than that in the $[Au(P_4)_2]^+$ cation (2.410(1) Å).[9] The coordinated P–P bond lies perpendicular to the approximate mirror plane passing through Au, P(5) and the *ipso* carbon. In subsequent discussions we refer to this orientation as the *horizontal* isomer. The other P–P bonds in the P_4 unit are slightly contracted {2.155(5)–2.210(6) Å} compared to those in free P_4, a common feature in P_4 coordination chemistry. The Au(1)–P(1,2) bond distances of 2.442(2) Å and 2.446(2) Å are statistically equivalent, and P(5)–Au(1)–P(2,3) angles are 148.97(8) and 150.67(7)° respectively. The P(5)–Au(1)-$PP_{centroid}$ angle is close to linear at 169.9°, with minimal interaction with the flanking aromatic ring of the o-biphenyl group of the JohnPhos ligand (the closest contact is Au(1)–C_{ipso} at 3.124(9) Å, which, according to a report by Echavarren *et al.,* is indicative of a very weak interaction between the two atoms[10]).

The coordination of the P_4 unit may be altered by employing a more sterically encumbered phosphine ligand, in this case ^{t}BuXPhos. The solid-state structure of [{^{t}BuXPhosAu}(η^2-P_4)][$GaCl_4$] (**2**) again shows the P_4 tetrahedron bonded to the gold centre in an η^2- fashion, but the coordinated P–P bond is now rotated by approximately 90° relative to **1**, such that it lies in the mirror plane (defined by Au–P(5)–C_{ipso}) rather than perpendicular to it (the *vertical* coordination mode). Moreover, the coordinated P–P bond is rather longer than that in P(^{t}Bu)$_2$(*o*-biphenyl) {2.4182(8) Å *vs* 2.341(3) Å)} but the Au(1)–P(5) distance is the same within error {2.3301(5) Å vs 2.3218(18) Å}. The Au–P(1) and Au-P(2) bonds are also now distinctly asymmetric: 2.4067(6) Å and 2.4869(6) Å, respectively, while the P(5)–Au(1)–P(1) and P(5)–Au(1)–P(2) angles are 171.309(2)° and 128.274(2)°, respectively. The overall coordination geometry defined by the three phosphorus donor atoms is therefore, to a first approximation, T-shaped. In the context of the M(I)(η^2-P_4) and M(III)(κ^2-P_4) continuum discussed in the introduction, it appears that the binding in **2** is significantly displaced towards the M(III)(κ^2-P_4) end, as judged by the P–P distance and also the characteristic switch from approximately tetrahedral (**1**) to approximately planar (**2**) coordination geometries at the metal. We return to this point in the discussion of electronic structure.

In order to further increase the electron donating character of the ligand,[11] we also synthesised the corresponding *N*-heterocyclic carbene complex [{IPrAu}(η^2-P_4)][SbF_6] (**3**). The solid-state structure of **3** again shows white phosphorus coordinated to gold in an η^2-

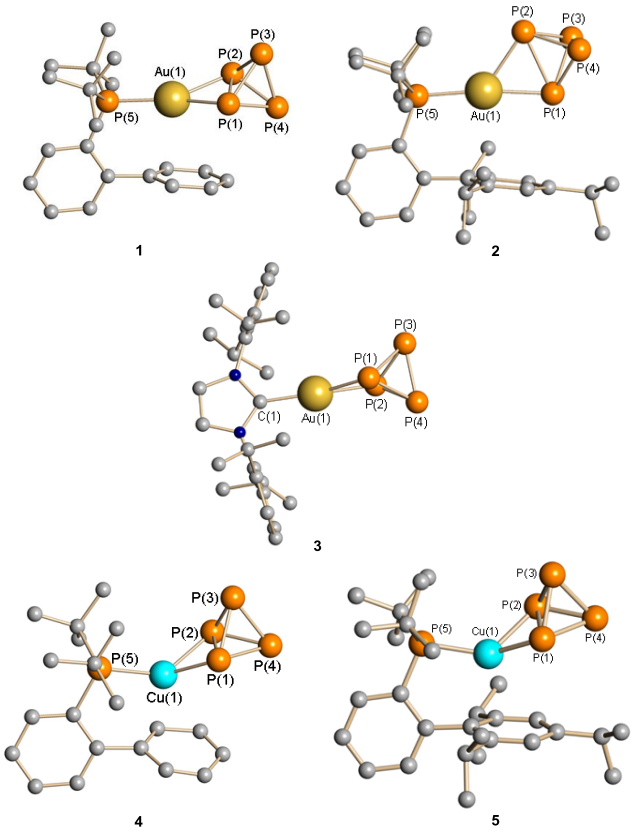


Figure 1. Molecular structures of the cations of **1**, **2**, **3**, **4** and **5**. In all cases the anions and all hydrogen atoms have been omitted for clarity.

fashion, and the horizontal coordination mode is much more similar to **1** than **2**. The Au–P(1,2) distances of 2.4333(7) Å and 2.4352(6) Å are statistically identical, the coordinated P–P bond is 2.357(1) Å {*cf.* 2.341(3) Å in **1**} and the coordination geometry again approximates trigonal planar. Thus it appears that the steric bulk ([P^{t}Bu$_2$(*o*-biphenyl) *vs* ^{t}BuXPhos) has a greater impact on the P–P distance than the donor properties of the ligand (P^{t}Bu$_2$(*o*-biphenyl) *vs* IPr).The solid-state structures of the copper analogues of **1** and **2** (**4** and **5**, respectively) showed the P_4 unit again binding to the copper(I) centre in an η^2- fashion, but in both cases the horizontal coordination mode is preferred, reminiscent of **1** and quite distinct from **2**. The coordinated P–P bonds again lengthen, but to a lesser extent than observed in **1** (2.285(3) Å (**4**) and 2.2912(12) Å (**5**) vs 2.341(3) Å in **1**). These values are also distinctly shorter than the coordinated P–P bond in the copper–P_4 coordination polymer previously reported in our group {2.3744(7) Å}. In both **4** and **5** the Cu makes close contacts with the C_{ortho}–C_{ipso} edge of the flanking arene ring {2.302(7) Å (**4**) and 2.324(2) Å (**5**)} and the P_4 moiety is tilted away from the biphenyl unit. Echavarren *et al.* noted a similar distortion in a related copper complex of acetonitrile.[10] We comment further on the significance of the interaction of the arene with the metal in the subsequent discussion of electronic structure.

Table 1. Key bond dimensions of the cations of **1**, **2, 3**, **4** and **5**.

	1	**2**	**3**	**4**	**5**
M-P(1)	2.442(2)	2.4067(6)	2.4352(6)	2.310(4)	2.3253(11)
M-P(2)	2.446(2)	2.4869(6)	2.4333(7)	2.315(4)	2.3602(12)
M-L[a]	2.3218(18)	2.3301(5)	2.035(2)	2.243(4)	2.2535(10)
P(1)-P(2)	2.341(3)	2.4182(8)	2.3571(10)	2.281(5)	2.2912(12)
P(1)-P(3)	2.171(4)	2.1981(9)	2.1666(10)	2.165(6)	2.1873(12)
P(1)-P(4)	2.155(5)	2.1799(8)	2.1642(11)	2.160(5)	2.1728(12)
P(2)-P(3)	2.174(4)	2.1697(9)	2.1704(10)	2.177(6)	2.1668(13)
P(2)-P(4)	2.167(4)	2.1686(9)	2.1704(11)	2.174(6)	2.1893(13)
P(3)-P(4)	2.210(6)	2.1967(10)	2.1941(11)	2.225(7)	2.2192(13)
L-M-PP$_{centroid}$	169.9	157.1	175.4	138.0	137.1

[a] Distance between M and the donor atom of the supporting ligand (*i.e.*, either the P of PR_3 or the C of NHC)

NMR spectroscopy

The $^{31}P\{^1H\}$ NMR spectrum of **1** gives a broad signal at $\delta_P \approx 75$ ppm for the phosphine ligand and a broad peak at –454 ppm for the P_4 ligand, consistent with a dynamic process leading to scrambling of all four phosphorus atoms of the P_4 cage. This may originate from an intramolecular process involving the "tumbling" of the P_4 tetrahedron that interconverts the coordinated and non-coordinated phosphorus centres, or alternatively a process involving breaking the M–P_4 bond and subsequent rebinding. We note that a dynamic process exchanging, in both solution and solid state, the P-atoms of mononuclear and dinuclear white phosphorus complexes has been reported.[12] Previously isolated $[M(P_4)_2]^+$ (M = Cu,[13] Ag,[14] Au[9]) compounds also exhibit rapid fluxionality which could not be frozen out even at temperatures as low as –90 °C. In contrast, variable temperature ^{31}P NMR spectroscopy on **1** proved to be more revealing (Figure 2). Cooling **1** to –20 °C causes the resonance at 75 ppm {P(5)} to resolve into an apparent quintet, due to coupling to four phosphorus atoms of the P_4 unit {P(1–4)} that appear equivalent

on the NMR timescale. The quintet for this resonance is also observed at –40 and –60 °C, but at –80 and –90 °C the multiplicity of this peak changes to a triplet. The anticipated triplet of triplets was not observed, presumably because the 3-bond coupling to the non-coordinated phosphorus atoms is not resolved. The resonance due to the P_4 unit is similarly temperature dependent: at –60 °C the broad peak at $\delta_P \approx$ –454 ppm resolves into a broad doublet which becomes complex multiplet at –90 °C, resulting from the two different phosphorus environments in the P_4 unit coupling to each other and to P(5). The second order splitting pattern has been modelled as an A_2MX_2 spin system (see Supporting Information).

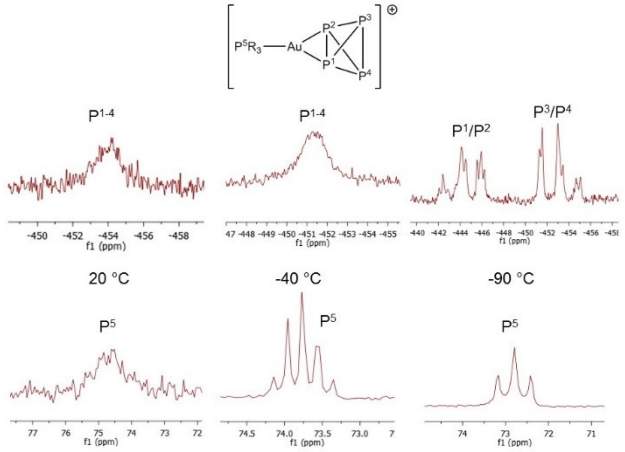


Figure 2. Variable temperature $^{31}P\{^1H\}$ NMR spectra of CD_2Cl_2 solutions of **1**.

The $^{31}P\{^1H\}$ NMR spectra of **2** shows the same general pattern as **1**, with two singlets at $\delta_P \approx$ 73.2 {P(5)} and –454.8 {P(1–4)} ppm at room temperature. Cooling to –40 °C leads to broadening of the peak at –454 ppm and splitting of the 73 ppm resonance into a quintet. At –90 °C, the peak at $\delta_P \approx$ 73 ppm resolves into a triplet and the peak for the P_4 tetrahedron generates the same second order splitting pattern as described above for **1**. The room temperature spectrum of **3** also gives a very broad signal at $\delta_P \approx$ –465 ppm, which resolves into a triplet at –460.4 and a broad peak at –450 ppm upon cooling to –90 °C. The room temperature $^{31}P\{^1H\}$ NMR spectra of the copper analogues, **4** and **5**, also show sharp singlets for the P_4 unit at $\delta_P \approx$ –467.7 ppm (**4**) and –492.9 ppm (**5**) and a broad singlet for the phosphine ligand at $\delta_P \approx$ 29.3 ppm (**4**) and 28.6 ppm (**5**). Even at –90 °C, however, the resonances for the P_4 unit do not resolve into a second order splitting pattern.

Computational analysis

In an attempt to rationalise the observed structural and spectroscopic trends, we have used density functional theory to explore the potential energy surfaces for **1**, **2**, **4** and **5**. The optimised structure of **1** shown in Figure 3 (**1-h**) is very similar to the X-ray data, with the P_4 unit adopting a horizontal coordination mode. The coordinated P–P bond is somewhat longer than in the experiment {2.41 Å vs 2.341(3) Å} but the Au-C_{ipso} distance of 3.10 Å matches well with the crystallographic value of 3.124(9) Å. The coordinated P–P bonds are systematically over-estimated by ~0.06 Å in all systems studied here, and the same trend has also emerged in other studies (see for example Table 1 in reference 7). We have also located a second local minimum for **1** (**1-v**, corresponding to the vertical coordination mode seen in **2**) only very marginally less stable than the global minimum (+8 kJ/mol). The coordination geometry is approximately square planar, with a longer coordinated P–P bond (2.45 Å in **1-v** *vs* 2.41 Å in **1-h**), two quite distinct Au–P distances of 2.45 Å (*trans* to PR_3) and 2.52 Å (*trans* to the aryl group). The fourth coordination site is filled by a C=C double bond from the arene ring which is brought into bonding distance of the metal by a distinct tilt, leading to very asymmetric Au–C_{ortho} distances of 3.20 Å and 3.61 Å. The tilting of the arene ring in **1-h** is much less pronounced, (Au–C_{ortho} = 3.33 Å and 3.42 Å), suggesting a weaker interaction. It is interesting to note that the Au-C_{ipso} distances are rather similar in **1-h** and **1-v** (3.10 Å and 3.13 Å, respectively), and so the asymmetry in Au-C_{ortho} distances, rather than the Au-C_{ipso} distance in isolation, appears to be the best gauge of the strength of the metal arene interaction in these cases. Analysis of the topology of the electron density reveals a bond critical point at the midpoint of the coordinated P-P bond in both **1-h** and **1-v**, although the density is somewhat smaller in the latter (0.068 e $Å^{-3}$ in **1-v** vs 0.073 e $Å^{-3}$ in **1-h** and 0.078 e $Å^{-3}$ in $[Ag(P_4)_2]^{+}$,[2a]). The structural information and the computed densities therefore converge to suggest that two minima, **1-h** and **1-v**, map part of the continuum between Au(I)(η^2-P_4) and Au(III)(κ^2-P_4) limits, the square planar geometry being highly characteristic of the latter.

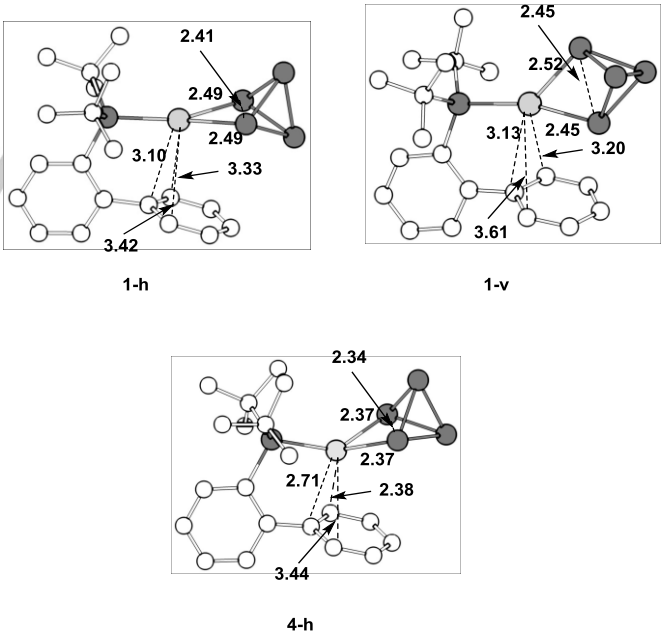


Figure 3. DFT-optimised structural parameters for **1-h**, **1-v** and **4-h**.

In the case of **2**, we have been able to identify only a single minimum corresponding to vertical isomer (**2-v**): all attempts to locate the alternative horizontal form resulted in rotation of the P_4 unit. Steric effects therefore clearly play a critical role in pushing the P_4 unit into the vertical coordination position, where donation from

the arene ring can be used to maximum effect. In the copper analogues, **4** and **5**, we have also located only a single local minimum corresponding to an η^2-coordination mode, in this case the horizontal rather than vertical isomer. As was the case for the gold complexes, the coordinated P–P bond length is overestimated by ~0.06 Å, but the geometry is otherwise in excellent agreement with experiment. The structures differ from **1-h** in that the arene ring is now distinctly tilted such that one C=C double bond occupies the fourth coordination site, but in this case of an approximately tetrahedral Cu centre. These subtle differences in structure between gold and copper complexes are entirely consistent with well-established trends: the tendency of **1-h** to remain 3-coordinate and planar while **4-h** is 4-coordinate and tetrahedral is typical of the coordination chemistry of the late transition members of the first and third transition series (contrast, for example, $Pt(CO)_3$ *vs* $Ni(CO)_4$).

As noted above, the fluxionality of the P_4 unit is, in principle, consistent with a number of reaction pathways. The potential energy surface for **1** is shown in Figure 4, including the horizontal and vertical isomers discussed above. **1-h** and **1-v** are connected *via* a low-lying transition state (**1-TS0** in Figure 4, +12 kJ/mol), very similar to Krossing and van Wüllen's value of 5 kJ/mol for the difference between D_{2h}- and D_{2d}-symmetric structures of $[Ag(P_4)_2]^+$, from which we conclude that effectively free rotation of the P_4 cluster about the Au–PR_3 axis (*i.e.* along the bisector of the coordinated P-P bond) occurs in solution at all temperatures. We have also identified a low-lying η^1-coordinated intermediate, **1-I**, approximately 29 kJ/mol above the global minimum. The P–Au–P angle is now almost perfectly linear and P–P bonds lie in the range 2.19–2.25 Å, all of which is very characteristic of an Au(I) oxidation state and a largely unactivated P_4 unit. In reference 2a, isomers of $[Ag(P_4)_2]^+$ with η^1-P_4 coordination modes were located in a similar energy range (+27 kJ/mol) but were identified as saddle points rather than minima. The transition state, **1-TS1** is structurally very similar to **1-I** and lies marginally higher at +41 kJ/mol. We note, however, that the precise height of the η^1-η^2 barrier is rather dependent on methodology – at the B3LYP-D3 level it is only 27 kJ/mol while with MP2 it rises to +63 kJ/mol, more consistent with the observation that the bound and unbound phosphorus atoms can be distinguished at –90 °C.

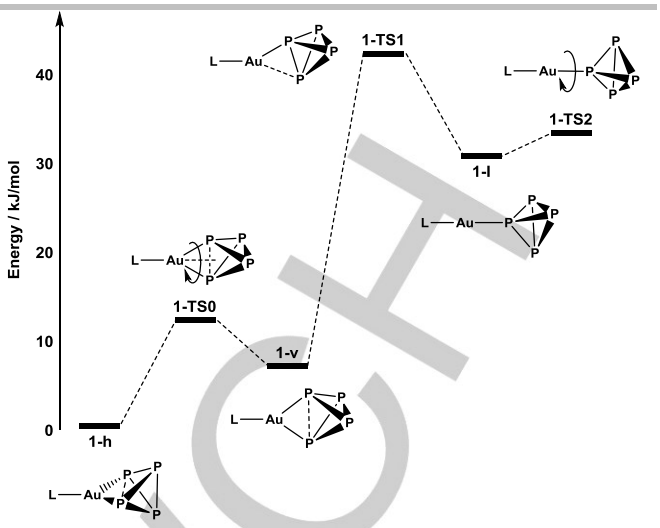


Figure 4. Potential energy surface for the dynamic processes in **1** (BP86-D3).

Conclusions

A series of novel $[LM(I)–P_4]^+$ (M = Au, Cu) complexes have been synthesised and structurally characterised. Their solid-state structures highlight the effect of the auxiliary ligand on the coordination mode of white phosphorus. In the case of gold, the coordination chemistry is typical of heavier transition elements: there is a distinct preference for planar coordination over tetrahedral, and also a marked shift towards Au(III) *vs* Au(I) character. The Au(III) character is revealed by the adoption of square planar geometries (with the arene ring filling the fourth coordination site) and the elongation of the coordinated P–P bond. In contrast, the coordination chemistry of the copper analogues is very typical of Cu(I), featuring approximately tetrahedral geometries with a C=C bond of the arene again filling the fourth coordination position. All the complexes were fluxional in solution and, in the case of the gold, the dynamic process can be frozen out at –90 °C to reveal distinct resonances. Calculations indicate that the fluxionality occurs *via* an η^1-coordinated M(I) intermediate where the P_4 unit is deactivated.

Experimental Section

General Experimental

All reactions were performed under an atmosphere of nitrogen using standard Schlenk or glove box techniques; solvents were dried using an Anhydrous Engineering Grubbs-type system (alumina columns). White phosphorus was obtained as a generous gift from Rhodia plc and purified according to a procedure described previously.[4] The gold complexes [P^{t}Bu$_2$(*o*-biphenyl)AuCl] and [P(^{t}Bu)$_2$(2',4',6'-triisopropylbiphenyl)AuCl] were prepared according to modified literature methods[15] from tetrachloroauric(III) acid donated by Umicore. [(IPr)AuCl] (IPr = 1,3-bis[2,6-diisopropylphenyl-imidazol-2-ylidene]) was used as received from the supplier. [P^{t}Bu$_2$(*o*-biphenyl)CuI] and [P(^{t}Bu)$_2$(2',4',6'-triisopropylbiphenyl)CuI] were

prepared by addition of the desired phosphine to a methanol solution of copper(I) iodide and refluxing overnight to yield a white precipitate. All other reagents were of analytical grade and obtained from commercial suppliers and were used without further purification.

^{31}P NMR spectra were obtained using a Jeol ECS 400 MHz multinuclear spectrometer. ^{1}H and ^{13}C spectra were referenced to internal solvent peaks, ^{31}P NMR spectra were referenced to an external sample of 85% H_3PO_4

Complexes **1**-**5** were prepared by either Reaction Type A (**1** and **2**) or Reaction Type B (**3**-**5**) as shown in Scheme 1. General synthetic procedures for each reaction type are given followed by specific characterisation data for each complex.

Reaction Type A: White phosphorus (0.05 mmol, 6 mg) was added to a solution containing 0.05 mmol of LAuCl {L = JohnPhos or tBuXPhos) and $GaCl_3$ (0.05 mmol, 9 mg) in dichloromethane (3 mL). The solution was stirred for 1 h in the absence of light then filtered through Celite and washed with dichloromethane (2 × 2 mL). The resulting solutions were concentrated and crystals were grown from CH_2Cl_2/hexane layers. Yields were quantitative by ^{31}P NMR spectroscopy.

Data for 1: Crystalline yield: 15 mg (36%). **^{1}H NMR** (400 MHz, 20 °C, CD_2Cl_2) δ_H 7.88 (m, Ar*H*, 1H), 7.62 (m, Ar*H*, 1H), 7.53 (t, Ar*H*, 1H), 7.45 (t, Ar*H*, 1H), 7.28-7.20 (m, Ar*H*, 2H), 1.45 (d, $J_{H\text{-}P}$ = 16.3 Hz, C(CH_3)$_3$, 18H) ppm; **^{13}C NMR** (100 MHz, 20 °C, CD_2Cl_2) δ_C 148.88 (d, $J_{C\text{-}P}$ = 13.7 Hz), 143.77 (d, $J_{C\text{-}P}$ = 6.5 Hz), 135.16 (s), 133.96 (d, $J_{C\text{-}P}$ = 7.8 Hz), 132.29 (d, $J_{C\text{-}P}$ = 2.5 Hz), 130.54 (s), 130.40 (s), 130.03 (s), 128.70 (d, $J_{C\text{-}P}$ = 7.4 Hz), 125.85 (d, $J_{C\text{-}P}$ = 44.9 Hz), 39.20 (d, $^{1}J_{C\text{-}P}$ = 21.3 Hz), 31.26 (d, $^{2}J_{C\text{-}P}$ = 6.3 Hz) ppm; **^{31}P{^{1}H} NMR** (121.4 MHz, 20 °C, CD_2Cl_2) δ_P 75.8 (br), –453.6 (br) ppm; **^{31}P{^{1}H} NMR** (121.4 MHz, –90 °C, CD_2Cl_2) δ_P 72.8 (t, J = 45.8 Hz), –444.1 (m), –453.0 (m) ppm; **Calc. for $C_{20}H_{27}AuCl_4GaP_5$:** C, 28.91; H, 3.28; Found: C, 31.29; H, 3.69 %. The discrepancy between calculated and observed values for elemental analysis is as a result of placing the sample under vacuum (10^{-2} Torr, 15 mins) as part of the isolation procedure, leading to dissociation and subsequent loss of P_4 and the high values for %C and %H values.

Data for 2: The product crystallises with a single molecule of CH_2Cl_2 in the lattice. This is removed by exposing the sample to vacuum prior to isolation. The following data is for the solvent free material. Crystalline yield 22 mg (46%). **^{1}H NMR** (400 MHz, 20 °C, CD_2Cl_2) δ_H 7.90 (m, Ar*H*, 1H), 7.63 (m, Ar*H*, 2H), 7.25 (m, Ar*H*, 1H), 7.09 (s, Ar*H*, 2H), 3.13 (sep, J = 6.9 Hz, C*H*(CH$_3$)$_2$, 1H), 2.35 (sep, J = 6.8 Hz, C*H*(CH$_3$)$_2$, 2H), 1.49 (d, J = 16.45 Hz, C(CH_3)$_3$, 18H), 1.41 (d, J = 6.79 Hz, CH(CH_3)$_2$, 6H), 1.18 (d, J = 6.79, CH(CH_3)$_2$, 6H), 0.92 (d, J = 6.79 Hz, CH(CH_3)$_2$, 6H) ppm; **^{13}C NMR** (125.7 MHz, 20 °C, CD_2Cl_2) δ_C 135.74 (d, J = 8.56 Hz), 132.25 (s), 128.59 (s), 123.56 (s), 39.55 (d, ^{1}J = 20.10 Hz), 34.55 (s), 31.74 (d, ^{2}J = 5.59 Hz), 31.48 (s), 26.07 (s), 24.62 (s), 23.92 (s) ppm; **^{31}P{^{1}H} NMR** (121.4 MHz, 20 °C, CD_2Cl_2) δ_P 73.3 (br), –454.8 (br) ppm; **^{31}P{^{1}H} NMR** (121.4 MHz, –90 °C, CD_2Cl_2) δ_P 70.3 (t, J = 46.8 Hz), –442.9 (m), –458.4 (m) ppm; **Calc. for $C_{29}H_{45}AuCl_4GaP_5$:** C, 36.40; H, 4.74; Found: C, 36.65; H, 4.87 %.

Reaction Type B: White phosphorus (0.05 mmol, 6 mg) was added to a suspension of 0.05 mmol of LMX (M = Au, X = Cl, L = IPr; M = Cu, X = I, M = Cu, X = I, L = JohnPhos) and $AgSbF_6$ (0.05 mmol, 17 mg) in dichloromethane (3 mL). The suspension was stirred for 1 h in the absence of light then filtered through Celite and washed with dichloromethane (2 × 2 mL). The resulting solutions were concentrated and crystals were grown from CH_2Cl_2/hexane layers. The yields was quantitative by ^{31}P NMR.

Data for 3: Crystalline yield 12 mg (38%). **^{1}H NMR** (400 MHz, 20 °C, CD_2Cl_2) δ_H 7.59 (t, J = 7.8 Hz, 2H, Ar*H*), 7.41, (s, 2H, Imid-*H*) 7.37 (d, = 7.8 Hz, 4H, Ar*H*), 2.46 (sep, J = 6.9 Hz, 4H, C*H*(CH$_3$)$_2$), 1.26 (d, J = 6.9 Hz, CH(CH_3)$_2$), 1.23 (d, J = 6.9 Hz, CH(CH_3)$_2$) (overlapped doublet, integral 24H) ppm; **^{31}P{^{1}H} NMR** (121.4 MHz, 20 °C, CD_2Cl_2) δ_P –464.5 (br) ppm; **^{31}P{^{1}H} NMR** (121.4 MHz, –90 °C, CD_2Cl_2) δ_P –450 (br), –460.7 (m) ppm.

Data for 4: Crystalline yield 27 mg (37%).**^{1}H NMR** (500 MHz, 20 °C, CD_2Cl_2) δ_H 7.95-7.91 (1H, m, Ar*H*), 7.71-7.60 (4H, m, Ar*H*), 7.54-7.49 (1H, m, Ar*H*), 7.40-7.36 (2H, m, Ar*H*), 7.35-7.32 (1H, m, Ar*H*), 1.33 (d, $J_{H\text{-}P}$ = 15.5 Hz, 18H, C(CH_3)$_3$) ppm; **^{13}C{^{1}H} NMR** (125.7 MHz, 20 °C, CD_2Cl_2) δ_C 148.62 (d, $J_{C\text{-}P}$ = 19.9 Hz), 143.04 (d, $J_{C\text{-}P}$ = 9.0 Hz), 134.52 (s), 134.09 (s, br), 132.56 (d, $J_{C\text{-}P}$ = 7.26 Hz), 132.29 (d, $J_{C\text{-}P}$ = 2.05 Hz), 129.25(s), 129.21 (s), 127.43 (s), 127.12 (d, $J_{C\text{-}P}$ = 31.89 Hz), 35.86 (d, $^{1}J_{C\text{-}P}$ = 16.01 Hz), 30.86 (d, $^{2}J_{C\text{-}P}$ = 7.12 Hz) ppm; **^{31}P{^{1}H} NMR** (202.3 MHz, 20 °C, CD_2Cl_2) δ_P 29.3, –468.9 ppm; **^{31}P{^{1}H} NMR** (121.4 MHz, –90 °C, CD_2Cl_2) δ_P 26.6, –457.8 (br) ppm; **Calc. for $C_{20}H_{27}CuF_6P_5Sb$:** C, 33.29; H, 3.77; Found: C, 33.61; H, 3.54 %

Data for 5: Crystalline yield 25 mg (29%). **^{1}H NMR** (400 MHz, 20 °C, CD_2Cl_2) δ_H 7.93-7.87 (m, Ar*H*, 1H), 7.64-7.59 (m, Ar*H*, 2H), 7.33 (s, Ar*H*, 2H), 7.30-7.26 (m, Ar*H*, 1H), 3.03 (sep, J = 6.9 Hz, C*H*(CH$_3$)$_2$, 1H), 2.43 (sep, $J_{H\text{-}P}$ = 6.8 Hz, C*H*(CH$_3$)$_2$, 2H), 1.38 (d, $J_{H\text{-}P}$ = 7.2 Hz, CH(CH_3)$_2$), 1.37 (d, $J_{H\text{-}P}$ = 7.2 Hz, CH(CH_3)$_2$), 1.35 (d, $J_{H\text{-}P}$ = 15.0 Hz, C(CH_3)$_3$) (overlapping peaks, integral = 30H), 0.96 (d, $J_{H\text{-}P}$ = 6.2 Hz, CH(CH_3)$_2$, 3H); **^{13}C NMR** (125.7 MHz, 20 °C, $CDCl_3$) δ_C 152.38 (s), 147.44 (br), 135.42 (s), 133.72 (d, $J_{C\text{-}P}$ = 7.7 Hz),131.84 (s), 130.18 (s), 129.95 (s), 128.95 (s), 127.03 (br), 36.15 (d, $J_{C\text{-}P}$ = 14.08 Hz), 34.41 (s), 31.85 (s), 31.31 (d, $J_{C\text{-}P}$ = 7.2 Hz), 26.6 (s), 24.20 (s), 23.31 (s) ppm; **^{31}P{^{1}H} NMR** (121.4 MHz, 20 °C, CD_2Cl_2) δ_P 28.6 (br), –492.9 (br) ppm; **^{31}P{^{1}H} NMR** (121.4 MHz, –90 °C, CD_2Cl_2) δ_P 24.4 (br), –452 (br), –466.8 (s) ppm; **Calc. for $C_{29}H_{45}CuF_6P_5Sb$:** C, 41.08; H, 5.35; Found: C, 43.13; H, 5.80 %. The discrepancy between calculated and observed values for elemental analysis is as a result of placing the sample under vacuum (10^{-2} Torr, 15 mins) as part of the isolation procedure, leading to dissociation and subsequent loss of P_4 and the high values for %C and %H values.

Single Crystal X-ray Crystallography

Experiments were performed on **1**-**5** using either a Bruker-AXS SMART APEX three circle diffractometer employing Mo-K_α radiation

(λ = 0.71073 Å) or a Microstar diffractometer employing Cu-K_α radiation (λ = 1.5418 Å). Intensities were integrated from several series of exposures, each exposure covering 0.3° in *ω*. Absorption corrections were applied based on multiple and symmetry-equivalent measurements. Hydrogen atoms were constrained to ideal geometries and refined with fixed isotropic displacement parameters. Selected Crystallographic and Data Collection Parameters for Compounds **1**-**5** are shown in Table 2. CCDC 1439692-1439696 contains the supplementary crystallographic data for this paper. These data can be obtained free of charge from The Cambridge Crystallographic Data Centre via www.ccdc.cam.ac.uk/data%5Frequest/cif

Table 2. Selected Crystallographic and Data Collection Parameters for Compounds **1**-**5**.

	1	**2·CH_2Cl_2**	**3**	**4**	**5**
CCDC deposition number	1439692	1439693	1439694	1439695	1439696
Radiation	Cu-K_α	Mo-K_α	Mo-K_α	Mo-K_α	Mo-K_α
Wavelength (Å)	1.5418	0.71073	0.71073	0.71073	0.71073
Size/mm	0.54×0.11×0.10	0.42×0.28×0.26	0.77×0.11×0.04	0.18×0.17×0.17	0.13×0.11×0.11
Empirical Formula	$C_{20}H_{27}AuCl_4GaP_5$	$C_{30}H_{47}AuCl_6GaP_5$	$C_{27}H_{36}AuF_6N_2P_4Sb$	$C_{20}H_{14}CuF_6P_5Sb$	$C_{29}H_{45}CuF_6P_5Sb$
M	830.75	1041.96	945.17	721.56	847.79
Crystal System	Monoclinic	Triclinic	Monoclinic	Triclinic	Triclinic
Space Group	*P*2(1)/*c*	$P\bar{1}$	*P*2(1)/*n*	$P\bar{1}$	$P\bar{1}$
a/Å	12.2858(19)	8.8067(2)	9.2810(3)	13.3910(6)	8.8000(18)
b/Å	8.8186(14)	12.6087(4)	17.5603(5)	14.2523(6)	14.010(3)
c/Å	26.275(4)	18.7608(5)	20.6174(7)	16.2037(8)	14.490(3)
α/°	90	89.8020(10)	90	91.172(3)	79.77(3)
β/°	96.759(6)	82.2230(10)	95.478(2)	118.927(3)	85.87(3)
γ/°	90	77.8600(10)	90	90.200(3)	83.05(3)
V/Å^3	2826.9(8)	2017.23(10)	3344.82(18)	2705.8(2)	1742.8(6)
Z	4	2	4	4	2
ρ_{calc}/g cm^{-3}	1.952	1.712	1.877	1.771	1.616
μ/mm^{-1}	17.017	4.916	5.434	2.130	1.666
T/K	100(2)	100(2)	100(2)	100(2)	100(2)
$2\theta_{max}$	133.46	55.28	67.34	55.36	67.82
Reflections: total/independent	14937/4855	52426/9381	74936 /12329	13098/13098	11548/11548
R_{int}	0.0441	0.0240	0.0431	-	-
Final *R*1 (I>2σ), *wR*2 (all data)	0.0568, 0.1573	0.0168, 0.0428	0.0249, 0.0424	0.0620, 0.1489	0.0333, 0.0609
Largest peak, hole/eÅ^{-3}	3.477, -1.754	0.764, -0.505	0.974, -1.386	3.718, -1.398	0.599, -0.599

Computational details

All gas-phase calculations on [{P^{t}Bu$_2$(*o*-biphenyl)}Au(η^2-P$_4$)]$^+$, the related intermediates and transition states were performed using the Gaussian 09 software package,[16] with the density functional method BP86.[17] The SDD[18] basis set was used for Au while TZP[19] was used for P, and polarization functions were added (Au: ζ_f = 1.05, P: ζ_d = 0.387).[20] For the six C atoms of the arene ring, the TZP basis set was used while for all the other C and H atoms, SVP[21] was used. The atoms in molecules (AIM) analysis was performed with the AIM2000 software package[22] using an all-electron basis set of double zeta quality (ADZP)[23] for Au, instead of the SDD pseudopotential and associated basis set. Frequency calculations were carried out to verify all of the stationary points as energy minima (zero imaginary frequency) and transition states (one imaginary frequency), and to provide free energies at 298.15 K including entropic contributions. Single point calculations for all the structures were performed with the BP86+D3[24] method with the same basis sets, in order to obtain dispersion-corrected relative free energies. The energies quoted in this paper are all dispersion-corrected unless specifically mentioned.

Acknowledgements

We thank the University of Bristol for funding (L.C.F.), the European Union for funding PhoSciNet through COST Action CM0802, and Rhodia plc for their generous gift of white phosphorus. We thank Dr Martin Murray (Bristol) for his help in modelling nmr spectra.

Keywords: Coinage metals • White phosphorus • Cations • P_4 activation • Density functional theory

[1] a) B. M. Cossairt, N. A. Piro, C. C. Cummins, *Chem. Rev.* **2010**, *110*, 4164-4177; b) M. Caporali, L. Gonsalvi, A. Rossin, M. Peruzzini, *Chem. Rev.* **2010**, *110*, 4178-4235; c) M. Scheer, G. Balazs, A. Seitz, *Chem. Rev.* **2010**, *110*, 4236-4256.

[2] a) I. Krossing, L. van Wüllen, *Chem. Eur. J.* **2002**, *8*, 700-711; b) H. C. Tai, I. Krossing, M. Seth, D. V. Deubel, *Organometallics* **2004**, *23*, 2343-2349; c) P. Dapporto, S. Midollini, L. Sacconi, *Angew. Chem. Int. Ed.* **1979**, *18*, 469-469; d) I. de los Rios, J. R. Hamon, P. Hamon, C. Lapinte, L. Toupet, A. Romerosa, M. Peruzzini, *Angew. Chem. Int. Ed.* **2001**, *40*, 3910-+; e) M. Peruzzini, L. Marvelli, A. Romerosa, R. Rossi, F. Vizza, F. Zanobini, *Eur. J. Inorg. Chem.* **1999**, 931-933.

[3] A. P. Ginsberg, W. E. Lindsell, *J. Am. Chem. Soc.* **1971**, *93*, 2082-2084.

[4] L. C. Forfar, T. J. Clark, M. Green, S. M. Mansell, C. A. Russell, R. A. Sanguramath, J. M. Slattery, *Chem. Commun.* **2012**, *48*, 1970-1972.

[5] a) W. E. Lindsell, K. J. McCullough, A. J. Welch, *J. Am. Chem. Soc.* **1983**, *105*, 4487-4489; b) A. P. Ginsberg, W. E. Lindsell, K. J. McCullough, C. R. Sprinkle, A. J. Welch, *J. Am. Chem. Soc.* **1986**, *108*, 403-416.

[6] B. M. Cossairt, C. C. Cummins, A. R. Head, D. L. Lichtenberger, R. J. F. Berger, S. A. Hayes, N. W. Mitzel, G. Wu, *J. Am. Chem. Soc.* **2010**, *132*, 8459-8465.

[7] a) J. S. Dewar, *Bull. Soc. Chim. Fr.* **1951**, *18*, C71-C79; b) J. Chatt, L. A. Duncanson, *J. Chem. Soc.* **1953**, 2939-2947.

[8] D. V. Deubel, *J. Am. Chem. Soc.* **2002**, *124*, 12312-12318.

[9] L. C. Forfar, T. J. Clark, M. Green, S. M. Mansell, C. A. Russell, R. A. Sanguramath, J. M. Slattery, *Chem. Commun.* **2012**, *48*, 1970-1972.

[10] P. Perez-Galan, N. Delpont, E. Herrero-Gomez, F. Maseras, A. M. Echavarren, *Chem. Eur. J.* **2010**, *16*, 5324-5332.

[11] M. Di Vaira, M. P. Ehses, M. Peruzzini, P. Stoppioni, *Eur. J. Inorg. Chem.* **2000**, 2193-2198.

[12] V. Mirabello, M. Caporali, V. Gallo, L. Gonsalvi, D. Gudat, W. Frey, A. Ienco, M. Latronico, P. Mastrorilli, M. Peruzzini, *Chem. Eur. J.* **2012**, *18*, 11238-11250.

[13] G. Santiso-Quiñones, A. Reisinger, J. Slattery, I. Krossing, *Chem. Commun.* **2007**, 5046-5048.

[14] I. Krossing, *J. Am. Chem. Soc.* **2001**, *123*, 4603-4604.

[15] A. K. Al-Sa'Ady, C. A. McAuliffe, R. V. Parish, J. A. Sandbank, R. A. Potts, W. F. Schneider, in *Inorg. Synth.*, John Wiley & Sons, Inc., **2007**, pp. 191-194.

[16] Gaussian 09, Revision D.01, M. J. Frisch, G. W. Trucks, H. B. Schlegel, G. E. Scuseria, M. A. Robb, J. R. Cheeseman, G. Scalmani, V. Barone, B. Mennucci, G. A. Petersson, H. Nakatsuji, M. Caricato, X. Li, H. P. Hratchian, A. F. Izmaylov, J. Bloino, G. Zheng, J. L. Sonnenberg, M. Hada, M. Ehara, K. Toyota, R. Fukuda, J. Hasegawa, M. Ishida, T. Nakajima, Y. Honda, O. Kitao, H. Nakai, T. Vreven, J. A. Montgomery, Jr., J. E. Peralta, F. Ogliaro, M. Bearpark, J. J. Heyd, E. Brothers, K. N. Kudin, V. N. Staroverov, T. Keith, R. Kobayashi, J. Normand, K. Raghavachari, A. Rendell, J. C. Burant, S. S. Iyengar, J. Tomasi, M. Cossi, N. Rega, J. M. Millam, M. Klene, J. E. Knox, J. B. Cross, V. Bakken, C. Adamo, J. Jaramillo, R. Gomperts, R. E. Stratmann, O. Yazyev, A. J. Austin, R. Cammi, C. Pomelli, J. W. Ochterski, R. L. Martin, K. Morokuma, V. G. Zakrzewski, G. A. Voth, P. Salvador, J. J. Dannenberg, S. Dapprich, A. D. Daniels, O. Farkas, J. B. Foresman, J. V. Ortiz, J. Cioslowski, and D. J. Fox, Gaussian, Inc., Wallingford CT, 2013.

[17] a) A. D. Becke, *Phys. Rev. A* **1988**, *38*, 3098-3100; b) J. P. Perdew, *Phys. Rev. B* **1986**, *33*, 8822-8824.

[18] D. Andrae, U. Haussermann, M. Dolg, H. Stoll, H. Preuss, *Theor. Chim. Acta.* **1990**, *77*, 123-141.

[19] P. L. Barbieri, P. A. Fantin, F. E. Jorge, *Mol. Phys.* **2006**, *104*, 2945-2954.

[20] a) A. W. Ehlers, M. Böhme, S. Dapprich, A. Gobbi, A. Hollwarth, V. Jonas, K. F. Köhler, R. Stegmann, A. Veldkamp, G. Frenking, *Chem. Phys. Lett.* **1993**, *208*, 111-114; b) A. Höllwarth, M. Böhme, S. Dapprich, A. W. Ehlers, A. Gobbi, V. Jonas, K. F. Köhler, R. Stegmann, A. Veldkamp, G. Frenking, *Chem. Phys. Lett.* **1993**, *208*, 237-240.

[21] A. Schafer, H. Horn, R. Ahlrichs, *J. Chem. Phys.* **1992**, *97*, 2571-2577.

[22] F. Biegler-Konig, J. Schonbohm, D. Bayles, *J Comput Chem* **2001**, *22*, 545-559.

[23] A. C. Neto, F. E. Jorge, *Chem. Phys. Lett.* **2013**, *582*, 158-162.

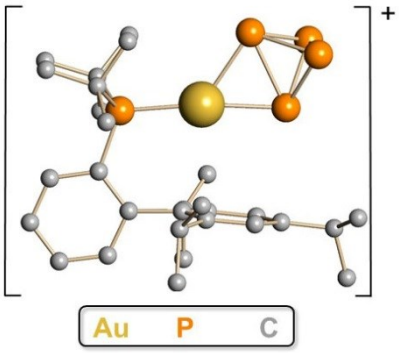
[24] S. Grimme, J. Antony, S. Ehrlich, H. Krieg, *J. Chem. Phys.* **2010**, *132*.

WILEY-VCH

Entry for the Table of Contents (Please choose one layout)

FULL PAPER

A series of cationic white phosphorus complexes of the coinage metals Au and Cu have been synthesised and investigated both in the solid state and in solution. Electronic structure calculations have been used to probe both static and dynamic features of the complexes.



Laura C. Forfar, Dihao Zeng, Michael Green, John E. McGrady and Christopher A. Russell**

Page No. – Page No.

Probing the Structure, Dynamics and Bonding of Coinage Metal Complexes of White Phosphorus

WILEY-VCH